

ALMA MATER STUDIORUM - UNIVERSITA' DI BOLOGNA

DOTTORATO DI RICERCA IN
INGEGNERIA ELETTRONICA, INFORMATICA E DELLE
TELECOMUNICAZIONI

CICLO: XXVI

Settore Concorsuale di afferenza: 09/E3 Elettronica
Settore Scientifico disciplinare: ING-INF/01 Elettronica

Sparse Signal Representation of Ultrasonic Signals for Structural Health Monitoring Applications

Presentata da: **Alessandro Perelli**

Coordinatore Dottorato:

Prof. **Alessandro Vanelli Coralli**
.....

Relatore:

Prof. **Guido Masetti**
.....

Correlatore:

Dr. Ing. **Luca De Marchi**
.....

Correlatore:

Prof. **Nicolò Speciale**
.....

ESAME FINALE ANNO 2014

... to my family

Abstract

Assessment of the integrity of structural components is of great importance for aerospace vehicles and systems, land and marine transportation, civil infrastructures and the oil industry, as well as other biological and mechanical applications. In such a context, guided waves (GW)-based inspection is an attractive means for structural health monitoring (SHM).

In this thesis, the study and development of techniques to process ultrasonic signals and time-frequency analysis in the context of applications of non-destructive testing of structures will be presented. In particular, the research topics will focus on the implementation of an embedded system for the localization of impacts on aluminum plates and of composite material together with the time-frequency analysis techniques for compression and reconstruction of the ultrasonic signals and compressive sensing techniques for the acquisition with a sampling frequency lower than the Nyquist one and localization of defects.

In guided wave inspections, it is necessary to address the problem of the dispersion compensation based on the unitary warping operator that maps the frequencies axis through a function derived by the group velocity of the material. This operator is used to remove from the acquired signals the dependence on the distance traveled.

It was subsequently developed an embedded system for structural monitoring based on ultrasonic waves to detect impacts. The procedure developed is based on sampling of signals acquired by 4 piezoelectric sensors placed in a sparse manner on the structure of interest and a card with STM32F4 Microcontrollers ARM Cortex - M4,

which is used to implement the signal processing algorithm. The problem of the determination of the instant of impact has been solved through the cross-correlation of the signals acquired in warped frequency domain that has been implemented by applying the Fourier transform followed by the non-uniform cross-correlation classical in the frequency domain and subsequently using the classical inverse Fourier transform. Through the cross-correlation of signals related to the same event but acquired in different positions, the difference of the distances traveled can be determined and used to locate the impact through a hyperbolic positioning algorithm.

As regards the study of techniques for time-frequency analysis of ultrasonic signals, a new procedure for compression and reconstruction of ultrasonic signals based on Compressive Sensing (CS) has been developed and applied guided waves analysis. Beside the study of subsampling techniques for the acquisition of signals, an algorithm for the dispersive localization of structural defects based on the concept of (CS) for the reconstruction of the impulse response of the structure under examination will be presented. To locate the defect, it is necessary to identify the impulse response of the medium and the contribution due to the reflections caused by the defect. This algorithm uses the convolutive “model” of the propagation of ultrasonic guided waves with a sparse representation in the warped frequency domain. This system has been applied both to decrease the sampling frequency to improve both the spatial localization of defects in monitoring systems using Lamb waves. The stage of reconstruction is based on an approach of alternating minimization and iterative estimation of the support to improve the accuracy through the estimation of both the shape of the pulse excitation of the impulse response. The proposed model has been tested via simulation and finite element Comsol PZFlex and currently there is an ongoing activity of validation of the results of composite plates in the laboratory.

Sommario

In questa tesi viene presentato lo studio e lo sviluppo di tecniche di processamento di segnali ultrasonici e analisi tempo-frequenza nell'ambito di applicazioni di test non distruttivo di strutture. In particolare gli argomenti di ricerca si si concentrano sull'implementazione su sistema embedded di algoritmi per la localizzazione di impatti in piastre di alluminio e di materiale composito insieme a tecniche di analisi tempo-frequenza per la compressione e ricostruzione di segnali ultrasonici e tecniche di compressive sensing per l'acquisizione con frequenze di campionamento inferiori a quella di Nyquist e localizzazione di difetti.

Nelle applicazioni basate su guide d'onda è necessario affrontare preliminarmente il problema della dispersione per questo motivo la fase di studio è iniziata dall'analisi di algoritmi di compensazione della dispersione basati sull'operatore unitario di warping che mappa l'asse delle frequenze attraverso una funzione definita a partire dalla velocità di gruppo del materiale in esame. Tale operatore viene utilizzato per rimuovere dai segnali acquisiti la dipendenza dalla distanza percorsa.

Successivamente è stato sviluppato un sistema embedded per il monitoraggio strutturale basato su onde ultrasoniche per il rilevamento di impatti. La procedura sviluppata si basa sul campionamento dei segnali acquisiti da 4 sensori piezoelettrici posti in maniera sparsa sulla struttura di interesse e una scheda STM32F4 con microcontroller ARM Cortex-M4 che è utilizzato per implementare l'algoritmo di processamento dei segnali.

Il problema della determinazione dell'istante di impatto è stato risolto attraverso

la cross-correlazione dei segnali acquisiti nel dominio della frequenza warped che è stato implementata applicando la Trasformata di Fourier non uniforme seguita dalla cross-correlazione classica nel dominio della frequenza e successivamente utilizzando la classica Trasformata di Fourier Inversa. Attraverso la cross-correlazione di segnali relativi allo stesso evento ma acquisiti in diverse posizioni, la differenza delle distanze percorse può essere determinata e usata per localizzare l'impatto attraverso un algoritmo di posizionamento iperbolico.

Per quanto riguarda lo studio di tecniche tempo-frequenza per l'analisi di segnali ultrasonici, una nuova procedura per la compressione e ricostruzione di segnali ultrasonici basata sul Compressive Sensing è stata sviluppata ed applicata all'analisi della propagazione di onde guidate dispersive; infine è stato effettuato un confronto con uno schema di riferimento tradizionale rappresentato dall'algoritmo Embedded Zerotree Wavelet e codifica Huffman.

Nell'ambito dello studio di tecniche di sottocampionamento per l'acquisizione di segnali dispersivi al fine della localizzazione di difetti strutturali verrà presentato un algoritmo basato sul concetto di Compressed sensing per la ricostruzione della risposta impulsiva della struttura in esame. Per localizzare il difetto è necessario individuare nella risposta impulsiva del mezzo il contributo dovuto alle riflessioni indotte dal difetto stesso. Tale algoritmo utilizza il modello "convoluzione" della propagazione di onde guidate ultrasoniche con una rappresentazione sparsa nella base nel dominio frequenza warped. Tale sistema è stato applicato sia per diminuire la frequenza di campionamento sia per migliorare la localizzazione spaziale dei difetti in sistemi di monitoraggio tramite onde Lamb. Lo stadio di ricostruzione è basato su un approccio di minimizzazione alternata e stima iterativa del supporto per migliorare l'accuratezza tramite la stima sia della forma dell'impulso eccitazione che della risposta impulsiva. Il modello proposto è stato testato tramite simulatore agli elementi finiti Comsol e PZFlex ed attualmente è in corso una attività di validazione dei risultati su piastre di composito in laboratorio.

Acknowledgements

This thesis is the culmination of three memorable years spent at the University of Bologna and I would be remiss not to thank all the wonderful people that have contributed, directly or otherwise, to its creation. First and foremost, I wish to express my gratitude to my advisors Prof. Guido Masetti, Dr. Ing. Luca De Marchi who always followed me with patience, Prof. Nicolò Speciale and Prof. Alessandro Marzani for life in general and to be a constant source of research inspiration and for the great opportunity to travel in amazing places for conferences and to know in deep the research atmosphere. I thank each of them for helping me grow as a researcher. I wish to thank Dr. Steven Freear for their great perspective and feedback and his group of researcher, Sevan, Benjamin, Peter, David, James, Robert, Chau, Mohamed for the friendly atmosphere and for the unforgettable moments spent at the University of Leeds.

My academic experience in Bologna has been enriched by a motley crew of students, post-docs, professors. I wish to express my thanks in particular to Francesca, Mahdi, Roberto with whom I experienced the beauty of walk and bicycle on Bologna hills also with Luca, Pasquale “the boss”, Gaetano, Martino, Simona, Giovanni, Federico, Fabio, Giuliano, Ilaria, Nicola, Susanna.

I would like to thank my first student I helped as thesis co-supervisor, Tommaso for the friendship, the beautiful conversations and research moments. I could not have asked for a more interesting and fun group to work with.

Outside of work, I have been fortunate to live in Bologna, a stunning city, full of

history, full of people, students (including the unknown curly girl...). Bologna is definitely a place to live. I cannot forget to remember the memorable moment spent every day on summer with my old bicycle on the fascinating Bologna hills always discovering new and unexpected stunning landscapes.

Thanks to my roommate Francesco for their valiant efforts to teach me how to cook, and for providing several memorable dialogues at night. Special thanks to have met my Leeds flatmates and student now scattered across the globe for the unforgettable fun-filled experience and friendship: Christelle, Waleed, Javier, Cayetano, Mark, Shirakata, Raed, Huynh, Sam, the International Cafè group, for the great memories and beautiful moments and life spent in Leeds. Sorry if I miss someone... but I take you in my heart with my family that helped me always in my life.

I hope that they continue to find happiness in wherever their paths lead them.

Contents

List of Figures	xii
List of Tables	xvii
Introduction	1
1 Guided Waves based SHM	5
1.1 Introduction	5
1.2 Basic Model of Propagating Lamb Waves	7
1.3 Rayleigh-Lamb equations	8
1.4 Guided Waves on Composites	10
1.5 Genetic Algorithm	12
1.6 Numerical and Experimental Testing	14
2 Structural Health Monitoring Applications	17
2.1 Passive systems for SHM	19
2.2 Active systems for SHM	19
2.3 Signal processing for Structural Health Monitoring	24
3 Frequency Warping Operator	26
3.1 Introduction	26
3.2 Notation	27
3.3 Frequency Warping	27
3.4 Dispersion Compensation Representation	29
4 Impact Localization	32
4.1 Motivation	32
4.2 Introduction	33
4.3 Dispersion Compensation with the Warped Transform	36
4.3.1 The warping frequency transform (WFT)	36
4.3.2 Warping a wave detected passively	39
4.3.3 Warping Reverberating Waves	40

4.4	Warped Wavelet Transform using Cross-Correlating Basis	41
4.5	Hyperbolic positioning	42
4.6	Cramèr-Rao bound	43
4.7	Experimental verification	47
4.8	Discussion	56
5	Frequency Warped Wavelet	58
5.1	Introduction	58
5.2	Frequency Warped Wavelet Analysis	61
5.3	Frequency Warped Wavelet Multiresolution	66
5.3.1	Exponential B-Spline Multiresolution	69
5.4	Frequency Warped Cross Wavelet Analysis	71
5.5	Cramèr - Rao lower bound	73
5.6	Experimental verification	75
5.7	Discussion	83
6	Embedded Ultra-Low Power Device for Impact Localization	84
6.1	Introduction	84
6.2	Motivation	85
6.3	Hardware Design	87
6.4	Experimental Verification	89
6.5	Composite Z-stiffened Plate	93
6.6	SHM System: Node Sensor and PZT Transducers	96
6.7	Discussion	97
7	Damage Localization	99
7.1	Introduction	99
7.2	Group delay compensation	101
7.2.1	Step 1: dispersion compensation	101
7.2.2	Step 2: warped signal compression	106
7.3	Experimental verification	108
7.3.1	Data acquisition	108
7.3.2	Two-step signal processing	111
7.3.3	Defect imaging	113
7.4	Discussion	116
8	Localization of Defects in Irregular Waveguides by Dispersion Compensation and Pulse Compression	117
8.1	Introduction	117
8.2	Defect Locating Procedure	119
8.2.1	Group delay computation	119
8.3	Reference and irregular portions of the waveguide	121
8.4	Compensation of the reference portion (RP)	121
8.5	Compensation of the irregular portion (IP)	122
8.6	Numerical Application	123

8.7	Results	128
8.8	Discussion	130
9	Warped-Wigner-Hough Transformation of Lamb Waves for Automatic Defect Detection	131
9.1	Introduction	131
9.2	The Warped Frequency Transform (WFT)	132
9.3	The Wigner-Hough Transform (WHT)	132
9.4	Warping Map Design and Wave Simulation	133
9.5	Defect Detection	135
9.6	Discussion	138
10	Compressive Sensing	139
10.1	Review of Compressive Sensing	140
10.2	Analog Compressive Sampling Acquisition	141
10.3	Model-based Compressive Sensing	143
10.3.1	Convolutional Models for Pulse Streams	144
10.4	Recovery of dispersive pulse streams	145
10.4.1	Frequency Warped Convolutional Models	145
10.4.2	Pulse Stream Recovery in the Frequency Warped domain . . .	147
10.4.3	Alternating Minimization With Exhaustive Search	148
10.4.4	Iterative Support Estimation	149
11	Model-Based Compressive Sensing for Damage Localization	152
11.1	Introduction	152
11.2	Experimental verification	156
11.3	Discussion	163
12	Multi-Channel Distributed Compressed Sensing for Impact Local- ization in Composite Plates	164
12.1	Introduction	164
12.2	Recovery of Anisotropic Dispersive Pulse Streams	165
12.2.1	Frequency Warped Dictionary Design	167
12.2.2	Warped Convolutional Anisotropic Models	168
12.2.3	Separation-Based Joint Decoding	170
12.2.4	Pulse Stream Recovery in the Frequency Warped domain . . .	172
12.3	Verification	173
12.3.1	Results	175
13	Compressive Sensing for Wireless Transmission	177
13.1	Introduction	177
13.2	Parametrized Discrete Wavelet Packet Transform	179
13.3	Data compression procedures	183
13.3.1	Embedded Zerotree wavelet coding	183

13.3.2 Compressed Sensing Best-Basis Wavelet Packet	184
13.4 Compressed Sensing in Group-Delay Covariant Basis	186
13.5 Experimental Verification	189
13.5.1 Best Basis Wavelet Packet with Embedded Zerotree Coding	191
13.5.2 Performance comparison	194
13.5.3 Impact Localization Performances with and without signal compression	196
13.6 Discussion	197
Conclusions	199
Publications	202
Bibliography	206

List of Figures

0.1	Aerospace, oil and gas industry, chemical and power generation plants are potential fields of application for SHM.	2
1.1	One dimensional plate model. A surface stress $\mathbb{T}(\omega)$ normal to the plate excites propagating modes in the plate.	7
1.2	Lamb waves dispersion curves for a 2.54-mm thick aluminum plate. (a) Group velocity $c_g(f)$, (b) wavelength $\lambda(f)$	10
1.3	Extraction of modal group-delays through the reassigned spectrogram.	12
1.4	Calculation of the distance between an extracted ridge point and the slowness curve for a given mode.	13
1.5	Ridge extraction from experimental bamboo data.	16
3.1	Tiling of the time-frequency plane (a) for the short-time Fourier transform and (b) for the wavelet transform. Atoms are symbolically represented by rectangles. The solid curves represent the dispersive group delay curves for the Lamb waves for a traveled distance of 1 m.	30
4.1	A typical three-step acoustic emission source location procedure.	33
4.2	Warping map $w(f)$ for A_0 wave dispersion compensation and its functional inverse $w^{-1}(f)$ designed according to Equation 4.1.	37
4.3	$c_g(f)$ dispersion curves for the Lamb waves propagating in an aluminium 0.003 m thick-plate.	37
4.4	Graph of the proposed localization algorithm	40
4.5	Cramèr - Rao lower bound for the four sensors configurations tested experimentally in Section 4.7. Isolines express CRLB in mm.	46
4.6	Sample acquired signals by the passive monitoring system.	48
4.7	Wavelet transform of the two warped cross-correlating signals obtained for impact located in $x = 0.15$ m $y = 0.15$ and the related $\ a_j(n)\ $ curves.	49
4.8	Comparison in function of the difference in distance between the warped cross-correlated signal and the curve $\ a_j(n)\ $	51
4.9	Source localization results.	53

4.10	Cumulative distribution of the localization errors.	54
4.11	Comparison between the Cramèr-Rao lower bound and the experimentally estimated positions.	56
5.1	A typical three-step acoustic emission source location procedure.	59
5.2	Tiling of the time-frequency plane for the frequency warped wavelet transform (a) for the A_0 and (b) S_0 mode (c) A_0 and S_0 . The solid curves represent the dispersive group delay curves for the Lamb waves for a traveled distance of 1 m.	65
5.3	A_0 frequency warped E-spline wavelet function at $n = 6$ and $n = 7$	71
5.4	Graph of the proposed DDOA algorithm.	72
5.5	Experimental setup.	76
5.6	Sample acquired signals by the passive monitoring system: (a) signals in time domain, (b) Warped time domain version.	77
5.7	Comparison in function of the difference in distance between the warped cross-correlated signal and the curve $\ x_n[m]\ $: (a) impact in $x = 0.45$ m $y = 0.35$ m, (b) impact in $x = 0.85$ m $y = 0.15$ m.	78
5.8	Source localization results.	80
5.9	Cumulative distribution of the localization errors.	81
5.10	Comparison between the Cramèr-Rao lower bound and the experimentally estimated positions: 3 sensors asymmetric respect to the edges.	82
6.1	Structure of the embedded SHM system for impact detection	86
6.2	Experimental setup	89
6.3	Current consumption for different sampling frequencies	90
6.4	Localization error for different sampling frequencies	91
6.5	Dependency of the localization error with the current	92
6.6	Dependency of $\frac{I_d(mA)}{e(mm)}$ with the sampling frequency	92
6.7	Composite Z-stiffened plate provided by Critical Materials with four PZT transducers installed.	93
6.8	Predicted wavelength and group velocity dispersion curves (left column). Predicted dispersion curves over imposed the signals acquired from a frequency sweep (right plot).	95
6.9	Comparison between the estimated (crosses \times) and actual (circles \circ) impact locations. A mean error smaller than 10 mm was achieved in coordinate estimation.	97
7.1	(a) group velocity dispersion curves $c_g(f)$ for the Lamb waves propagating in an aluminum 3 mm thick-plate (Young modulus $E = 69$ GPa, Poisson's coefficient $\nu = 0.33$, density $\rho = 2700$ kg/m ³). (b) Warping map $w(f)$ for A_0 wave dispersion compensation and its functional inverse $w^{-1}(f)$ designed according to Eq. 7.1.	102
7.2	Dispersion compensation of a dispersive signal $s(t, D)$. (a) exciting spiky pulse $s(t, 0)$ starting at $t = 0$ s. (b) dispersive signal $s(t, D)$ at a traveling distance $D = 300$ mm. (c) warped signal $\mathbf{W}_w\{s(t, D)\}$	103

7.3	(a) actuated chirped pulse $s(t, 0)$. (b) simulated dispersive wave $s(t, D)$ acquired at a traveling distance $D = 300$ mm. (c) warped signal $\mathbf{W}_w\{s(t, D)\}$. Subplots (d), (e) and (f) represent the spectrograms of the signals in (a), (b) and (c), respectively. In the same plots, the dashed lines represent group delays estimated according to Eq. (7.6), Eq. (7.8) and Eq. (7.9), respectively.	105
7.4	Subplots (a), (b), and (c) represent the time-waveform $s(t, D)$, the warped waveform $\mathbf{W}_w\{s(t, D)\}$, and the chirp compressed warped signal $\mathbf{F}^{-1}S_i^{\text{comp}}$, at a traveling distance $D = 300$ mm, respectively. In subplots (d), (e) and (f) the same information for a traveling distance $D = 500$ mm.	107
7.5	Experimental set up used to validate the defect location procedure: \mathbf{A} actuator, \mathbf{R} receivers, \mathbf{M} added mass.	108
7.6	Gaussian modulated chirp used as input signal sent from the central PZT transducer \mathbf{A}	109
7.7	Signals acquired by the PZT sensors. The mass is in $x = 0.35$ m, $y = 0.35$ m, and a chirped signal was actuated.	110
7.8	Spectrogram of the signal acquired by Receiver 1 in Fig. 7.7. The superimposed dots \circ represent the dispersive group delay for the A_0 mode scattered by the defect.	111
7.9	Estimated Lamb waves frequency response of the PZT transducers adopted in this study. The dashed line represents the cut off frequency selected for filter design.	112
7.10	Envelopes of the warped compressed signals $E_R(x) = \text{env}(\mathbf{F}^{-1}S_R^{\text{comp}})$, $R \in \{1, 2, 3\}$	113
7.11	Defect imaging with the processed signals of Fig. 7.10	114
7.12	Comparison between the estimated (crosses \times) and actual (circles \circ) defect positions. A mean error smaller than 5 mm was achieved in coordinates estimation.	115
7.13	Proposed procedure cumulative error in the location of the 36 emulated defects.	115
8.1	(a) Irregular waveguide composed by two aluminum plates 8 mm thick and a plate 4 mm thick; the three portions are connected with 45° short tapered portions. (b) Schematic cross-section of the irregular waveguide. Note the different scale in the x and y directions	118
8.2	Time and frequency representation of the imposed displacement used to mainly excite the S_0 mode in the irregular waveguides.	124
8.3	(a) Plane strain (#1 - #3) models used to compute the time-transient responses. (b) Time-transient responses $v_A(t)$ acquired at $x = 201$ mm for the three cases (#1 - #3).	125
8.4	Guided wave propagation in the pristine irregular plate. Snapshots of the Von Mises stress at $20 \mu\text{s}$, $40 \mu\text{s}$, $60 \mu\text{s}$ and $70 \mu\text{s}$. Deformation scale factor was assumed equal to $1e^7$	126

8.5	Snapshots of the Von Mises stress in proximity of the defect taken at $54.4 \mu\text{s}$, $63 \mu\text{s}$, $72 \mu\text{s}$ for the model #2. Deformation scale factor was assumed equal to $2e^7$	127
8.6	(a-c-e) Spectra of $v_A(t)$ for the three examined cases. S_0 group delay curves for the incipient W1 and the notch/BC reflection W2n paths have been superimposed. (b-d-f) Normalized H_{env} of the compensated signals. The vertical red lines mark the actual defect position.	129
9.1	Computational flow of the Frequency Warping operator \mathbf{W}_w . \mathbf{F} and \mathbf{F}^{-1} are the direct and inverse Fourier Transform operators, respectively, while $w(f)$ and $\dot{w}(f)$ are the warping map and its first derivative.	132
9.2	Slowness dispersion curves for the Lamb waves propagating in a 2.54 mm-thick aluminum plate	133
9.3	Schematic representation of the damaged aluminum plate used in the time-transient FEM simulations (plate dimensions are in mm)	134
9.4	Time-dependent out-of-plane displacements recorded at three different positions on the plate	135
9.5	Results of the warping procedure applied to waveforms in Figure 9.4.	136
9.6	(a) Result of the equalization procedure applied to signal v_{wC} in Figure 9.5(c). (b) Wigner-Ville distribution.	137
9.7	Wigner-Hough Transform of the equalized warped signal in Figure 9.6(a). Peaks at $\theta = \{\frac{\pi}{2}, \frac{3\pi}{2}\}$ correspond to vertical lines in Figure 9.6(b); ρ coordinates provide the distance in pixels from the center of the analyzed image.	137
10.1	Compressed Sensing acquisition scheme: random modulation pre-integration	142
11.1	Sketch of the considered example: the signal is actuated in A, scattered by the defect D, reflected by the edge E, and sensed in R. Consequently, three waves are captured in the acquired waveform: those traveling along paths P1, P2 and P3, respectively.	153
11.2	(a) Actuated pulse s_0 , (b) N-dimensional synthetic signal s , (c) M-dimensional measurements vector y . In this example $N=900$ and $M=300$	154
11.3	Results of the CS decomposition procedure in terms of (a) estimated actuated pulse $\hat{s}_0 = \mathbf{W}^\dagger \hat{h}_w$ (where \hat{h}_w is the estimated impulse response in the warped domain), and (b) estimated warped reflectivity function \hat{x}_w	155
11.4	Experimental set-up used to validate the proposed CS procedure: A actuator, R receivers, m added mass.	157
11.5	Experimental results: (a) input chirp signal sent to the power amplifier and then to the PZT actuator (A), (b) signal acquired by sensor R_1 when the mass is placed at coordinates $x = 0.85$ m and $y = 0.45$ m.	158

11.6	Experimental results achieved by processing the acquired signal in Figure 11.5(b) with the proposed CS approach: (a) estimated actuated pulse, (b) reflectivity function reconstructed by the CS algorithm with superimposed the real distances related to the direct, scattered by the defect, and reflected paths.	159
11.7	Spectrogram of (a) the actuated chirp s_0 and of (b) the recovered estimated chirp \hat{s}_0	160
11.8	Cumulative error distribution in the estimation of $D_{A,m,X}$	162
12.1	Simplified aircraft wing model used in the simulations. Simulated set up used to validate the defect location procedure with PZFlex and Solidworks CAD importing	173
12.2	Simulated signals acquired by the 3 sensors whose coordinates are reported in Table 12.1.	174
12.3	Sparse signal after the CS recovery	175
12.4	Localization error comparison between compensation with and without Compressed Sensing acquisition	176
13.1	Computational tree of the Discrete Wavelet Transform.	180
13.2	Computational tree of the Wavelet Packet decomposition.	181
13.3	Pruned (Best Basis) Wavelet Packet decomposition.	181
13.4	Wavelet Packet with Embedded Zerotree-Huffman coding System	184
13.5	Best Basis WP Compressed Sensing scheme	185
13.6	Tiling of the time-frequency plane for the frequency warped wavelet transform for the A_0 . The solid curves represent the dispersive group delay curves for the Lamb waves for a traveled distance of 1 m.	187
13.7	Group velocity curve for the propagating A_0 mode for an aluminum plate of 3 mm of thickness	187
13.8	Best Basis Frequency Warped Wavelet Packet Compressed Sensing scheme	188
13.9	Sketch of the experimental setup adopted to acquire the lamb wave signals generated by impacts	189
13.10	Error ϵ in the nonlinear approximation of the acquired signals through the largest M coefficients for the parameterized Best Basis WP representation.	190
13.11	Reconstructed signals results in dependence of the EZT threshold	192
13.12	Performance comparison between EZT algorithm and Wavelet Compressed Sensing related to the PRD at different SNRs with CR = 70%.	194
13.13	Performance comparison related to the PRD at different compression ratios with SNR= 30dB.	195
13.14	Comparison of the localization cumulative error with and without signal compression.	196

List of Tables

1.1	Elastic properties $C_{ij}^{exp}(\theta^0)$ in [Gpa].	14
1.2	Identification results for $\Delta = 20$. Elastic coefficients in [GPa].	15
4.1	Sensors positions for the considered symmetrical and asymmetrical topologies.	47
5.1	Sensors positions for the considered symmetrical and asymmetrical topologies.	75
6.1	Acquisition and ADC settings	87
6.2	Algorithm computational cost	88
6.3	Mean Current Consumption	90
6.4	Properties of individual constituents of the CRFP laminated	94
6.5	Mechanical characterization of the CFRP (S.D. - Standard Deviation)	94
7.1	Actuator and receivers topology.	109
11.1	Actuator and receivers topology.	157
12.1	Actuator and receivers topology.	173
12.2	Localization error dependency on the quantization.	176
13.1	Best-Basis Compressed Sensing Algorithm	186
13.2	WP Filter coefficients.	190
13.3	Performances of the wavelet parametrized filter according to the EZW threshold.	191
13.4	Performance comparison of the Compressed Sensing framework with and without frequency warping (impact in (0.30, 0.30) m)	193
13.5	Localization error performances without and with compression according to the EZW threshold.	197

Introduction

The main objective of Nondestructive Evaluation (NDE) is the detection and characterization of defects that may compromise the integrity and the operability of a structure. Conventional inspection can be expensive and time consuming and, very often, the normal service of complex structures may be significantly affected.

In the last few decades the possibility of assessing continuously the integrity of complex structures has fostered intense research in the field of Structural Health Monitoring (SHM) and several SHM approaches based on different inspection techniques have been proposed [1].

The basic concept of SHM consists in inspecting a structure using permanently attached or embedded sensors. It is evident that a reliable SHM system can potentially alter the way complex structures are operated and maintained, because an optimal functionality can be guaranteed minimizing the time in which the structure is out of service and reducing significantly plant outage, as well as the costs associated with conventional inspection.

SHM can also be useful in estimating the remaining life of components and can be used to assess whether their replacement is needed.

Hence SHM appears extremely attractive for a wide number of engineering applications ranging from the aerospace industry, i.e. health monitoring of the fuselage of aircraft while in service, to the chemical and power generation industries, i.e. inspection of storage tanks, pressure vessels and pipelines.

Figure 0.1 shows some possible engineering applications for SHM.



Figure 0.1: Aerospace, oil and gas industry, chemical and power generation plants are potential fields of application for SHM.

The feasibility of an SHM methodology is strongly dependent on the possibility of effectively inspecting the structure from only a few locations.

Furthermore, it is crucial that the data recorded can be reliably interpreted to make damage detection possible. In addition, the development of a reliable SHM technology poses new challenges in several different fields, such as development of smart materials, integration of sensors with the structure to be inspected, acquisition and transmission of large amounts of data [2].

Among the SHM technologies, those based on ultrasonic guided waves have attracted a considerable attention in recent years. Ultrasonic guided waves offer the possibility of inspecting large areas from a small number of sensor positions and guided wave inspection is now an established approach in NDE. In addition, it has been demonstrated that acoustic emission signals in typical aircraft structures are a combination of the fundamental A_0 and S_0 modes and that long propagation distances can be achieved [3], [4].

Guided wave inspection is therefore attractive for the development of an SHM system for the inspection of complex structures. However, guided wave inspection of complex structures is difficult as the reflections from different features overlap.

Hence the ultrasonic time traces become very complicated and damage detection is

a difficult task, i.e. the reflection from the damage site can be masked by reflections coming from benign features.

The structure of this thesis broadly follows the sequence in which research was conducted during this work.

In Chapter 1 a brief review of Lamb waves based SHM propagation is described and an inverse procedure based on ultrasonic guided wave propagation is proposed for the bamboo fibers reinforced composites characterization. The procedure consists of an optimization problem in which the discrepancy between the experimental dispersion curves and those predicted through a numerical formulation is minimized. This tool can be also exploited to predict the dispersion curves for complex materials such as Carbon fibers or generic composite materials. This work has been published in [5].

Chapter 2 provides background informations about guided waves for SHM. In particular, the concepts of single unit and sparsely distributed arrays are illustrated and several applications of these two approaches found in literature are introduced. Subsequently the desirable requirements for robust signal processing of complicated ultrasonic time traces are described.

Chapter 3 describes the warping procedure in the frequency domain and how it can be exploited to compensate the dispersion of the Lamb waves leading to a sparsification of the signals.

In Chapters 4, 6, 5 the proposed algorithms to deal with the problem of passive monitoring, i.e. impact localization are addressed. At first a framework based on the cross-correlation between the dispersion compensated signals is described with the theoretical lower limit on the localization. The proposed algorithm has been implemented in an embedded board able to achieve low power consumption and experimentally verified on an aluminum and carbon fiber plate. Finally an improved version of the previous algorithm is developed in order to reduce the interference due to reflection; this can be obtained performing a wavelet analysis on the cross-correlated signal or performing a multiresolution wavelet analysis using a suitable family of frequency warping bases.

This developed works have been published in [6], [7], [8], [9].

In Chapter 7 a non-linear Lamb wave signal processing strategy aimed at extending the capability of active-passive networks of PZT transducers for defect detection is proposed. In particular, the proposed signal processing allows to use chirp shaped pulses in actuation, instead of classically applied spiky pulses. To this purpose, the acquired Lamb waves are processed by means of a two step procedure: a Warped Frequency Transform (WFT) to compensate the dispersive behavior of ultrasonic guided waves, followed by a pulse compression procedure. This damage localization procedure has been proposed in [10].

Chapter 8 presents a pulse-echo procedure suitable to locate defect-induced reflections in irregular waveguides. In particular, the procedure extracts the distance of propagation of a guided wave scattered from a defect within the echo signal, revealing thus the source-defect distance [11].

In Chapter 9 a non-linear signal processing is investigated to improve the defect detectability of Lamb wave inspection systems. The approach is based on a Warped Frequency Transform (WFT) to compensate the dispersive behavior of ultrasonic guided waves, followed by a Wigner-Ville time-frequency analysis and the Hough Transform to further improve localization accuracy. This work was presented in [12].

Chapters 10, 11, 12 present the new paradigm of Compressive Sensing (CS) in order to deal with the concept of sparsity of the signals. A CS approach for ultrasonic signal decomposition suitable to achieve high performance in Lamb waves based defects detection procedures in isotropic and composite materials has been developed.

This developed work has been published in [13].

Finally in Chapter 13 a novel signal compression and reconstruction procedure suitable for guided wave based SHM applications is presented. The proposed approach combines the wavelet packet transform and frequency warping to generate a sparse decomposition of the acquired dispersive signal. The sparsity of the signal in the considered representation is exploited to develop data compression strategy based on the Compressive sensing (CS) theory. The work has been presented in [14].

Guided Waves based SHM

Anxiety's like a rocking chair. It gives you something to do, but it doesn't get you very far.

Jodi Picoult

1.1 Introduction

Isotropic elastic bulk media support two types of wave motion, longitudinal and shear. A longitudinal wave has its displacement in the direction of propagation, while a shear wave has its displacement perpendicular to the direction of propagation. These waves propagate with different velocities, where the velocity of the shear wave, c_S , is lower than the longitudinal wave's velocity, c_L .

Consider a harmonic plane wave, $s(x, t)$, propagating along the x -axis in a medium. Harmonic refers to a wave consisting of a single angular frequency, ω . Waves having constant phase over a plane, in this case perpendicular to the x -axis, are referred to as plane waves.

The wave at position x and time t , can be described in complex form as

$$s(x, t) = Ae^{j(\omega t - kx)}$$

where k is the wavenumber and A is the amplitude of the wave.

The wavenumber k is related to the phase velocity of the wave, c_p , as

$$k = \frac{\omega}{c_p}$$

Henceforth, the harmonic dependency $e^{j\omega t}$ will be assumed implicitly for notational convenience. The longitudinal and shear waves mentioned above both have frequency independent phase velocities, which results in linear frequency-wavenumber relationships. This means that these waves are non-dispersive and the shape of the waves will be preserved during propagation. When the dimensions of the media approach the order of the wavelength, it starts behaving as a wave guide.

Waves propagating in a wave guide are called guided waves. Such waves in infinite elastic plates were first described and analyzed by Horace Lamb in 1917, and they are therefore called Lamb waves.

In application oriented publications, a commonly occurring name for guided waves in plates are guided Lamb waves. In contrast to bulk waves, guided waves are dispersive, i.e. they have frequency dependent velocity. This means that the shape of a wave packet changes during propagation. Another property Lamb waves shares with other types of guided waves is the possible existence of multiple propagation modes. These so called Lamb modes follow different dispersion relationships, i.e., the relation between phase velocity and frequency depends on the mode. As a consequence, there may be several propagation velocities even for a single frequency. Depending on the thickness of the plate and the frequency of the wave, anywhere from two to infinitely many Lamb modes can propagate in the plate.

Compared to Rayleigh waves, which propagate in a shallow zone below the surface of a material, Lamb waves have through-thickness displacement permitting detection of defects both within and close to the surface of the plate. This, along with their ability to propagate over long distances, make them suitable for both inspection and monitoring of plate structures. Beside Lamb waves, there is another type of guided wave modes in plates called shear horizontal (SH) modes. These modes propagate with displacements in-plane, i.e. parallel to the plate, compared to Lamb waves which have only out-of-plane, i.e. perpendicular to the plate, components perpendicular

to the direction of propagation. The SH-waves have not been given any special consideration in this work since the setup used for the experiments cannot detect this type of wave motion.

1.2 Basic Model of Propagating Lamb Waves

Consider an isotropic homogeneous plate of thickness d illustrated in Figure 1.1. In this plate, harmonic waves of angular frequency ω can propagate in a number of Lamb modes.

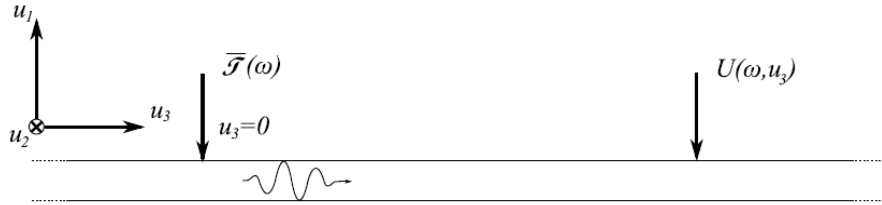


Figure 1.1: One dimensional plate model. A surface stress $\mathbb{T}(\omega)$ normal to the plate excites propagating modes in the plate.

Let $c_{p,n}(\omega)$ denote the phase velocity of the n -th mode at ω , yielding the corresponding wavenumber $k_n(\omega) = \omega/c_{p,n}(\omega)$.

Consider now a line source producing a harmonic surface stress perpendicular to the plate at $u_3 = 0$, with u_3 indicated in the figure, and let $\mathbb{T}(\omega)$ denote the amplitude of the stress. The excitation of mode n from the surface stress is modeled by the transfer function $H_n(\omega)$.

The normal displacement on the plate surface of the resulting wave propagating in the u_3 direction is then given by

$$U_n(\omega, u_3) = H_n(\omega)\mathbb{T}(\omega)e^{-jk_n(\omega)u_3}$$

The total displacement at u_3 is given as a superposition of the modes

$$U(\omega, u_3) = \sum_n H_n(\omega)\mathbb{T}(\omega)e^{-jk_n(\omega)u_3} \quad (1.1)$$

where the sum ranges over the possible modes at frequency ω . The above scenario corresponds to a line source. A better representation of the small array elements considered in this work is to consider them as pointlike sources. Such a source, producing an out-of-plane harmonic stress with amplitude $\mathbb{T}(\omega)$ at the origin, generates a cylindrical wave that will diverge radially as it propagates. Its displacement field can be approximated by

$$U(\omega, r) = \sum_n \frac{1}{\sqrt{r}} H_n(\omega) \mathbb{T}(\omega) e^{-jk_n(\omega)r}$$

1.3 Rayleigh-Lamb equations

Consider again the plate introduced in the previous section with thickness d . Lamb modes can be either symmetric, i.e. with symmetric wave shapes across the plate thickness, or antisymmetric, i.e. with antisymmetric wave shapes. A wavenumber, k , of a possible propagating Lamb mode for a given frequency, ω , is a real solution to the Rayleigh-Lamb characteristic equations

$$\frac{\tan(qd/2)}{\tan(pd/2)} = -\frac{4k^2pq}{(q^2 - k^2)^2} \quad \text{for symmetric modes} \quad (1.2)$$

$$\frac{\tan(qd/2)}{\tan(pd/2)} = -\frac{(q^2 - k^2)^2}{4k^2pq} \quad \text{for antisymmetric modes} \quad (1.3)$$

$$(1.4)$$

where

$$p^2 = (\omega/c_L)^2 - k^2 \quad \text{and} \quad q^2 = (\omega/c_S)^2 - k^2$$

c_L is the longitudinal wave velocity and c_S is the shear wave velocity.

As mentioned earlier, for a given frequency there are typically several wavenumbers satisfying the Rayleigh-Lamb equations 1.2, each corresponding to a separate mode. For the lowest frequencies there are two solutions, the fundamental (anti-)symmetric $(A_0)S_0$ mode. The successive solutions for increasing frequencies, result in higher order modes. These are numbered $(A_1)S_1$, $(A_2)S_2$, and so forth. The frequency limit above which a particular mode can exist is called the mode's cut-off frequency. To allow a simple notation in equations a single index, $n = 0, 1, 2, 3, \dots$, is used to

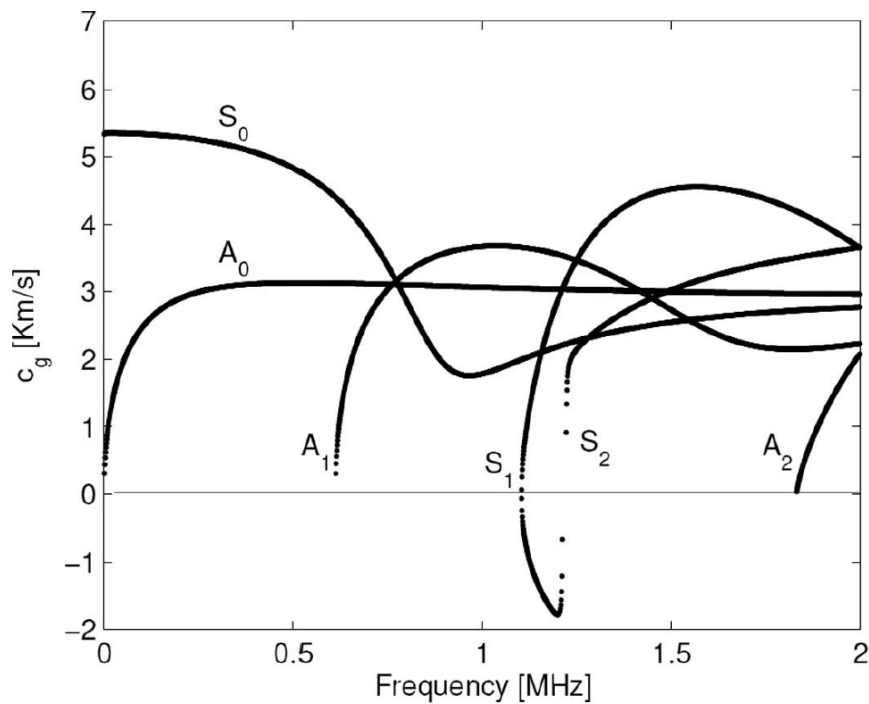
identify modes S_0 , A_0 , S_1 , A_1, \dots . The group velocity is the velocity at which the envelope of a narrowband wave packet propagates.

It is related to the wavenumber as

$$c_g = \frac{d\omega}{dk}$$

The group velocity provides insight into the amount of dispersion each mode is subjected to in various frequency bands. At frequencies where the group velocity changes sharply the wave is severely dispersed, while a frequency region with constant group velocity indicates low dispersion. As mentioned earlier, for non-dispersive media there is a linear relationship between the frequency and wavenumber, making the group velocity equal to the phase velocity $c_p = c_g$.

Figure 1.2 shows the phase and group velocities of the solutions to 1.2 for a 3 mm aluminium plate.



(a)

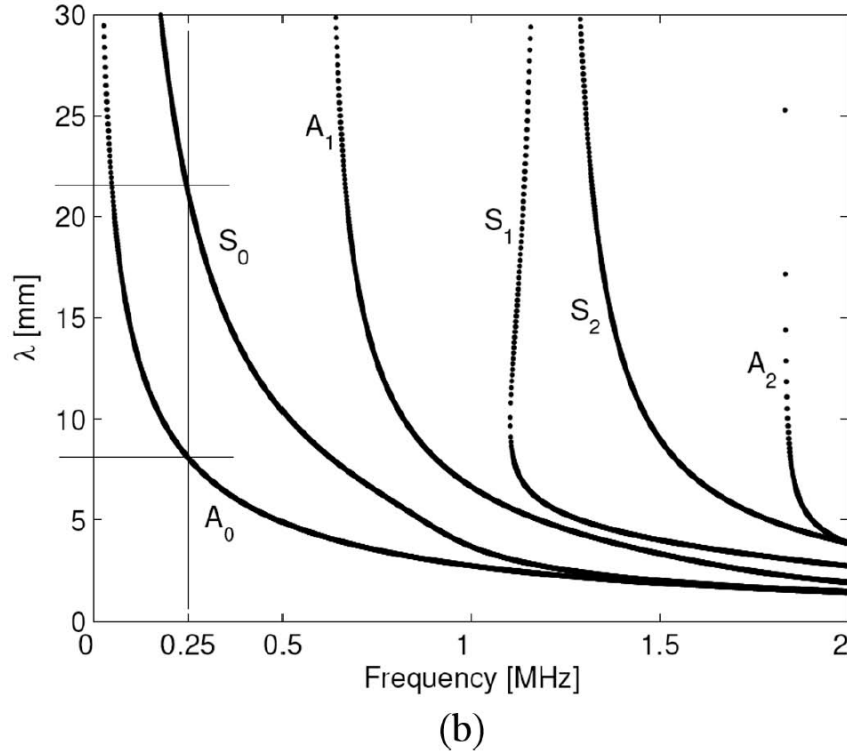


Figure 1.2: Lamb waves dispersion curves for a 2.54-mm thick aluminum plate. (a) Group velocity $c_g(f)$, (b) wavelength $\lambda(f)$.

In the next Section a procedure to estimate the dispersion curves for bamboo fibers which could be applied for generic composite materials is presented.

1.4 Guided Waves on Composites

In the present study, an inverse procedure based on ultrasonic guided wave propagation is proposed for the bamboo fibers reinforced composites characterization. The procedure consists of an optimization problem in which the discrepancy between the experimental dispersion curves and those predicted through a numerical formulation is minimized.

Elastic stress waves analysis is an especially attractive method for identification of elastic constants of either isotropic or orthotropic materials [15].

Numerous approaches based on bulk waves (BW) were proposed [16], and, more re-

cently, researchers are exploiting the dispersive properties of guided waves (GW) to characterize material properties in waveguides such as beam-like or plate-like structures. Compared to BW, the use of GW for material characterization provides a set of information at several different frequencies that can proficiently used for the identification procedure. In fact, for a given waveguide geometry, the wave dispersive behavior is related to material properties.

As the wave dispersive features and the inverse methods are numerous, the literature on inverse methods based on the propagation of GW is extensive [17].

In this Section we investigate the usage of group velocity dispersion curves and Genetic Algorithms (GA) to determine the elastic constants of waveguides.

In particular, we investigate guided wave characterization of bamboo laminates. The use of GA coupled with ultrasonic testing for material characterization is not new. For instance, Balasubramaniam and Rao [18] reconstructed material stiffness properties of unidirectional fiber-reinforced composites from obliquely incident ultrasonic BW data by using GA. More recently, a GA procedure where the optimization function is based on the Lamb waves velocities calculated for a single frequency-thickness value at different angles of propagation (using a circular array of receivers) was proposed to reconstruct all nine elastic moduli of orthotropic plates [19].

In this study, the novelty consists in extracting dispersive guided waves data, i.e. not at a single frequency-thickness value but over a frequency range, for a reduced number of directions of propagation (reduced number of sensors), to build the GA objective function.

In particular, the objective function is built on the discrepancy between the group velocity dispersion curves of few waves computed numerically, by Semi-Analytical Finite Element (SAFE) formulations [20], and those obtained experimentally. Group velocity curves can be extracted experimentally over a wide frequency range from a single time-transient event via time-frequency transforms (TFRs). The GA driven procedure iteratively updates the material properties in the SAFE formulation in order to minimize the fitness function. The iteration is terminated when the set GA decision making criteria are satisfied.

1.5 Genetic Algorithm

The material parameters C_{ij} are estimated by satisfying a fitness function based on the discrepancy between the experimental and numerically predicted group velocity curves, c_g^{exp} and c_g^{num} , respectively. Experimentally, group velocity curves can be extracted from a single time-transient measurement by means of time-frequency transform (TFR) [21], as schematically depicted in Figure 1.3.

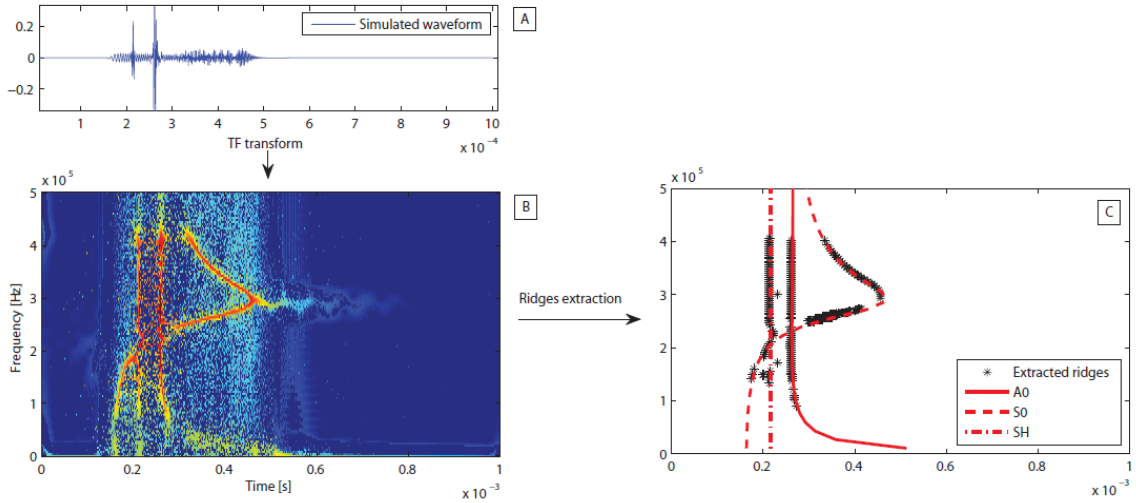


Figure 1.3: Extraction of modal group-delays through the reassigned spectrogram.

A TFR yields a contour plot that retains the time-frequency energy content of the propagative waves. For a known distance of propagation (distance source-receiver), the c_g^{exp} for each wave can be obtained by taking the time of arrival of the corresponding TFR peaks at the various frequency values. In our approach, the reassigned spectrum [22] is computed on the acquired waveforms related to different orientations. The TFR ridges corresponding to the dispersion curves are deduced from the stationary points of the reassignment operators. Numerically, group velocity curves are computed by using a SAFE formulation [20]. The plate, considered infinite in the in-plane 1-2 directions, can be composed of several distinct lamina in the thickness (direction 3) and is characterized by the elastic properties C_{ij} . Given a frequency $w_i = 2\pi f_i$, and the wave propagation direction θ , the group velocity $c_g^{num}(\theta, f_i)$ for

the different modes can be obtained. The proposed fitness function reads as:

$$J(C_{ij}) = \sum_{\theta_i=1}^{N_\theta} \left\{ \sum_{k=1}^R \Phi(C_{ij}, \theta_j, \mathbf{P}_K, D) \right\} \quad (1.5)$$

where $\Phi(C_{ij}, \theta_i, \mathbf{P}_K, D)$ is the distance between a given extracted ridge point \mathbf{P}_K , and the slowness curves D/c_g^{num} calculated for material parameters C_{ij} and direction θ_i as shown in Figure 1.4).

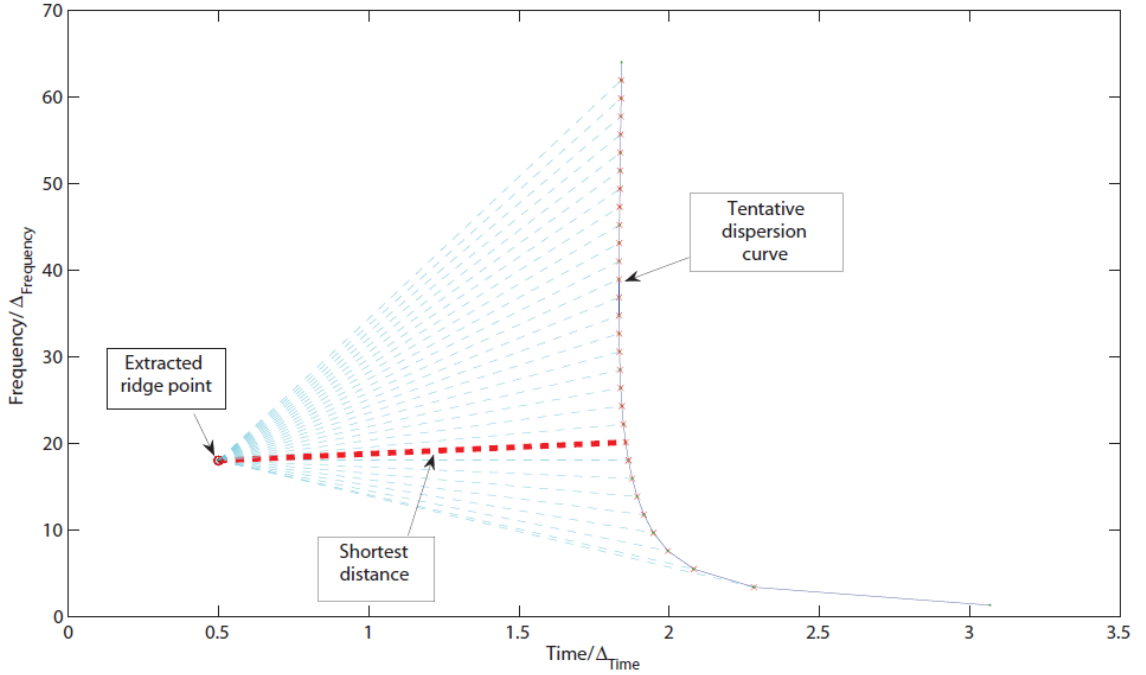


Figure 1.4: Calculation of the distance between an extracted ridge point and the slowness curve for a given mode.

The iterative GA procedure is initiated by assuming an initial guess of the plate elastic properties C_{ij}^0 . These guesses are used to compute the initial group velocities values c_g^{num} . Based on these values the fitness function of Eq. 1.5 is evaluated the first time. The GA procedure iteratively updates the values of the mechanical parameters C_{ij} in the procedure until the GA requirements are reached. The minimization process is treated as a constrained optimization problem. Constraints are related to the lower (LB) and upper (UP) values that the design variables, C_{ij} , can take ($LB \leq C_{ij} \leq UP$).

1.6 Numerical and Experimental Testing

A transversely isotropic plate 1 mm thick is simulated. The plate has an overall material density $\rho = 1560 \text{ kg/m}^3$ and its elastic coefficients referred to the principal axes 1-2-3, where 1 $\equiv \theta^0$ is the fiber direction and 3 is the through-thickness direction, are given in Table 1.1.

11	12	13	22	23	33	44	55	66
143.8	6.2	6.2	13.3	6.5	13.3	3.6	5.7	5.7

Table 1.1: Elastic properties $C_{ij}^{exp}(\theta^0)$ in [Gpa].

In this study, guided waves are computed in the frequency range 0–500 kHz, for which up to three guided modes exist ($n_m = 3$), namely A_0 , S_0 and SH_0 , 3 SAFE elements were used to guarantee an accurate solution. The group velocities were computed at 20 different frequency values ($n_f = 20$) by using a frequency step of around 35 kHz ($f_i = 1, 35, 95, 70, 90, 700$ kHz). Four different wave propagation directions were considered ($\theta_1 = 35$, $\theta_2 = 55$, $\theta_3 = 70$ and $\theta_4 = 85$). Different set of θ_i were tested. The values in Table 1 were used to extract the dispersion curves c_g^{exp} and to simulate wave modes propagation in the 4 directions. Next, an initial guess of the material properties C_{ij}^0 was generated as:

$$C_{ij}^0(\theta^0) = C_{ij}^{exp}(\theta^0) \times \left[1 - rand \frac{\Delta}{100} \right], \quad \forall ij$$

where *rand*, the random function of Matlab, generates a pseudorandom number between 0 and 1 and $0 \leq \Delta \leq 104$ is used to scale the random number. These values were passed to the GA scheme as a set of initial values.

The GA procedure, takes the initial values into account and computes $C_{ij}^0(\theta_i)$, c_g^{num} , and evaluates the fitness evaluated for each of the 50 chromosomes of the initial population. Next, the GA perform mutation, crossover and elitism until the imposed decision criteria are satisfied.

Here, the tolerance for the fitness function was taken as $toll = 1e^{-30}$ and the maximum

number of generations was set equal to 500. The number of elite, the crossover fraction and the migration fraction were taken as 2, 0.8 and 0.2, respectively.

The results of the identification procedure, obtained for $\Delta = 10$ are collected in Table 1.2.

C_{ij}	C_{ij}^{exp}	C_{ij}^0	e% init	C_{ij}^{ID}	e% final
C_{11}	143.8	125.00	13.077	142.7	0.76283
C_{12}	6.2	5.9312	4.3359	6.0666	2.15156
C_{13}	6.2	5.9312	4.3359	6.0666	2.1515
C_{22}	13.3	13.756	3.4262	13.302	0.01287
C_{23}	6.5	8.826	35.784	6.4856	0.22093
C_{33}	13.3	13.756	3.4262	13.302	0.01287
C_{44}	3.4	2.4649	27.504	3.408	0.23635
C_{55}	5.7	7.2786	27.694	5.6804	0.34348
C_{66}	5.7	7.2786	27.694	5.6804	0.34348

Table 1.2: Identification results for $\Delta = 20$. Elastic coefficients in [GPa].

As it can be seen for both cases, all the nine elastic coefficients are identified with great accuracy.

Experimentally, the inverse procedure scheme is tested to characterize the elastic material properties of a sandwich panel, which consists in $[0^\circ/90^\circ/0^\circ/90^\circ]$ unidirectional layers of bamboo fibres plus an intermediate isotropic core of balsa wood.

Each bamboo lamina has a thickness of 0.25 mm, the balsa core thickness is 5 mm, for an overall laminate thickness of 7 mm.

Experimental data were obtained by adopting a PZT setup. The exciting signal is a chirp pulse as shown Figure 1.5.

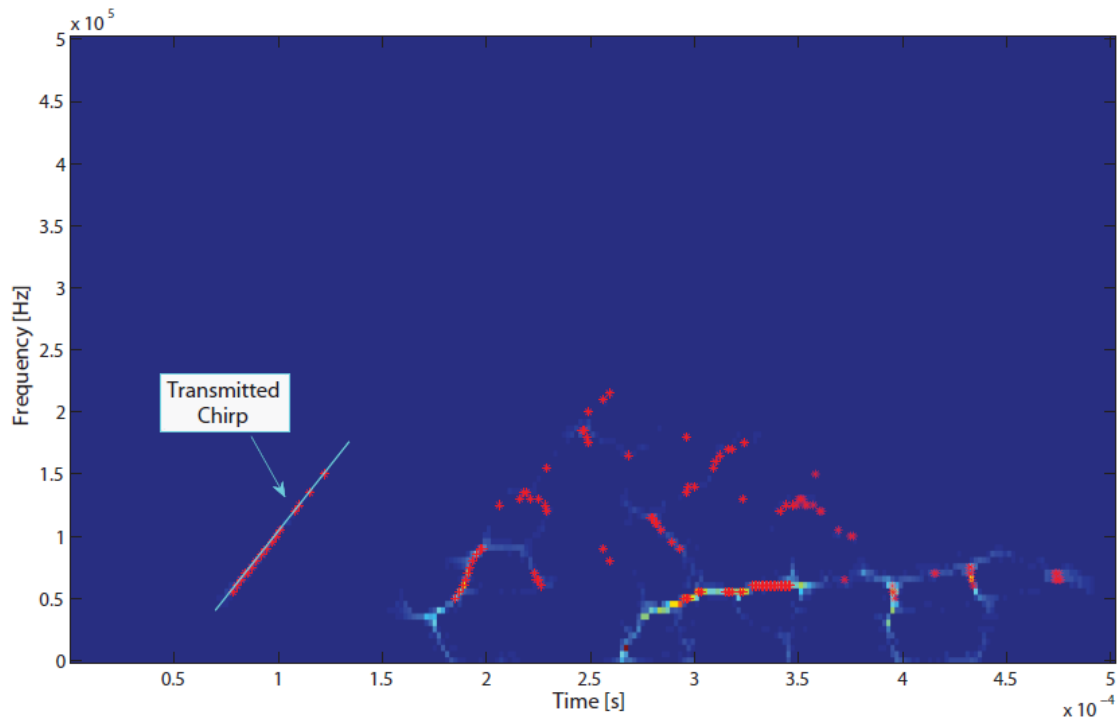


Figure 1.5: Ridge extraction from experimental bamboo data.

A suitable charge amplifier was designed to increase the ultrasonic signal dynamic range. The elastic parameters extracted with the proposed GA procedure are compared to the ones extracted with destructive procedures showing a good agreement.

Chapter 2

Structural Health Monitoring Applications

People could put up with being bitten by a wolf
but what properly riled them up was a bite from
a sheep.

James Joyce

In the last few decades Structural Health Monitoring (SHM) has attracted considerable attention with the increasing need for the development of systems able to monitor continuously the structural integrity of complex structures.

Damage detection in the structure by visual inspection or by conventional nondestructive techniques can be prohibitive for many reasons, such as the inaccessibility of some areas. In addition, conventional nondestructive techniques can be quite demanding in terms of the time required for the inspection which results in a prolonged period in which the structure to be monitored is not available.

This problem is particularly important in the aerospace industry and chemical and nuclear plants. To address these issues considerable effort is currently focused on the development of convenient SHM equipment that can effectively detect the occurrence of damage in the structure and can provide information regarding the location and the severity of damage and possibly about the remaining life of the structure.

An SHM system, able to continuously assess the health of a structure, can potentially change the way in which safety critical structures are monitored and maintained over

their lifetimes, reducing significantly the duration of the period in which the structure to be inspected is out of service. Therefore the development of an efficient SHM system is crucial for the opportunity of maintaining a continuous assessment of the integrity of the structure, in order to facilitate the detection of critical defects and the observation of the growing of pre-existing cracks, originally below the critical size.

The purpose of this Chapter is to specify the main features of a guided wave SHM system and the requirements to make this kind of equipment competitive with traditional inspection methods. The concept of SHM can be applied to several industrial fields; without loss of generality we will be especially oriented to the description of a monitoring system for structures of interest in aerospace industry. According to their operational strategy SHM systems can be divided in two main groups that in the following will be termed passive SHM and active SHM systems. A passive SHM system is based on detecting changes in a chosen property of the structure in a passive way. Typical examples are given by the detection of strain fields induced by crack growth, of changes in the vibration characteristics, or of cyclically-operating structures due to growth of defects.

The main difference between a passive and an active SHM system is represented by the fact that in the latter the sensors are directly excited and the excitation is therefore transmitted to the structure. The response of the structure to this excitation represents the information to be measured and evaluated in order to obtain information regarding the integrity of the structure. An example of this approach is provided by the vibration based techniques in which the structure is excited with a pulse and the vibration modes are evaluated by response measurements in the structure with accelerometers placed at strategic positions. The two different approaches for the design of a Structural Health Monitoring system will be further discussed in the following sections. In particular the next section will describe briefly the application of passive systems for SHM and subsequently our attention will be concentrated on the application of active systems for the monitoring of complex structures.

2.1 Passive systems for SHM

Among the passive SHM systems, Acoustic Emission (AE) represents the most extensively used technique for defect detection on complex structures. The basic idea is that crack propagation and the growth of a pre-existing defect, including corrosion, generates waves which can propagate in the structure and can be received by sensors located several metres away from the source with sufficient amplitude. The successful reception of these waves by sparsely distributed sensors shows the signals are propagating across several features in the structure; hence a study of acoustic emission is also a good starting point for better understanding of the issues related to an active guided wave SHM system. Although potentially attractive and widely used for investigation of complex structures, AE presents some relevant drawbacks which restrain its application in SHM. In particular it is important to stress that AE is highly sensitive to noise or background noise interference, which are especially severe in aircraft applications. More importantly, many damage types, such as failure in ductile materials, give very low sound emission, making impractical reliable application of the AE technique. In addition commercial AE systems cannot estimate quantitatively the severity of the damage in the structure; hence other NDE methods are required for a complete examination of the structure under inspection in order to provide quantitative results.

2.2 Active systems for SHM

Among the active SHM systems used to evaluate complex structures the most studied are those based on vibration mode analysis and on the use of sound waves (either guided waves or bulk waves). Both use sensors to transmit an excitation to the structure and to gather information on the integrity by analysing the response. Since ultrasonic guided waves can propagate for long distances they offer the possibility of inspecting large areas from a small number of sensor positions.

The main idea is to measure and evaluate the reflections of these waves from features

or from defects through convenient signal processing techniques making possible the location of defects and the assessment of the effective integrity of the structure. The sensors employed in guided wave-based systems are generally used both as emitters and receivers of sound waves. The inspection strategies for SHM are based on the conventional NDT techniques of inspection in pitch-catch mode or pulse echo mode. Different concepts of sensor arrays have been proposed and some examples will be discussed in the following sections. There are several cases of successful guided wave inspection systems developed for the inspection of structures that are characterized by their relative simplicity and low feature density, such as pipes, rails, plates and small structures, which will be discussed in the next sections. These systems allow the operator to detect the location of damage in the structure. Although these structures are fairly simple, they can be considered a good idealisation for the design of an SHM system which could be also employed for the inspection of complex structures.

Single mode transduction for an active Guided wave SHM system

The choice of which guided wave mode to use in any inspection system and over what frequency range is of crucial importance. In particular when the feature density is quite high as in an airframe, the classical strategy is to increase the inspection frequency so that the wavelength is reduced, in order to obtain discrete echoes from successive features. It has been demonstrated that the modes propagating in typical aircraft structures in the high frequency range are very complex and that it was not possible to obtain reliable propagation across a succession of typical stiffeners and joints.

However, it has been shown that acoustic emission signals propagate long distances through aircraft structure and are usually a combination of A_0 and S_0 Lamb waves in the relatively low acoustic emission frequency regime below the cut-off frequency of the A_1 mode. Therefore the low frequency region appears the more suitable for the excitation of an SHM system. Hence the choice of the excitation is restricted to three possible modes (S_0 , SH_0 and A_0). However, the S_0 mode suffers from an increasingly long wavelength at low frequencies, and hence lower defect resolution.

The slower SH_0 mode has a correspondingly shorter wavelength, but is difficult to excite in a simple fashion for SHM applications. The A_0 mode is commonly regarded as being highly attenuated in structures in contact with liquid and therefore of limited applicability for long range testing. However, there is a low frequency regime where it is not attenuated by surrounding liquid because its phase velocity is too low to allow energy leakage.

In addition, the wavelength for the A_0 mode in the region of interest is always lower than the wavelengths of the S_0 and SH_0 modes and therefore the A_0 mode can still offer reasonably high resolution in detection capability.

An SHM system operating at low frequencies will be excited by transducers by applying localized forces in the same direction as the characteristic displacement of the mode to be excited. When an harmonic point force is applied to the surface of the structure, guided waves will be produced and will propagate in circular wave-fronts centred in the transducers.

Guided wave SHM arrays

SHM systems based on guided waves can be divided in two main groups with respect to the concept of transducer arrays adopted. The two groups can be termed as (i) single unit arrays, (ii) sparsely distributed arrays. Single unit arrays contain a relatively large number of individual transducers in a single housing and typically each element is used as a transmitter and receiver. If the response at each element is measured when each element in turn is switched as a transmitter, focusing techniques can be used to propagate a beam in each direction around the array.

Several projects have been conducted on the development of single unit arrays for SHM and some of them will be discussed in the next section. The second conceptual design for SHM arrays is represented by a distributed sparse array of simple elements. According to this approach, point source transducers will be distributed throughout the structure, in order to create a network of simple elements permanently attached to the structure.

A sparsely distributed array is able in principle to detect the presence of a crack

regardless of its geometry and relative position with respect to the elements of the array. Damage location can be achieved through triangulation, since theoretically the information from three independent sensors regarding the arrival time of the reflected wave from the crack is required.

In contrast, a permanently attached single array would encounter detection problems for defects lying along certain orientations (e.g. parallel to the direction of propagation of the guided waves), or in the case of a deployable single array several different inspection positions would be required in order to identify the presence of a defect; a sparsely distributed array would allow several different sensors to receive signals from a single transmitter, so there would be a combination of transmitter-receiver for every crack orientation. However, since the amplitude of the reflections coming from a defect is dependent on the angle of incidence of the guided waves, it is still possible to have detection problems, especially in correspondence of those angles of incidence for which the reflectivity is null. In addition, the performance of distributed sparse arrays can be strongly dependent on the environmental conditions, such as temperature variations and surface conditions of the structure under inspection.

There are other practical advantages in using a sparsely distributed array for SHM instead of a single unit array. An element in a sparsely distributed array is a single channel device which requires relatively straightforward electronics compared to the electronics needed by a multi-element deployable array. In addition, for the coverage of a given area the number of distributed sensor elements required is lower than the number of elements required in a single array unit.

Damage localisation with a single array unit is necessarily based on beam steering, which requires the array to be several wavelengths in diameter and to contain a minimum number of elements per wavelength and consequently the exciting and receiving routines and the correct phasing between the transducers can become extremely complex.

Whereas activity in the development of single unit array is a well established research field in SHM, the development of a sparse distributed array of simple elements for SHM represents a relatively new area of investigation and poses new challenges in

terms of miniaturization and integration of the sensor elements with the structure and in terms of efficient signal processing techniques able to treat the amount of data recorded by the sensors. A feasibility study [23] about the possibility of using a distributed array of guided wave sensors to monitor an entire structure has been conducted at the University of Bristol. Another study of spatially distributed array for in-situ location of defects in large plate-like structures has been proposed by Michaels [24]. The approach proposed is based on the use of broadband Lamb waves and in the continuous monitoring of the received signals, in order to achieve damage location. In particular several signals were recorded for different frequencies and for all the possible transmitter-receiver pairs; the signals were conveniently combined for generating several images for the same structural state. The combination of several images result in an improved damage detection.

Another piece of work conducted by Michaels is based on the generation of two dimensional images of plate-like structures by means of tomographic and phased array methods. The images are obtained combining the signals recorded by a sparse array of distributed ultrasonic transducers. This approach has been used for damage detection problems in aluminium plates by comparing the image obtained for the undamaged plate with the image obtained after small drilled holes have been introduced as artificial defects. Significant effort has been also devoted to the integration of SHM system with the structure to be inspected.

An interesting work, proposed by Giurgiutiu [25], is based on the use of piezoelectric wafer active sensors (PWAS) that can be directly mounted on the surface of plate-like structures or even embedded between layers of composite structures. These transducers were used in both pitch-catch and pulse-echo configurations to generate/receive Lamb wave modes and were used successfully for crack detection also on a real aircraft panel. An important step in the integration of SHM system with complex structure is represented by the SMART layer developed by Acellent Technologies Inc. in collaboration with Stanford University. The layer can be mounted on existing structure or integrated into composite structures providing built-in nondestructive assessment of the internal and external integrity of the structure. The SMART layer consists of

a network of piezoelectric elements supported on a flexible printed circuit substrate. In this way a whole array of sensors can be embedded in the structure and issues related to the integration of the monitoring system are significantly reduced. In addition, by exploiting the flexibility of the printed circuit technique, a large variety of size, shapes and complexity are possible for the SMART layer. Basic shapes include a circular and three-dimensional shell. Furthermore the printed circuits guarantee a very good integration because they are able to deform with the structure. Following the pioneering work on the SMART layer, an interesting project for the development of a hybrid piezoelectric-fibre optical diagnostic system for aerospace structures has been proposed by Qing et al.. A more complex SMART layer, containing a network of piezoelectric elements and fibre gratings, is used in the same fashion to evaluate the integrity of metallic and complex structures. Piezoelectric actuators input a controlled excitation to the structure and fibre optical sensors are used for monitoring the corresponding structural response. With this approach decoupling between input and output signals can be achieved, since the piezoelectric transducers use electrical channels and the fibre optical sensors use optical means. This equipment can be used to perform in-situ detection of structural defects and damage including delaminations and corrosion.

2.3 Signal processing for Structural Health Monitoring

From what has been previously reported we can deduce that SHM is an attractive research field of continuously growing importance and it can potentially modify the way in which complex structures are designed, operated and maintained during their lifetimes. We observed that ultrasonic guided waves offer the possibility of inspecting large areas from a small number of sensor positions, since they can propagate over long distance. Therefore guided waves represent a promising means for the inspection of complex structures and their characteristics have been extensively studied in

conventional nondestructive evaluation. However, inspection of complex structures is difficult as the reflections from different features overlap. Estimating the number and amplitude of the wave packets contained in ultrasonic time traces is therefore crucial for the development of a successful guided wave inspection system, in order to enable damage to be detected and located by identifying changes in the measured signal over time. Therefore an appropriate and robust signal processing tool for Structural Health Monitoring must be able to resolve closely spaced events and to distinguish reflections due to the presence of a defect from reflections caused by structural features. Other desired requirements for signal processing algorithms to be applied in SHM, can be briefly listed as follows:

- Ability to reduce the noise on the damage estimate;
- Capability of enhancing the SNR in the data, for instance removing distortion introduced by the measurement channel;
- Robustness to modelling error, since material properties, noise characteristics and other variables may be only approximately known and therefore the algorithms should be able to cope with the related uncertainties;
- High flexibility and easy implementation for handling the signal processing of large amounts of data recorded at sensors embedded in the structure.

The main objective of this work is to devise suitable signal processing techniques that can be effectively used to retrieve useful information about the integrity of a complex structure monitored by a sparse distributed array of piezoelectric sensors.

Furthermore in the following a new framework is presented in order to exploit the concept of sparsity of the ultrasonic signals within a proper basis to achieve high resolution through the use of the Compressive sensing.

Chapter 3

Frequency Warping Operator

The road of excess leads to the palace of wisdom.

William Blake

3.1 Introduction

Guided Waves (GWs) have characteristic dispersive time-frequency representations (TFRs). Unfortunately, any TFR is subjected to the time-frequency uncertainty principle. This, in general, limits the capability of TFRs to characterize multiple, closely spaced guided modes from a time transient measurement, over a wide frequency range. To overcome this limitation, a warped frequency transform (WFT) is presented that in force of a more flexible tiling of the time frequency domain shows enhanced modes extraction capabilities. Such tiling is chosen to match the dispersive spectro-temporal structure of the waveguide by selecting an appropriate map of the time frequency plane. The proposed transformation is fast, invertible, and covariant to group delay axis. In particular, the design and calculation strategies for maps tailored to Lamb waves propagating in an aluminium plate are described.

The results show that the proposed WFT limits interference patterns which appears with others TFRs and produces a sparse representation of the Lamb waves pattern that can be suitable for identification and characterization purposes.

In this Chapter the warping operator is introduced. Furthermore a new tiling of the TF plane is performed through an innovative reshape of the wavelet filters in the frequency domain. This leads to a new nonstationary wavelet multiresolution scheme able to improve the reconstruction of the ultrasonic signal.

3.2 Notation

Throughout this Chapter, lower case letters are used to represent signals in time domain while upper case letters represent signals in frequency domain. The symbols \mathbb{F} and \mathcal{F} are used to denote the Fourier operator respectively in continuous and discrete domain. All signals are considered to be elements of the Hilbert space of square-integrable functions $L^2(\mathcal{R})$, which has inner product

$$\langle s, h \rangle = \int_{\mathcal{R}} s(\tau)h^*(\tau)d\tau$$

for $s, h \in L^2(\mathcal{R})$ and norm $\|h\|^2 = \langle h, h \rangle$ where $(\cdot)^*$ denotes the complex conjugate. Operators on the Hilbert space are expressed using boldface capital letters.

The notation $(\mathbf{U}s)(x)$ is used to denote processing the signal s by the operator \mathbf{U} and evaluating the result at x . A unitary operator \mathbf{U} is a linear transformation that maps the Hilbert space into itself. Unitary operators preserve energy and inner products;

$$\begin{aligned}\|\mathbf{U}s\| &= \|s\| \\ \langle \mathbf{U}s, \mathbf{U}h \rangle &= \langle s, h \rangle\end{aligned}$$

As a consequence, a unitary operator maps a set of orthonormal bases in $L^2(\mathcal{R})$ into another set of orthonormal bases in $L^2(\mathcal{R})$. The symbols \mathbf{W} and \mathcal{W} are used to denote the Warping operator respectively in continuous and discrete time warped domain.

3.3 Frequency Warping

The construction of warped wavelets is based on the design of discrete and continuous time frequency warping operators in order to compensate the dispersion of a single

dispersive propagation mode. Since that an infinite number of TFRs and processing tools can be obtained by using unitary transformations, as reported in [26], we propose a unitary operator based on frequency warping which can be used for the analysis of dispersive guided waves. These operators deform the frequency axis with a proper warping function $w(f)$ [27]. To guarantee invertibility of this process, $w(f)$ must be chosen so that

$$\frac{dw(f)}{df} \doteq \dot{w}(f) > 0 \quad \Rightarrow \quad \exists w^{-1}, w^{-1}(w(f)) = f,$$

where \dot{w} represents the first derivative of the map w with respect to frequency and w^{-1} is the functional inverse of w . So a regular class of warping operators whose warping characteristic is a smooth monotonically increasing function is considered. Given a generic signal $s(t)$, the continuous frequency warping operator $\mathbb{F}(\mathbf{W}(s))(f)$ is defined as follows:

Definition 3.3.1: *Suppose that w is a strictly increasing and continuously differentiable real function. Given any $s \in \mathbf{L}^2(\mathbb{R})$ the warping operator \mathbf{W} is defined by its action in the Fourier domain as*

$$(\mathbb{F}\mathbf{W}s)(f) = \sqrt{\frac{dw(f)}{df}} (\mathbb{F}s)(f)$$

The warping operator results in a unitary transformation which preserves orthogonality. For discrete-time signals of finite duration N , the warping operator is a matrix whose entries are defined as follows

$$\mathcal{W}(m, n) = \frac{1}{M} \sum_{k=0}^{M-1} \sqrt{\dot{w}\left(\frac{k}{M}\right)} e^{j2\pi\left(m\frac{k}{M} - nw\left(\frac{k}{M}\right)\right)}, \quad m \in \mathbb{Z}_M, \quad n \in \mathbb{Z}_N \quad (3.1)$$

By considering the discrete Fourier transform of size $M \times M$,

$$\mathcal{F}(k, n) = e^{-j2\pi n \frac{k}{M}}, \quad k, n \in \mathbb{Z}_M$$

and the nonuniform discrete Fourier transform of size $M \times N$, scaled along rows according to the orthogonalizing factor $\sqrt{\dot{w}\left(\frac{k}{M}\right)}$ the discrete warping operator in Eq. (3.1) can be expressed as

$$\mathcal{W}(m, n) = \mathcal{F}^{-1} \mathcal{F}_w \quad (3.2)$$

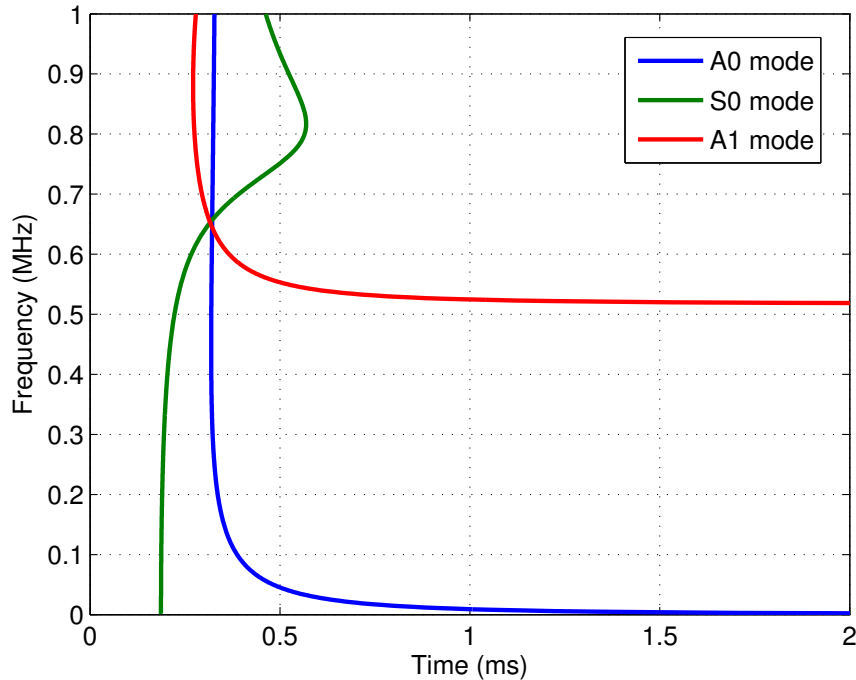
A fast computation of the discrete warping operator is achieved by means of this decomposition. \mathcal{F}^{-1} can be computed with the fast Fourier transform (FFT) algorithm and \mathcal{F}_w can be efficiently factorized with the nonuniform-FFT algorithm [28].

3.4 Dispersion Compensation Representation

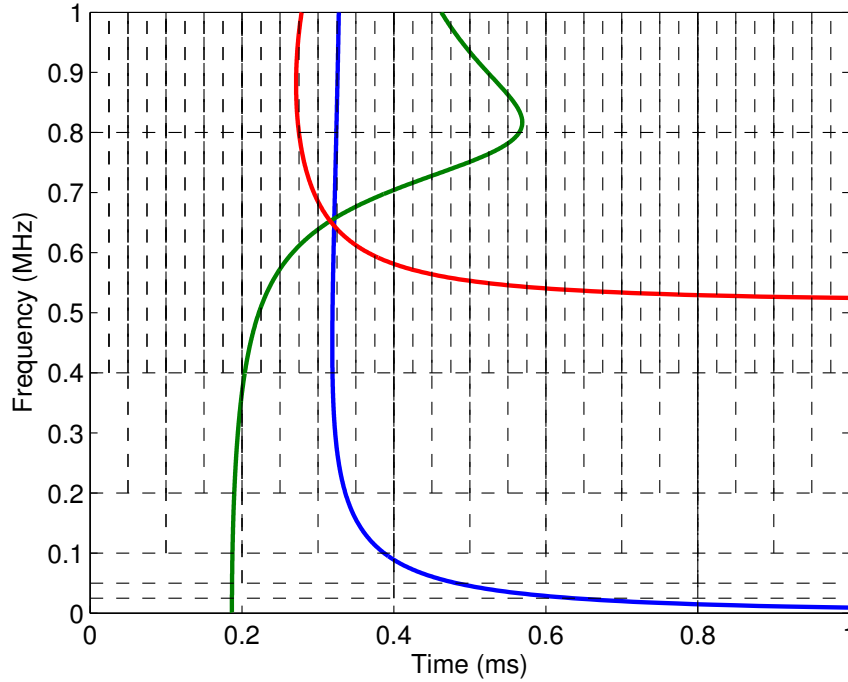
The aim of the dispersion compensation procedure is to design a time-frequency (TF) representation matching with the group delay curves, leading to a sparsification of the acquired signal in the new domain.

The group delay is defined as the derivative of signal phase response, and it is a measure of the time delay introduced in each sinusoidal component.

Figure 3.1(a) shows the tiling of the Short Time Fourier Transform (STFT), with constant resolution atoms in the TF plane, while the tiling of the Wavelet Transform, characterized by a multiscale resolution, is depicted in Figure 3.1(b).



(a)



(b)

Figure 3.1: Tiling of the time-frequency plane (a) for the short-time Fourier transform and (b) for the wavelet transform. Atoms are symbolically represented by rectangles. The solid curves represent the dispersive group delay curves for the Lamb waves for a traveled distance of 1 m.

From Figure 3.1 it is clear that neither the STFT with fixed TF resolution nor the wavelet with multiscale TF resolution are suited to finely estimate the superimposed curves. The procedure of warping a signal belongs to group delay shifts covariant (GDSC) since that the TFR of the signal s which undergoes a change $\tau(f)$ in the group delay ($s \rightarrow s_{disp}$) corresponds to the TFR of the original signal shifted by $\tau(f)$

$$(\mathbb{F}S_{disp})(f) = e^{-j2\pi \int \tau(f)df} (\mathbb{F}S)(f)$$

$$\text{TFR}[s_{disp}](t, f) = \text{TFR}[s](t - \tau(f), f)$$

It was shown in [21] that a GDSC can be obtained by warping a signal and then analysing it with a TFR of the Cohen class, such as the spectrogram, if

$$K \frac{dw^{-1}(f)}{df} = \tau(f) \quad (3.3)$$

where K is an arbitrary constant. Therefore, it is possible to design an appropriate GDSC TFR for a given dispersive system by properly setting the derivative of the functional inverse warping map $w^{-1}(f)$.

To reproduce the warped tiling of the TF plane we suppose that the actuated signal \hat{s} is a Dirac delta centered in $t = \tau_w$. Its spectrum and group delay $\tau_g(f, \hat{s})$ can be computed as

$$\begin{aligned} (\mathbb{F}\hat{s})(f) &= e^{-j2\pi f\tau_u} \\ \tau_g(f, \hat{s}) &= -\frac{1}{2\pi} \frac{d \arg(\mathbb{F}s)(f)}{df} = \tau_u \end{aligned}$$

By applying the warping operator, the following distortion is obtained:

$$\begin{aligned} (\mathbb{F}\mathbf{W}\hat{s})(f) &= \sqrt{\dot{w}(f)} e^{-j2\pi w(f)\tau_u} \\ \tau_g(f, \mathbf{W}\hat{s}) &= -\frac{1}{2\pi} \frac{d \arg(\mathbb{F}\mathbf{W}s)(f)}{df} = \tau_u \end{aligned}$$

Based on a priori knowledge of the group velocity $c_{g_M}(f)$ for the propagating mode M , the warping map is selected according to the rule

$$K\dot{w}(f) = \frac{1}{c_{g_M}(f)}$$

which corresponds to the group delay

$$\tau_g(f, \mathbf{W}\hat{s}) = \dot{w}(f)\tau_u = \frac{\tau_u}{K \cdot c_{g_M}(f)} \quad (3.4)$$

The group delay associated with a guided wave \hat{s}_w at a distance D from the source is given by

$$\tau_g(f, \hat{s}_w) = \frac{D}{c_{g_M}(f)}$$

The warping operator directly maps the dispersive time waveforms to an equivalent non-dispersive domain where each instant τ_u can be directly converted to the propagation distance D according to $D = \frac{\tau_u}{K}$ where K is a normalization constant which is selected so that the frequency axis is mapped onto itself

$$K = \frac{2}{f_s} \int_0^{\frac{f_s}{2}} \frac{df}{c_{g_M}(f)};$$

f_s is the maximum frequency for which the dispersion relation $c_{g_M}(f)$ is considered so the sampling frequency in a discrete case. $\frac{1}{\Delta D}$ represents the Nyquist wavenumber in the equivalent non-dispersive domain.

Impact Localization

There are two types of sillies: those who doubt of nothing and those who doubt of everything.

J. Ligne

4.1 Motivation

A strategy for the localization of acoustic emissions (AE) in plates with dispersion and reverberation is proposed. The procedure exploits signals received in passive mode by sparse conventional piezoelectric transducers and a three-step processing framework.

The first step consists in a signal dispersion compensation procedure, which is achieved by means of the Warped Frequency Transform.

The second step concerns the estimation of the differences in arrival time (TDOA) of the acoustic emission at the sensors. Complexities related to reflections and plate resonances are here overcome via a wavelet decomposition of cross-correlating signals where the mother function is designed by a synthetic warped cross signal. The magnitude of the wavelet coefficients in the warped distance-frequency domain, in fact, precisely reveals the TDOA of an acoustic emission at two sensors.

Finally, in the last step the TDOA data are exploited to locate the acoustic emission source through hyperbolic positioning. The proposed procedure is tested with a

passive network of three/four piezo-sensors located symmetrically and asymmetrically with respect to the plate edges.

The experimentally estimated AE locations are close to those theoretically predicted by Cramèr-Rao lower bound.

4.2 Introduction

Arrays of piezoelectric transducers have been used to locate acoustic emissions (AE) in waveguides. Several array shapes have been investigated, including single-ring or fully populated circular patterns [23], two-dimensional square arrays [25] or more complicated configurations realized with piezoelectric paint [29].

In SHM applications, the minimization of the array elements is fundamental to reduce not only the hardware complexity associated to transducers wiring and multiplexing circuitry but also the intensive signal processing of the large amounts of recorded data. For this reason, there is growing interest in minimizing the number of sensors by optimizing their positioning, as well as by increasing the resolution of AE localization procedures [30], [31], [32], [33].

In passive procedures, when the acoustic emission, generated for instance by an impact, crosses a certain threshold in one of the sensors, the trigger information is sent to all remaining devices [34]. At this point, part of the data are recorded and processed to pin-point the source location.

The source point of an AE is typically located with a three-step procedure [35] schematically depicted in figure 4.1 where:

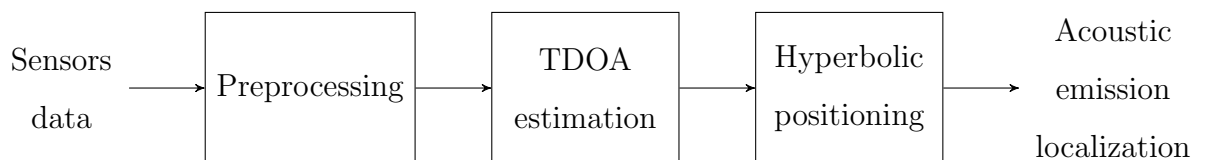


Figure 4.1: A typical three-step acoustic emission source location procedure.

- i) the first step consists in a signal processing filtering procedure. In guided waves based applications this step is required to tackle dispersion, which is the most relevant limiting factor against choosing high sensors inter-distances.

The solutions proposed in [36] and in [37] rely on the limitation of the dispersive effect by using narrowband wavelet filters. Unfortunately, narrowband filtering, while limiting the effects of dispersion, worsens the temporal resolution in time-difference of arrival (TDOA) estimation, as a result of the acoustic corollary of the uncertainty principle.

Many transformations have been introduced in order to accomplish this task, including the short time Fourier transform, the wavelet transform, filter banks and all their variations and mutual combination addressed to generalize their intrinsic characteristics [38]. Nevertheless, such transformations have some restrictive properties which make them not suitable in some applications.

In particular, some requirements, like fast computation and orthogonality, limit the degrees of freedom in choosing the proper time-frequency representation.

In order to approach the aim of an arbitrary time-frequency tiling, the application of a preliminary invertible transformation to reshape the frequency axis can be considered [39], [40].

In the present approach, the dispersion compensation procedure based on the Warped Frequency Transform (WFT) [21] is used. The WFT has some noteworthy properties which can be used for localization, as it can be exploited to remove from the acquired waveforms the dependence on the travelled distance. In addition, the low computational cost of WFT which is comparable with FFT performance makes the new tool suitable for real time applications [41]. In this work, the effect of this processing method in presence of strong plate edge reflections and resonances is evaluated.

- ii) The second step performs an estimation of the TDOA among the signals acquired by the different sensors. Generally such differences are measured with either threshold-based procedures [42], [43], or peak detection techniques [44],

[45], or, more robustly, through cross-correlation [35], [46]. As mentioned in the previous point, the higher the bandwidth of the received (dispersion compensated) signal, the lower the uncertainty in time-difference estimation. Indeed, various strategies have been proposed in order to whiten the received signals, such as Generalized Cross-Correlation (GCC) algorithms [47], or Phase Transforms (PHAT) [48]. However, the effectiveness of these strategies is limited in case of non-perfect dispersion compensation or in reverberating structures.

To overcome this limit, a novel cross-correlation analysis method based on Wavelet transform is presented in this Chapter. It will be shown through dedicated experiments how this procedure produces reliable TDOA estimation.

- iii) In the last step the acoustic location is computed from TDOA data by means of a hyperbolic positioning [49], [50]. The performance of the procedure is evaluated by comparing the estimated positions with the theoretical limit in localization accuracy achieved by hyperbolic positioning computed via the Cramèr-Rao bound (CRB).

As it will be shown in Section 4.7, the experimental results are in good agreement with the predicted theoretical limit. Thus, it is proved that the CRB can be adopted as a tool to design the optimal sensors positioning for a given application.

The Chapter is organized as follows: point i), ii), and iii) are discussed in Section 4.3, Section 4.4 and Section 4.5, respectively. Experimental validations of the proposed work, consisting in impacts localization in an aluminum plate by using three or four PZT sensors, with different spatial distribution over the plate surface, are shown in Section 4.7. The conclusions end the Chapter.

4.3 Dispersion Compensation with the Warped Transform

4.3.1 The warping frequency transform (WFT)

As described in Chapter 3, given a dispersive guided wave signal $s(t)$ whose frequency representation is

$$S(f) = \mathbf{F} \{s(t)\},$$

being \mathbf{F} the Fourier Transform operator, the Frequency Warping operator \mathbf{W}_w reshapes the periodic frequency axis by means of a proper function $w(f)$, that we will call from now on *warping map*, such as:

$$\begin{aligned} s_w(t) &= \mathbf{W}_w \{s(t)\} \\ \mathbf{F} \{s_w(t)\} &= \sqrt{\dot{w}(f)} \cdot S(w(f)) \end{aligned}$$

where $s_w(t)$ is the warped signal, and $\dot{w}(f)$ represents the first derivative of $w(f)$.

It has been shown in [51] that in order to compensate the signal with respect to a particular guided mode, $w(f)$ can be defined through its functional inverse, as:

$$K \frac{dw^{-1}(f)}{df} = \frac{1}{c_g(f)} \quad (4.1)$$

where $\frac{1}{c_g(f)}$ is the nominal dispersive slowness relation of the wave we want to consider, being $c_g(f)$ its group velocity curve and K is a normalization parameter selected so that $w^{-1}(0.5) = w(0.5) = 0.5$. Equivalently, the inverse warping map w^{-1} can be defined with respect to the wave phase velocity $c_{ph}(f)$ or wavenumber $k(f)$.

A sample warping map is depicted in Figure 4.2 along with its functional inverse.

It was computed according to Equation 4.1 by considering the group velocity curve of the Lamb A_0 mode represented in Figure 4.3.

The curves were obtained by using the Semi-Analytical Finite Element (SAFE) formulation proposed in [20] considering a 0.003 m thick aluminium plate with Young modulus $E = 69$ GPa, Poisson's coefficient $\nu = 0.33$ and material density $\rho = 2700$ kg·m⁻³.

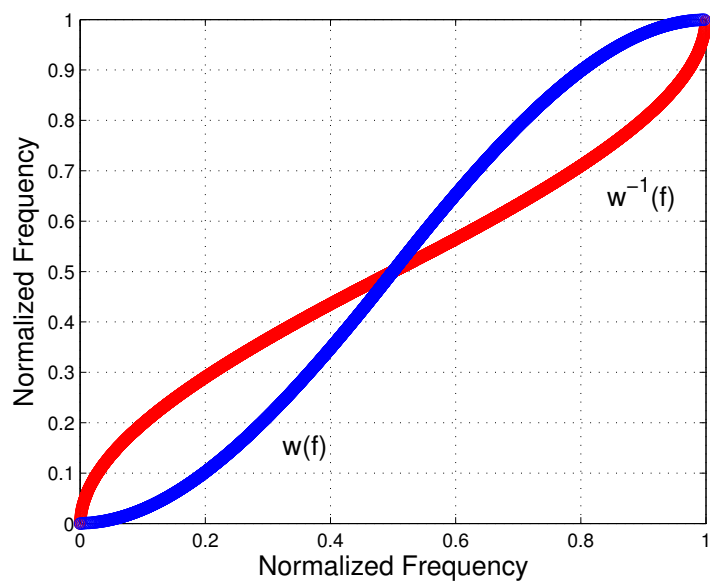


Figure 4.2: Warping map $w(f)$ for A_0 wave dispersion compensation and its functional inverse $w^{-1}(f)$ designed according to Equation 4.1.

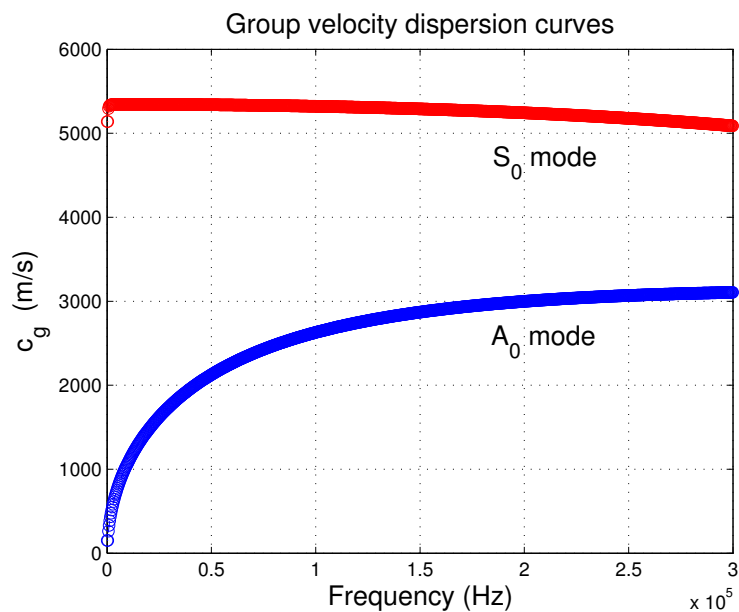


Figure 4.3: $c_g(f)$ dispersion curves for the Lamb waves propagating in an aluminium 0.003 m thick-plate.

The NUFFT is based on an oversampled Discrete Fourier Transform (DFT) followed by an interpolation method optimal in the min-max sense of minimizing the worst-case approximation error over all signals of unit norm [28].

The basic idea is to first compute an oversampled FFT of the given signal and then interpolate optimally onto the desired nonuniform frequency locations using small local neighborhoods in the frequency domain.

To compute the DFT at a collection of (non uniformly spaced) frequency locations ω_m which represent the warping map $w(f)$,

$$S(\omega_m) = \mathbf{F}_w \{s_n\} = \sum_{n=0}^{N-1} s_n e^{-j\omega_m n} \quad m = 1, \dots, M$$

first a convenient $K \geq N$ must be assumed so that the K -point FFT of s_n

$$S(\omega_k) = \mathbf{F} \{s_n\} = \sum_{n=0}^{N-1} s_n e^{-j\frac{2\pi}{K}kn} \quad k = 1, \dots, K$$

where $\frac{2\pi}{K}$ is the fundamental frequency of the K -point DFT. The nonzero x_n are algorithm design variables that have been called scaling factors.

The second step of most NUFFT methods is to approximate each $S(\omega_m)$ by interpolating $S(\omega)$ using some of the neighbors of ω_m in the DFT frequency set.

Linear interpolators have the following general form:

$$\hat{S}(\omega_m) = \sum_{k=0}^{K-1} u_k^*(\omega_m) S(\omega_k) \quad m = 1, \dots, M$$

where the $u_k^*(\omega_m)$ denote the interpolation coefficients selected through a min-max criterion. For each desired frequency location ω_m the coefficient vector the worst-case approximation error between $S(w(f))$ and $\hat{S}(\omega_m)$ is determined. As demonstrated in [52], the interpolator coefficients $u_k^*(\omega_m)$ can be obtained by an analytic formula derived from the following optimization criterion:

$$\min_{u(\omega_m) \in \mathcal{C}^J} \max_{s \in \mathcal{R}^N} |\hat{S}(\omega_m) - S(\omega_m)|$$

Both the scaling vector and the interpolators are design variables, so ideally, we would optimize simultaneously over both sets using the previous criterion.

4.3.2 Warping a wave detected passively

In passive monitoring techniques the time instant in which an acoustic emission starts is unknown. Let us consider the effect of warping when an actuated wave is excited at a generic instant t_{d_1} .

The Fourier Transform of the actuated wave is given by:

$$(\mathbb{F}s_a)(f, 0) = (\mathbb{F}s_0)(f, 0) \cdot e^{-j2\pi t_{d_1} f} \quad (4.2)$$

being $(\mathbb{F}s_0)(f, t_0)$ the Fourier Transform of the excited wave (incipient pulse centered in $t = 0$). An undamped guided wave at a traveled distance D from the source point, $s(t, D)$, can be modeled in the frequency domain as a dispersive system whose response is:

$$\begin{aligned} (\mathbb{F}s)(f, D) &= (\mathbb{F}s_a)(f, 0) \cdot e^{-j2\pi \int \tau(f, D) df} \\ &= (\mathbb{F}s_0)(f, 0) \cdot e^{-j2\pi t_{d_1} f} \cdot e^{-j2\pi \int \tau(f, D) df} \end{aligned} \quad (4.3)$$

In force of Eq. (4.1), Eq. (4.3) can be rewritten as:

$$(\mathbb{F}s)(f, D) = (\mathbb{F}s_0)(f, 0) \cdot e^{-j2\pi t_{d_1} f} \cdot e^{-j2\pi w^{-1}(f)KD} \quad (4.4)$$

where the distortion results from the nonlinear phase term.

Consider now that the generated dispersive wave $s(t)$ is acquired by two different sensors (1 and 2) after having traveled two different distances of propagation, D_1 and D_2 . The warped Fourier transforms of the recorded signals $s(t, D_1)$ and $s(t, D_2)$ are given by:

$$\begin{aligned} (\mathbb{F}\mathbf{W}s)(t, D_1) &= \sqrt{\dot{w}(f)} \cdot (\mathbb{F}s_0)(w(f), 0) \cdot e^{-j2\pi w(f) t_{d_1}} \cdot \underline{e^{-j2\pi fKD_1}} \\ (\mathbb{F}\mathbf{W}s)(t, D_2) &= \sqrt{\dot{w}(f)} \cdot (\mathbb{F}s_0)(w(f), 0) \cdot e^{-j2\pi w(f) t_{d_1}} \cdot \underline{e^{-j2\pi fKD_2}} \end{aligned} \quad (4.5)$$

where the right hand terms can be distinguished only for the underlined distance-dependent linear phase shifts, which causes simple translations of the warped signals on the warped time axis. Therefore, the warped signals acquired by the different transducers have a constant frequency modulation due to the term $e^{-j2\pi w(f) t_{d_1}}$.

This property can be fruitfully exploited by using signal correlation techniques and Eq. (4.5), since in the frequency domain the cross-correlation of two warped signals $s_w = s_{w_i} \star s_{w_k}$ is:

$$\begin{aligned} \mathbf{F} \{s_w\} &= \mathbf{FW}_w \{s(t, D_i)\} \cdot (\mathbf{FW}_w)^* \{s(t, D_k)\} \\ &= \mathbf{F}_w \{s(t, D_i)\} \cdot (\mathbf{F}_w)^* \{s(t, D_k)\} \\ &= \dot{w}(f) \cdot |S_0(w(f), 0)|^2 \cdot e^{-j2\pi fK(D_i - D_k)} \end{aligned}$$

Thus, the abscissa value at which the cross-correlation envelope of two signals peaks in the warped domain can be directly related to the difference in distance of propagation by the two dispersive signals [53]. The algorithm graph is shown in Figure 4.4.

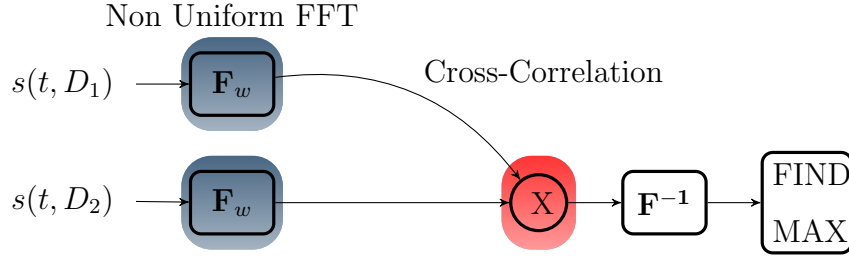


Figure 4.4: Graph of the proposed localization algorithm

4.3.3 Warping Reverberating Waves

It has been shown in [54] that if the edge of the plate is assumed to be cut perfectly square and the A_0 wave is assumed to be normally incident, for frequencies below the A_1 cutoff, such in this case, there is no mode conversion, therefore, an incident A_0 mode reflects simply delayed in phase as A_0 . To model the system a signal with reverberations that has been warped Fourier transformed with the A_0 map it is necessary to add in Equation 4.5 an interference contribute to the term due to the direct path:

$$\begin{aligned} \mathbf{FW}_w \{s(t, D_i)\} &= \sqrt{\dot{w}(f)} \cdot S_0(w(f), 0) \cdot e^{-j2\pi w(f) t_{di}} \cdot \\ &\cdot \left[\underbrace{e^{-j2\pi fK D_i}}_{\text{direct path}} + \underbrace{\sum_{k=1}^N \Gamma_k e^{-j2\pi fK D_k}}_{\text{reverberation}} \right] \end{aligned} \quad (4.6)$$

where N is the number of the multiple reflections considered, Γ_k is the reflection coefficient related to the k -th path which is close to 1 in the case of perfect edges and D_k is the distance travelled by the k -th reflected path from the source position to the sensor i -th.

The Equation 4.6 states that the reverberation of the plate edges is modelled in the warped fourier domain as a sum of weighted exponential functions which depend on the distances travelled by the reflected wave paths.

In this case, the Fourier transform of the cross-correlation of two warped signals acquired by two sensors $s(t, D_1)$ e $s(t, D_i)$ becomes:

$$\begin{aligned} & \mathbf{FW}_w \{s(t, D_1)\} \cdot (\mathbf{FW}_w)^* \{s(t, D_i)\} = \\ & = \dot{w}(f) \cdot |S_0(w(f), 0)|^2 \cdot \left[\underbrace{e^{-j2\pi f K(D_1 - D_i)}}_{\text{direct path}} + \underbrace{\sum_{k=1}^N \Gamma_k e^{-j2\pi f K(D_1 - D_k)}}_{\text{reverberation}} \right] \end{aligned} \quad (4.7)$$

Equation 4.7 shows that cross correlating two warped signals leads to the cancelation of the frequency modulation effect but does not remove the term due to multiple reflections; therefore, because of the constructive interference in the presence of reverberations, not even cross-correlation methods are effective for robust estimation of travelled differences.

4.4 Warped Wavelet Transform using Cross-Correlating Basis

To improve the estimation of the difference in travelled distance a warp-frequency decomposition on the $M - 1$ cross-correlated signals, being M the number of different sensors used, is proposed.

The warped cross-correlated signal:

$$s_{cross_w}(t) = \mathbf{F}^{-1} \{ \mathbf{FW}_w \{s(t, D_1)\} \cdot (\mathbf{FW}_w)^* \{s(t, D_i)\} \} \quad (4.8)$$

is decomposed through a wavelet analysis.

For our purpose, a mother wavelet $\psi(t)$ was derived by optimizing the matching with the cross-correlation of two warped triangular pulses with arbitrary duration [55]. Finally, the unitary operator \mathbf{W}_w was used to define the proper basis in the warped domain and compute the wavelet coefficients $a_j(n)$ of two cross correlated signals obtained by Equation 4.8 as:

$$a_j(n) = 2^{-j/2} \int_{-\infty}^{\infty} s_{cross_w}(t) \cdot \psi(2^{-j}t - n) dt$$

Once the values of $a_j(n)$ have been found, the estimated difference in distance $D_1 - D_i$ is the translation j^* which corresponds to the maximum of the norm of the vector $a_j(n)|_{j=j^*}$

$$\max_j \|a_j(n)\| \quad \text{where} \quad \|a_j(n)\| = \sqrt{\sum_{m=1}^{N_j} a_j^2(m)} \quad (4.9)$$

where N_j is the number of scales considered.

4.5 Hyperbolic positioning

To locate the impact position in a plate (i.e. in a bi-dimensional space), at least $M = 3$ passive sensors are necessary. Given the coordinates of the sensors positions (x_i, y_i) and having estimated the differences in travelled distance Δd_{1i} between the waves acquired by the first sensor and the remaining, a hyperbolic positioning method (also called *multilateration*) can be applied to locate the point source. Such a method exploits the differences in distance to determine hyperbolas on which the impact point $\bar{x} = (x_p, y_p)$ must lie:

$$\Delta d_{1i} = \sqrt{(x_1 - x_p)^2 + (y_1 - y_p)^2} - \sqrt{(x_i - x_p)^2 + (y_i - y_p)^2} \quad (4.10)$$

The intersection of the different hyperbolas, obtained by solving the system of $M - 1$ equations with the Levenberg-Marquardt algorithm [56], is taken to be the impact position. It has been verified that the impact localization performances do not depend on the choice of the reference sensor (sensor 1 in our case) that it can be chosen arbitrary.

4.6 Cramèr-Rao bound

The Cramèr-Rao bound [57] gives the lower bound on the covariance of the impact positions estimated from the difference distance

$$\Delta d_{1i} = d_{1p} - d_{ip}$$

where d_{ip} is the distance between the i -th sensor and the point $\bar{x} = (x_p, y_p)$.

To calculate this bound the system of non-linear equations

$$\Delta d_{1i} = \tilde{\Delta} d_{1i}(\bar{x}) + e_i \quad i = 1, \dots, M - 1 \quad (4.11)$$

must be linearized near the impact positions $\bar{x} = (x_p, y_p)$ and the corresponding difference distance travelled Δd_{1i} .

In the above equations and following the symbol $\tilde{\cdot}$ indicates the estimation of the relative physical quantity while e_i represents the error related to sensor i .

Given $M - 1$ difference distance of arrival measurements, the linearized system which represents the relationship between the position and the travelled distance differences is

$$\tilde{\Delta} d = S \cdot \tilde{t}(\bar{x}, t_0) = S \cdot \tilde{t}(\bar{x}) + S \cdot \bar{e} = S \cdot C \cdot \bar{x} + S \cdot \bar{e} \quad (4.12)$$

where $\tilde{\Delta} d$ is a vector containing the $M - 1$ difference distances, $\tilde{t}(\bar{x})$ is a vector of M elements formed by the estimated travelled time from the M sensors that it is assumed to be independent on the initial impact instant t_0 , \bar{e} is the vector containing the errors from all the M sensors and with

$$S = \begin{bmatrix} 1 & -1 & & 0 \\ \vdots & & \ddots & \\ 1 & 0 & & -1 \end{bmatrix} \quad (4.13)$$

representing a full-rank $(M - 1) \times M$ matrix and C the $(M \times 2)$ matrix of partial derivatives whose elements are

$$\begin{aligned} C_{i1} &= \frac{1}{v_s} \cdot \frac{x_p - x_i}{\sqrt{(x_p - x_i)^2 + (y_p - y_i)^2}} \\ C_{i2} &= \frac{1}{v_s} \cdot \frac{y_p - y_i}{\sqrt{(x_p - x_i)^2 + (y_p - y_i)^2}} \end{aligned} \quad (4.14)$$

In Equation 4.14 v_s is an equivalent speed of sound in the material obtained through the time-distance mapping described in the warping procedure and it can be computed as $v_s = K \cdot f_s$ where K is the normalization parameter used in Equation 4.1 and f_s is the sampling frequency. Note that this condition implies that the measurement vector $\tilde{\Delta}d$ is not affected by the presence of the nonzero clock offset t_0 .

The Cramèr-Rao bound for the position estimate is

$$CRB = [C^T S^T \cdot R_h^{-1} \cdot SC]^{-1} \quad (4.15)$$

where R_h is the $(M - 1) \times (M - 1)$ covariance matrix of the noise vector $\bar{v} = S \cdot \bar{e}$ that can be obtained as

$$R_h = E [\bar{v} \cdot \bar{v}^T] = S \cdot E [\bar{e} \cdot \bar{e}^T] \cdot S^T = S \cdot R \cdot S^T \quad (4.16)$$

where E is the expectation.

In practical cases measurement errors are independent identically distributed gaussian random variables with zero mean and standard deviation σ_d .

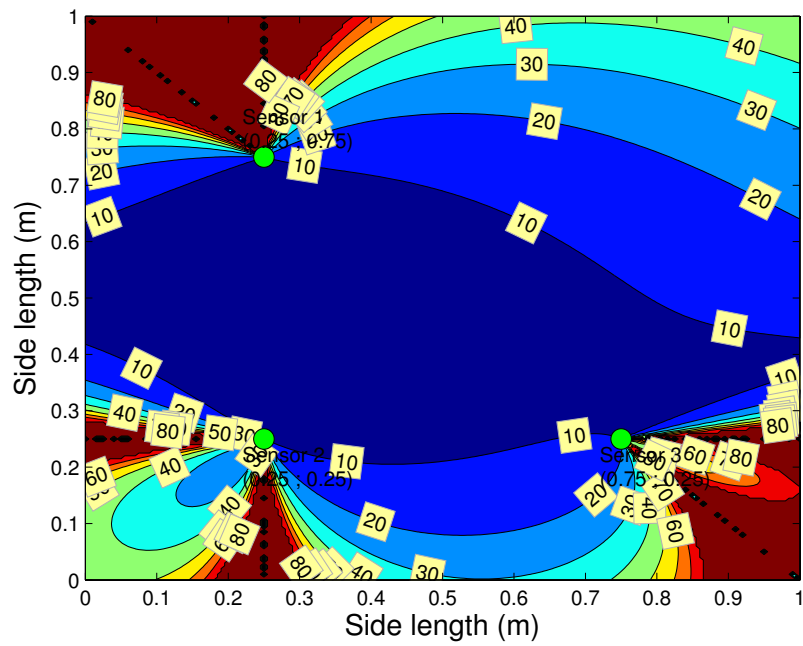
The covariance matrix is diagonal and its elements are equal to the variance σ_d^2 so $R = \sigma_d^2 \cdot \mathbf{I}$ where \mathbf{I} is the identity matrix.

The Cramèr-Rao bound can be written as:

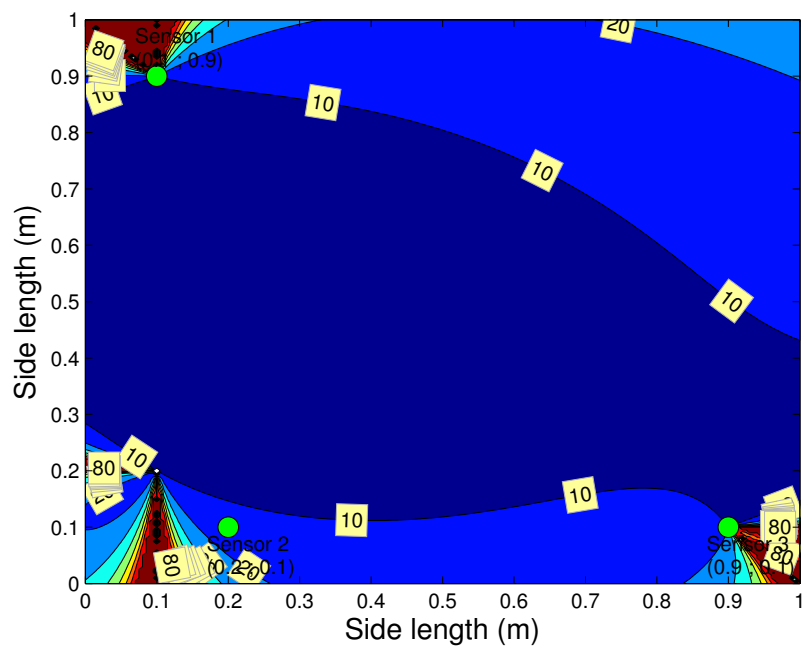
$$CRB = \left\{ C^T S^T \cdot [S \cdot (\sigma_d^2 \cdot \mathbf{I}) \cdot S^T]^{-1} \cdot SC \right\}^{-1}$$

The minimum theoretical estimation error of the source positions, expressed in mm, given by the Cramèr-Rao lower bound (CRLB) is shown in Figure 4.5 for the four plate-PZTs configurations that will be tested in the experiments described in Section 4.7.

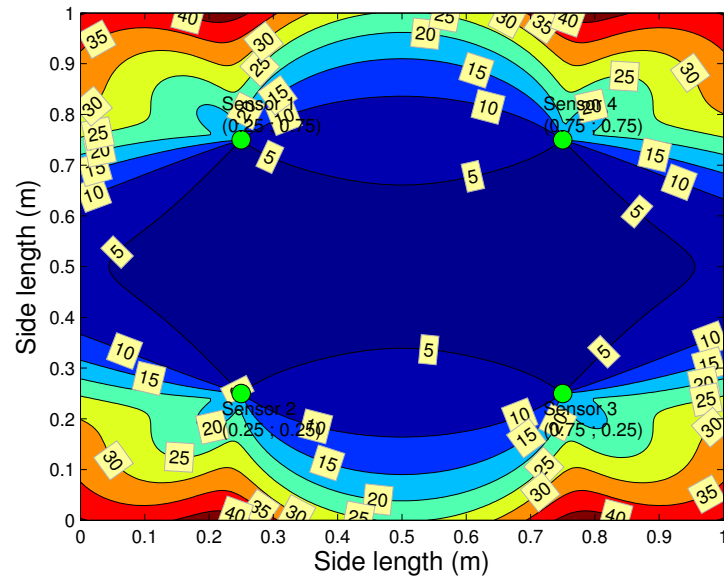
Results in Figure 4.5 show how the theoretical localization of an AE source is better in the convex area bounded by the sensors while is greatly deteriorated outside this area. Moreover, it is important to notice that the Cramèr-Rao lower bound does not take into account the reflection due to the edges.



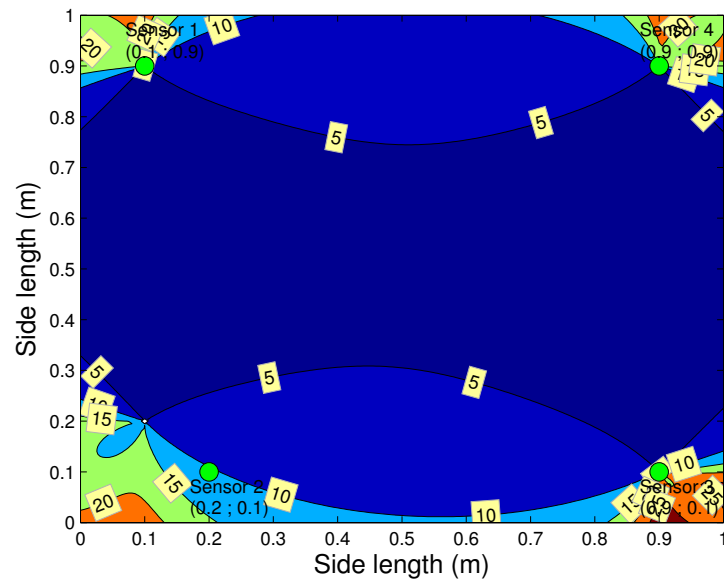
(a) 3 sensors symmetric respect to the edges



(b) 3 sensors asymmetric respect to the edges



(c) 4 sensors symmetric respect to the edges



(d) 4 sensors asymmetric respect to the edges

Figure 4.5: Cramèr - Rao lower bound for the four sensors configurations tested experimentally in Section 4.7. Isolines express CRLB in mm.

4.7 Experimental verification

As a case study, we exploited the proposed tool to locate impacts in an aluminium 1050A square plate $1\text{ m} \times 1\text{ m}$ and 0.003 m thick. Four different experiments were carried out using four and three sensors distributed in a symmetrical and asymmetrical configuration with respect to the edges of the plate.

The positions of the sensors are collected in Table 4.1.

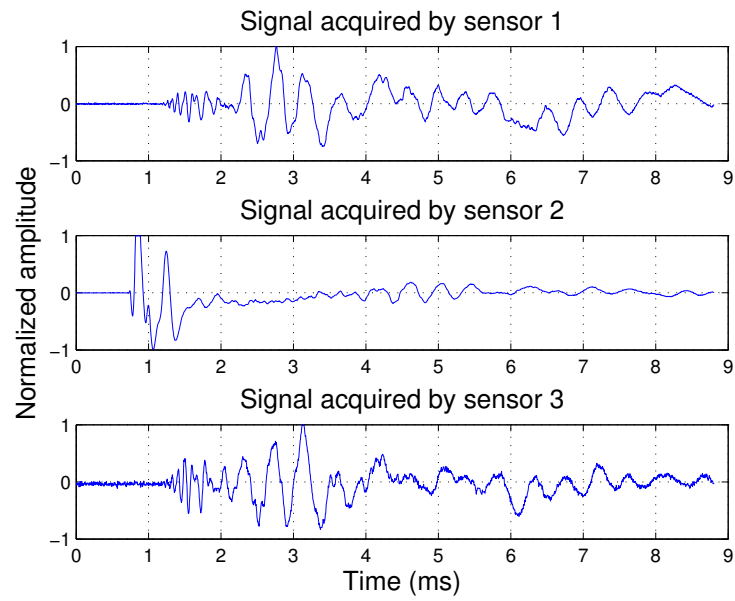
Topology	Coordinates	Sensor 1	Sensor 2	Sensor 3	Sensor 4
asymmetrical	x (m)	0.10	0.20	0.90	0.90
	y (m)	0.90	0.10	0.10	0.90
symmetrical	x (m)	0.25	0.25	0.75	0.75
	y (m)	0.75	0.25	0.25	0.75

Table 4.1: Sensors positions for the considered symmetrical and asymmetrical topologies.

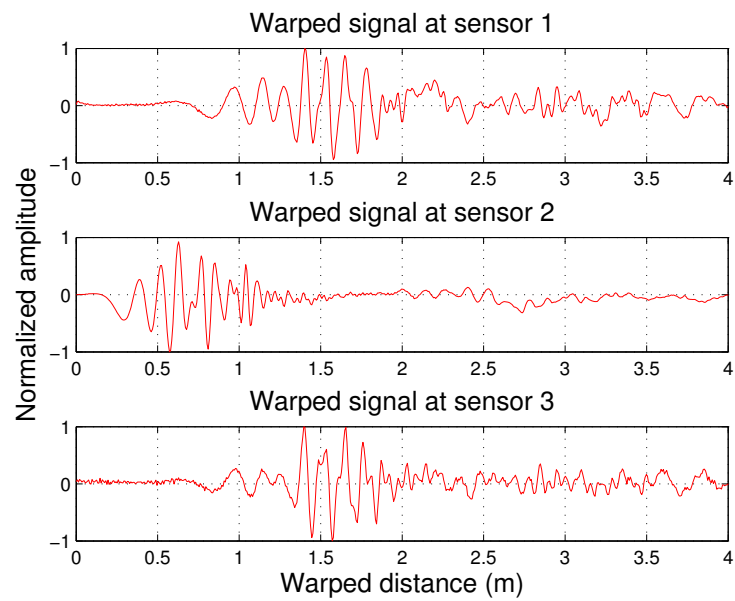
Guided waves were excited by hitting the plate with a pencil orthogonally to the surface. The generated signals were recorded using the LC534 series LeCroy oscilloscope at a sampling frequency of 300 kHz . Acquisitions were triggered when the signal received from one of the PZT discs (PIC181, diameter 0.01 m , thickness 0.001 m) reached a threshold level of 140 mV ; pre-trigger recordings were enabled to obtain the previous history of each signal. The sampling frequency was sufficiently high to avoid aliasing effects, as the frequency content of the acquired signals vanishes above 60 kHz .

In Test 1 three PZT discs were placed asymmetrically with respect to the edges, as schematically depicted in Figure ??(b). Figure 4.6(a) shows the experimental waveforms detected by the three sensors after having excited the plate at the following coordinates: $x = 0.15\text{ m}$, $y = 0.15\text{ m}$.

As can be seen by observing Figure 4.6(a), it would be extremely difficult to estimate the difference in time of arrival by using classical thresholding or peak detection procedures. In fact, such estimation is complicated by the effect of dispersion which introduces a distance-dependent group delay shift.



(a) Signals in time domain



(b) Warped time domain version

Figure 4.6: Sample acquired signals by the passive monitoring system.

In order to compensate for dispersion, first the WFT operator must be defined. For such a scope, the Lamb waves group velocity dispersion curves for the 0.003 m thick aluminium plate were obtained considering the following nominal properties for the aluminium: $E = 69$ GPa, $\nu = 0.33$ and $\rho = 2700$ kg \cdot m $^{-3}$. The curves are those represented in Figure 4.3.

In the [0–300] kHz frequency range, only the two fundamental A_0 and S_0 Lamb waves can propagate through this plate. Since for out-of-plane excitation the energy in the A_0 mode is considerably greater than that retained by the S_0 mode, the group velocity curve of the A_0 mode was used to shape the warping operator according to Equation 4.1. Next, by processing the acquired signals with the WFT, the waveforms depicted in Figure 4.6(b) are obtained. In the new waveforms, the group delay dependence on distance is removed. However, spurious components arise due to the edges' reflections and a frequency modulation remains because of the actuating time is unknown.

At this point, the wavelet transform is applied to the two cross-correlated warped signals. The warp-frequency representation and the trend of the wavelet coefficients norm $\|a_j(n)\|$ are shown in Figure 4.7.

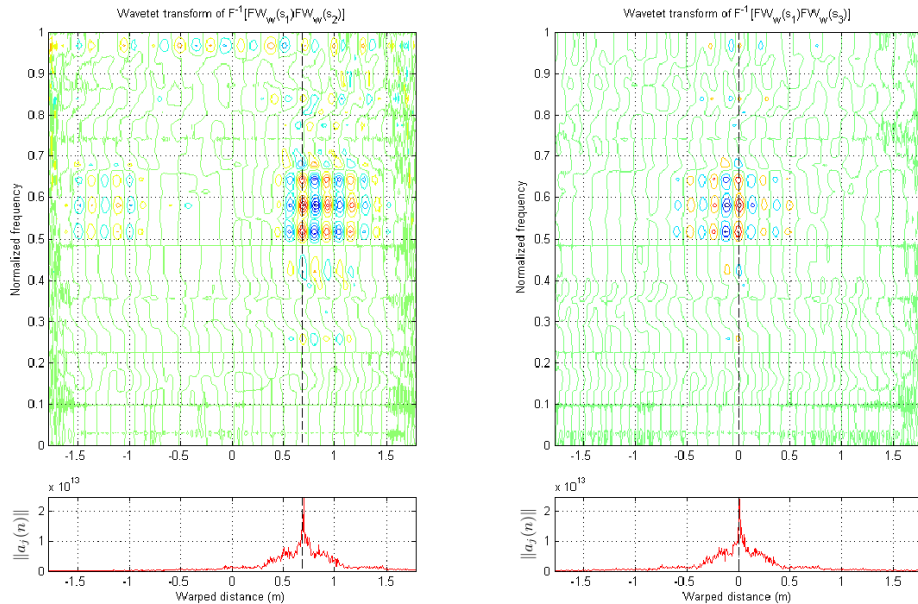
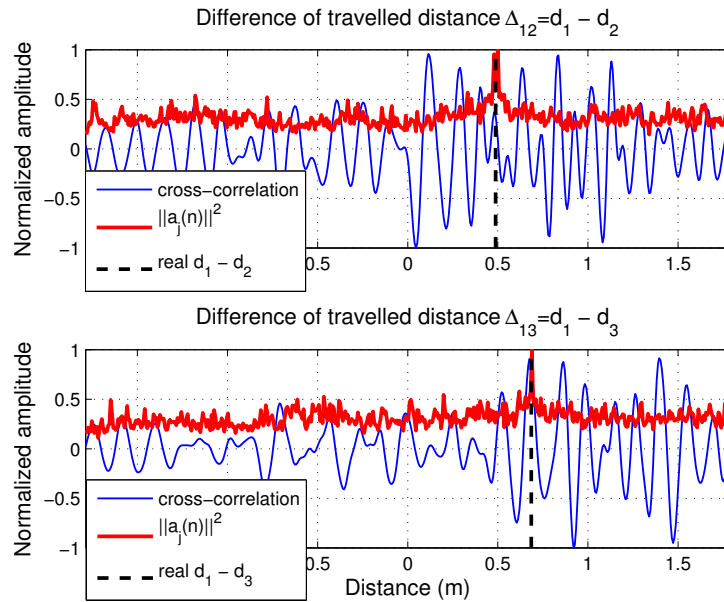


Figure 4.7: Wavelet transform of the two warped cross-correlating signals obtained for impact located in $x = 0.15$ m $y = 0.15$ and the related $\|a_j(n)\|$ curves.

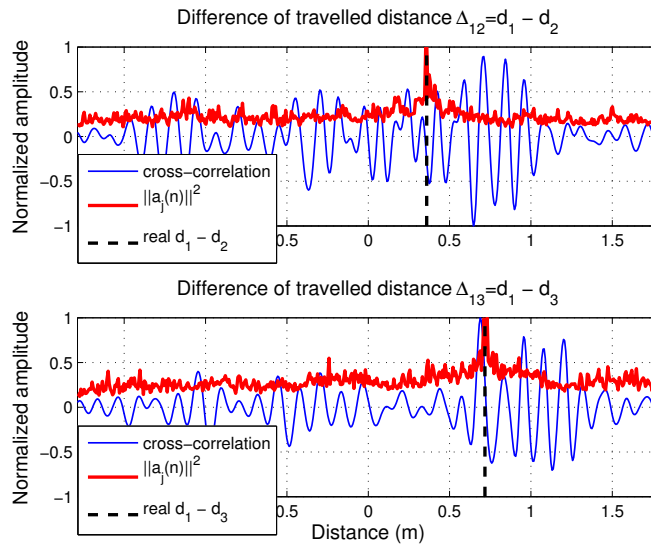
It can be seen from this figure how the proposed wavelet warped basis is suitable for analysing the cross-correlated signal as the abscissa of the maximum value of $\|a_j(n)\|$ is very closed to the true difference in distance travelled ($D_{12} = 0.618$ m and $D_{13} = 0$ m) that has been depicted in figure with a black dash line.

It is also important to underline the localization improvement obtained through this method with respect to the analysis of the simple peaks of the cross-correlating signals proposed in [53]. Figure 4.8 shows the comparison between the warped cross-correlated signals and the curves $\|a_j(n)\|$ for two different impacts ($x = 0.65$ m, $y = 0.15$ m) and ($x = 0.75$ m, $y = 0.25$ m). As it can be seen the peaks of the cross-correlating signals are spread and the related abscissa are not very close to the true difference of travelled distance and this is due to the non negligible interference term. So in presence of reverberations the cross-correlation of warped signals can lead to large errors, as shown in Figure 4.8(b), while the new localization procedure closely estimates the true difference in travelled distances.

The source location is detected through multilateration as described in Section 4.5, solving the system of equations with the Levenberg-Marquardt algorithm.



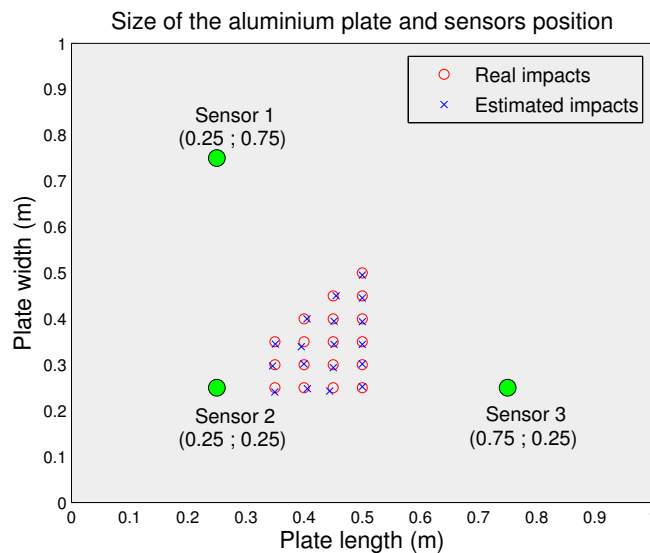
(a) Impact in $x = 0.65$ m $y = 0.15$ m



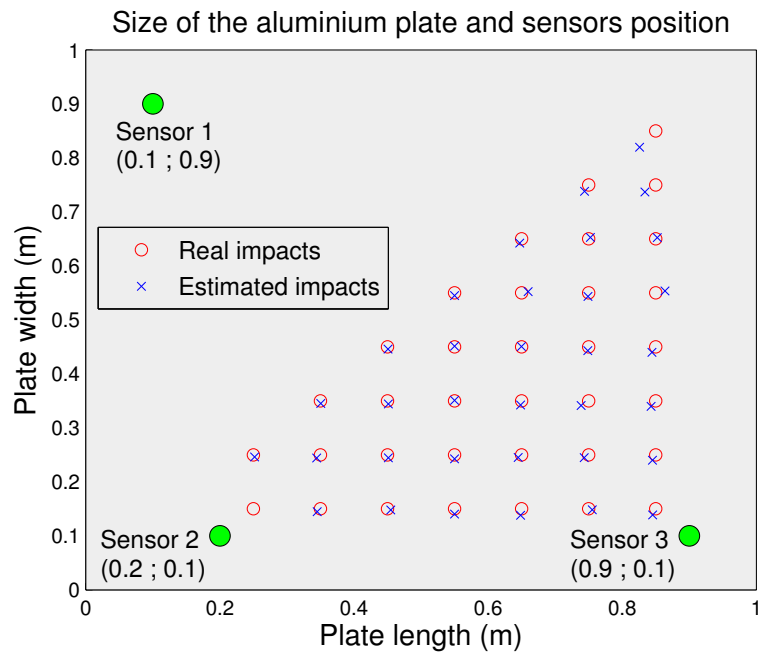
(b) Impact in $x = 0.75$ m $y = 0.25$ m

Figure 4.8: Comparison in function of the difference in distance between the warped cross-correlated signal and the curve $\|a_j(n)\|$.

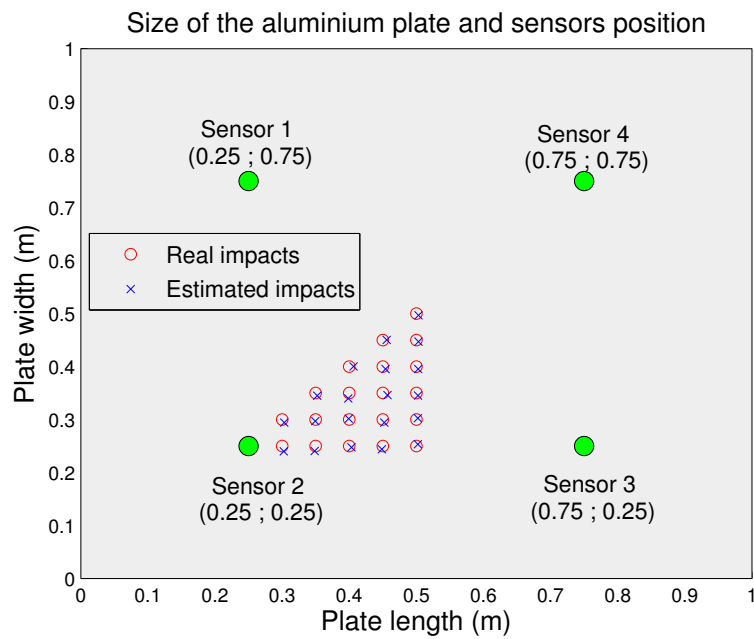
The results of the proposed procedure for impacts localization can be seen in Figure 4.9 where the target and estimated impact points denoted by circles \circ and crosses \times , respectively, are shown.



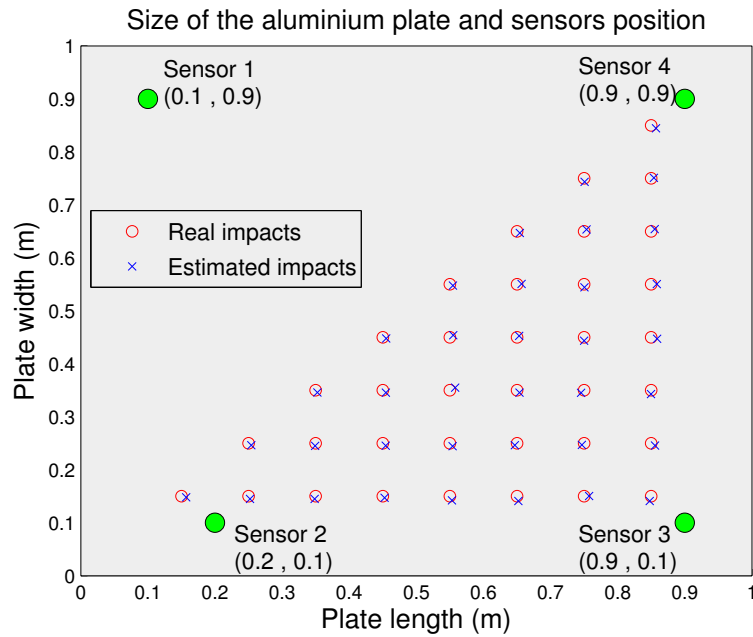
(a) 3 sensors symmetric respect to the edges



(b) 3 sensors asymmetric respect to the edges



(c) 4 sensors symmetric respect to the edges



(d) 4 sensors asymmetric respect to the edges

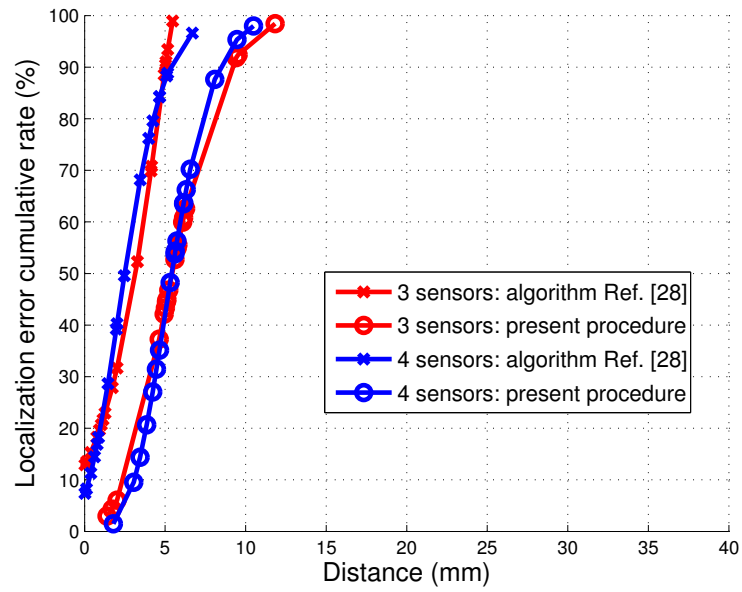
Figure 4.9: Source localization results.

Such estimations are performed in a purely passive manner, i.e. ignoring the time instant at which the acoustic emission starts.

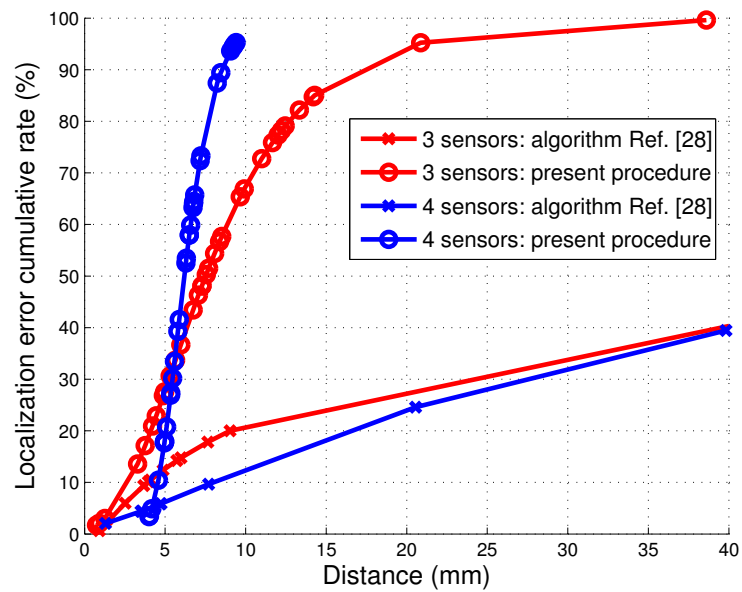
The comparison between the proposed procedure and the algorithm described in [53] is given through the analysis of the cumulative distribution of the localization error for the four considered configurations of the PZT transducers which is shown in Figure 4.10.

Figure 4.10(a) shows that, in case of sensors placed at small distances and regular positions, TDOA algorithms based on the pure cross-correlation analysis (such as the one proposed in [53]) produce reliable and precise localization results. The accuracy is compromised when the sensors position is irregular, close to the edges and, consequently, prone to reverberations. In such cases the warped wavelet analysis offers an improved localization accuracy as shown in Figure 4.10(b).

Finally a comparison between the experimental results and the Cramèr-Rao lower bound is presented.



(a) Sensors symmetric respect to the edges



(b) Sensors asymmetric respect to the edges

Figure 4.10: Cumulative distribution of the localization errors.

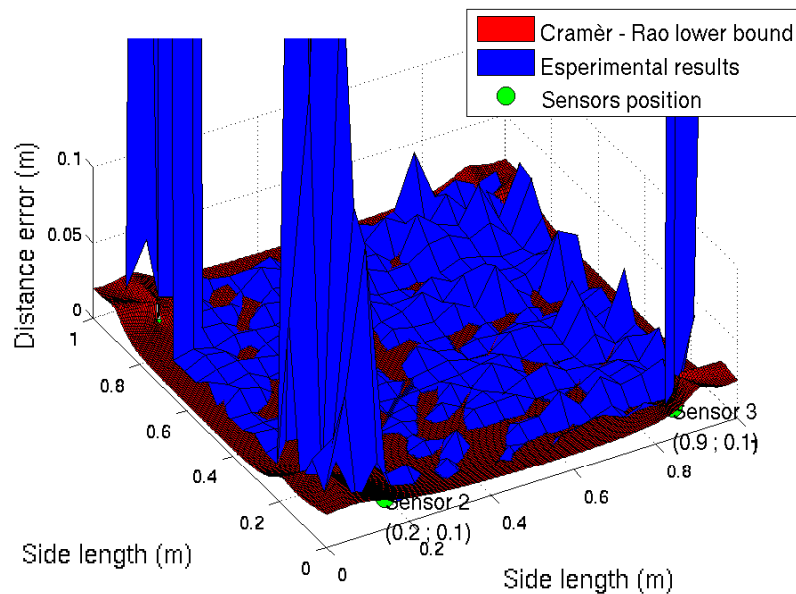
In the lower bound estimation, the measurement errors are considered as independent identically distributed gaussian random variables with zero mean.

Their standard deviation σ_d can be estimated as:

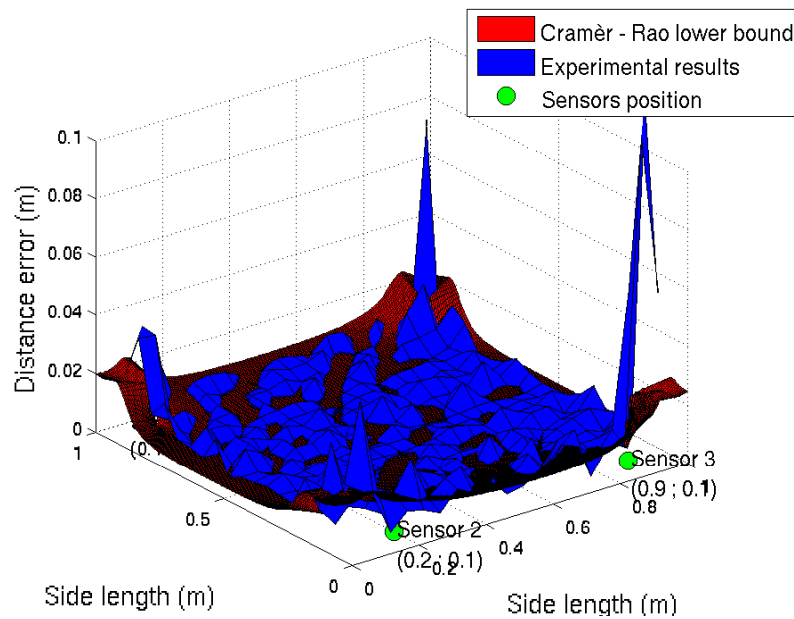
$$\sigma_d = 2 \cdot \frac{v_s}{f_s} = 2 \cdot \frac{1570}{10^6} = 3 \text{ mm}$$

being $f_s = 1 \text{ MHz}$ the sampling frequency and $v_s = 1570 \text{ m} \cdot \text{s}^{-1}$ the equivalent speed of sound in the warped domain.

As can be seen in Figure 4.11, the impact position errors are very close to the theoretical limit given by the Cramèr-Rao lower bound in the convex area bounded by the sensors. Conversely, when the source is placed in the external area between sensors and the plate edges, the localization errors increase roughly respect to the Cramèr-Rao bound because of the dominant phenomenon of reflection that totally corrupts the cross-correlated signal.



(a) 3 sensors asymmetric respect to the edges



(a) 4 sensors asymmetric respect to the edges

Figure 4.11: Comparison between the Cramèr-Rao lower bound and the experimentally estimated positions.

4.8 Discussion

In this Chapter a method to extract the difference in distance travelled by stress guided waves is proposed. The method applies a dispersion compensation procedure on the signals acquired by passive sensors, thus overcoming the difficulties associated with arrival time detection based on classical thresholding procedures.

Then a suitable wavelet decomposition is applied to the cross-correlating signals to reduce the effect of multiple edge reflections. The analysis of the wavelet transform magnitude reveals the difference in distance travelled by the wave to reach the different sensors. Finally, multilateration is applied.

Excellent performance in terms of point of impact localization is shown through experiments since the estimated impact positions are very close to the Cramèr-Rao lower bound.

Further, the reliability of the proposed approach in presence of reverberation make

the new tool suitable for automatic acoustic emission localization procedures. Future developments include the generalization of the proposed approach to applications in which higher order modes contaminate the acquired data, and to applications characterized by anisotropic propagation, such as detection of impacts in composite plates.

Chapter 5

Frequency Warped Wavelet

Don't part with your illusions. When they are gone you may still exist, but you have ceased to live.

Mark Twain

5.1 Introduction

This Chapter presents an improved impact localization algorithm based on the application of the frequency warping operator for E-spline wavelet multiresolution analysis. A novel impact localization algorithm based on the frequency warping unitary operator applied to E-spline wavelet multiresolution analysis is presented.

Unitary frequency warped representation is important to analyse class of signal covariant to group delay shift as those propagating through frequency-dependent channels. The innovative key points behind the developed framework are:

- to perform a nonstationary wavelet multiresolution analysis on the acquired signals;
- to design a proper scaling wavelet through the frequency warping operator;
- application of the frequency warped wavelet multiresolution on the cross-correlated signal to achieve an accurate time difference of arrival (TDOA) estimation.

Finally, the TDOA data are exploited to locate the acoustic emission source through hyperbolic positioning.

In this work the impact localization is performed with a three-step procedure schematically depicted in Figure 5.1; in particular the first block represents an extension of the algorithm proposed in [6], [7].

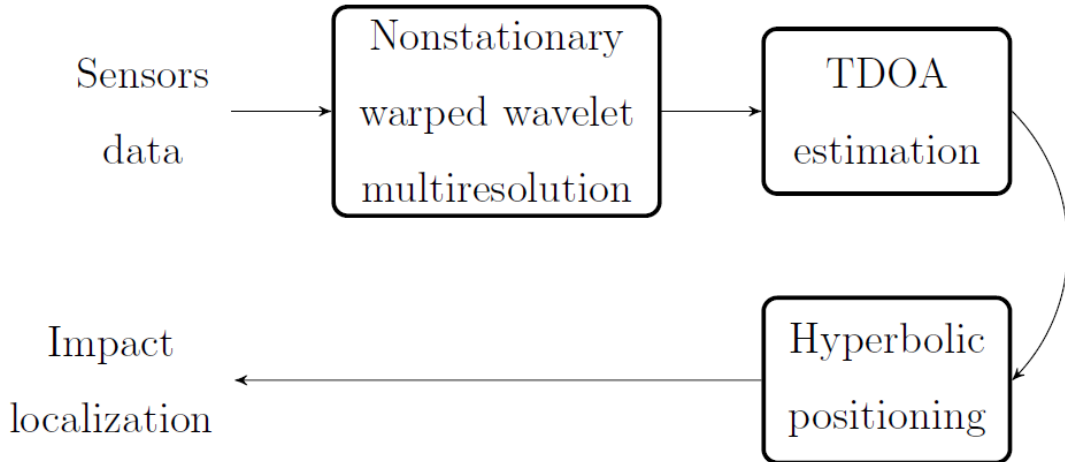


Figure 5.1: A typical three-step acoustic emission source location procedure.

In this Chapter we propose to design a novel wavelet decomposition of the dispersive acquired signal based on the following concepts: perform a frequency warped wavelet decomposition in which the scaling function is obtained applying a unitary frequency warping operator on the classical E-spline orthogonal scaling wavelet family.

The warping map is designed properly in order to compensate the dispersion due to the wave propagation and to achieve sparse signal representation in the new frequency warped domain.

In order to deal with multi modal dispersive compensation a multiresolution wavelet analysis on the cross-correlated warped signal is proposed instead of a continuous wavelet analysis as presented in [6].

In particular a modification of the classic construction of warped E-spline is developed in order compensate both the S_0 and A_0 mode of Lamb waves using a single multiresolution analysis with S_0/A_0 warped filter bank design for different wavelet

level.

The main difference with the classical construction of E-spline multiresolution analysis is that the multiresolution spaces are derived from scale-dependent generating functions [58], so the scaling functions at different scales are not dilates of one another. From an algorithmic standpoint, Mallat Fast Wavelet Transform algorithm can still be applied; the only adaptation consists in using scale-dependent filter banks.

The main idea is to design a proper tiling of the time-frequency plane where for each scale a scale dependent frequency warped scaling function is constructed according to the dominant dispersive mode in the actual frequency band.

The Chapter is organized as follows: a brief review of the frequency warped wavelet theory with definitions is presented in Section 5.2.

In Section 5.3 the properties concerning nonstationary multiresolutions and the application of the frequency warped operator on the wavelet time-frequency decomposition are described.

In Section 5.4 the proposed cross wavelet algorithm based on the nonstationary multiresolution wavelet frequency warped decomposition is detailed.

In order to demonstrate the effectiveness of the proposed framework, we have investigated lamb wave transmission over aluminum plate that suffers from severe multi modal frequency dispersions and multipath reflections.

Experimental validations of the proposed work, consisting in impacts localization by using three PZT sensors, with different spatial distribution over the plate surface, are shown in Section 5.6.

The aim of this work is to achieve an higher resolution in impact localization starting from algorithm described in [7], in order to improve the analysis of the warped cross-correlation signal with a new nonstationary warped wavelet decomposition.

5.2 Frequency Warped Wavelet Analysis

A novel wavelet decomposition design scheme of the dispersive acquired signal is proposed, based on the following concepts: perform a frequency warped wavelet decomposition in which the scaling function is obtained applying a unitary frequency warping operator on the classical E-spline orthogonal scaling wavelet family.

In order to deal with multi modal dispersive compensation a multiresolution wavelet analysis on the cross-correlated warped signal is proposed instead of a continuous wavelet analysis as presented in [6]. In particular a modification of the classic construction of warped E-spline is developed in order compensate both the S_0 and A_0 mode of Lamb waves using a single multiresolution analysis with S_0/A_0 warped filter bank design for different wavelet level; the main difference with the classical construction of E-spline multiresolution analysis is that the multiresolution spaces are derived from scale-dependent generating functions [58], so the scaling functions at different scales are not dilates of one another.

From an algorithmic standpoint, Mallat Fast Wavelet Transform algorithm can still be applied; the only adaptation consists in using scale-dependent filter banks.

The main idea is to design a proper tiling of the time-frequency plane where for each scale a scale dependent frequency warped scaling function is constructed according to the dominant dispersive mode in the actual frequency band.

We start to review the theory which deal with the frequency warped wavelet analysis. In particular it will be described how the mother wavelet and scaling functions can be derived starting from the classic wavelet theory with the application of the frequency warped operator.

It is important to notice that respect to the classic wavelet analysis the main difference is that the shift in time is not invariant; the first step is to define an operator unitary equivalent to the ordinary shift operator $(\mathbf{S}s)(t) = s(t - 1)$ via the warping operator built on the phase function $w(f)$. We define the time warped-invariant generalized shift operator \mathbf{T} defined in the Fourier domain by the product

$$(\mathbf{FT}s)(f) = (\mathbf{F}s)(f)e^{-j2\pi w(f)} \quad (5.1)$$

By Eq. (5.1), for any $m \in \mathbb{Z}$, the action of \mathbf{T}^m is equivalent to multiplication by $e^{-j2\pi mw(f)}$. The warping operator \mathbf{W} establishes a unitary equivalence of the generator \mathbf{T} and the shift-by-one operator \mathbf{S} where $\mathbf{T} = \mathbf{W}\mathbf{S}\mathbf{W}^\dagger$.

$$\begin{aligned} (\mathbb{F}\mathbf{W}^\dagger\mathbf{T}s)(f) &= \sqrt{\frac{dw^{-1}(f)}{df}}(\mathbb{F}s)(w^{-1}(f))e^{-j2\pi w(w^{-1}(f))} \\ &= \sqrt{\frac{dw^{-1}(f)}{df}}(\mathbb{F}s)(w^{-1}(f))e^{-j2\pi f} = (\mathbb{F}\mathbf{S}\mathbf{W}^\dagger s)(f) \end{aligned} \quad (5.2)$$

It immediately follows that

$$\forall m \in \mathbb{Z}, \mathbf{T}^m = \mathbf{W}\mathbf{S}^m\mathbf{W}^\dagger.$$

Therefore the group of generalized shift operators is unitarily equivalent to the group of ordinary shift operator. An other unitary operator is the dyadic dilatation operator defined as

$$(\mathbf{D}_{\frac{1}{2}}s)(t) = \sqrt{\frac{1}{2}}s\left(\frac{t}{2}\right)$$

with the following properties: inverse $\mathbf{D}_{\frac{1}{2}}^{-1} = \mathbf{D}_2$ and n -th power $\mathbf{D}_{\frac{1}{2}}^n = \mathbf{D}_{\frac{1}{2^n}}$.

The action of the dilatation operator in the Fourier domain is

$$(\mathbb{F}\mathbf{D}_{\frac{1}{2}}s)(f) = \sqrt{2}(\mathbb{F}s)(2f).$$

The property (5.2) is preserved through scale since the scaled warping operator $\mathbf{D}_{\frac{1}{2}}^n\mathbf{W}$ because

$$\forall (n, m) \in \mathbb{Z}^2, \mathbf{D}_{\frac{1}{2}}^n\mathbf{T}^m\mathbf{D}_{\frac{1}{2}}^{-n} = \mathbf{D}_{\frac{1}{2}}^n\mathbf{W}\mathbf{S}^m\mathbf{W}^\dagger\mathbf{D}_{\frac{1}{2}}^{-n}.$$

The next proposition shows that this Riesz basis is unitarily equivalent to an auxiliary Riesz basis obtained by repeated applications of the ordinary shift operator. This basis spans a shift-invariant subspace of $\mathbf{L}^2(\mathbb{R})$ unitarily equivalent to the space V_0 spanned by the warped Riesz basis.

The next proposition provides equivalent Fourier domain conditions for a function to generate an orthogonal warped Riesz basis.

Proposition 5.2.1: *Let \mathbf{T} be the generalized shift generator with warping characteristic $w(f)$ and scale factor $\frac{1}{2}$. A function $\xi(t)$ generates a Riesz basis $\{\mathbf{T}^m\xi(t)\}_{m \in \mathbb{Z}}$*

for the space $V_0 = \overline{\text{span}\{\mathbf{T}^m \xi \mid m \in \mathbb{Z}\}}$ if and only if there exist two constants $A > 0$ and $B > 0$ such that for almost all $\omega = 2\pi f \in [-\pi, \pi]$,

$$\frac{1}{B} \leq \sum_{k=-\infty}^{+\infty} |\bar{Z}(\omega + k)|^2 \leq \frac{1}{A},$$

where $\bar{Z} = \mathbf{F}(\mathbf{W}^\dagger \mathbf{T}^m \xi)$.

Furthermore, let $\{\mathbf{T}^m \xi(t)\}_{m \in \mathbb{Z}}$ be a Riesz basis for V_0 and let

$$\Phi(f) = \mathbf{F}[\varphi](f) = \frac{\bar{Z}(\omega)}{\sqrt{\sum_{k=-\infty}^{+\infty} |\bar{Z}(\omega + k)|^2}}.$$

Then $\{\mathbf{D}_{\frac{1}{2}}^n \mathbf{T}^m \bar{\varphi}\}_{m \in \mathbb{Z}}$, where $\bar{\varphi} = \mathbf{W}\varphi$, is an orthonormal basis for V_n for any $n \in \mathbb{Z}$.

Like ordinary scaling functions, warped scaling functions are strategical for the construction of warped wavelet bases.

Based on our results for warped Riesz bases, the following definition of warped scaling function can be provided:

Definition 5.2.1: A scaling function is a function $\varphi \in \mathbf{L}^2(\mathbb{R})$ such that the families $\{\mathbf{D}_{\frac{1}{2}}^n \mathbf{T}^m \bar{\varphi}\}_{m \in \mathbb{Z}}$ are orthonormal for any $n \in \mathbb{Z}$.

From 5.2.1 it follows that $\bar{\varphi} \in \mathbf{L}^2(\mathbb{R})$ is a scaling function if and only if

$$\sum_{m=-\infty}^{+\infty} \frac{dw^{-1}(\omega)}{d\omega} |\bar{\Phi}(w^{-1}(\omega + m))|^2 = 1$$

In the Fourier domain the warped wavelets are related to the dyadic wavelets as follow:

$$\begin{aligned} \bar{\Psi}_{n,m}(\omega) &= (\mathbf{F}\mathbf{W}\psi_{n,m})(\omega) \\ &= \sqrt{\frac{dw(\omega)}{d\omega}} \Psi_{n,m}(w(\omega)) \\ &= \sqrt{2^n \frac{dw(\omega)}{d\omega}} \Psi(2^n w(\omega)) e^{-j2^n m w(\omega)} \end{aligned}$$

The warped wavelets are not simply generated by dilating and translating a mother wavelet. Rather, the translated wavelets are generated by all-pass filtering $e^{-j2^n m w(\omega)}$. Scaling also depends on the warping map $w(\omega)$.

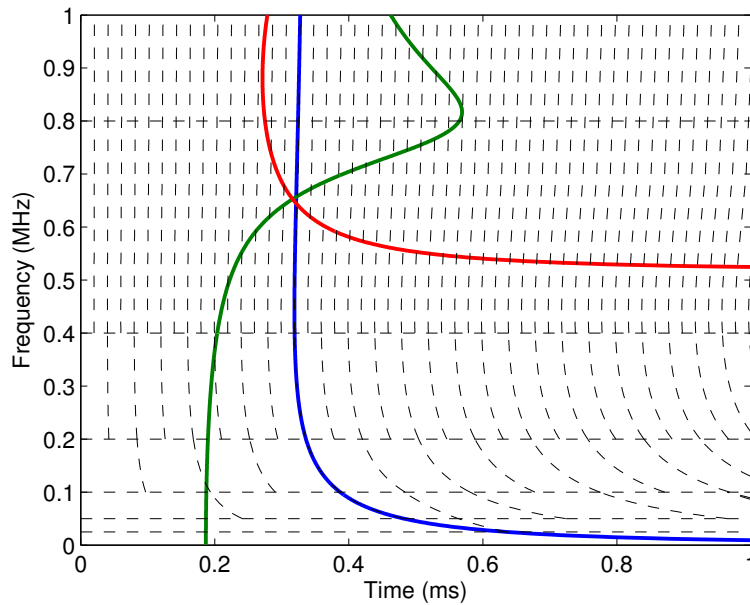
Figs. 5.2(a) and (b) show how the GDSC Wavelet tiling TF plane

$$\text{TFR}_W[s_{disp}](t, f) = \text{WT}[\mathbf{W}s](tKc_g(f), w^{-1}(f))$$

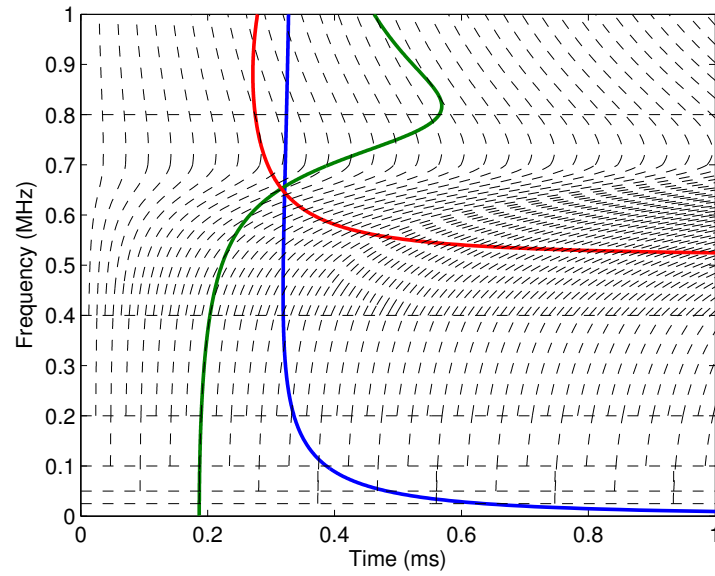
leads to match with a single dispersive mode but the resolution on the frequency axis is not variable.

Similarly, the tiling of the STFT plane shaped according to the warping map for a single mode is described in [21].

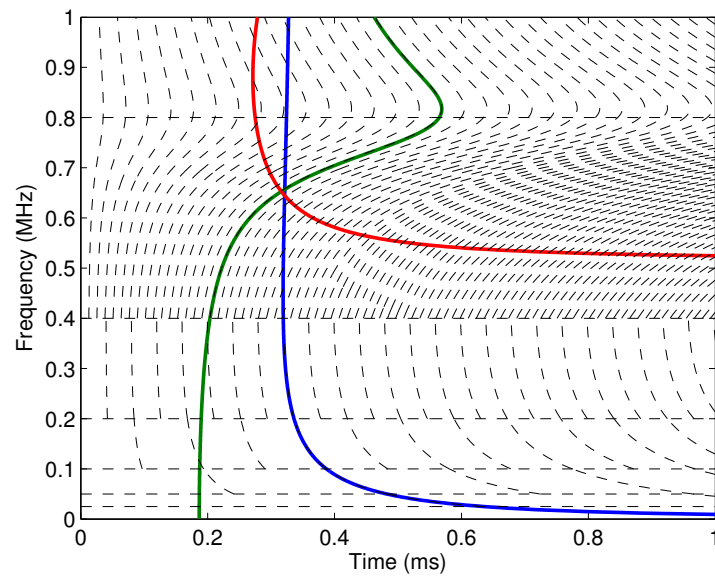
Atoms change their shape versus time with the dispersive properties of the single mode. But using the single mode combined effect of frequency warping and STFT it is impossible to match the group delay characteristics of multiple modes, for example S_0/A_0 , for different frequency band.



(a)



(b)



(c)

Figure 5.2: Tiling of the time-frequency plane for the frequency warped wavelet transform (a) for the A_0 and (b) S_0 mode (c) A_0 and S_0 . The solid curves represent the dispersive group delay curves for the Lamb waves for a traveled distance of 1 m.

In the following section the proposed frequency warped wavelet multiresolution analysis with scale dependent scaling functions is described; the presented algorithm is able to tackle S_0 and A_0 propagation in order to obtain a tiling of the TF plane like those represented in Figure 5.2(c).

5.3 Frequency Warped Wavelet Multiresolution

The important difference between the Warped Nonstationary Wavelet Multiresolution (WNWM) and stationary multiresolutions encountered in classical wavelet theory is that each space can be generated using a different function, depending on the scale parameter n . In addition, we impose that these so-called scaling functions are orthonormal to their integer translates. The fundamental structure we are interested in is derived from the work [58].

In Section 5.2 we have described how frequency warping scaling can be designed starting from the scaling function in time domain through the unitary operator.

The problem is that the warped scaling function changes for each time warped translation so from an algorithmic point of view a time variant filter is needed to implement the procedure and this solution is cumbersome to compute. In order to overcome this problem the following relation can be used. Given an orthogonal and complete set of dyadic wavelets $\{\psi_{n,m}\}_{n,m \in \mathbb{Z}}$ where

$$\psi_{n,m}(t) = 2^{-\frac{n}{2}} \psi(2^{-n}t - m) = D_{\frac{1}{2}}^n S^m \psi(t)$$

one defines the warped wavelets as $\bar{\psi}_{n,m} = W \psi_{n,m}$.

The set $\{\bar{\psi}_{n,m}\}_{n,m \in \mathbb{Z}}$ is orthogonal since

$$\langle W \psi_{n',m'}, W \psi_{n,m} \rangle = \langle \psi_{n',m'}, W^\dagger W \psi_{n,m} \rangle = \langle \psi_{n',m'}, \psi_{n,m} \rangle = \delta_{n',n} \delta_{m',m}$$

and complete since, by unitary equivalence, given $x \in \mathbf{L}^2(\mathbb{R})$ it is always possible to find $y \in \mathbf{L}^2(\mathbb{R})$ such that $s = Wy$. Hence, by expanding y over the dyadic wavelet set and exploiting the continuity of the warping operator, we have

$$s(t) = Wy(t) = W \sum_{n,m \in \mathbb{Z}} y_{n,m} \psi_{n,m} = \sum_{n,m \in \mathbb{Z}} y_{n,m} \bar{\psi}_{n,m}(t),$$

where

$$y_{n,m} = \langle y, \psi_{n,m} \rangle = \langle x, W\psi_{n,m} \rangle = \langle x, \bar{\psi}_{n,m} \rangle = \langle W^\dagger x, \psi_{n,m} \rangle.$$

Therefore the signal is unwarped by means of the inverse warping operator W^\dagger , then the expansion coefficients on a nonstationary wavelet basis in the classical sense are computed. The following Proposition introduce the Nonstationary multiresolution Spaces using the unwarped signal y ; as stated before this is equivalent to the space generated by the generalized shift operator \mathbf{T} introduced in Eq. (5.1)

Definition 5.3.1: (*Warped Nonstationary Multiresolution Spaces*): Given an integer n_0 and a sequence of functions $(\bar{\varphi}_n(t))_{n \leq n_0}$ in $\mathbf{L}^2(\mathbb{R})$, the spaces

$$V_n = \left\{ (\mathbf{W}^\dagger s)(t) = \sum_{m \in \mathbb{Z}} c[m] \varphi_n \left(\frac{t - 2^n m}{2^n} \right) \mid c \in l^2(\mathbb{Z}) \right\}$$

for $n \leq n_0$, define a nonstationary multiresolution if and only if

- for all $n \leq n_0 - 1$, $V_{n+1} \subset V_n$;
- $\bigcup_{n \leq n_0} V_n$ is dense in $\mathbf{L}^2(\mathbb{R})$: $\bigcap_{n \in \mathbb{Z}} V_n = \{0\}$, $\overline{\bigcup_{n \in \mathbb{Z}} V_n} = \mathbf{L}^2(\mathbb{R})$;
- V_0 is closed under \mathbf{T} ; that is $s \in V_0 \Leftrightarrow (\mathbf{T}^m f) \in V_0 \quad \forall m \in \mathbb{Z}$
- for the scale factor $a = \frac{1}{2} \quad \forall n \in \mathbb{Z}$, $s \in V_n \Leftrightarrow (\mathbf{D}_{\frac{1}{2}} s) \in V_{n+1}$

In a classical (stationary) multiresolution [59], the functions $(\varphi_n(t))_{n \leq n_0}$ are equal to a single function $\varphi(t)$, the scaling function. Therefore, we shall call the functions $(\varphi_n(t))_{n \leq n_0}$ scaling functions.

The Definition 5.3.1 implies the existence of scaling filters $h_n \in l^2(\mathbb{Z})$ such that

$$\varphi_{n+1} \left(\frac{t}{2^{n+1}} \right) = \sum_{m \in \mathbb{Z}} h_n[m] \varphi_n \left(\frac{t - 2^n m}{2^n} \right) \quad (5.3)$$

As the notation suggests, the scaling filters are scale-dependent in general. One can also consider the frequency-domain version of the scaling relation Eq. (5.3) which is

$$2\hat{\varphi}_{n+1}(2\omega) = H_n(e^{j\omega})\hat{\varphi}_n(\omega).$$

The following standard result gives a consequence of the biorthogonality for the scaling filters.

Proposition 5.3.1: *Assume that the scaling functions $(\tilde{\varphi}_n)_{n \leq n_0}$ and $(\varphi_n)_{n \leq n_0}$ generate multiresolutions as in Definition 5.3.1. Also assume that they are real-valued, compactly supported, and mutually biorthogonal for all $n \leq n_0$. Then, for all $n \leq n_0 - 1$, the scaling filters $\tilde{h}_n[m]$ and $h_n[m]$ have finite length and their z -transforms satisfying*

$$H_n(z)\tilde{H}_n(z^{-1}) + H_n(-z)\tilde{H}_n(-z^{-1}) = 4.$$

From the scaling filters, one can construct the wavelet filters

$$\begin{aligned} G_n(z) &= z^{2k_n+1}\tilde{H}_n(-z^{-1}) \\ \tilde{G}_n(z) &= z^{2k_n+1}H_n(-z^{-1}) \end{aligned}$$

where the integers k_n is chosen arbitrarily. Then the wavelets are given by

$$\begin{aligned} \psi_{n+1}(t) &= \sum_{m \in \mathbb{Z}} g_n[m]\varphi_n(2t - m) \\ \tilde{\varphi}_{n+1}(t) &= \sum_{m \in \mathbb{Z}} \tilde{g}_n[m]\tilde{\varphi}_n(2t - m) \end{aligned}$$

At each scale n , the dilated and shifted functions $\psi_{n,m}(t) = 2^{-n/2}\psi_n(t/2^n - m)$ and $\tilde{\psi}_{n,m}(t) = 2^{-n/2}\tilde{\psi}_n(t/2^n - m)$ generate spaces W_n and \tilde{W}_n , respectively; the previous definitions and the biorthogonality constraint imply that

$$\begin{cases} V_n = V_{n+1} \oplus W_{n+1} & \text{and } W_{n+1} \perp \tilde{V}_{n+1} \\ \tilde{V}_n = \tilde{V}_{n+1} \oplus \tilde{W}_{n+1} & \text{and } \tilde{W}_{n+1} \perp V_{n+1} \end{cases}$$

A n_0 -scale wavelet decomposition of a function $f \in \mathbf{L}^2(\mathbb{R})$ is given by

$$f = \sum_{m \in \mathbb{Z}} x_{n_0}[m]\varphi_{n_0,m} + \sum_{n \leq n_0} \sum_{m \in \mathbb{Z}} y_n[m]\psi_{n,m}$$

where $x_n[m] = \langle f, \tilde{\varphi}_{n,m} \rangle$ and $y_n[m] = \langle f, \tilde{\psi}_{n,m} \rangle$.

Respect to the stationary theory, the wavelets $\tilde{\psi}_{n,m}$ are no more dilates and translates of a single mother wavelet.

The decomposition in terms of the discrete sequences $x_n[m]$ and $y_n[m]$ at the different scales n is implemented with a filter bank according to Mallat's fast wavelet algorithm [59] but in this case the filters depend on the scale parameter n .

5.3.1 Exponential B-Spline Multiresolution

The nonstationary multiresolution spaces $(V_n)_{n \leq n_0}$ used at starting point to analyse the dispersive signals is constructed from exponential B-splines.

An exponential reproducing kernel $\phi(t)$ is a function that together with its shifted version is able to reproduce exponentials. That is, for any given set of $M + 1$ values $(\gamma_0, \dots, \gamma_M)$ it is possible to have

$$\sum_{m \in \mathbb{Z}} c_{n,m} \phi\left(\frac{t}{T} - m\right) = e^{\gamma_n \frac{t}{T}}, \quad n = 0, 1, \dots, M$$

given the right choice of weights $c_{n,m}$. Note that γ_n may be complex.

One important family of such kernels are the exponential splines (E-splines) [60]. These functions are extensions of the classical B-splines described above in that they are built with exponential segments instead of polynomial ones.

The first order E-spline is a function $\beta_{\gamma_n(t)}$ with Fourier transform

$$\widehat{\beta}_{\gamma_n}(\omega) = \frac{1 - e^{\gamma_n - j2\omega}}{j\omega - \gamma_n}.$$

The E-splines of degree N are constructed by N successive convolutions of first-order ones

$$\widehat{\beta}_{\vec{\gamma}}(\omega) = \prod_{n=1}^N \frac{1 - e^{\gamma_n - j\omega}}{j\omega - \gamma_n}$$

where

$$\vec{\gamma} = (\gamma_1, \dots, \gamma_N) \text{ and } \omega = 2\pi f.$$

It is shown in [60] that an E-spline has compact support and it can reproduce any exponential in the subspace spanned by $\{e^{\gamma_1 t}, \dots, e^{\gamma_N t}\}$. It is important to notice that exponential B-splines tend to classical M th-order B-splines as the parameter-vector $\vec{\gamma}$ tends to $0 \in \mathcal{C}^M$.

One can check that exponential B-splines satisfy the scaling relation

$$2\widehat{\beta}_{2^{n+1}\vec{\gamma}}(2\omega) = 2^{1-M} R_{2^n\vec{\gamma}}(e^{j\omega}) \widehat{\beta}_{2^n\vec{\gamma}}(\omega)$$

where $R_{\vec{\gamma}}(z) = \prod_{m=1}^M (1 + e^{\gamma_m z^{-1}})$.

In the proposed construction, this corresponds to

$$\begin{aligned}\varphi_n(t) &= \beta_{2^n \vec{\gamma}}(t) \\ H_n(z) &= 2^{1-M} R_{2^n \vec{\gamma}}(z).\end{aligned}$$

We can consider the embedded shift-invariant spaces defined by

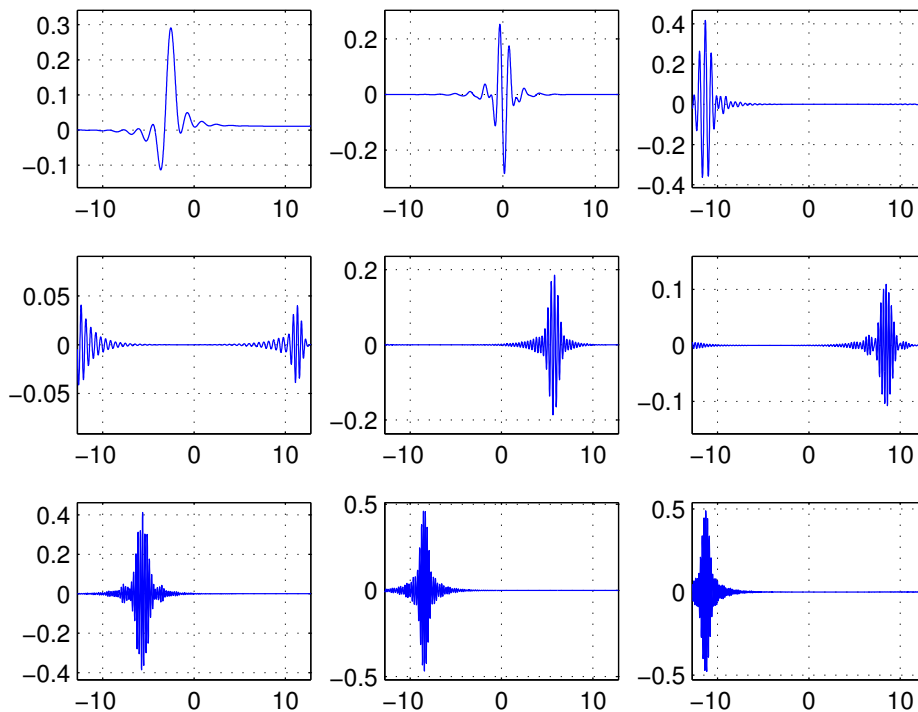
$$V_n = \left\{ (\mathbf{W}^\dagger s)(t) = \sum_{m \in \mathbb{Z}} c[m] \beta_{2^n \vec{\gamma}} \left(\frac{t - 2^n m}{2^n} \right) \mid c \in l^2(\mathbb{Z}) \right\}$$

At a fixed scale n , the function $\beta_{2^n \vec{\gamma}}(t)$ generates a Riesz basis if and only if $\vec{\gamma}$ has no distinct purely imaginary components γ and γ' such that

$$2^n(\gamma - \gamma') = j2\pi k$$

for some $k \in \mathbb{Z}$.

In Figure 5.3 are depicted the A_0 frequency warped E-spline wavelet function at $n = 6$ and $n = 7$



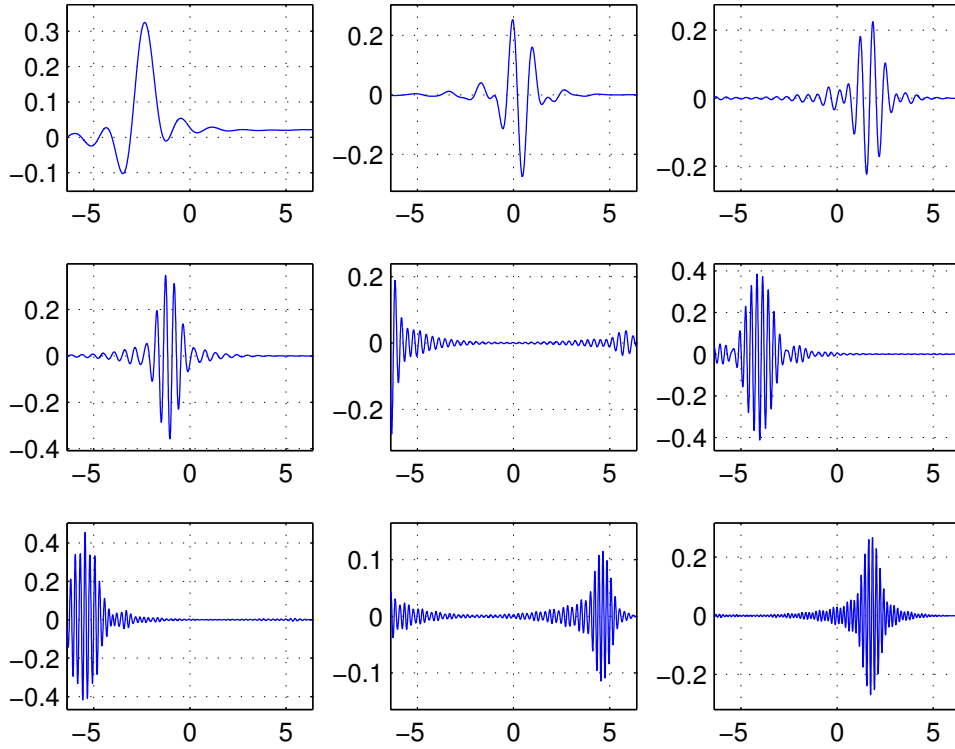


Figure 5.3: A_0 frequency warped E-spline wavelet function at $n = 6$ and $n = 7$

5.4 Frequency Warped Cross Wavelet Analysis

Signals are acquired by each sensor are warped both by the inverse frequency warping operator for A_0 and S_0 mode; for each couple of warped A_0/S_0 signals the cross-correlated signal is calculated.

Given the two cross-correlated signals related to A_0 and S_0 warping we perform the described non stationary frequency warped wavelet multiresolution analysis using for different dyadic frequency bands: in frequency bands between

$$\left[2 \cdot f_{sampling}, \frac{f_{sampling}}{2} \right]$$

the wavelet filters are selected according to the S_0 warping map while in the interval

$\left[0, \frac{f_{sampling}}{2}\right]$ filters are designed according to the A_0 mode.

Once the values of $x_n[m]$ have been found, the estimated difference in distance $D_1 - D_i$ is the translation n^* which corresponds to the maximum of the norm of the vector

$$x_n[m]|_{n=n^*} : \max_n \|x_n[m]\| \quad \text{where} \quad \|x_n[m]\| = \sqrt{\sum_{m=1}^{N_n} x_n^2[m]},$$

where N_n is the number of scales considered.

The proposed algorithm can be summarized in the graph shown in Figure 5.4.

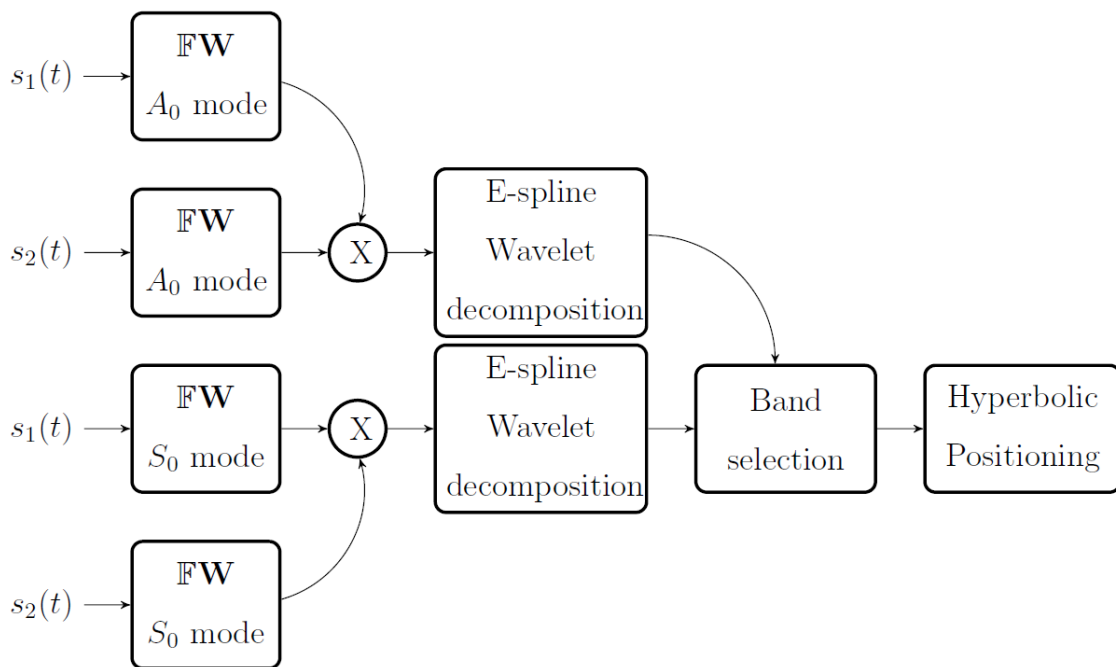


Figure 5.4: Graph of the proposed DDOA algorithm.

5.5 Cramèr - Rao lower bound

Given the cross-correlated signal in time domain

$$s_{ik}(t, \Delta D_{ik}) = s(t, D_i) * s(t, D_k),$$

the cross-correlation of two warped signals in frequency is

$$\begin{aligned} (\mathbb{F}\mathbf{W} s_{ik})(f, \Delta D_{ik}) &= (\mathbb{F}\mathbf{W} s)(f, D_i) \cdot ((\mathbb{F}\mathbf{W})^* s)(f, D_k) = \\ &= \frac{dw(f)}{df} |(\mathbb{F}s_0)(w(f), 0)|^2 e^{-j2\pi fK(D_i - D_k)} \end{aligned}$$

In the following, estimation of ΔD_{ik} is addressed given the noisy cross correlated signal $z_{ik}(t, \Delta D_{ik}) = s_{ik}(t, \Delta D_{ik}) + \eta(t)$ where $\eta(t)$ is the uncorrelated white Gaussian noise which is independent by $s_{ik}(t, \Delta D_{ik})$. Applying the Frequency Warping Operator of $z_{ik}(t, \Delta D_{ik})$ yields

$$\begin{aligned} (\mathbb{F}\mathbf{W} z_{ik})(f, \Delta D_{ik}) &= (\mathbb{F}\mathbf{W} s)(f, D_i) \cdot ((\mathbb{F}\mathbf{W})^* s)(f, D_k) + (\mathbb{F}\mathbf{W} \eta)(f) \\ &= \frac{dw(f)}{df} |(\mathbb{F}s_0)(w(f), 0)|^2 e^{-j2\pi fK(D_i - D_k)} + N(w(f)) \end{aligned}$$

We propose the following estimator for $\Delta D_{ik} = D_i - D_k$ in the frequency discrete domain

$$\begin{aligned} \hat{\Delta D}_{ik} &= \arg \max_{\hat{\Delta D}_{ik}} |(\mathbb{F}\mathbf{W} s)(f, D_i) \cdot ((\mathbb{F}\mathbf{W})^* s)(f, D_k) + (\mathbb{F}\mathbf{W} \eta)(f)|^2 \\ &= \arg \max_{\hat{\Delta D}_{ik}} \left| \sum_{n=0}^{\frac{N}{2}-1} \left\{ \frac{w(f_{n+1}) - w(f_n)}{f_{n+1} - f_n} |(\mathbb{F}s_0)(w(f_n), 0)|^2 e^{-j2\pi f_n K(\hat{\Delta D}_{ik})} + N(w(f_n)) \right\} \right|^2 \end{aligned}$$

where N is the number of samples. The computation of the variance of $\hat{\Delta D}_{ik}$ is performed utilizing the following formula

$$\begin{aligned} \text{var}(\hat{\Delta D}_{ik}) &= \mathbb{E} \left\{ \frac{d(|(\mathbb{F}\mathbf{W} z_{ik})(f, \hat{\Delta D}_{ik} - \Delta D_{ik})|^2)}{d(\hat{\Delta D}_{ik} - \Delta D_{ik})} \right\} = \\ &= \mathbb{E} \left\{ \frac{d(|(\mathbb{F}\mathbf{W} s)(f, D_i) \cdot ((\mathbb{F}\mathbf{W})^* s)(f, D_k) + (\mathbb{F}\mathbf{W} \eta)(f)|^2)}{d(\hat{\Delta D}_{ik} - \Delta D_{ik})} \right\}_{\hat{\Delta D}_{ik} = \Delta D_{ik}} \end{aligned}$$

where \mathbb{E} represents the expectation operator. We derive the following expressions supposing that the bandwidth of $(\mathbb{F}s_0)(f)$ is limited between $[f_L, f_H] \in [0, \frac{1}{2}]$ with

with a constant power spectral density (PSD), variance σ_{s_0} , the variance of the noise $(\mathbb{F}\eta)(f)$ is σ_η

$$\begin{aligned}
& \mathbb{E} \left\{ \frac{d(|(\mathbb{F}\mathbf{W}s)(f, D_i) \cdot ((\mathbb{F}\mathbf{W})^*s)(f, D_k) + (\mathbb{F}\mathbf{W}\eta)(f)|^2)}{d(\hat{\Delta}D_{ik} - \Delta D_{ik})} \right\} = \\
& = \mathbb{E} \left\{ \frac{\partial}{\partial(\hat{\Delta}D_{ik} - \Delta D_{ik})} \left| \left(\sum_{f_p=f_L}^{f_H} \frac{dw(f_p)}{df_p} |(\mathbb{F}s_0)(w(f_p), 0)|^2 e^{-j2\pi f_p K(\hat{\Delta}D_{ik} - \Delta D_{ik})} \right. \right. \right. \\
& \quad \left. \left. \left. + N(w(f_p)) \right) \right| \left| \left(\sum_{f_l=f_L}^{f_H} \frac{dw(f_l)}{df_l} |(\mathbb{F}s_0)(w(f_l), 0)|^2 e^{-j2\pi f_l K(\hat{\Delta}D_{ik} - \Delta D_{ik})} + N(w(f_l)) \right) \right| \right\} = \\
& = 4\pi K \cdot \sum_{f_p=f_L}^{f_H} \sum_{f_l=f_L}^{f_H} \frac{dw(f_p)}{df_p} \frac{dw(f_l)}{df_l} f_p f_l \mathbb{E} \{ |(\mathbb{F}s_0)(w(f_p), 0)|^2 |(\mathbb{F}s_0)(w(f_l), 0)|^2 \} \\
& \quad e^{-j2\pi(f_p+f_l)K(\hat{\Delta}D_{ik} - \Delta D_{ik})} + \\
& \quad + 2\pi K \sum_{f_p=f_L}^{f_H} \frac{dw(f_p)}{df_p} f_p |(\mathbb{F}s_0)(w(f_p), 0)|^2 e^{-j2\pi f_p K(\hat{\Delta}D_{ik} - \Delta D_{ik})} \cdot N(w(f_p)) + \\
& \quad + 2\pi K \cdot \sum_{f_l=f_L}^{f_H} \frac{dw(f_l)}{df_l} f_l |(\mathbb{F}s_0)(w(f_l), 0)|^2 e^{-j2\pi f_l K(\hat{\Delta}D_{ik} - \Delta D_{ik})} \cdot N(w(f_l))
\end{aligned}$$

Since that

$$\begin{aligned}
\mathbb{E} \{ |(\mathbb{F}s_0)(w(f_p), 0)|^2 \} & = \mathbb{E} \left\{ \sum_{n=0}^{N-1} s_0(n) e^{-j2\pi w(f_n)k/N} \sum_{m=0}^{N-1} s_0(m) e^{-j2\pi w(f_m)k/N} \right\} = \\
& = \begin{cases} \frac{1}{2(f_H - f_L)} N \sigma_{s_0}^2 & f_p \in [f_L, f_H] \\ 0 & \text{otherwise} \end{cases} \\
\mathbb{E} \{ N(w(f_p)) \} & = \begin{cases} \sqrt{\frac{N}{2(f_H - f_L)}} \sigma_\eta & f_p \in [f_L, f_H] \\ 0 & \text{otherwise} \end{cases}
\end{aligned}$$

Imposing the constraint $\hat{\Delta}d_{ik} = \Delta_{ik}$ yields

$$\begin{aligned}
& \mathbb{E} \left\{ \frac{d(|(\mathbb{F}\mathbf{W}s)(f, D_i) \cdot ((\mathbb{F}\mathbf{W})^*s)(f, D_k) + (\mathbb{F}\mathbf{W}\eta)(f)|^2)}{d(\hat{\Delta}D_{ik} - \Delta D_{ik})} \right\}_{\hat{\Delta}D_{ik} = \Delta D_{ik}} = \\
& 4\pi K \frac{1}{4(f_H - f_L)^2} N^2 \sigma_{s_0}^4 \sum_{f_p=f_L}^{f_H} \left(\frac{dw(f_p)}{df_p} \right)^2 f_k^2 + \\
& + 4\pi K \left(\frac{N}{2(f_H - f_L)} \right)^{3/2} \sigma_{s_0}^2 \sigma_\eta \sum_{f_p=f_L}^{f_H} \frac{dw(f_p)}{df_p} f_p
\end{aligned}$$

and in the continuous frequency domain

$$\frac{\pi K}{2} \left(\frac{N}{(f_H - f_L)^2} \right)^{3/2} \sigma_{s_0}^2 \left(\sigma_{s_0}^2 \int_{f_L}^{f_H} \left(\frac{dw(\xi)}{d\xi} \right)^2 \xi^2 d\xi + \sigma_\eta \int_{f_L}^{f_H} \frac{dw(\xi)}{d\xi} \xi d\xi \right)$$

5.6 Experimental verification

As a case study, we exploited the proposed tool to locate impacts in an aluminum 1050A square plate 1 m \times 1 m and 0.003 m thick.

Two different experiments were carried out using three sensors distributed in a symmetrical and asymmetrical configuration with respect to the edges of the plate.

The positions of the sensors are collected in Table 5.1.

Topology	Coordinates	Sensor 1	Sensor 2	Sensor 3
asymmetrical	x (m)	0.10	0.20	0.90
	y (m)	0.90	0.10	0.10
symmetrical	x (m)	0.25	0.25	0.75
	y (m)	0.75	0.25	0.25

Table 5.1: Sensors positions for the considered symmetrical and asymmetrical topologies.

Guided waves were excited by hitting the plate with a pencil orthogonally to the surface.

The generated signals were recorded using the LC534 series LeCroy oscilloscope at a sampling frequency of 512 kHz.

Acquisitions were triggered when the signal received from one of the PZT discs (PIC181, diameter 0.01 m, thickness 0.001 m) reached a threshold level of 140 mV; pre-trigger recordings were enabled to obtain the previous history of each signal.

Figure 5.5 shows the experimental setup.

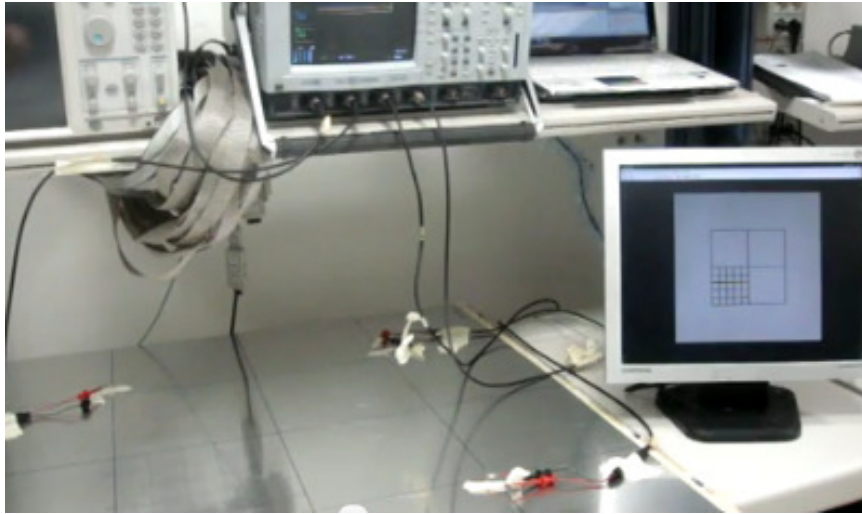
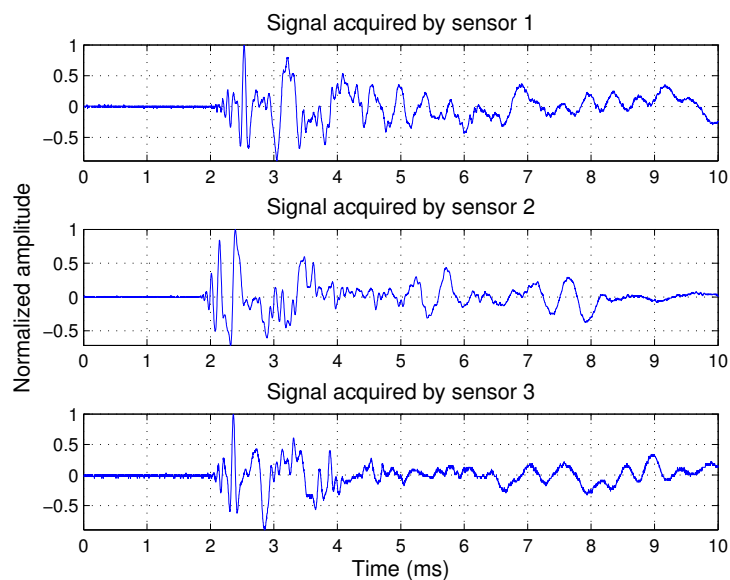


Figure 5.5: Experimental setup.

The sampling frequency was sufficiently high to avoid aliasing effects, as the frequency content of the acquired signals vanishes above 60 kHz. Two configurations have been tested: three PZT discs were placed symmetrically and asymmetrically with respect to the edges, as schematically depicted in Figure 5.8(a), (b).

Figure 5.6(a) shows the experimental waveforms detected by the three sensors after having excited the plate at the following coordinates: $x = 0.45$ m, $y = 0.35$ m.



(a)

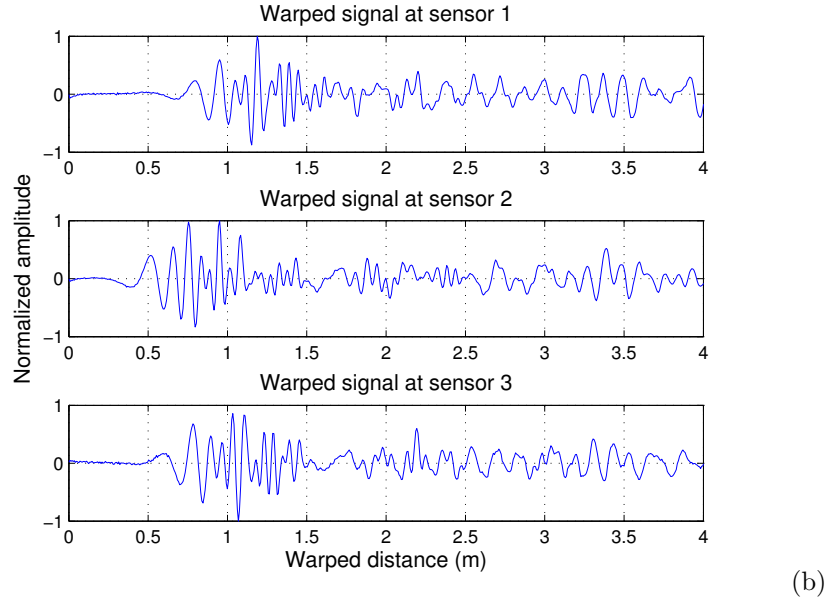


Figure 5.6: Sample acquired signals by the passive monitoring system: (a) signals in time domain, (b) Warped time domain version.

As can be seen by observing Figure 5.6(a), it is extremely difficult to estimate the difference in time of arrival by using classical thresholding or peak detection procedures. In fact, such estimation is complicated by the effect of dispersion which introduces a distance-dependent group delay shift.

The Lamb waves group velocity dispersion curves for the 0.003 m thick aluminum plate were obtained considering the following nominal properties for the aluminum: $E = 69$ GPa, $\nu = 0.33$ and $\rho = 2700$ kg \cdot m $^{-3}$ in order to compensate for dispersion, first the WFT operator must be defined [20]. In the [0 – 300] kHz frequency range, only the two fundamental A_0 and S_0 Lamb waves can propagate through this plate. Since for out-of-plane excitation the energy in the A_0 and S_0 mode is considerably greater than the other modes; the group velocity curves of the A_0 and S_0 modes are used to shape the two warping operator.

Next, by processing the acquired signals with the WFT, the waveforms depicted in Figure 5.6(b) are obtained from the A_0 mapping. In the new waveforms, the group delay dependence on distance is removed. However, spurious components arise due to the edges' reflections and also components due to the non compensated S_0 mode.

At this point, the wavelet multiresolution analysis is applied to the two cross-correlated warped signals.

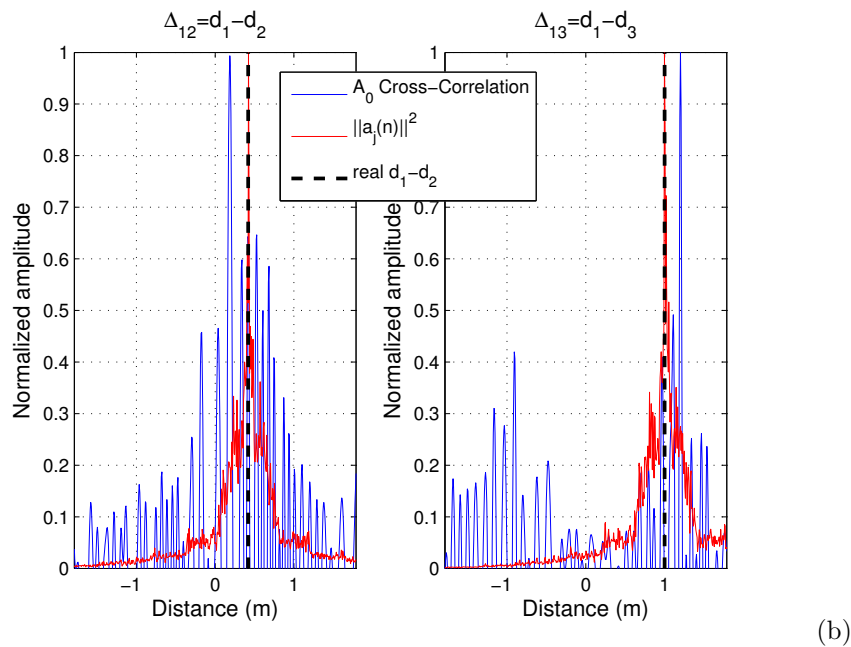
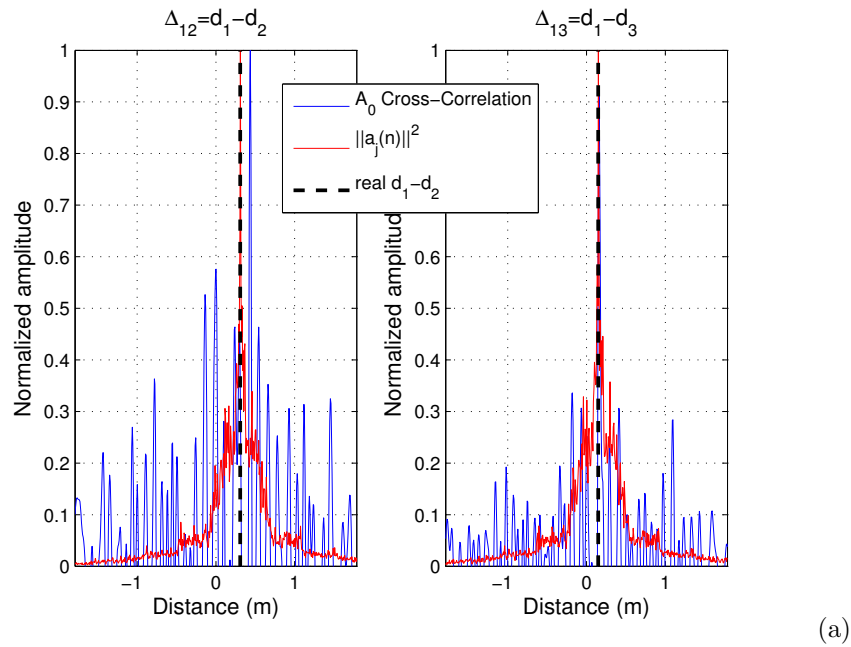
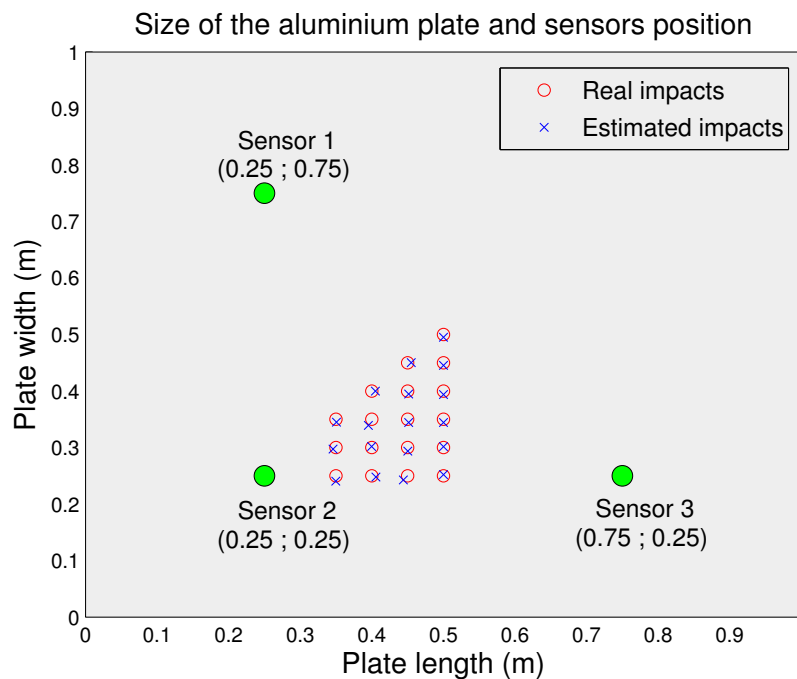


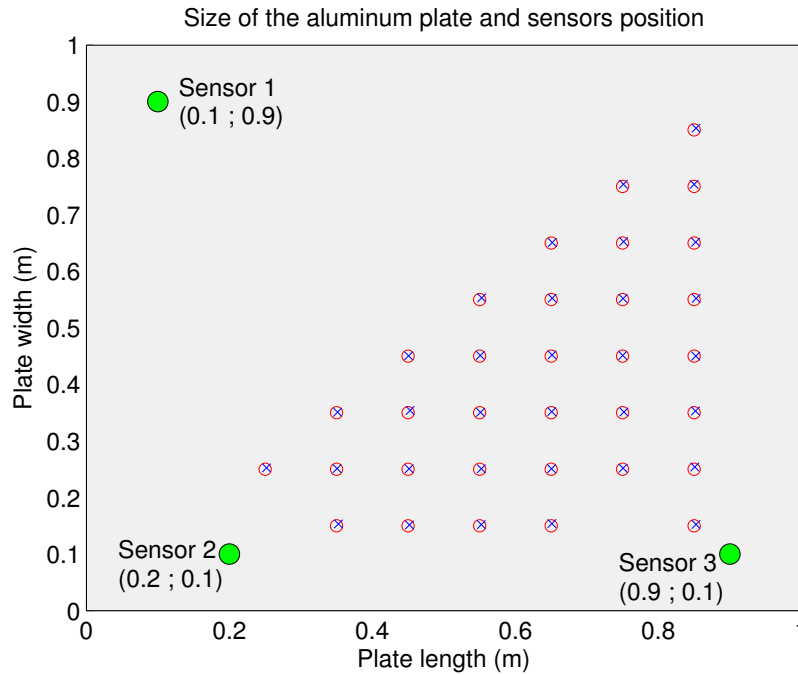
Figure 5.7: Comparison in function of the difference in distance between the warped cross-correlated signal and the curve $\|x_n[m]\|$: (a) impact in $x = 0.45$ m $y = 0.35$ m, (b) impact in $x = 0.85$ m $y = 0.15$ m.

Figures 5.7(a) and (b) show the comparison between the warped cross-correlated signals and the curves $\|x_n[m]\|$ for two different impacts ($x = 0.45$ m, $y = 0.35$ m) and ($x = 0.85$ m, $y = 0.15$ m).

It is important to underline the localization improvement obtained through this method with respect to the analysis of the simple peaks of the cross-correlating signals which are spread and the related abscissa are not very close to the true difference of traveled distance and this is due to the non negligible interference term. Without multimode compensation the cross-correlation of warped A_0 signals can lead to large errors, as shown in Figure 5.7(b), while the proposed algorithm closely estimates the true difference in traveled distances. The source location is detected through multi-lateration, solving the system of equations with the Levenberg-Marquardt algorithm. The results of the proposed procedure for impacts localization can be seen in Figure 5.8 where the target and estimated impact points, denoted respectively by circles \circ and crosses \times , are shown.



(a) 3 sensors symmetric respect to the edges



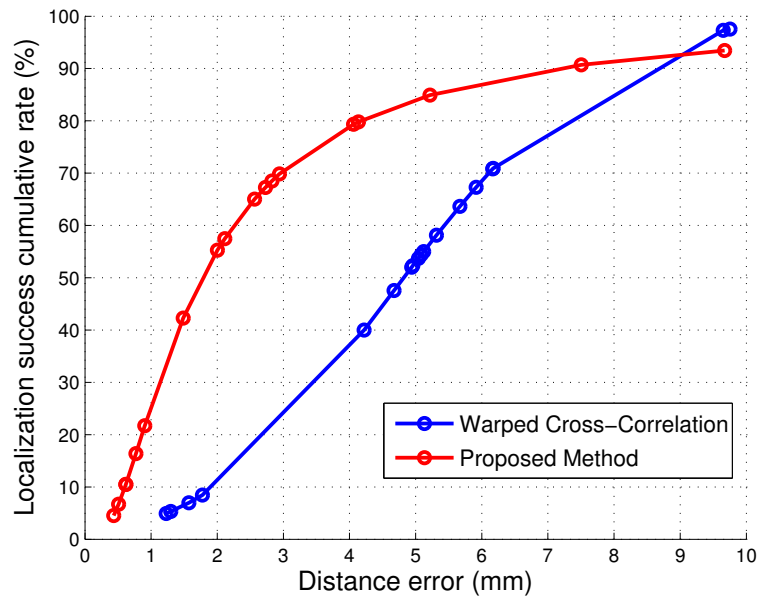
(b) 3 sensors asymmetric respect to the edges

Figure 5.8: Source localization results.

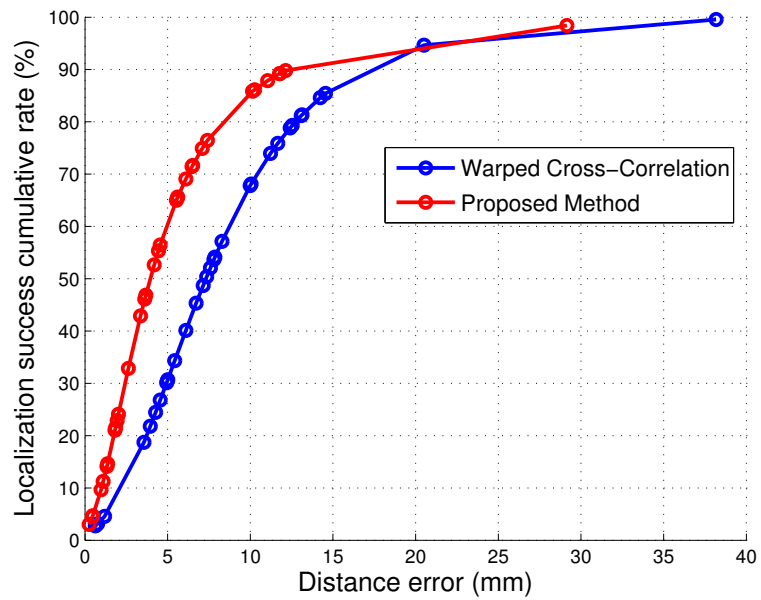
Such estimations are performed in a purely passive manner, ignoring the time instant at which the acoustic emission starts.

Experimental results reported in Figure 5.8 and [7] are slightly different. The small deviation is due to the fact that with the proposed multiresolution analysis, based on scale-dependent generating functions, a compensation of the S_0 mode is also performed in some frequency bands. Since that for the propagation on the aluminum plate the energy retained by the S_0 mode is considerably less respect to the energy retained by the A_0 mode this contribute in the localization error on the aluminum plate is not so huge.

The comparison of the experimental results between the the proposed procedure and the algorithm described in [7] is given through the analysis of the cumulative distribution of the localization error for the two considered configurations of the PZT transducers which is shown in Figure 5.9.



(a) Sensors symmetric respect to the edges



(b) Sensors asymmetric respect to the edges

Figure 5.9: Cumulative distribution of the localization errors.

Figure 5.9(a), (b) show the improvement in performances on the localization error of the developed algorithm. The accuracy is compromised when the sensors position is irregular, close to the edges and, consequently, prone to reverberations. In such cases the warped wavelet analysis offers an improved localization accuracy as shown in Figure 5.9(b).

Finally a comparison between the experimental results and the Cramèr-Rao lower bound is shown in Figure 5.10.

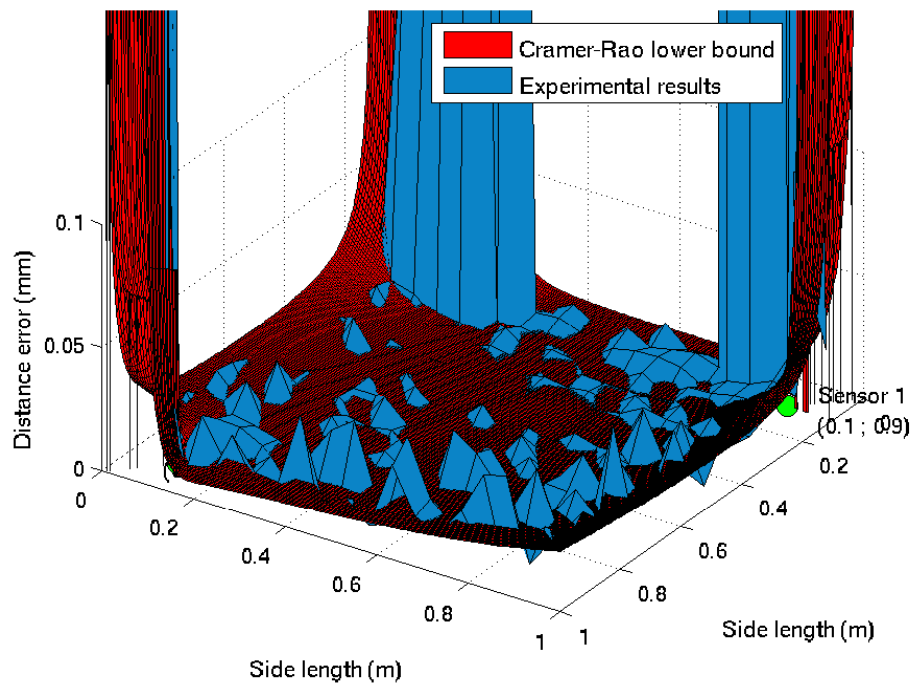


Figure 5.10: Comparison between the Cramèr-Rao lower bound and the experimentally estimated positions: 3 sensors asymmetric respect to the edges.

In the lower bound estimation, the measurement errors are considered as independent identically distributed gaussian random variables with zero mean. Their standard deviation σ_d can be estimated as $\sigma_d = 2 \cdot \frac{v_s}{f_s} = 3$ mm, being $f_s = 1$ MHz the sampling frequency and $v_s = 1570$ m \cdot s $^{-1}$ the equivalent speed of sound in the warped domain. As can be seen in Figure 5.10, the impact position errors are very close to the theoretical limit given by the Cramèr-Rao lower bound of the hyperbolic positioning algorithm in the convex area bounded by the sensors. Conversely, when the source

is placed in the external area between sensors and the plate edges, the localization errors increase roughly respect to the Cramèr-Rao bound because of the dominant phenomenon of reflection that totally corrupts the cross-correlated signal.

5.7 Discussion

In this Chapter a method to extract the difference in distance traveled by stress guided waves is proposed. The method applies a dispersion compensation procedure on the signals acquired by passive sensors, thus overcoming the difficulties associated with arrival time detection based on classical thresholding procedures. A frequency warped wavelet multiresolution analysis is applied to the cross-correlating signals to compensate multimodal dispersion. The analysis of the wavelet transform magnitude reveals the difference in distance traveled by the wave to reach the different sensors. Finally, multilateration is applied. Excellent performance in terms of point of impact localization is shown through experiments since the estimated impact positions are very close to the Cramèr-Rao lower bound. Further, the reliability of the proposed approach in presence of reverberation make the new tool suitable for automatic acoustic emission localization procedures.

Future developments include the implementation of the algorithm on embedded board for Structural Health Monitoring and the applications of the proposed framework to anisotropic propagation, such as detection of impacts in composite plates.

Chapter 6

Embedded Ultra-Low Power Device for Impact Localization

To be ignorant of one's ignorance is the malady of the ignorant.

Amos Bronson Alcott

6.1 Introduction

This Chapter describes the development of a miniaturized, self-contained and low power device for automated impact detection that can be used in a distributed fashion without central coordination.

One of the popular structural health monitoring (SHM) applications of both automotive and aeronautic fields is devoted to the non-destructive localization of impacts in plate-like structures. The aim of this work is to develop a miniaturized, self-contained and low power device for automated impact detection that can be used in a distributed fashion without central coordination.

The proposed device uses an array of four piezoelectric transducers, bonded to the plate, capable to detect the guided waves generated by an impact, to a STM32F4 board equipped with an ARM Cortex-M4 microcontroller and a IEEE802.15.4 wireless

transceiver. The waves processing and the localization algorithm are implemented on-board and optimized for speed and power consumption. In particular, the localization of the impact point is obtained by cross-correlating the signals related to the same event acquired by the different sensors in the warped frequency domain.

Finally the performance of the whole system is analysed in terms of localization accuracy and power consumption, showing the effectiveness of the proposed implementation.

6.2 Motivation

A current trend in the SHM field is to create wireless sensor networks with low power consumption or even energetically autonomous [61, 62]. One promising solution would be a SHM system that could be embedded into the structure, inspect the structural hot spots and download data or diagnostic results wirelessly to a remote station [63, 64, 65]. A lot of literature has been produced on the use of sensor-array-based methods for high-speed acquisition and data processing. However, generally such approaches use a large number of individual sensors that usually are bulky, heavy and require wiring back to a central location. Moreover when large-scale deployment are implied, the power consumption of the system is hardly sustainable by the ordinary generation system present on board. In contrast to these traditional transducers, wireless sensors technology integrating small sensors and wireless communication are becoming vital in SHM, guaranteeing at the same time: (1) less wiring among sensors and between sensors and the central unit; (2) lower weight; (3) reduced power consumption and (4) real-time monitoring even in harsh environmental conditions.

In this Chapter a new PZT-based wireless embedded ultrasonic structural monitoring system for impact localization is proposed with advantages over traditional systems of compactness, light weight, low-power consumption and high efficiency and precision. The passive approach based on ultrasonic Lamb waves and conventional piezoelectric transducers (PZT discs) is capable of achieving high localization performance using a dispersion compensation algorithm with low computational cost.

The structure of the SHM system is illustrated in Fig. 6.1.

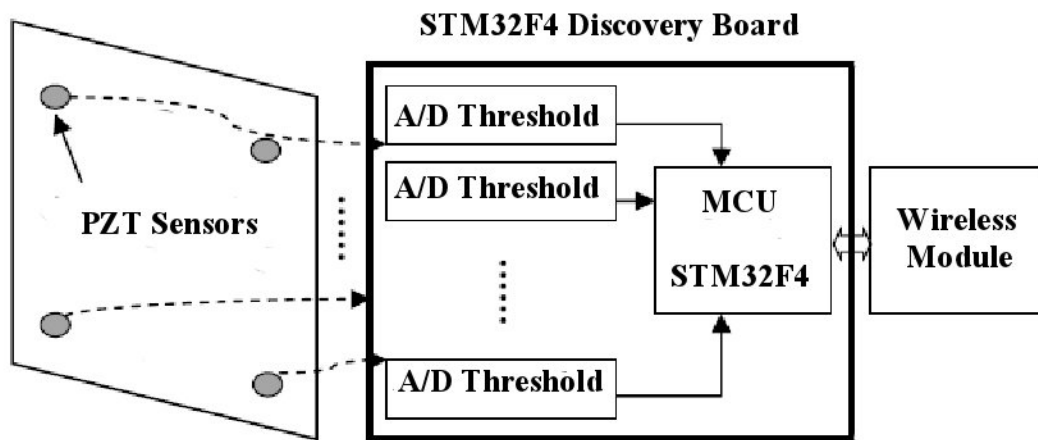


Figure 6.1: Structure of the embedded SHM system for impact detection

In the new SHM system, the signal conditioning, amplification and A/D converting circuits are replaced by a simple comparator circuit, in which the response signal from a piezoelectric transducer PZT sensor is directly changed into a digital queue by comparing it with a preset trigger value.

The device samples the signals in passive mode using 4 different piezoelectric transducers and the signals are elaborated on a Cortex-M4 based microcontroller.

By cross-correlating the dispersion-compensated signals, the impact point can be determined via hyperbolic positioning. Thus, when an impact occurs, only the data of its position is recorded and sent to the central system through wireless transmission.

The structure of this Chapter is as follows: the design and realization of the new PZT-based wireless digital impact monitoring system is described in detail in Section 6.3.

Section 6.4 shows the feasibility and stability of the embedded ultrasonic structural monitoring system and an experimental validation is presented.

6.3 Hardware Design

The system is composed by 4 different elements: (A) piezoelectric sensors, (B) acquisition chain, (C) processing electronic unit and (D) wireless transmission module.

(A) Piezoelectric sensors: when an impact occurs on an elastic structure, a stress wave is created and it propagates across the structure, radially from the point of impact. The stress wave can be caught by PZT sensors in a passive way.

The proposed system exploits at least 4 conventional piezoelectric transducers arranged in a geometrical fashion. The sensor array of piezoelectric elements needs to contain at least four sensor elements in order to provide reliable triangularization capabilities.

(B) Acquisition chain: The strong attenuation typical of composite materials usually requires sophisticated signal amplification and conditioning electronics in order to cope with the high gains and low noise typical of GW based diagnostic. In this work we propose a signal elaboration technique based on innovative time-frequency analysis techniques. PZT transducers are connected directly with the ADC ports of the STM32F4 board and each ADC channel is configured in dual mode with 250 kHz maximum sampling frequency since generally the spectral components of the Lamb waves lower rapidly above 60-100 kHz. The acquired values are stored in a DMA circular buffer; when the maximum value of the buffer exceeds the threshold value the trigger is sent and the Micro Controller Unit (MCU) performs the localization algorithm.

The acquisition settings are shown in Table 6.1:

Table 6.1: Acquisition and ADC settings

Inputs	4 sensors	Sampling frequency f_s	250 kHz
Input Range	± 2 V	Samples	2048
Acquisition period	8 ms	Sample resolution	12 bit

(C) **Processing electronic unit:** the center of the system is the processing core which contains function modules for data collection, processing and communication control. A Cortex-M4 based board is selected as main chip in the processing core. The MCU is specifically a STM32F4 evaluation board featuring a STM32F407VGT6 microcontroller with 1 MB Flash and 192 KB RAM. The strength point of the core is the CPU with FPU, adaptive real-time accelerator allowing 0-wait state execution from Flash memory and frequency up to 168 MHz.

The computational cost of the proposed algorithm is shown in Table 6.2.

Table 6.2: Algorithm computational cost

Non Uniform FFT	
1) FFT	$N = J \times M = 2^{12}$ points: complexity $O(N \log N)$
2) MIN-MAX	memory $w(f)$: $J \times M = 2^{12}$; complexity $O(JM)$ samples 12 bit: memory: $2^{12} \times 12 \approx 49$ KByte
Cross-Correlation: 3 products with signals of length 2^{11}	
Inverse FFT : $M = 2^{11}$ points complexity $O(M \log M)$	

(D) **Wireless transmission module:** when the device is used to monitor the structural health of large structures, each node in the network monitors a specific portion of the structure surface, eventually reporting to a central location in case of detected damage. The wireless communication technology allows long distance data transmission without wiring, simplifying the difficulties in multi-device network monitoring. To be compliant with the low-power requirements the device presents a RF wireless module ZigBee/IEEE802.15.4 compliant, connected to the main board using an Serial Peripheral Interface (SPI).

The network topology suitable for this kind of applications is mesh or star network, where each node in the network is able to communicate with the central gateway.

6.4 Experimental Verification

We exploited the proposed SHM system to locate impacts in an aluminum 1050A square plate $1\text{ m} \times 1\text{ m}$ and 3 mm thick. Four PZT discs (PIC181, diameter 10 mm, thickness 1 mm) were placed asymmetrically at the corners of a square as depicted in the experimental setup in Fig. 6.2.

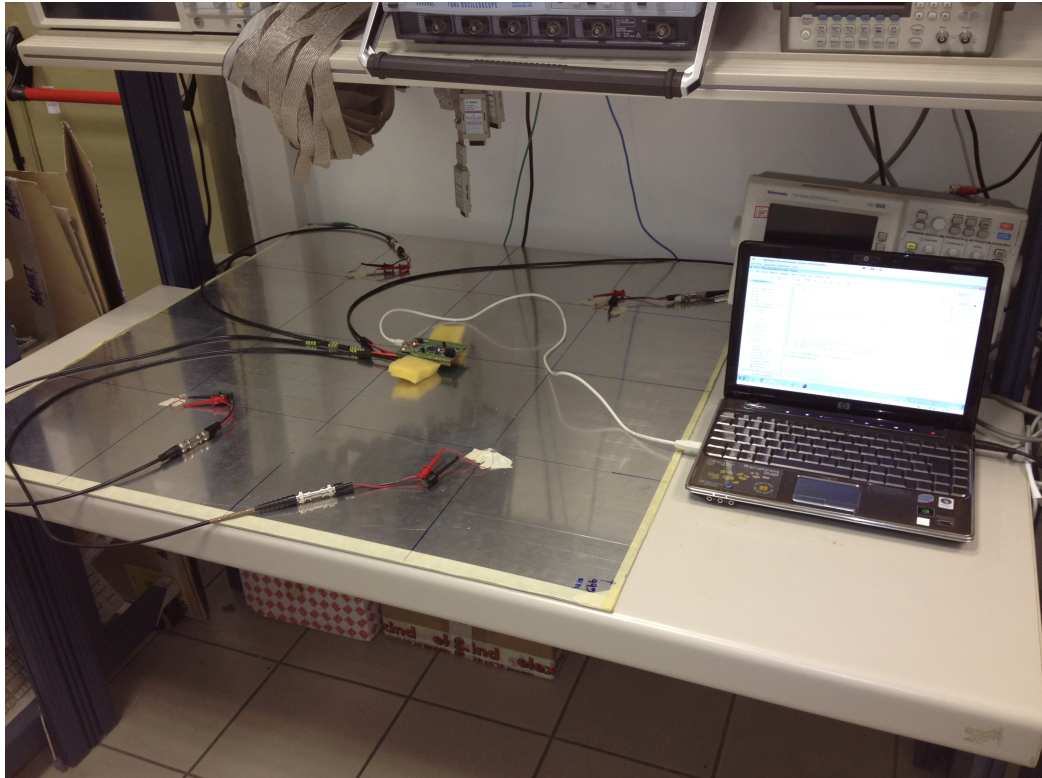


Figure 6.2: Experimental setup

Guided waves were excited by pencil-lead breaks. The ADC channels of the STM32F4 discovery board were set in dual mode to continuously acquire signals with a maximum sampling frequency of 250 kHz. The board was supplied with 3.3 V. Data were recorded in a circular DMA buffer and acquisitions triggered when the signal received from one of the PZT discs reached a threshold level of 50 mV. The sampling frequency was sufficiently high to avoid aliasing effects, as the frequency content of the acquired signal vanishes above 60 kHz. In order to analyse the dependency of the power consumption and the localization performances with the sampling frequency,

experiments were carried changing the frequency in the range [150 – 250] kHz. Results in Table 6.3 show how lowering the sampling frequency, the current consumption decreases but not in a linear manner; furthermore the MCU elaboration step is very sensible to the sampling frequency since the algorithm complexity is proportional to the sample buffer length which is reduced if the sampling frequency is lower.

Table 6.3: Mean Current Consumption

	ADC sampling	Signal Processing
$f_s = 250$ kHz	32 mA	63 mA
$f_s = 200$ kHz	27 mA	53 mA
$f_s = 150$ kHz	24 mA	50 mA

Fig. 6.3 shows the current consumption values measured for different sampling frequencies.

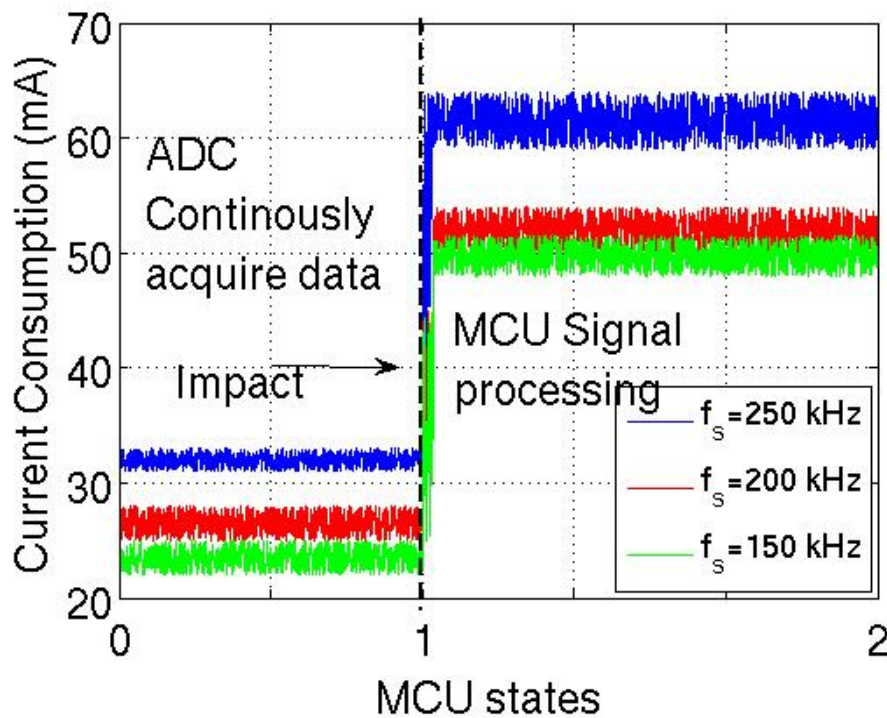


Figure 6.3: Current consumption for different sampling frequencies

Since the ADC sampling state is performed always in time the current reduction achieved with low frequency is noticeable. However, such reduction must be analysed with respect to the resolution achieved in the impact localization.

In Fig. 6.4 is reported the mean error of the difference distance of arrival measured on a set of $K = 10$ of experimental impacts on the aluminum plate.

The error is calculated as follow:

$$e = \frac{1}{3 * K} \sum_{k=1}^K \sum_{i=1}^3 (\Delta d_{1i} - \Delta \hat{d}_{1i}) \quad k = 1, \dots, 10 \quad i = 1, \dots, 3$$

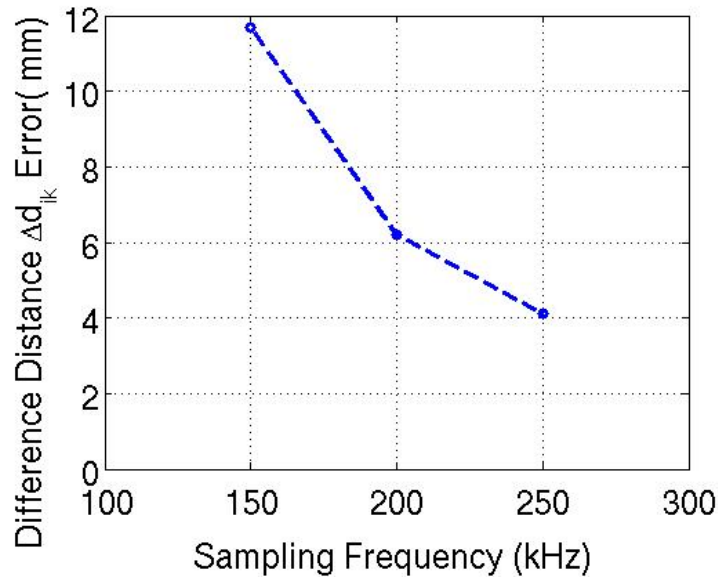


Figure 6.4: Localization error for different sampling frequencies

As it can be seen from Fig. 6.4, lowering the sampling frequency the positioning error rises; in contexts such as wing monitoring, the high localization resolution is an important constrain because facilitates the decision to be taken in critical phases such as aircraft takeoff and optimizes the number of sensors to be used to monitor large areas.

A good parameter able to take into account both the current consumption and the spatial resolution is $\frac{I_d (mA)}{e (mm)}$. Fig. 6.5 shows that $\frac{I_d (mA)}{e (mm)}$ is not constant, denoting that the impact localization error and the current consumption tends to be quadratic.

Fig. 6.6 shows the dependency of $\frac{I_d (mA)}{e (mm)}$ with the sampling frequency.

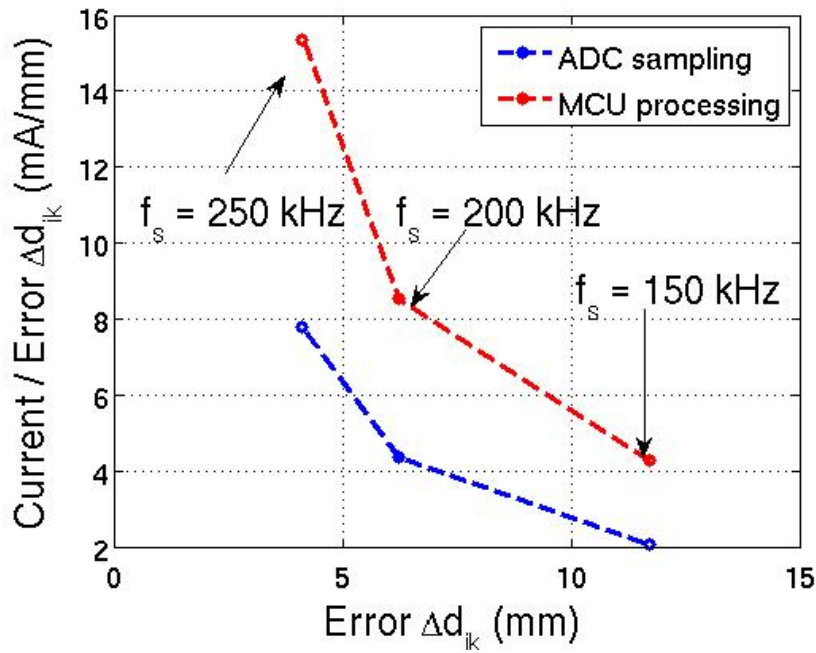


Figure 6.5: Dependency of the localization error with the current

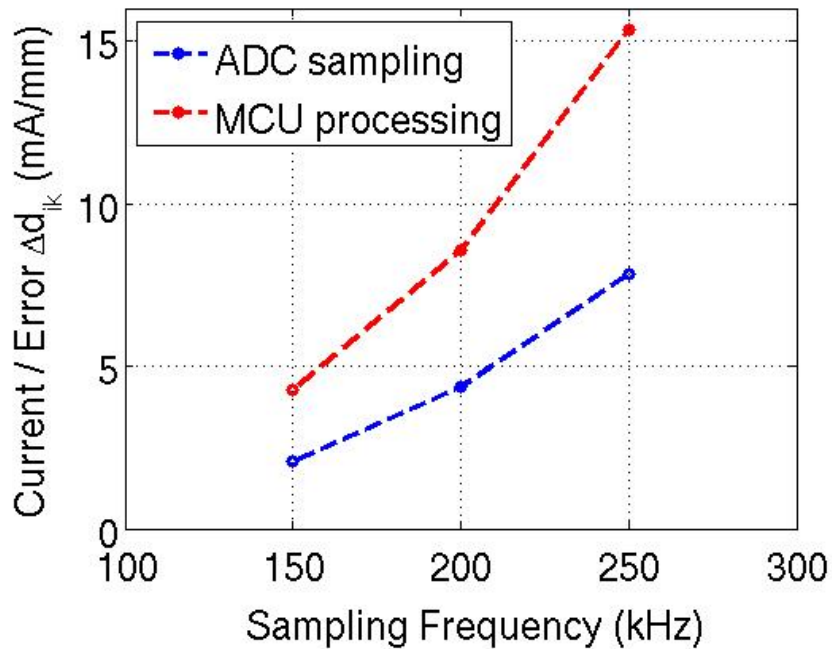


Figure 6.6: Dependency of $\frac{I_d(mA)}{e(mm)}$ with the sampling frequency

Finally the frequency sampling choice depends on the localization and current constraints, knowing that if the location is inaccurate it is necessary to scan in a larger area since that the defect induced from the impact can be below the surface and therefore not immediately visible and then the control times get longer.

6.5 Composite Z-stiffened Plate

As a case study, we exploited the proposed compressive sensing tool to locate impacts in a composite Z-stiffened plate Figure 6.7.

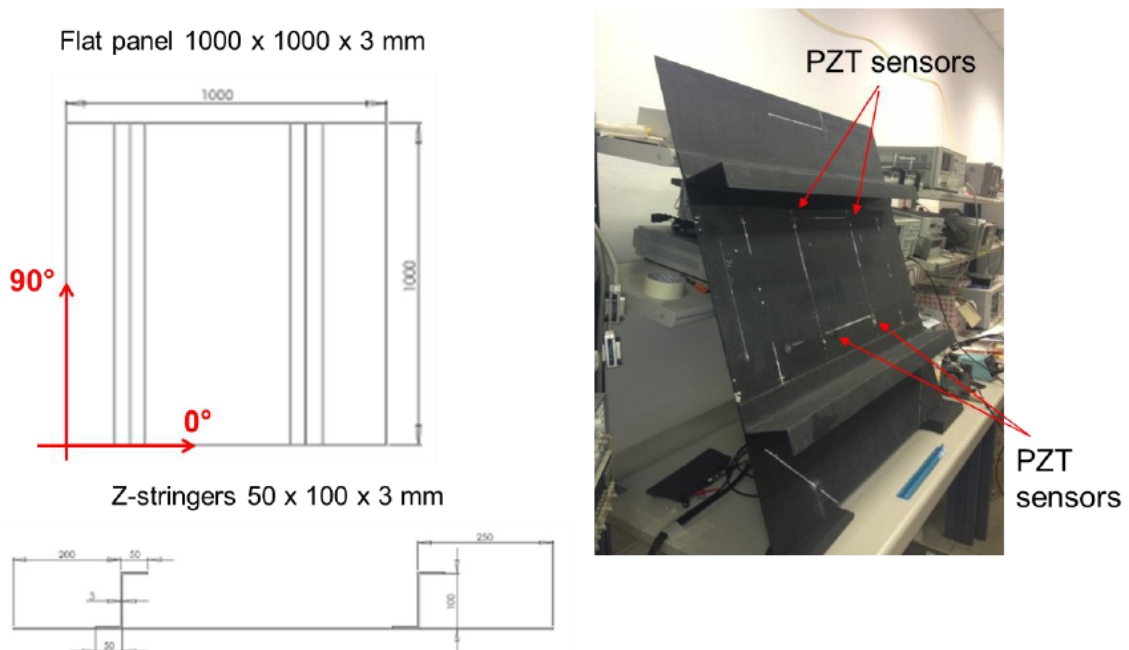


Figure 6.7: Composite Z-stiffened plate provided by Critical Materials with four PZT transducers installed.

The composite plate is 1000×1000 mm large and has two Z stringers on its bottom. The plate was produced in Carbon Fibre Reinforced Polymer (CRFP) laminated composite by Critical Materials Ltd.

The amount of carbon fibre in the CRFP is of 50 wt%. The Carbon Fabric is a $195 \text{ gr}/\text{m}^2$ plain weave. The resin is an epoxy Epikote Resin 04908, with an Epikure Curing Agent 04908 (hardner). The Resin/hardner mixing ratio was of 100/30 parts

by weight, being used 4630 gr of resin and 1389 gr of harder.

Table 6.4 shows the properties of individual constituents.

Table 6.4: Properties of individual constituents of the CRFP laminated

Fiber	Resin
Young modulus: 200 GPa	Young modulus: 2.90 GPa
Shear modulus: 50 GPa	Shear Modulus: 1.20 GPa
Density: 1700 kg/m^3	Density: 1200 kg/m^3

The Z-panel was manufactured by vacuum infusion technique. The flat rectangular plate has 13 lamina with plies with fibres oriented at 0/90°. The Z-stiffener has also 13 lamina but with plies of fibres oriented at +45/-45°. The total thickness of the Z-plate is 3 mm.

The mechanical properties of CRFP were assessed by tensile and flexural testing from samples cut from rectangular plates of 50 × 25 × 0.25 cm, with 11 plies with fibres oriented at 0/90°.

The final thickness of the plate is of 2.52 mm. The results are listed in Table 2. The measure density is of $1.38 \pm 0.04 kg/m^3$. The data of Table 6.5 were properly used (scaled to consider the 13 plies of the Z stiffened plate) to feed a Semi-Analytical Finite Element based tool aimed at predicting the dispersion curves at different angles of propagation.

Table 6.5: Mechanical characterization of the CFRP (S.D. - Standard Deviation)

	Horizontal		Vertical		Diagonal (45°)	
Tensile	σ_{max} (MPa)	$E_{0.2\%}$ (GPa)	σ_{max} (MPa)	$E_{0.2\%}$ (MPa)	σ_{max} (MPa)	$E_{0.2\%}$ (MPa)
Average	574 ± 40	61.6 ± 3.7	457 ± 36	48.4 ± 7.7	193 ± 4	124.1 ± 0.3
Flexural	σ_{max} (MPa)	$E_{0.2\%}$ (GPa)	σ_{max} (MPa)	$E_{0.2\%}$ (MPa)	σ_{max} (MPa)	$E_{0.2\%}$ (MPa)
Average	786 ± 46	45.5 ± 3.0	778 ± 46	47.1 ± 3.1	322 ± 34	138.5 ± 0.9

For instance in Figure 6.8 the dispersion curves at 0° are represented in terms of wavelength (λ) and group velocity.

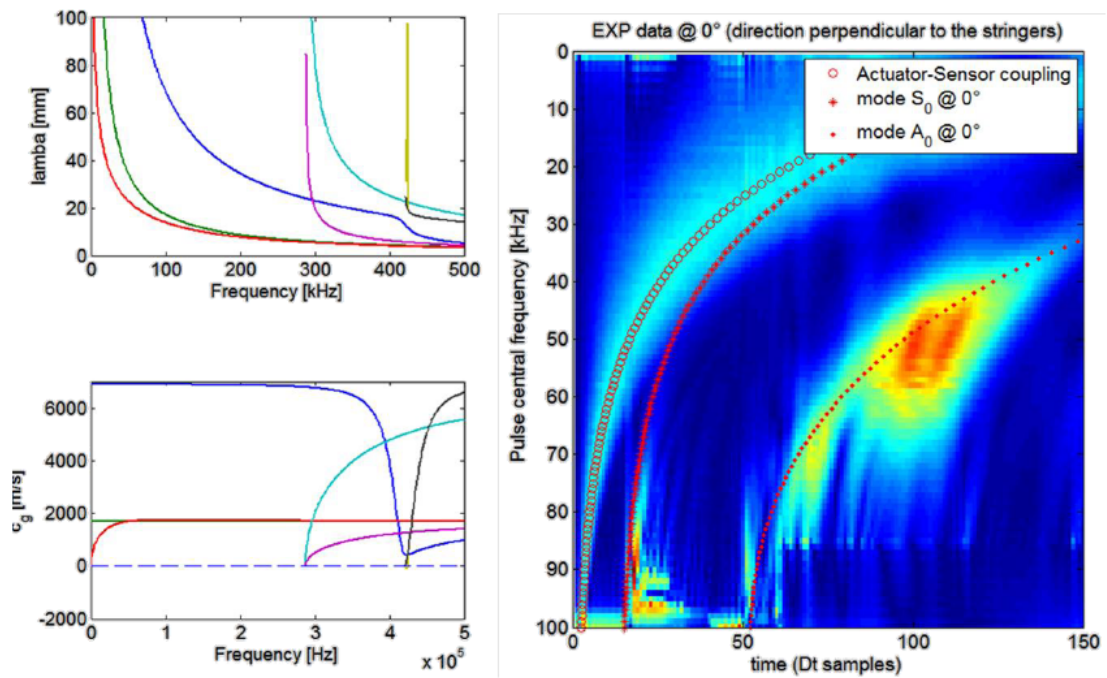


Figure 6.8: Predicted wavelength and group velocity dispersion curves (left column). Predicted dispersion curves over imposed the signals acquired from a frequency sweep (right plot).

As it can be seen from this plot, below 300 kHz only the A_0 , S_0 and SH_0 modes exist. Next, the curves were experimentally validated. In particular, a frequency sweep was run by exciting one PZT (PIC181, diameter 0.01 m, thickness 0.001 m) with a single cycle of sinusoid at central frequency varying from 0 to 100 kHz. Time waveforms were acquired at the other sensors placed at the corners of a square with 290 mm side length. In particular, in Figure 6.8 the responses acquired at the sensor oriented at 0° are represented as the absolute value of their Hilbert transform. As it can be seen from the image, the actuator-sensor coupling, and two guided modes are clearly visible. Over imposing the predicted dispersion curves to the image it can be seen that the other two modes match quite well with the predicted S_0 (fastest) and A_0 (slower) guided modes. The predicted dispersion curves for A_0 were thus used to design the frequency warping operator necessary to compensate the acquired signals from dispersion.

6.6 SHM System: Node Sensor and PZT Transducers

The embedded electronic system is composed by 4 conventional piezoelectric PZT transducers, a STM32F4 board equipped with an ARM Cortex-M4 microcontroller and a IEEE802.15.4 wireless transceiver.

To be compliant with the low-power requirements the device presents a RF wireless ZigBee module, connected to the main board using an SPI interface. Guided waves were excited by hitting the plate with a pencil orthogonally to the surface.

The generated signals were recorded by connecting the PZT transducers directly to the ADC ports of the STM32F4 board. The sampling frequency was set at 150 kHz since the spectral components of the Lamb waves vanish rapidly above 60-100 kHz. In the frequency range 0-50 kHz, thanks to the wavelength tuning effect, all wave modes but A_0 are filtered out in the acquisition process. Acquisitions were triggered when the signal received from one of the PZT discs reached a threshold level of 140 mV; pre-trigger recordings were enabled to obtain the previous history of each signal, although it was experimentally verified that pre-trigger recordings can be discarded in the time of flight estimation with a negligible degradation of the impact localization accuracy.

Given the coordinates of the sensor positions x_i and y_i and having estimated the differences in travelled distance between the waves acquired by the first sensor and the remaining, a hyperbolic positioning method is applied to locate the point source. Such a method exploits the differences in propagating distances to determine hyperbolae on which the impact point must lie. The intersection of the different hyperbolae, obtained by solving the system of $M - 1$ equations with the Levenberg-Marquardt algorithm, is taken to be the impact position.

The Levenberg-Marquardt algorithm is iterative and can be computationally onerous, for this reason such computation is performed by a central processing unit and not by the embedded microcontrollers.

The results of the proposed procedure for impact localization can be seen in Figure 6.9 where the target and estimated impact points denoted by circles and crosses, respectively, are shown.

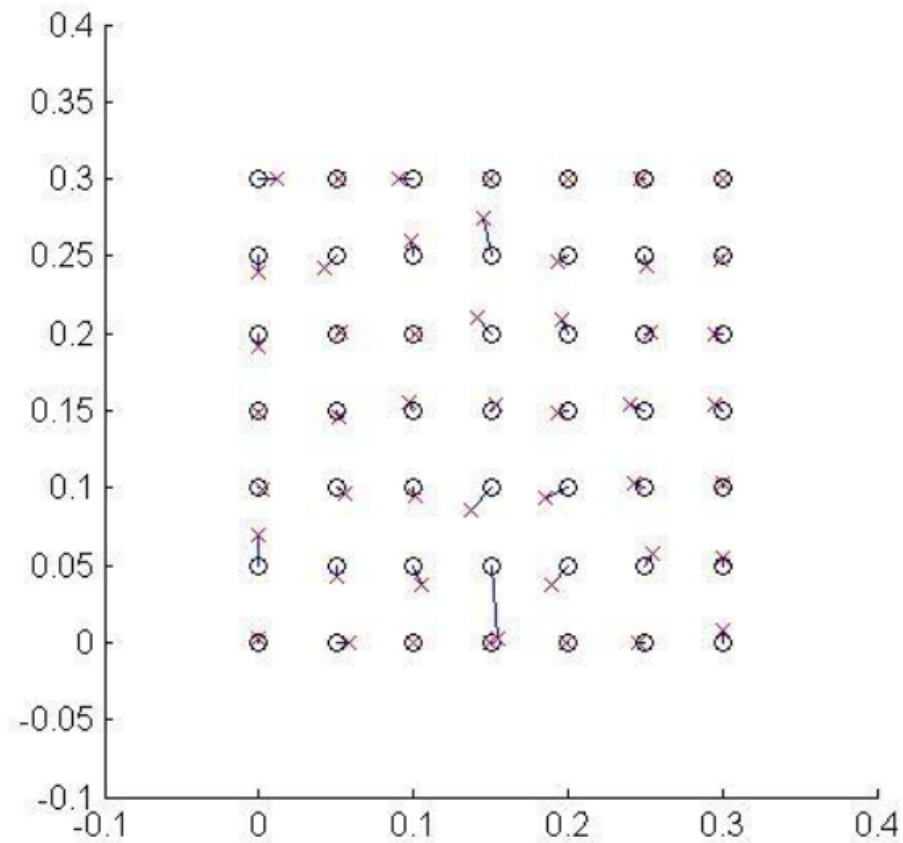


Figure 6.9: Comparison between the estimated (crosses \times) and actual (circles \circ) impact locations. A mean error smaller than 10 mm was achieved in coordinate estimation.

The power consumption of the STM32F4 board is around 80mW in the acquisition phase and 170mW during the time difference of arrival computation.

6.7 Discussion

In this Chapter an efficient wireless embedded structural monitoring system for impact localization based on Lamb waves is proposed. The method applies a dispersion

compensation procedure on the signals acquired by passive sensors, thus overcoming the difficulties associated with arrival time detection based on classical thresholding procedures.

The processing framework and the algorithm are implemented on a STM32F4 discovery board with advantages of compactness, low-power consumption, high efficiency and precision. The system was validated experimentally to locate impacts in a aluminum plate with four sparse PZT sensors.

Results shows the effectiveness of the proposed implementation with high localization accuracy and low current consumption.

Damage Localization

Nobody knows his own possibilities since that are tested.

Publio Siro

7.1 Introduction

Among the various applications based on GWs, numerous approaches have been proposed to detect defects in plates-like structures by means of Lamb waves [66] and [67]. Generally, active-passive networks of transducers are considered, where one or more actuators are used to generate GWs and the sensors work as wave detectors. The time-waveforms acquired by the receivers, triggered on the actuator, are subsequently analyzed to locate and characterize the defect.

Unfortunately, several dispersive modes appear simultaneously in the received signals, thus limiting the potential of such approaches. The modes, in fact, overlap in both time and frequency domains and simple Fourier analysis techniques are not able to separate them. Recent works in the area of time-frequency representations (TFRs) [68] [69] show great promise for applications in nondestructive evaluation and material characterization, as a mean to interpret ultrasonic propagation in various structures. In fact, since the propagation characteristics are directly related to both the intimate structure and mechanical properties of the medium, the dispersive properties of GWs

can reveal important informations for structural health monitoring purposes.

Nevertheless, fast identification and separation of Lamb modes is a challenging step in the process of damage detection, even in the time-frequency domain. Such task is complicated by the fact that high energy pulses have to be excited in order to get readable echoes from weak reflectors.

To excite such high energy pulses, two alternatives can be considered:

- short spiky pulses;
- chirped pulses.

Short pulses (usually few cycles sinusoids with Gaussian envelopes) are commonly adopted and somehow simpler to be interpreted, as many of the recently proposed dispersion compensation algorithms (see [70] and [51]) or time-frequency tools (e.g. [71], [72] and [73]) are perfectly suited to process them. However, the pulser circuit must handle very high voltages (up to 1 kV) and requires mains power supply. This can be unpractical in many situations, e.g. whenever a portable device has to be built, or when the available power supply is limited. In such cases, actuation by means of chirped pulses is the most effective solution.

Chirped pulse transmissions found its first wide-spread applications in radar systems. Essentially, such technique consists in transmitting long linear or non-linear frequency modulated signals, so that the pulse energy is stretched in time, but the resolution is not compromised thanks to the broad frequency spectrum of the signal itself. Broad-band chirped techniques have been previously applied to ultrasonic nondestructive testing (see [74] or [75]), but are unusual in GWs-based applications because of their dispersive detrimental effect.

In this Chapter, we discuss a novel methodology to tackle dispersion in case of chirped excitations. The proposed procedure is based on a two-step pulse compression strategy. In the first step, the Warped Frequency Transform (WFT) is exploited to compensate the group delay of the acquired signals from the dependency on the distance traveled by the waves [21]. The second step is aimed at the compressing the chirped frequency modulation. Next the compensated and compressed signals are used to feed

an imaging algorithm that reveals the position of the defect on the plate. The main benefit of the proposed strategy for active-passive networks of sensors is the possibility of using lower input power with respect to procedures based on spiky pulses. In addition, being fast as a standard Discrete Fourier Transform, the procedure is well suited for real-time SHM applications of plate-like structures.

The Chapter is organized as follows: the proposed group delay compensation procedure will be presented in section 7.2 together with some results on numerically simulated waveforms; an experimental validation is presented in section 7.3.

The conclusions end the Chapter.

7.2 Group delay compensation

7.2.1 Step 1: dispersion compensation

As shown in [76], the WFT can be exploited to compensate a signal from a Lamb wave dispersion induced by the traveled distance. To this aim, the warping map $w(f)$ has to be defined through its functional inverse, such as:

$$K \frac{dw^{-1}(f)}{df} = \frac{1}{c_g^M(f)} \quad (7.1)$$

where $1/c_g^M(f)$ is the nominal dispersive slowness relation of the M -th Lamb wave whose dispersive effect has to be compensated. K is a normalization parameter selected so that $w^{-1}(0.5) = w(0.5) = 0.5$.

A sample warping map is depicted in Fig. 7.1(b) along with its functional inverse. It was computed according to Eq. (7.1) by considering the group velocity curve of the A_0 mode represented in Fig. 7.1(a).

The Lamb waves group velocity curves of Fig. 7.1(a) were obtained by using the semi-analytical finite element (SAFE) formulation proposed in [20] considering a 3 mm thick aluminum plate with Young modulus $E = 69$ GPa, Poisson's coefficient $\nu = 0.33$ and density $\rho = 2700$ kg/m³.

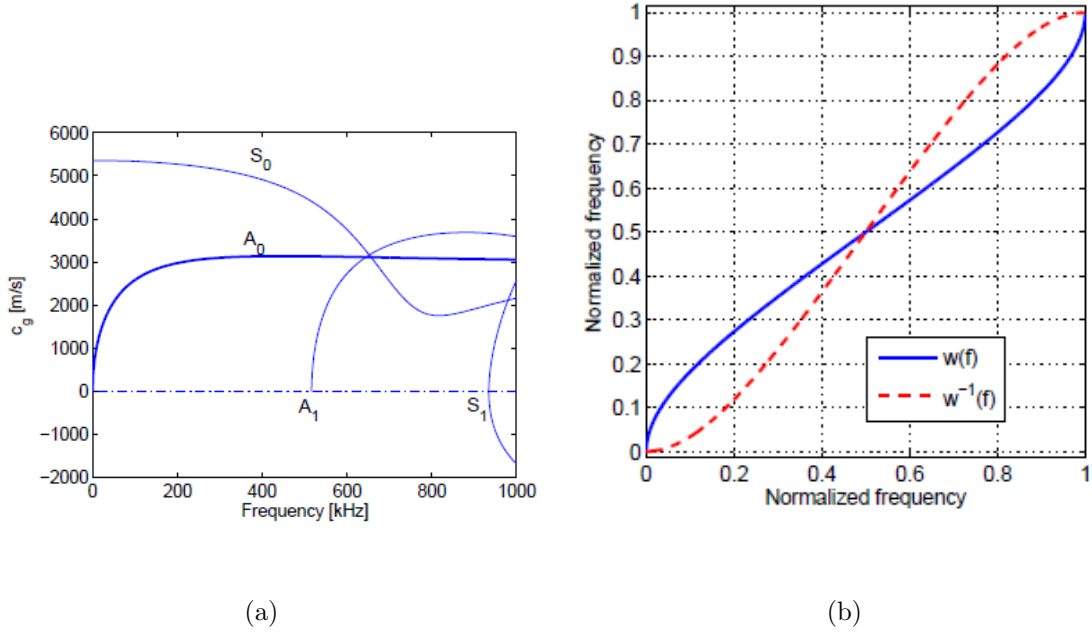


Figure 7.1: (a) group velocity dispersion curves $c_g(f)$ for the Lamb waves propagating in an aluminum 3 mm thick-plate (Young modulus $E = 69$ GPa, Poisson's coefficient $\nu = 0.33$, density $\rho = 2700$ kg/m³). (b) Warping map $w(f)$ for A_0 wave dispersion compensation and its functional inverse $w^{-1}(f)$ designed according to Eq. 7.1.

Let us indicate with $s(t, D)$ a time waveform of an undamped Lamb wave, for which the time of actuation is known and it is taken as the origin of the time axis ($t = 0$), at a traveled distance D from the actuator. $s(t, D)$ can be modeled in the frequency domain as a dispersive system whose response is:

$$S(f, D) = S(f, 0) \cdot e^{-j2\pi \int_0^f \tau_D^M(\alpha) d\alpha} \quad (7.2)$$

where $S(f, 0)$ is the Fourier transform of the exciting pulse in the point of actuation, and $\tau_D^M(f) = D/c_g^M(f)$ the dispersive group delay of the wave component of frequency f (it is assumed that the transducer is ideal and excites only the M -th Lamb wave mode of interest). Therefore, in force of Eq. (7.1) the right hand term of Eq. (7.2) can be rewritten as:

$$S(f, D) = S(f, 0) \cdot e^{-j2\pi D \int_0^f \frac{1}{c_g^M(\alpha)} d\alpha} = S(f, 0) \cdot e^{-j2\pi w^{-1}(f)KD} \quad (7.3)$$

in which a dispersive distortion results from the nonlinear phase term. Now, by applying the warping operator to $s(t, D)$ we obtain a new signal whose frequency

transform is

$$\mathbf{FW}_w\{s(t, D)\} = [\sqrt{\dot{w}(f)}S(w(f), 0)] \cdot e^{-j2\pi fKD} \quad (7.4)$$

By looking at this equation, it can be clearly seen how the dispersive effect of the distance is converted into a simple time delay proportional to the distance itself $\hat{\tau}_D^M = KD$, as the phase term presents a linear dependence on warped frequencies (i.e. frequencies of the warped signal).

To show the effect of the WFT in active-passive techniques, in the following the warping operator is tested on some time-waveforms generated synthetically for a given distance D by forcing the guided modes time delay to an applied exciting pulse by using Eq. 7.2. For a selected propagation distance D , and for each guided mode of interest, the time delay is computed as $D/c_g^M(f)$.

For example, considering a triangular pulse with total duration equal to 10^{-5} s and unitary amplitude (see Fig. 7.2(a)) the signal in Fig. 7.2(b) was generated via the above mentioned procedure by considering only the A_0 mode group velocity curve in the $[0 - 300]$ kHz frequency range (represented in Fig. 7.1(a)) and a propagation distance of $D = 300$ mm.

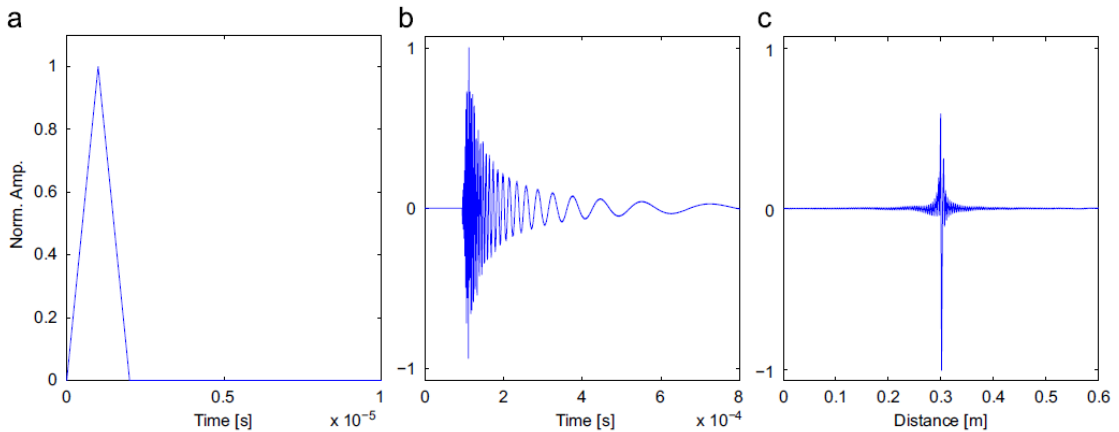


Figure 7.2: Dispersion compensation of a dispersive signal $s(t, D)$. (a) exciting spiky pulse $s(t, 0)$ starting at $t = 0$ s. (b) dispersive signal $s(t, D)$ at a traveling distance $D = 300$ mm. (c) warped signal $\mathbf{FW}_w\{s(t, D)\}$.

The compensated signal obtained by processing the dispersive signal of Fig. 7.2(b) by designing the warping map according to the A_0 mode group velocity (as in Eq. (7.1)) is shown in Fig. 7.2(c).

The WFT dispersion compensation procedure cannot produce a perfect replica of the exciting function for two main reasons:

- the compensated pulse, whose Fourier transform is $\sqrt{\dot{w}(f)} \cdot S(w(f), 0)$, is defined in a new spatial domain different from the time domain of the actuating pulse whose Fourier transform is $S_0(f, 0)$;
- for the A_0 mode $c_g(0) = 0$, therefore it would be necessary to have an infinitely long acquired signal to perform a total compensation.

The unavoidable truncation of the dispersed signal results in an attenuation of the DC component after the processing and, consequently, an oscillating function in Fig. 7.2(c). Despite these limits, the x -axis of the warped signal can be directly related to the distance traveled by the wave thanks to Eq. (7.2).

Therefore, the warped signal turn to be perfectly suited for wave traveling distance estimation procedures. This is due to the adopted sharp impulsive pulse that makes the warped waveform in Fig. 7.2(c) rapidly evanescent out of the neighborhood of the actual traveled distance. However, similar conclusions do not hold for chirped excitation.

For instance, let us consider the chirped actuation in Fig. 7.3(a). The resulting dispersive signal considering the A_0 wave propagating for a distance $D = 300$ mm is depicted in Fig. 7.3(b), and the signal warped by using the warping map shaped according to the A_0 mode is shown in Fig. 7.3(c). As it can be seen, the spreading of the warped waveform on the distance axis is clearly visible. Such effect is due to the warping of the group delay of the incipient pulse.

Therefore, for the purpose of distance estimation in case of chirped exciting pulses a further signal processing step is required.

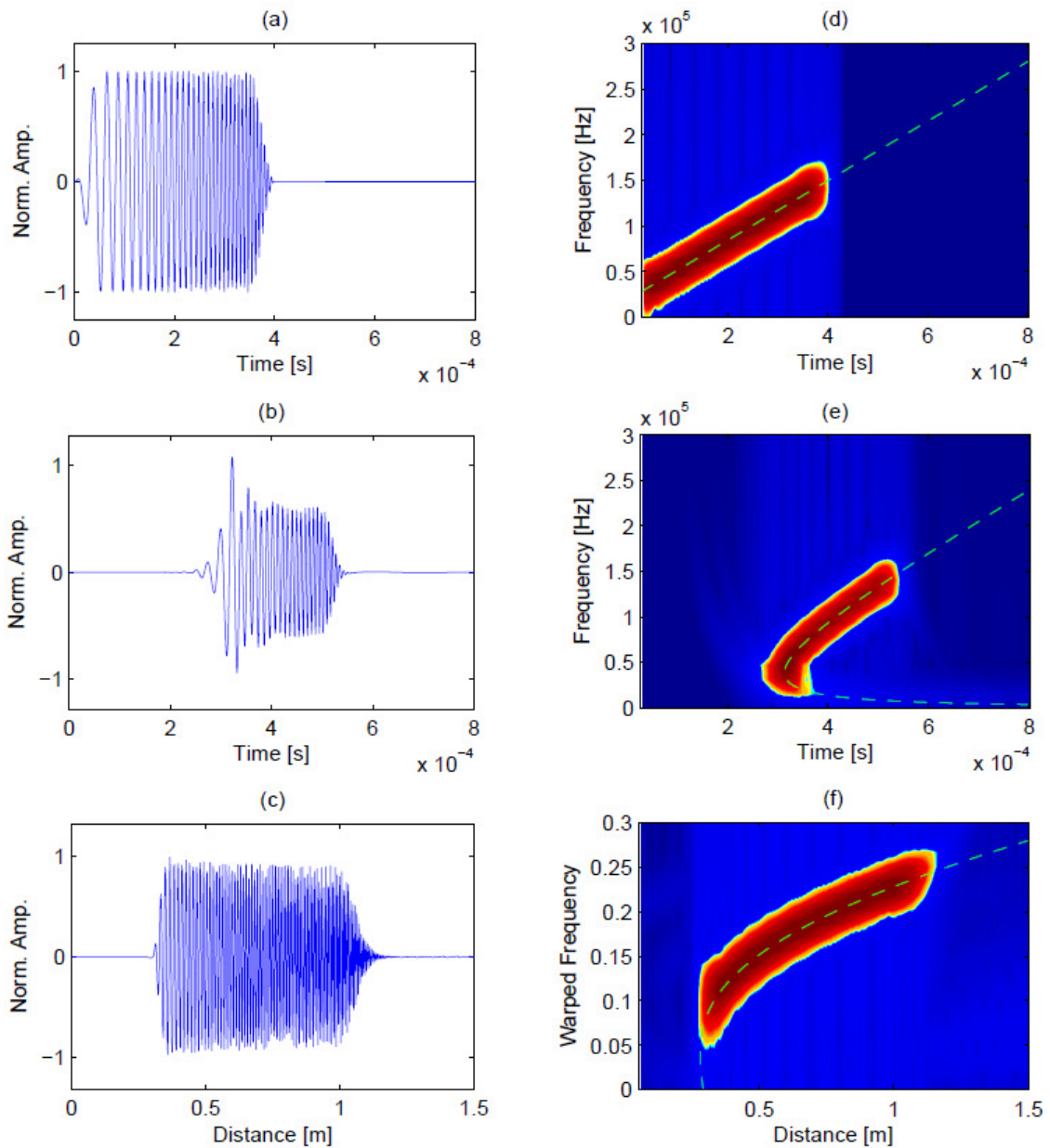


Figure 7.3: (a) actuated chirped pulse $s(t, 0)$. (b) simulated dispersive wave $s(t, D)$ acquired at a traveling distance $D = 300$ mm. (c) warped signal $\mathbf{W}_w\{s(t, D)\}$. Subplots (d), (e) and (f) represent the spectrograms of the signals in (a), (b) and (c), respectively. In the same plots, the dashed lines represent group delays estimated according to Eq. (7.6), Eq. (7.8) and Eq. (7.9), respectively.

7.2.2 Step 2: warped signal compression

Let us consider a chirped excitation $s(t, 0)$ with Fourier transform $S(f, 0)$. $S(f, 0)$ can be rewritten in terms of amplitude $A(f)$ and phase components, highlighting the group delay of the chirp pulse due to its frequency modulation $\tau_0^C(f)$ as:

$$S(f, 0) = A(f) \cdot e^{-j2\pi \int \tau_0^C(f) df} \quad (7.5)$$

$$\tau_0^C(f) \equiv -\frac{1}{2\pi} \frac{d \arg[\mathbf{F}s(t, 0)](f)}{df} \quad (7.6)$$

Now applying the warping operator to $s(t, 0)$ leads to the following distortion of the chirped pulse group delay that does not depend on the distance of propagation:

$$\begin{aligned} \hat{\tau}_0^C(f) &= \frac{d \int \tau_0^C(w(f)) dw(f)}{df} \\ &= \tau_0^C(w^{-1}(f)) \cdot c_g^M(w^{-1}(f)) \end{aligned} \quad (7.7)$$

Since the group delay of $s(t, D)$ can be estimated as:

$$\tau_D^{CM}(f) = \tau_0^C(f) + \tau_D^M(f) = \tau_0^C(f) + D/c_g^M(f) \quad (7.8)$$

the group delay of warped signal $\mathbf{W}_w s(t, D)$ in force of Eq. (7.7) and Eq. (7.1) is simply:

$$\hat{\tau}_D^{CM}(f) = \hat{\tau}_0^C(f) + \hat{\tau}_D^M(f) = \hat{\tau}_0^C(f) + KD \quad (7.9)$$

from which it can be noticed that $\hat{\tau}_0^C(f)$ is an adjunctive group delay which is present in all the warped signals actuated by the same chirp pulse independently from their traveled distances D_i .

It follows that the group delay due to the chirp modulation can be easily removed from the warped signals by forcing an opposite term $-\hat{\tau}_0^C(f)$ in their phase spectrum as:

$$S_i^{\text{comp}}(f, D_i) = \mathbf{F}\mathbf{W}_w\{s(t, D_i)\} \cdot e^{j2\pi \int \hat{\tau}_0^C(f) df} \quad (7.10)$$

By doing so, an effective compression of the chirped pulse is obtained in $\mathbf{F}^{-1}S_i^{\text{comp}}$, suitable for defect localization procedures, as can be seen in Fig. 7.4.

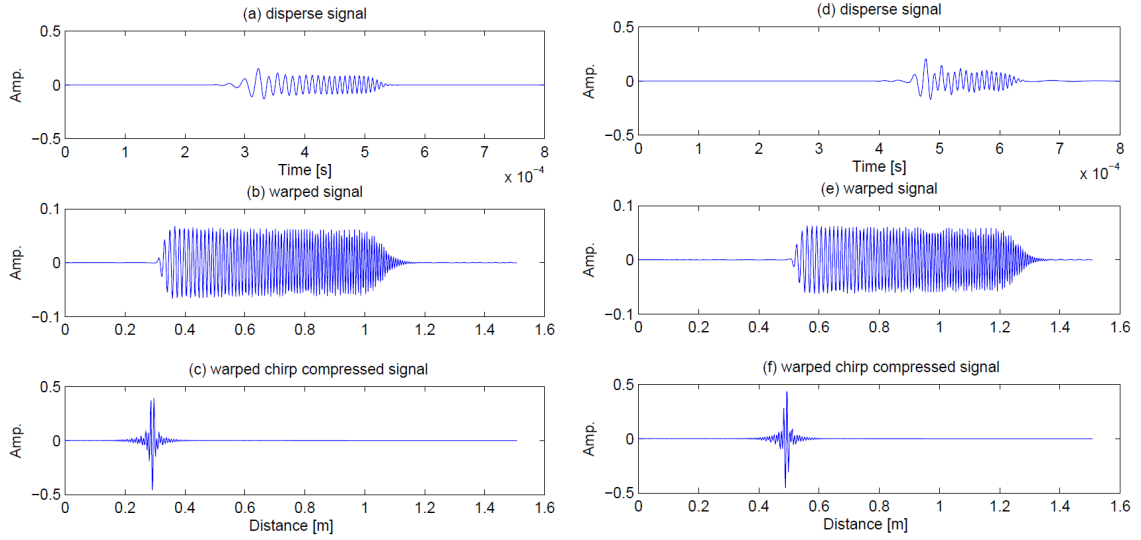


Figure 7.4: Subplots (a), (b), and (c) represent the time-waveform $s(t, D)$, the warped waveform $\mathbf{W}_w\{s(t, D)\}$, and the chirp compressed warped signal $\mathbf{F}^{-1}S_i^{\text{comp}}$, at a traveling distance $D = 300$ mm, respectively. In subplots (d), (e) and (f) the same information for a traveling distance $D = 500$ mm.

In particular for the chirped pulse in Fig. 7.3(a), in Fig. 7.4 are represented the dispersive signals at traveling distances of $D = 300$ mm and $D = 500$ mm, their warped signals and finally the compressed warped signals. In this figure, it is possible to evaluate the combined effect of the WFT and of the chirped frequency modulation compression procedure. The WFT produces very similar waveforms a part from a rigid translation on the warped x -axis (see Fig. 7.4(b) and Fig. 7.4(e)), thus compensating the A_0 Lamb wave dispersion. The subsequent application of Eq. 7.10 produces waveforms evanescent out of the neighborhood of the actual traveled distances (see Fig. 7.4(c) and Fig. 7.4(f)).

In certain applications, e.g. in case of multimodal propagation, it could be useful to process the acquired signal with pass-band filters. In such cases, it is of the utmost importance to take into account in the group delay compensation procedure the additional time delay introduced by the filter itself, i.e. $\tau^F(f)$. Similarly, the procedure can also be extended in cases where a further group delay term $\tau^G(f)$ is due to the irregular geometry of the waveguide [77].

7.3 Experimental verification

7.3.1 Data acquisition

As a case study, we exploited the proposed tool to locate defects in an aluminum 1050A square plate 1000×1000 mm and 3 mm thick. Four PZT discs (PIC181, diameter 10 mm, thickness 1 mm) were bonded to the plate using a high-strength Loctite glue.

In order to test the procedure in difficult conditions, the sensor topology is deliberately non-optimized, in fact, it is constituted by a very sparse array of sensors, placed asymmetrically with respect to the plate center, and close to edges of the plate in order to be prone to undesired reflections.

The experimental set-up is shown in Fig. 7.5.

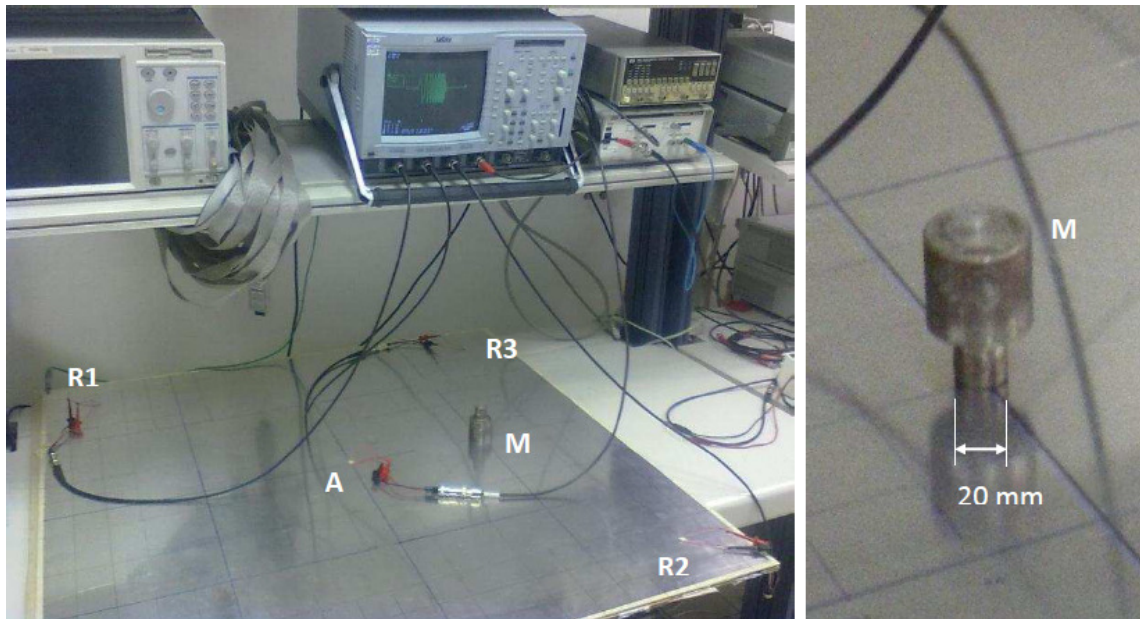


Figure 7.5: Experimental set up used to validate the defect location procedure: **A** actuator, **R** receivers, **M** added mass.

Guided waves were excited by actuating the central PZT transducer **A** with chirped signals with a maximum voltage of 12V thus compatible with battery power supply, as well as with aircraft electrical systems.

Defects have been emulated by a small steel cylindrical mass **M**, 20 mm of diameter and 500 gr of weight, posed in different positions on the plate and acoustically coupled simply with water, so that it generates quite weak reflections. The acquired waveforms at the three receivers **R1**, **R2** and **R3**, were recorded using the LC534 series LeCroy oscilloscope at a sampling frequency of 1 MHz.

The position of the transducers is defined in Table 7.1.

coordinates	actuator A	receiver R1	receiver R2	receiver R3
x (m)	0.50	0.10	0.90	0.90
y (m)	0.50	0.90	0.10	0.90

Table 7.1: Actuator and receivers topology.

Acquisitions were triggered when the actuated signal reached a threshold level of 140 mV. The sampling frequency was sufficiently high to avoid aliasing effects, as the frequency content of the acquired signal vanishes above 400 kHz.

As input signal a gaussian modulated chirp has been used in order to maximise the energy sent to the medium in a small time slot and it is shown in Fig. 7.6

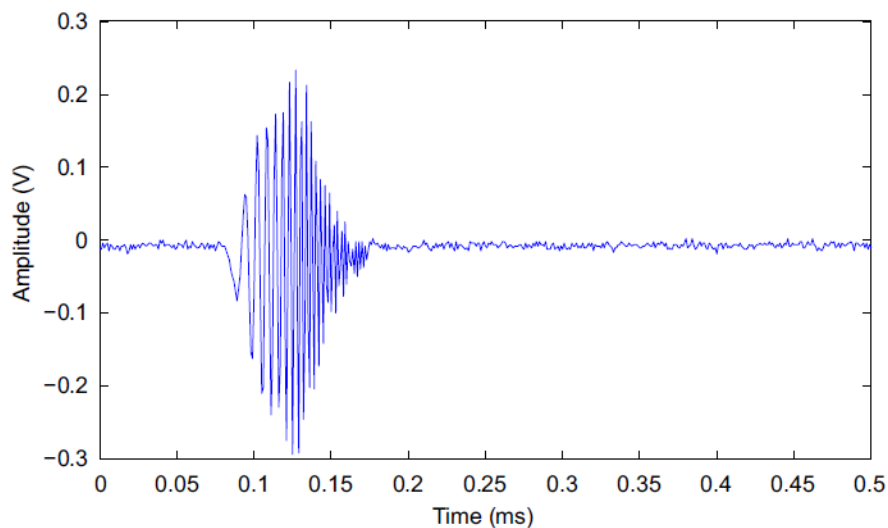


Figure 7.6: Gaussian modulated chirp used as input signal sent from the central PZT transducer **A**.

For example, the experimental waveforms detected by the 3 receivers, after having placed the mass at the coordinates $x = 0.35$ m and $y = 0.35$ m, are shown in Fig. 7.7.

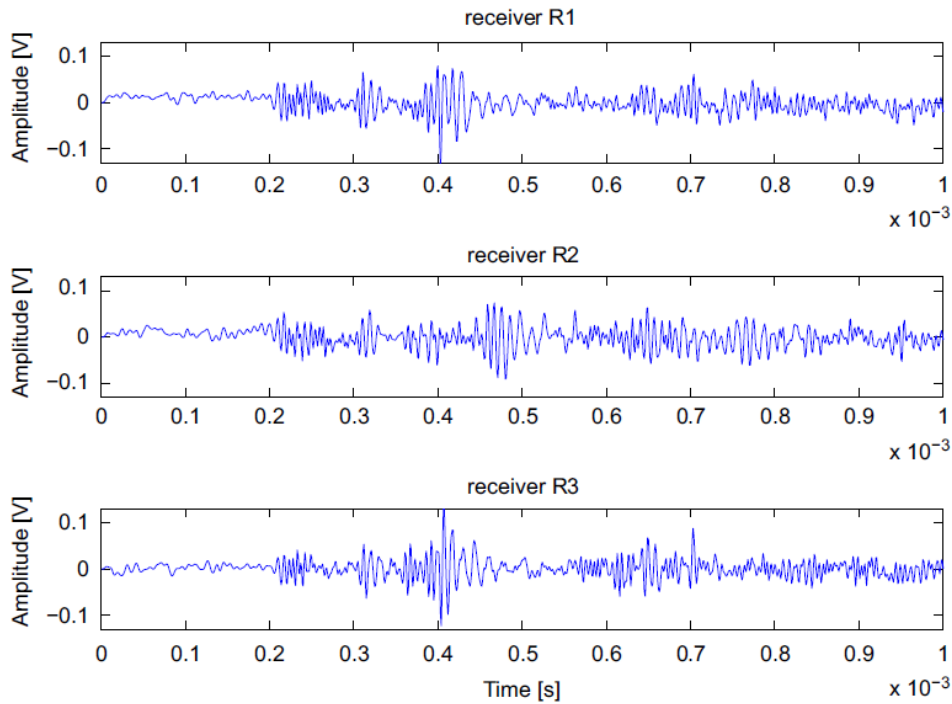


Figure 7.7: Signals acquired by the PZT sensors. The mass is in $x = 0.35$ m, $y = 0.35$ m, and a chirped signal was actuated.

As can be seen from the time waveforms, it is extremely difficult estimating the time of arrival of echoes due to the mass (emulated defect) among the other interfering waves due to edge reflections and multimodal propagation.

Such effects can be clearly observed in the spectrogram of the signal received by **R1** depicted in Fig. 7.8, in which because of multimodal propagation and edge reflections, many propagating waves are visible.

Moreover, such estimation is complicated by the effect of dispersion which introduces a distance dependent group delay shift.

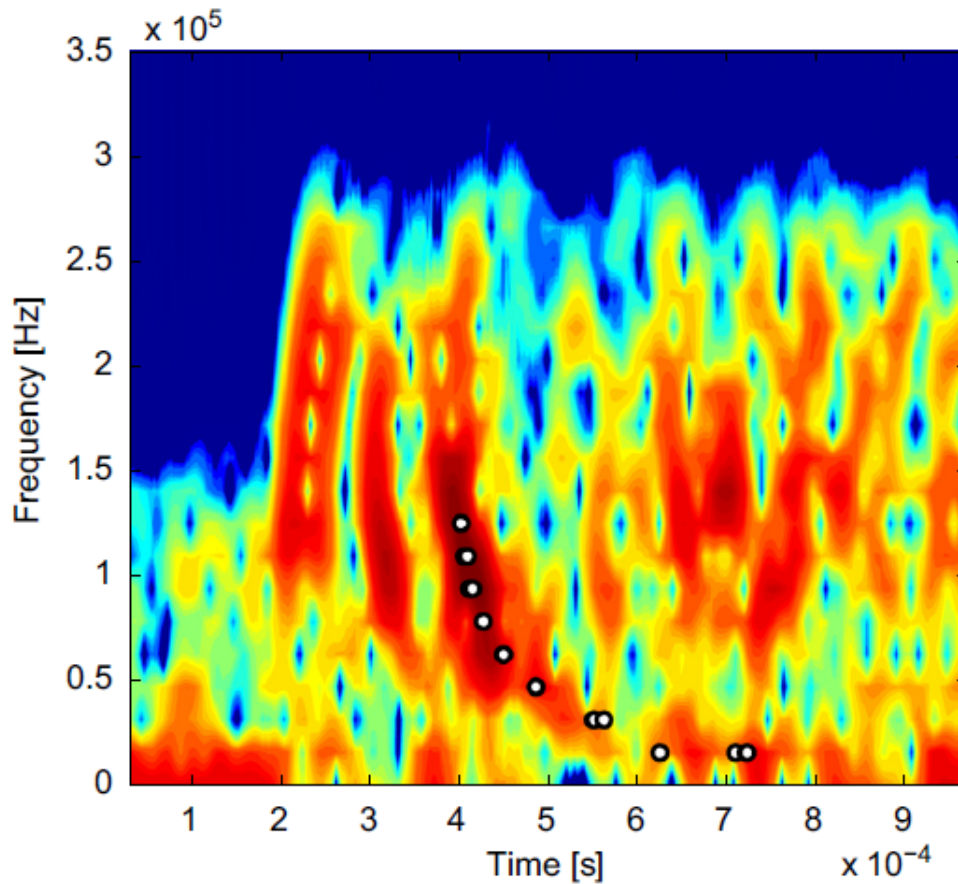


Figure 7.8: Spectrogram of the signal acquired by Receiver 1 in Fig. 7.7. The superimposed dots \circ represent the dispersive group delay for the A_0 mode scattered by the defect.

7.3.2 Two-step signal processing

In order to apply the proposed procedure to compensate and compress chirped actuated Lamb waves, first the WFT operator must be defined. For such a scope, the Lamb waves group velocity dispersion curves for the 3-mm thick aluminum plate were calculated, as detailed in Sec. 7.2. In the $[0 - 300]$ kHz frequency range, only the two fundamental A_0 and S_0 waves can propagate through this plate. Since in guided wave reflections due to surface defects (as the one emulated here) the energy in the A_0 mode is greater than the one retained by the S_0 mode, the group velocity curve

of the A_0 mode was used to shape the warping map $w(f)$ according to Eq. (7.1).

To lower the contribution of S_0 waves in the acquired waveforms, a Butterworth low pass filter was applied, and the relative $\tau^F(f)$ properly tabulated for the successive group delay compensation step.

The cut-off frequency of the filter was selected to be 130 kHz, such choice was performed by looking at the estimated frequency response of the PZT discs to the different propagating modes, as schematically depicted in Fig. 7.9.

The estimation was made by using the method detailed in [20].

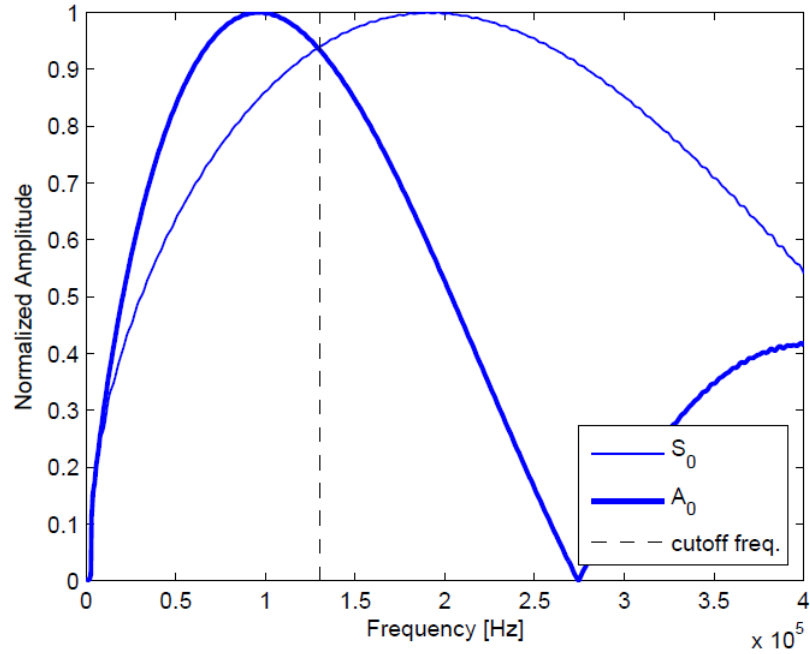


Figure 7.9: Estimated Lamb waves frequency response of the PZT transducers adopted in this study. The dashed line represents the cut off frequency selected for filter design.

Next, by processing the acquired signals with the WFT, new waveforms are obtained. In the new waveforms, the A_0 wave group delay dependency on distance $\hat{\tau}_D^M(f)$ is removed, but a further processing step is needed in order to compress the remaining frequency modulation, due to the combined effect of the chirped actuation and of the low-pass filtering. Such modulation can be removed with the procedure described in Sec. 7.2.2.

The envelopes of the compensated and compressed signals $E_R(x) = \text{env}(\mathbf{F}^{-1}S_R^{\text{comp}})$, $R \in \{1, 2, 3\}$ are shown in Fig. 7.10. It is worth noticing how the abscissa value corresponding to envelope maxima are directly related to the distances traveled by the waves scattered by the emulated defect. Envelopes are computed as the absolute values of the Hilbert Transform of the warped compressed signals.

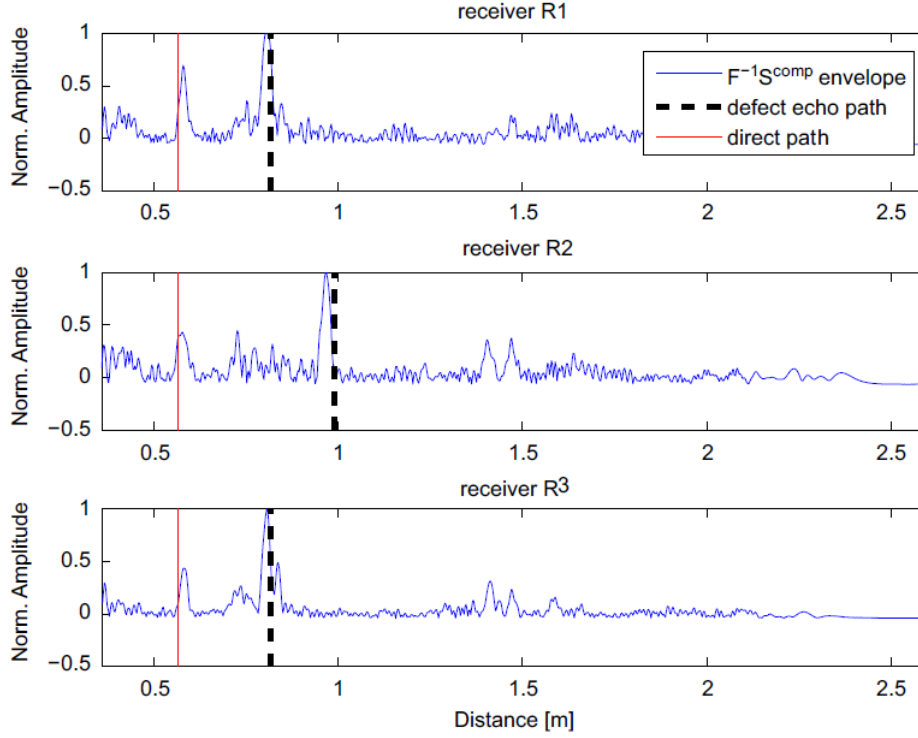


Figure 7.10: Envelopes of the warped compressed signals $E_R(x) = \text{env}(\mathbf{F}^{-1}S_R^{\text{comp}})$, $R \in \{1, 2, 3\}$.

7.3.3 Defect imaging

Finally, the defect can be imaged by applying to envelopes $E_R(x)$ this formula:

$$Im(\mathbf{P}_i) = \sum_{R=1}^3 E_R(|\overrightarrow{\mathbf{P}_A \mathbf{P}_i}| + |\overrightarrow{\mathbf{P}_R \mathbf{P}_i}|) \quad (7.11)$$

where \mathbf{P}_i is the generic point of coordinates $x - y$ over the plate surface, while \mathbf{P}_A and \mathbf{P}_R denote the actuator and the receiver positions, respectively. For instance, Eq. (7.11) applied to the signals of Fig. 7.10 produces the scatterer map in Fig. 7.11.

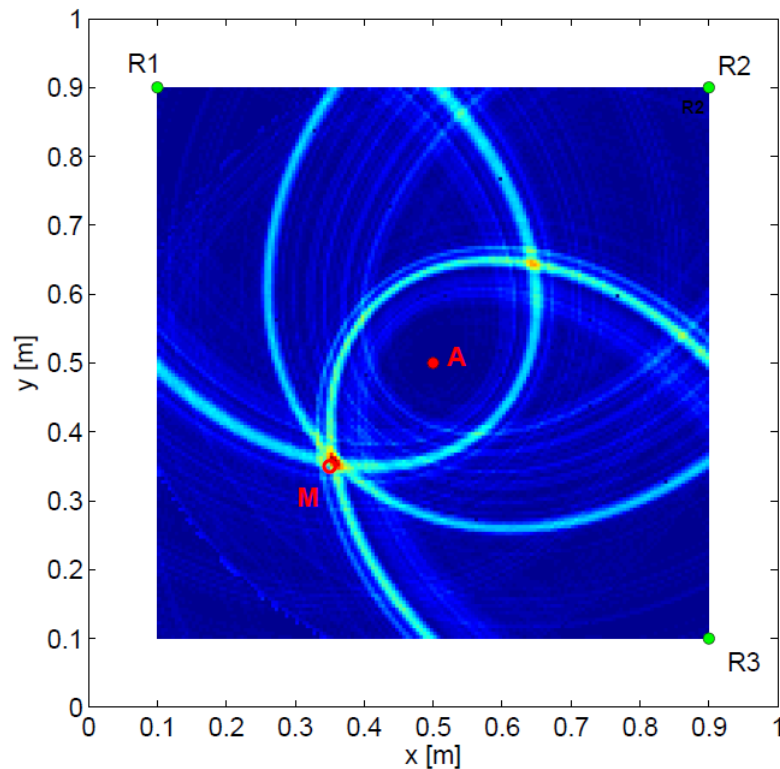


Figure 7.11: Defect imaging with the processed signals of Fig. 7.10

As can be seen, the ellipses determined by Eq. (7.11) intercept each other in a point which is very close to the actual position of the mass.

At this point, localization procedures based on the extraction of the peaks of Im can be easily implemented.

The high performances of the proposed procedure can be seen in Fig. 7.12, where 36 emulated defects and their estimated location positions, denoted by circles \circ and crosses \times , respectively, are shown. The maximum error s , denoted by circles \circ and crosses \times , respectively, are shown.

The maximum error in the estimation of the 36 impact point coordinates is smaller than 15 mm, a dimension compatible with the mass base radius, as it can be seen from the cumulative curve of Fig. 7.13.

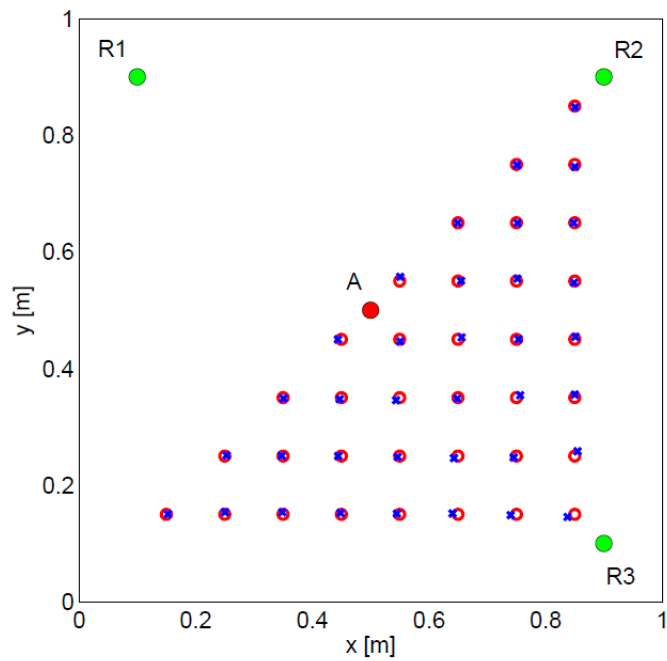


Figure 7.12: Comparison between the estimated (crosses \times) and actual (circles \circ) defect positions. A mean error smaller than 5 mm was achieved in coordinates estimation.

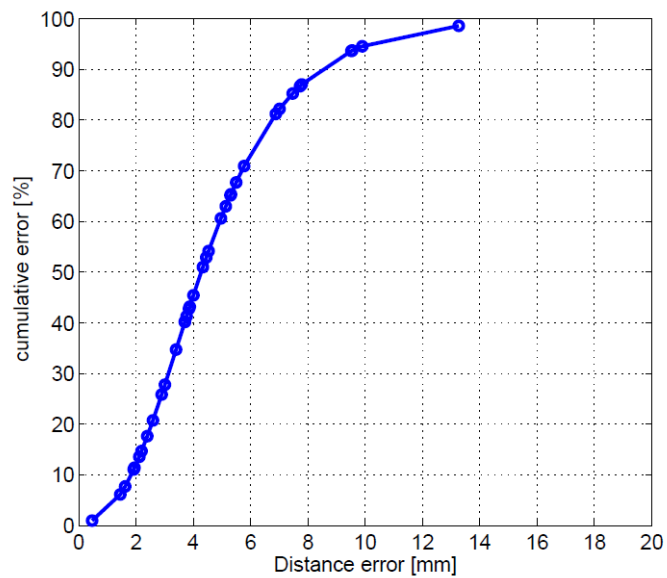


Figure 7.13: Proposed procedure cumulative error in the location of the 36 emulated defects.

7.4 Discussion

In this Chapter, a signal processing strategy aimed at locating defects in plates by means of analyzing actuated and received Lamb waves by PZT sensors is proposed. The method is suitable for chirped pulse actuations, and it is based on a two-step procedure applied to the acquired signals, thus overcoming the difficulties associated to arrival time detection of dispersive waves. By exploiting the dispersion compensation properties of the WFT, waveforms characterized by a unique time-frequency pattern are obtained. The actuated chirp frequency modulation is compressed in a subsequent processing step. Excellent performances in terms of defects localization are shown through experiments. It is worth noticing that the robustness of the wave traveled distance estimation allows to achieve such performances with sparse arrays of conventional transducers. Thanks to its unique potential the developed tool could pave a new class of procedures to locate defects in waveguides. Optimized and adaptive selection of the array shape and size is under investigation to further improve accuracy of the proposed approach.

Localization of Defects in Irregular Waveguides by Dispersion Compensation and Pulse Compression

You have never made a mistake if you have not
tried something new.

Albert Einstein

8.1 Introduction

In this Chapter a pulse-echo procedure suitable to locate defect-induced reflections in irregular waveguides is described. In particular, the procedure extracts the distance of propagation of a guided wave scattered from a defect within the echo signal, revealing thus the source-defect distance.

In NDT/SHM applications, several numerical procedures have been proposed to tackle the effect of dispersion in regular waveguides [70], [51], [24], [78]. However, to date, irregular waveguides have been scarcely considered. An irregular waveguide is composed by a sequence of segments with different dispersion properties (straight and curved geometry, different cross-sections, tapered portions, different materials, etc.).

A guided wave propagating along an irregular waveguide is affected by the different dispersive maps, one for each portion composing the irregular waveguide. As expected, the effect of multiple dispersive maps complicates further the received signal, and those approaches suitable to compensate for dispersion in regular waveguides fail. To overcome such problem, recently a processing procedure capable to compensate a guided waves signal from the dispersion due to a distance traveled in irregular waveguides has been proposed [79]. In particular, the procedure exploits the Warped Frequency Transform (WFT) to remove from the acquired echo signal the dispersion due to traveled distance in portions of waveguides characterized by different dispersive properties.

Here, an application on a plate-like structure made up by three plates with two different thicknesses connected by two tapered portions as the one shown in Figure 8.1, is proposed to prove the capabilities of the aforementioned approach to extend pulse-echo defect detection procedures to irregular waveguides.

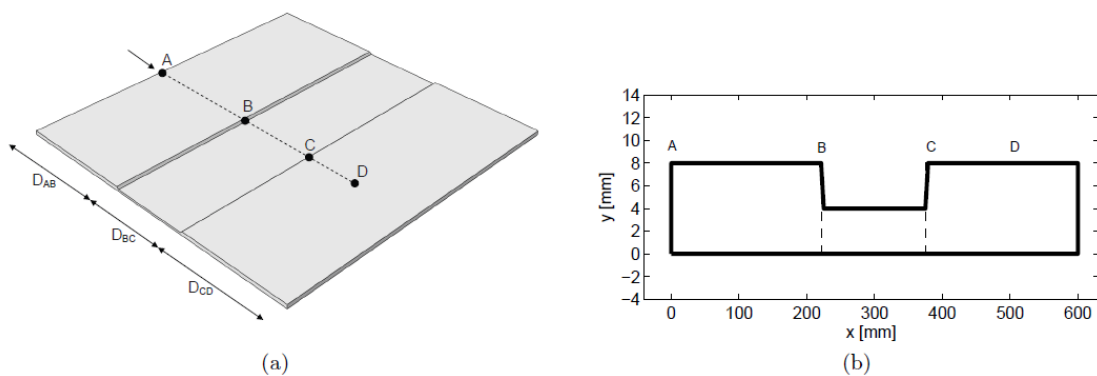


Figure 8.1: (a) Irregular waveguide composed by two aluminum plates 8 mm thick and a plate 4 mm thick; the three portions are connected with 45° short tapered portions. (b) Schematic cross-section of the irregular waveguide. Note the different scale in the x and y directions

The proposed approach can extend the range of application of guided waves based non-destructive testing (NDT) and Structural health monitoring (SHM) strategies to irregular waveguides.

8.2 Defect Locating Procedure

Schematically, the proposed procedure can be synthesized in the following steps:

1. computation of the M -th guided wave group delay for each segment of the irregular waveguide (a segment is a part of the irregular waveguide with unique dispersive properties);
2. definition of the reference portion (RP) and irregular portion (IP) of the irregular waveguide;
3. compensation of the dispersion due to traveled distance within the reference portion (RP) of the waveguide;
4. compression of the dispersion due to the traveled distance in the irregular portion (IP) of the waveguide.

8.2.1 Group delay computation

In a dispersive signal, the group delay is a measure of the time delay of each frequency component due to the distance of propagation. For a given distance and a given guided wave (GW), such time delay depends on the mode group velocity curve. If the waveguide is composed by segments with different dispersive properties, i.e. if the waveguide is irregular, the group delay of such wave will depend on the different group velocity curves, one for each segment.

The group delay in an irregular waveguide can be numerically calculated as a summation of group delays that the wave ideally experiences propagating in a sequence of waveguides with progressively changing cross-sections. The group delay of the M -th guided wave propagating for a distance $D = \sum_{i=1}^N \Delta x_i$ in an irregular waveguide composed by N segments, can be computed as [80]:

$$\tau_D^M(f) = \sum_{i=1}^N \tau_{\Delta x_i}^M(f) \quad (8.1)$$

where $\tau_{\Delta x_i}^M$ is the group delay that the wave experiences in the i -th segment of length Δx_i . For instance, referring to the case of Figure 8.1, the group delay for the M -th wave traveling from point A to point D , neglecting the short tapered portions, reads:

$$\tau_{DAD}^M(f) = \tau_{DAB}^M(f) + \tau_{DBC}^M(f) + \tau_{DCD}^M(f)$$

For a waveguide segment with uniform cross-section, the group delay can be computed as:

$$\tau_D^M(f) = \frac{D}{c_g^M(f, \Omega)} \quad (8.2)$$

where $c_g^M(f, \Omega)$ is the M -th wave group velocity and f denotes the frequency. Eq. 8.2 holds also for curved segments with uniform cross-section and constant radius of curvature. In such a case, the distance of propagation can be computed as $D = R\Delta\phi$, where R is the mean radius and $\Delta\phi$ is the angle subtended by the first and last cross-section of the curved waveguide [79].

In the case of a tapered segment, with moderately and continuously varying cross-section, the group delay can be computed as [77]:

$$\tau_D^M(f) = \int_0^D \frac{dx}{c_g^M(f, \Omega(x))}$$

where $\Omega(x)$ denotes the cross-section at a coordinate x along the tapered portion axis. It must be remarked that, as well known, a guided wave crossing two segments with different cross-section and/or traveling along tapered waveguides may experience wave reflection and mode conversion. However, as long as the attention is not on the wave energy that is reflected or converted in different guided modes but on the behavior that a specific GW undergoes while traveling along an irregular waveguide, Eq. 8.1 is acceptable for the computation of its group delay [81], [82], [83].

Obviously, this requires that the GW considered in each segment for the computation of the group delay is generated by the incoming wave that has been considered in the previous segment of waveguide.

8.3 Reference and irregular portions of the waveguide

The proposed processing requires the subdivision of the irregular waveguide into two portions: the reference portion (RP), within which the defect is sought, and the irregular portion (IP) composed by the remaining segments of the waveguide. Segments belonging to the irregular portion (IP) are characterized by different dispersive characteristics with respect to the ones of the regular portion (RP).

The group delay for the whole irregular waveguide can thus be written as:

$$\tau_D^M(f) = \tau_{D_R}^M(f) + \tau_{D_I}^M(f)$$

where $\tau_{D_R}^M(f)$ is the group delay that the wave experiences while traveling in the reference portion (RP) of the waveguide, and $\tau_{D_I}^M(f)$ takes into account the group delay of the GW gained while traveling along all the remaining waveguide segments characterized by different dispersive properties with respect to that of the reference portion (RP).

8.4 Compensation of the reference portion (RP)

In this step, the received signal is compensated from the dispersion of the M -th GW gained traveling along the reference portion (RP) of the irregular waveguide. The reference portion is characterized by a uniform cross-section Ω_R .

Let's suppose that a pulse $s(t, x)$, starting at the origin of the coordinate system $x = 0$, as shown in Figure 8.3(a), is used to excite the dispersive M -th guided wave in the waveguide. The response at a distance $x = D_R$, indicated as $s(t, D_R)$, can be modeled in the frequency domain as:

$$\begin{aligned} S(f, D_R) &= S(f, 0) e^{-j2\pi \int_0^f \tau_{D_R}^M(\alpha) d\alpha} \\ &= S(f, 0) e^{-j2\pi D_R \int_0^f \frac{1}{c_g^M(\alpha, \Omega)} d\alpha} \end{aligned}$$

where $S(f, 0) = \mathbf{F}s(t, 0)$ is the Fourier Transform of the exciting pulse in the point of actuation, being \mathbf{F} the Fourier Transform operator, and $\tau_{D_R}^M(f)$ is the group delay

of the M -th wave component of frequency f . As shown in previous works [21] the Warped Frequency Transform (WFT) can be used to fully compensate the signal $s(t, D_R)$ from the dispersion due to the traveled distance. To such aim, the Frequency Warping operator \mathbf{W}_w must be designed using a so-called warping map $w(f)$ defined, through its functional inverse, as:

$$k \frac{dw^{-1}(f)}{df} = \frac{1}{c_g^M(f, \Omega)}$$

where K is a normalization parameter selected so that $w^{-1}(0.5) = w(0.5) = 0.5$ and $c_g^M(f, \Omega)$ is the group velocity of the GW which dispersive effect has to be compensated. Such operator, if applied to $s(t, D_R)$, yield to a warped signal $s_w(t, D_R) = \mathbf{W}_w \{s(t, D_R)\}$, whose frequency transform $S_w(f, D_R)$ read as:

$$S_w(f, D_R) = \mathbf{F}\mathbf{W}_w \{s(t, D_R)\} = \left[\sqrt{\dot{w}(f)} S(w(f), 0) \right] \cdot e^{-j2\pi f K D_R} \quad (8.3)$$

It's worth noting that since the phase term in Eq. 8.3 presents a linear dependence on frequencies, the inverse Fourier Transform of Eq. 8.3, i.e. $\mathbf{F}^{-1}(S_w(f, D_R))$, peaks in correspondence of $K D_R$ and so directly related to the distance traveled by the wave D_R .

8.5 Compensation of the irregular portion (IP)

When the M -th guided wave propagates along an irregular waveguide, the above procedure is not suitable to fully compensate its dispersion. In fact, when the distance traveled by the guided wave $D = D_R + D_I$ includes both reference (D_R) and irregular (D_I) portions of the waveguide, the response $s(t, x)$ in $x = D$ in the frequency domain reads:

$$S(f, D) = S(f, 0) e^{-j2\pi \int_0^f \tau_{D_R}^M(\alpha) d\alpha} \cdot e^{-j2\pi \int_0^f \tau_{D_I}^M(\alpha) d\alpha}$$

It follows that, by applying the warping operator and Fourier transforming the warped signal, as done in the previous subsection, the following distortion in the phase term is obtained:

$$S_w(f, D) = \mathbf{F}\mathbf{W}_w \{s(t, D)\} = \left[\sqrt{\dot{w}(f)} S(w(f), 0) \right] \cdot e^{-j2\pi f K D_R} \cdot e^{-j2\pi \int_0^f \hat{\tau}_{D_I}^M(\alpha) d\alpha} \quad (8.4)$$

where:

$$\hat{\tau}_{D_I}^M(f) = \frac{d \int_0^f \tau_{D_I}^M(w(f))w(f)}{df} = K\tau_{D_I}^M(w^{-1}(f)) \cdot c_g^M(w^{-1}(f), \Omega_R)$$

is the group delay for the M -th wave induced by the irregular portion (IP) of the waveguide. Such group delay can be easily removed from the warped signal in Eq. 8.4 by forcing an opposite term $-\hat{\tau}_{D_I}^M(f)$ in its phase spectrum:

$$\begin{aligned} S_w^{comp}(f, D) &= S_w(f, D)e^{j2\pi \int_0^f \hat{\tau}_{D_I}^M(\alpha)d\alpha} \\ &= \mathbf{FW}_w \{s(t, D)\} = \left[\sqrt{\dot{w}(f)}S(w(f), 0) \right] \cdot e^{-j2\pi fKD_R} \end{aligned}$$

By doing so, a dispersion compensation of the actuated pulse suitable to extract the distance traveled by the M -th GW in the regular portion (RP) of the irregular waveguide, i.e. D_R , is obtained. In fact, the signal $\mathbf{F}^{-1}(S_w^{comp})$ peaks in correspondence of KD_R . It follows that defects located at unknown positions in the regular portion (RP) of an irregular waveguide, as long as they reflect part of the M -th wave, can be located by the proposed approach.

8.6 Numerical Application

In the following, Finite Element (FEM) analyses are used to simulate guided waves propagating in irregular waveguides. In particular, considering the irregular waveguide shown in Figure 8.1, three different cases were generated by placing a notch, or some purposely designed boundary conditions, at different positions along the system. Next, the recorded time-transient response for each case, is exploited to validate the proposed processing.

FEM simulations have been used to predict how guided waves propagate in the irregular aluminum waveguide shown in Figure 8.1. Aluminum was modeled as a homogeneous linear elastic material with the following nominal properties: Young's modulus $E = 69$ GPa, Poisson's coefficient $\nu = 0.33$ and density $\rho = 2700$ kg/m³. The analyses were performed using the finite element based code Abaqus/Explicit. Three models were considered, one with a notch placed at $x = 300$ mm (#1), the second with a notch placed at $x = 250$ mm (#2), and one model in which the

wave reflector was simulated by imposing boundary condition (BC) preventing the displacement along the y -direction (#3) at some points of the waveguide. The notch was simulated as a cross-section reduction to the half of the pristine thickness and a width of 2 mm.

Guided waves were generated by imposing a displacement shaped in time as a sharp triangular pulse with total duration of 1×10^{-5} sec (see Figure 8.2) in order to excite waves up to 100 kHz.

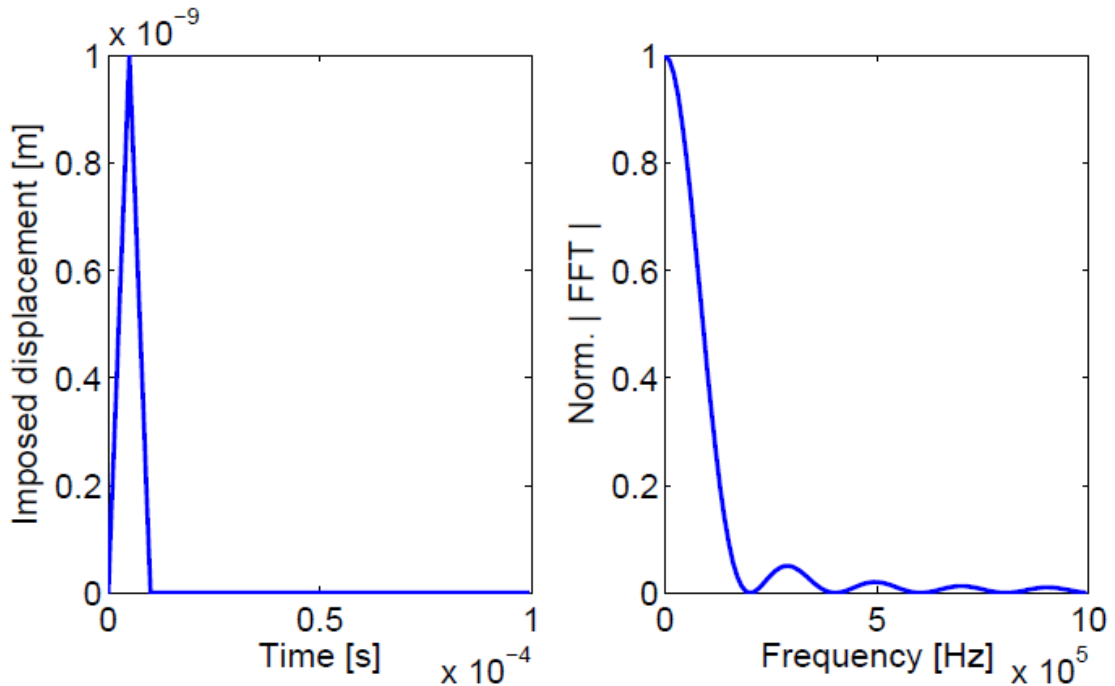


Figure 8.2: Time and frequency representation of the imposed displacement used to mainly excite the S_0 mode in the irregular waveguides.

The displacement was applied to the left edge of the plate in the x -direction, as indicated in Figure 8.3(b) by the red arrows, to mainly excite the S_0 mode. To ensure accuracy to the time-transient finite element simulations the plate domain was discretized with elements of maximum side length $L_{max} = 0.125$ mm and the time integration step was kept $\Delta t < 1e^{-8}$ s.

A plane strain condition on the propagation plane has been assumed by using linear four-node plate elements (CPE4R) and three-node plate elements (CPE3). The tri-

angular elements were used to properly mesh the short tapered portions. Under such assumption, the acquired signals (see Figure 8.3) are not affected by possible wave reflections generated by plate edges in z -direction and geometrical attenuation due to wave radiation in the z -direction is not considered.

Even if different from real applications, the assumed plane strain condition allows to the applied pulse to fully develop signal dispersion in the different considered segments, and thus is sufficient for the purposes of this work.

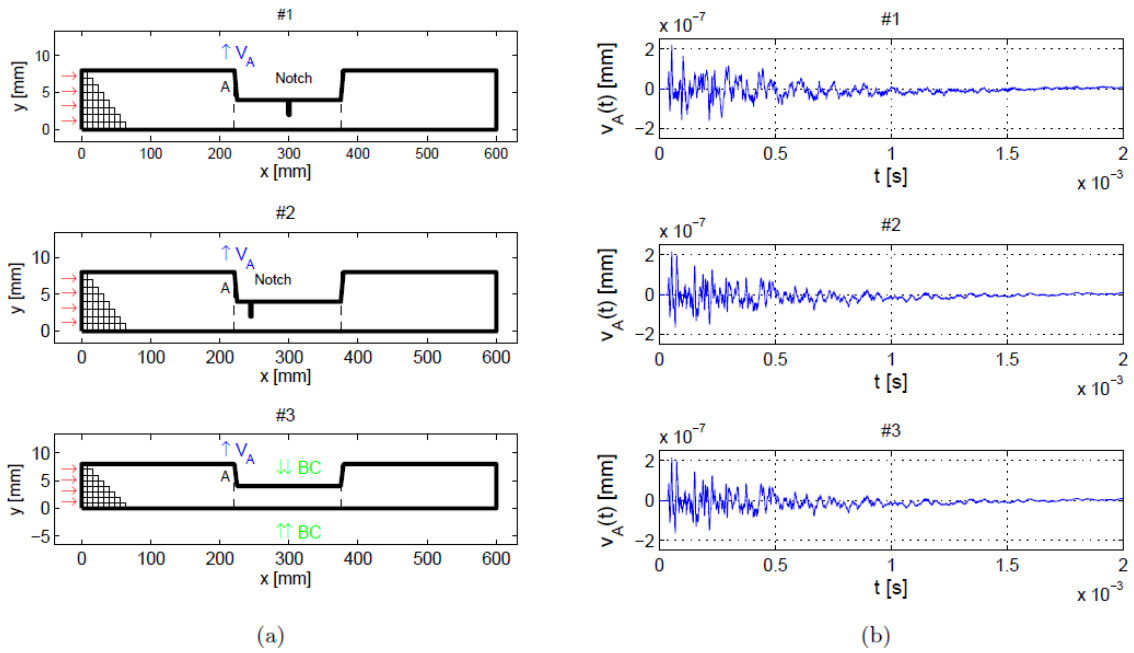


Figure 8.3: (a) Plane strain (#1 - #3) models used to compute the time-transient responses. (b) Time-transient responses $v_A(t)$ acquired at $x = 201$ mm for the three cases (#1 - #3).

In order to avoid unwanted wave reflections from the right edge of the waveguide, absorbing layers with increasing damping (ALID) were used. The ALID had the same material properties of the aluminum plate and only varied the mass proportional Rayleigh damping.

In particular, five plate regions with thickness of 8 mm, and exponentially decreasing lengths (42 mm, 33 mm, 27 mm, 21 mm and 18 mm, for a total length of 141 mm, i.e. the 23.5% of the total plate length) were added in sequence to the right edge of

the plate.

Damping was exponentially intensified along the five ALIDs increasing the Rayleigh mass proportional damping ($\mathbf{C} = \beta\mathbf{K} + \alpha\mathbf{M}$, where \mathbf{C} , \mathbf{K} and \mathbf{M} are the global damping, stiffness and mass matrices, respectively) assuming a parameter α equal to $[0.3866, 0.8587, 1.4354, 2.1397, 3.0000] \times 10^5 [t^{-1}]$.

In the end, each finite element model counted 390368 CPE4R elements and 64 CPE3 elements.

At first an analysis was conducted on a pristine model in order to analyse the behaviour of guided waves at the abrupt thickness change. Snapshots of guided waves propagation are shown in Figure 8.4 in terms of Von Mises stress.

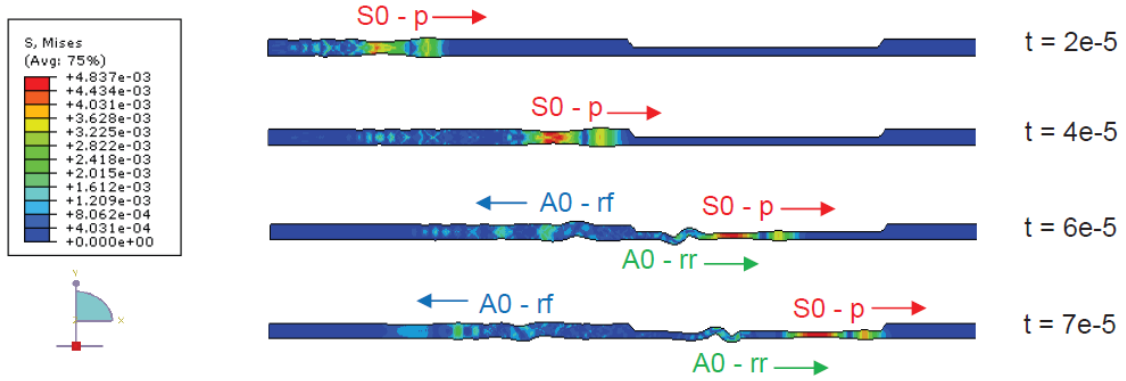


Figure 8.4: Guided wave propagation in the pristine irregular plate. Snapshots of the Von Mises stress at $20 \mu\text{s}$, $40 \mu\text{s}$, $60 \mu\text{s}$ and $70 \mu\text{s}$. Deformation scale factor was assumed equal to $1e^7$.

The figure shows clearly the S_0 mode within the first $40 \mu\text{s}$ propagating forward in the waveguide ($S_0\text{-p}$).

At the thickness change, a significant part of the energy is converted into an A_0 mode, part of which is reflected backward in the thick portion of the waveguide ($A_0\text{-rf}$) and part refracted forward in the thin portion of the waveguide ($A_0\text{-rr}$). Therefore, even if S_0 mode was mainly excited, a significant A_0 mode is expected in the thin portion of the irregular waveguide.

A similar mode conversion can be observed in a damaged waveguide at the notch location, as depicted in Figure 8.5 for the case #2, for instance.

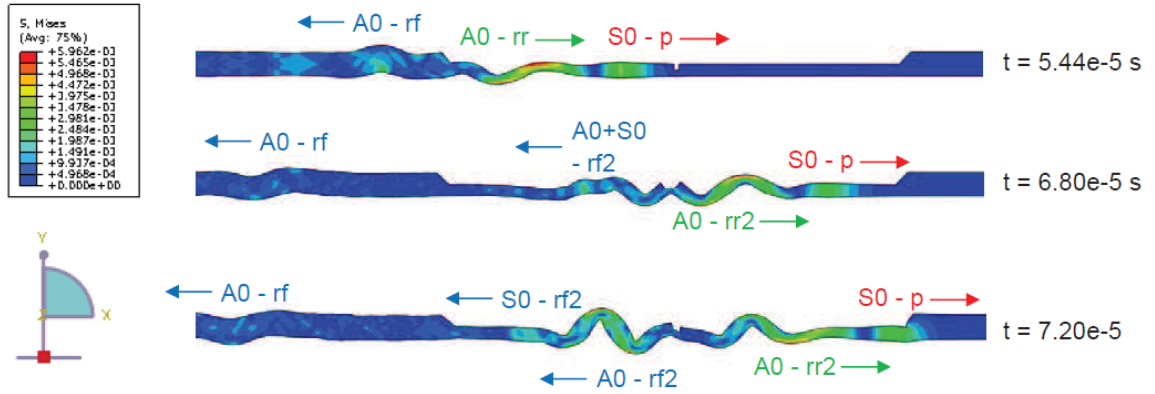


Figure 8.5: Snapshots of the Von Mises stress in proximity of the defect taken at $54.4 \mu\text{s}$, $63 \mu\text{s}$, $72 \mu\text{s}$ for the model #2. Deformation scale factor was assumed equal to $2e^7$.

Models #1 - #3 were analysed. For each case the out-of-plane displacement on the top of the plate $v_A(t)$ was recorded at position $x = 201 \text{ mm}$ (point A in Figure 8.3). The acquired time transient responses $v_A(t)$ for the three models are presented in Figure 8.3(b). As can be noted, the presence and position of the notch, as well as of the imposed boundary conditions (BC in model #3) cannot be inferred from the time-waveforms.

In order to apply the proposed processing on the recorded time-waveforms, first the WFT operator must be defined. In particular, suitable guide modes propagating in the reference (RP) and irregular (IP) portions of the waveguide must be selected in order to define proper warping maps $w(f)$, and thus the proper warping operators \mathbf{W}_w to compensate the signal.

To such aim, understanding the guided wave propagation phenomenon, and in particular those modes capable to propagate in irregular waveguides, is fundamental to the success of the proposed strategy.

- case #1: the thin plate (4 mm-thick) was assumed as reference portion (RP) of the irregular waveguide because the notch was placed in it; the WFT operator to compensate for the dispersion due to the RP was designed on the group

velocity curve of a hybrid $A_0 - S_0$ mode, computed as:

$$c_g^{A_0-S_0}(t) = 2 \frac{c_g^{A_0}(f) \cdot c_g^{S_0}(f)}{c_g^{A_0}(f) + c_g^{S_0}(f)}$$

while the remaining dispersion due to the traveled distance on the IP, i.e. the 8 mm plate, was compensated by warping the signal using a WFT operator built on the S_0 group velocity for the 8 mm plate.

- case #2: as for case #1.
- case #3: the thin plate (4 mm-thick) was assumed as reference portion (RP) since the wave reflector, i.e., the imposed BC, was placed in it; signal dispersion related to the reference portion was compensated by using a warped operator built on group velocity of the A_0 mode in the thin plate, while the remaining dispersion due to IP, i.e. the 8 mm plate, was compensated using the group velocity information of the S_0 .

Next, the two processing phases are applied: first the designed warped operators are applied to remove from the signals the group delay dependency on distance in $\tau_{D_R}^M(f)$, i.e., compensating the dispersion due to traveled distance in the regular portions of the waveguides D_R ; next the additional group delay introduced by the irregular part of the waveguide $\tau_{D_I}^M(f)$ is removed by forcing a proper $-\tau_{D_I}^M(f)$.

In this last step, the group velocity dispersion information of the S_0 mode propagating in the 8 mm thick plate has been used to build the warping operators, as detailed above. The effect of such processing leads to the new signals $S_w^{comp}(f, D)$.

8.7 Results

The spectra of the time-transient waveforms represented in Figure 8.3(b) for the cases #1, #2 and #3 are shown in Figure 8.6 at position (a), (c) and (e), respectively.

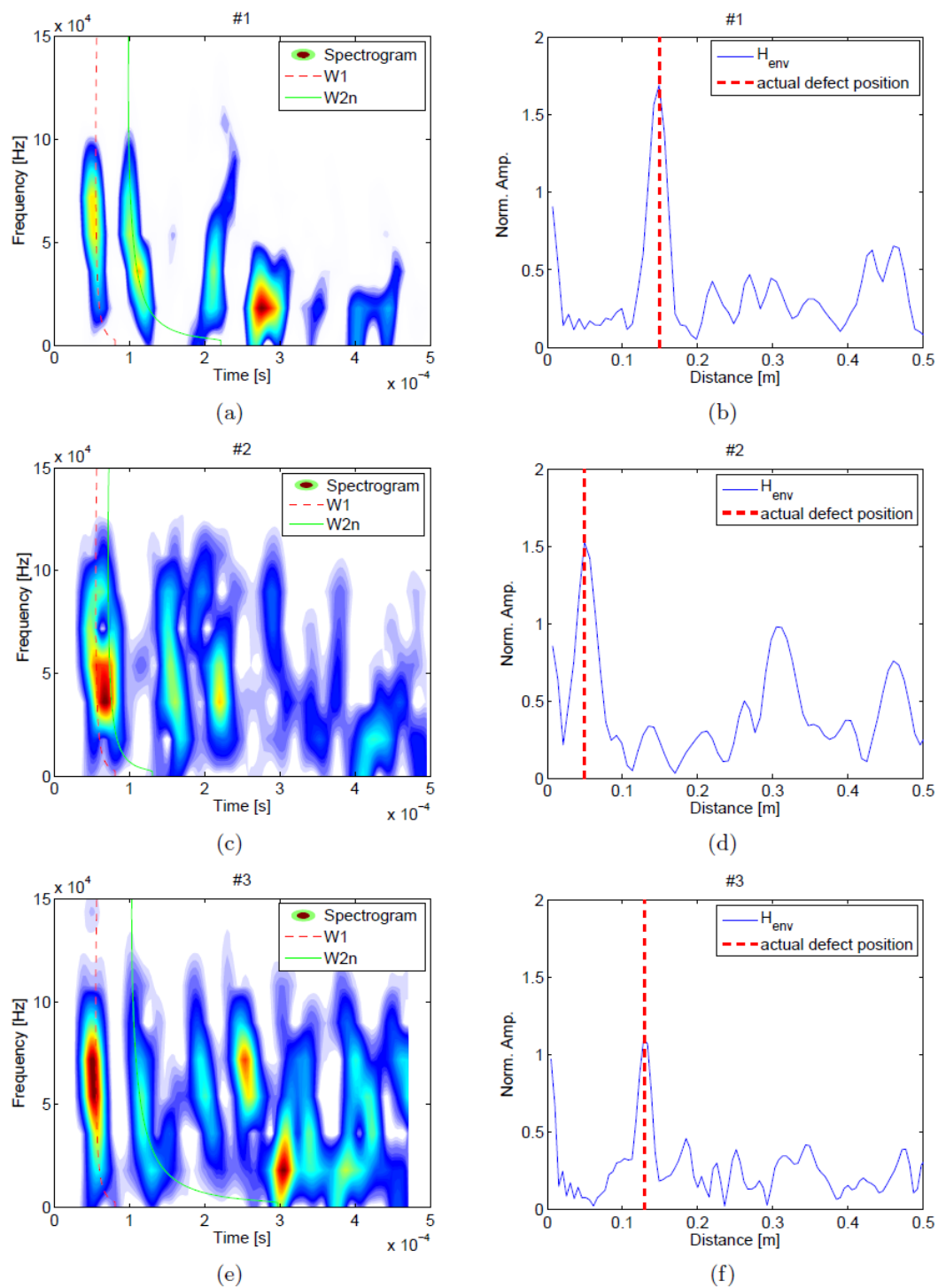


Figure 8.6: (a-c-e) Spectra of $v_A(t)$ for the three examined cases. S_0 group delay curves for the incipient W1 and the notch/BC reflection W2n paths have been superimposed. (b-d-f) Normalized H_{env} of the compensated signals. The vertical red lines mark the actual defect position.

On the spectra, the group delay curves computed by using the proposed procedure for the first arrival of S_0 (W1) as well as for the scattered S_0 wave from the notch/BC (W2n), have been over imposed. As it can be seen, the predicted group delay curves for the W2n wave match quite well with the lobes of energy within the spectra. This confirm the reliability of the group delay computation in irregular waveguides. On the right side of the spectra, Figure 8.6(b-d-f), the envelopes H_{env} of the inverse Fourier Transforms $\mathbf{F}^{-1}(S_w^{comp}(f, D))$ after normalization are represented.

Envelopes are computed as the absolute value of the Hilbert Transform, i.e.

$$H_{env} = \|H(\mathbf{F}^{-1}(S_w^{comp}(f, D)))\|$$

where H denotes the Hilbert operator. It is worth noticing that the energy of the processed signals is now concentrated near the actual distance traveled by the waves in the reference portion of the waveguide. In particular, the signals peak at 150 mm for cases #1 and #3, as the notch/BC location is the same, and at 50 mm for the case #2, i.e. at exactly twice the distances from the end of the tapered portion.

8.8 Discussion

In this Chapter, a signal processing strategy aimed at locating defects in irregular waveguides is proposed. The method is based on a two-step procedure applied to the acquired echo signals. The implemented signal processing directly reveals the distance traveled by the waves, thus overcoming the difficulties associated with wave arrival time detection in dispersive media. In particular, by exploiting the dispersion compensation properties of the WFT, waveforms characterized by a unique time-frequency pattern are obtained. The remaining time-frequency modulation is compressed in a subsequent processing step. This step is based on the estimation of the group delay in tapered, curved or irregular portions of the waveguide. The reported spectrograms showed that the adopted method has an excellent accuracy in group delay calculation. Such accuracy can be conveniently exploited for wave distance of propagation estimation, as shown by several numerical examples. Thanks to its unique potential the developed tool could lead to a new class of procedures to locate defects in waveguides.

Chapter 9

Warped-Wigner-Hough Transformation of Lamb Waves for Automatic Defect Detection

There is only one good, the knowledge, only one
evil, the ignorance.

Socrate

9.1 Introduction

To improve the defect detectability of Lamb wave inspection systems, application of non-linear signal processing was investigated. The approach is based on a Warped Frequency Transform (WFT) to compensate the dispersive behavior of ultrasonic guided waves, followed by a Wigner-Ville time-frequency analysis and the Hough Transform to further improve localization accuracy. As a result, an automatic detection procedure to locate defect-induced reflections was demonstrated and successfully tested by analyzing numerically simulated Lamb waves propagating in an aluminum plate. The proposed method is suitable for defect detection and can be easily implemented for real application to structural health monitoring.

9.2 The Warped Frequency Transform (WFT)

We recall that warping can be used to compensate dispersion in GWs by dening the warping map through the following relationship (see Chapter 3):

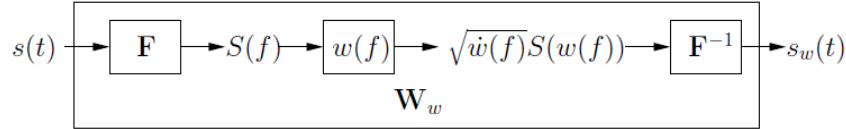


Figure 9.1: Computational flow of the Frequency Warping operator \mathbf{W}_w . \mathbf{F} and \mathbf{F}^{-1} are the direct and inverse Fourier Transform operators, respectively, while $w(f)$ and $\dot{w}(f)$ are the warping map and its first derivative.

9.3 The Wigner-Hough Transform (WHT)

After applying the WFT to properly excited GWs, *defect detection can be performed automatically* by considering a TFR of the warped signal. In fact, defect-induced reflections appear in the compensated waveform as well-localized spikes, thus producing vertical maxima lines in the TF plane, whose (warped) time location can be directly converted to the defect position. A simple TFR of $s_w(t)$ is provided by the Short Time Fourier Transform (STFT); however, energy distributions such as the Wigner-Ville Distribution (WVD) defined as

$$W_{s_w}(t, f) = \int_{-\infty}^{+\infty} s_w(t + \frac{\tau}{2}) s_w^*(t - \frac{\tau}{2}) \cdot e^{-j2\pi f\tau} d\tau$$

can be used to further improve localization accuracy since there are no predetermined window functions and loss of resolution. Automatic detection of the desired lines of energy maxima can be performed by applying the Hough Transform (HT) [84] to the WVD, resulting in the so-called Wigner-Hough Transform (WHT) [85].

Generally speaking, the HT is an image processing tool that performs an integration on all the possible lines of a given image I and maps the value of each integral to a plane (ρ, θ) corresponding to the polar parametrization of lines. High-intensity pixels concentrated on straight lines on I will therefore produce peaks in the (ρ, θ) domain.

In the Wigner-Hough Transform, the input image corresponds to the WVD of the considered signal and the presence of interference terms between different spectral components of the analyzed waveform induced by the WVD is largely compensated through the integration performed by the Hough operator, as these undesired components appear as alternating positive peaks and negative valleys in the TF plane.

9.4 Warping Map Design and Wave Simulation

As a case study, we exploit the described tools to locate defects in an aluminum plate where Lamb waves are excited. The plate thickness is $h = 2.54$ mm.

The group slowness $\frac{1}{c_g(f)}$ used to design the warping map is first computed by performing a Semi-Analytical Finite Element (SAFE) simulation [86], whose results are shown in Figure 9.2.

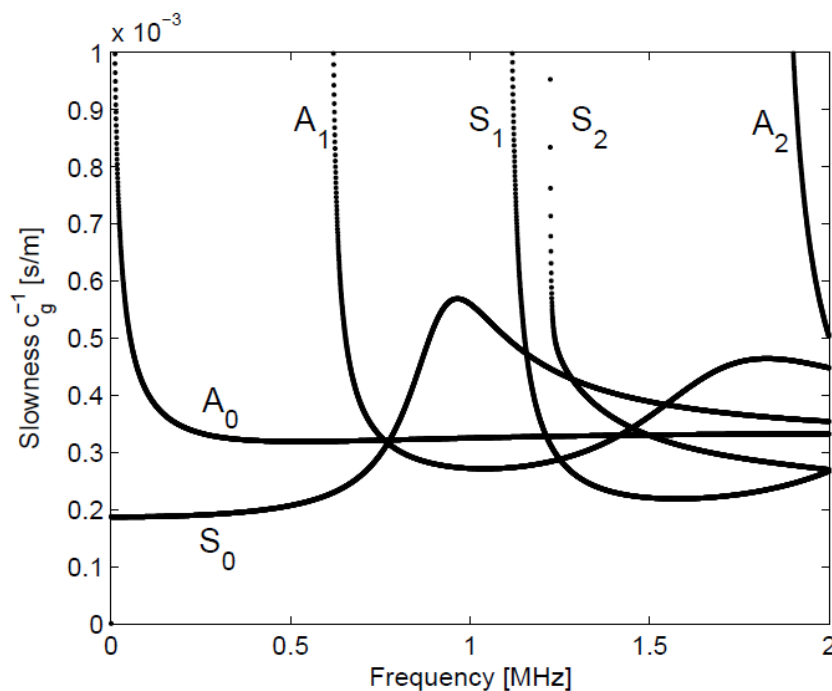


Figure 9.2: Slowness dispersion curves for the Lamb waves propagating in a 2.54 mm-thick aluminum plate

For acoustic emission below 500 kHz, only the two fundamental waves A_0 and S_0 can propagate through the plate. Therefore, the slowness curves of these two modes have been used to build $w(f)$.

As a second step, time waveforms related to Lamb waves propagating in the aluminum plate were obtained numerically by means of dedicated Finite Element (FEM) simulations. Thanks to the Lamb problem symmetry, a x - y plane strain condition was assumed, as shown in Figure 9.3.

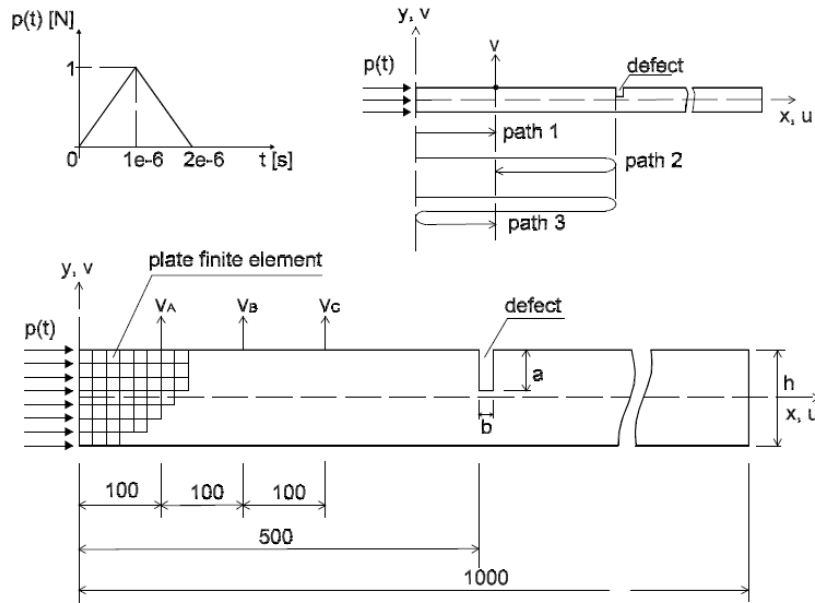


Figure 9.3: Schematic representation of the damaged aluminum plate used in the time-transient FEM simulations (plate dimensions are in mm)

A notch of width $b = 0.25$ mm and depth a , such that $a = h = 0.3$, placed on the top side at the center of the plate ($x = 500$ mm), was considered. Lamb waves were excited by applying an impulsive force $p(t)$ to the left edge of the plate towards the x -direction: this mainly stimulates the symmetric S_0 mode.

The force was shaped in time as a triangular window with a total duration of $2 \mu s$ (see the top-left of Figure 9.3) in order to excite consistent Lamb waves up to 500 kHz. Time-dependent out-of-plane displacements $v(t)$ were recorded at three points on the top side of the plate ($y = h = 2$), namely A , B and C , respectively located at $x_A = 100$ mm, $x_B = 200$ mm and $x_C = 300$ mm.

The recorded waveforms are shown in Figure 9.4.

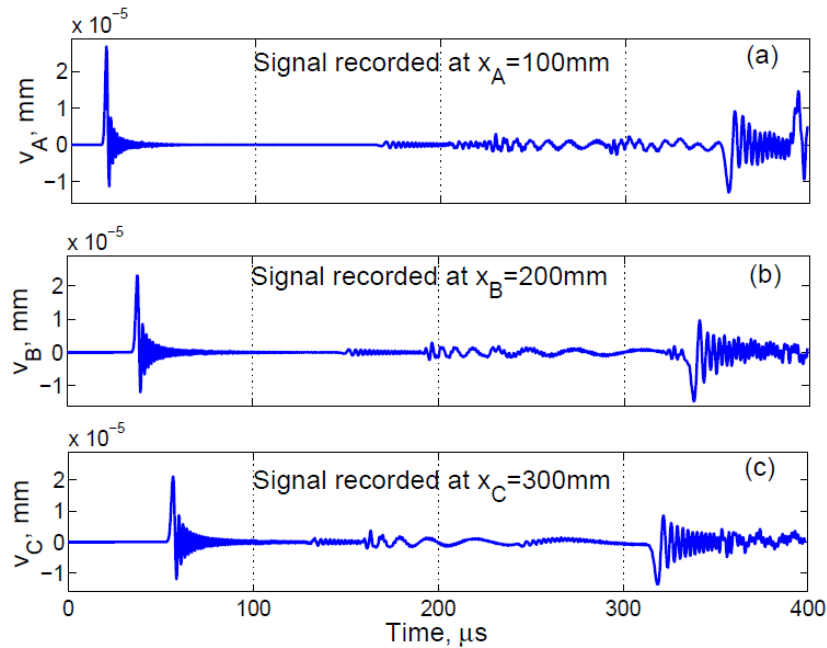


Figure 9.4: Time-dependent out-of-plane displacements recorded at three different positions on the plate

The leftmost peak in each signal corresponds to the passage of the excited S_0 mode through the recording position, while oscillations in the central part of the waveforms are due to defect-induced reflections, which also excite the slower A_0 mode. Spreading of these oscillations clearly reveals the effect of dispersion.

Finally, further reflections from the plate edges are responsible for the complicated behavior observed in the rightmost part of the signals.

9.5 Defect Detection

The warping map was designed to achieve compensation for the S_0 mode as this was the originally excited component. Results of this procedure are plotted in Figure 9.5 directly as a function of the traveled distance.

The path followed by the compensated mode S_0 can be easily tracked by observing local peaks in these signals, as illustrated in 9.5(c), and location of the defect can be inferred by the position of reflected peaks.

However, this information can be hardly retrieved from the warped waveforms themselves in general, due to interference from the A_0 mode and possible acquisition noise in real-world applications.

As shown in Section 9.3, a more robust and automated approach involves detection of vertical maxima lines in a space-frequency representation of the warped signals. Before performing such transformation, a pre-processing step is often required to emphasize the amplitude of reflection-induced peaks.

As a test case, an equalization algorithm consisting in dividing the signal by local averages of its samples was applied to waveform v_{wC} in Figure 9.5(c).

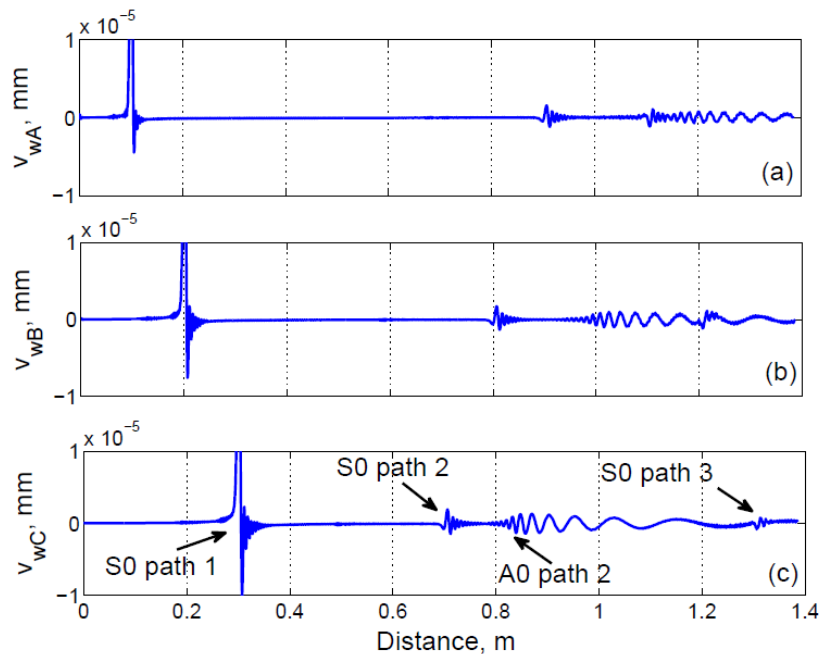


Figure 9.5: Results of the warping procedure applied to waveforms in Figure 9.4.

The equalized signal and its Wigner-Ville distribution are displayed in Figure 9.6(a) and (b), respectively.

The adopted equalization approach effectively enhances the amplitude of relevant peaks, while attenuating the A_0 mode. Well-localized vertical maxima lines corresponding to “S0 path 1” and “S0 path 2” are clearly visible in Figure 9.6(b), while the non-compensated A_0 mode results in curved features.

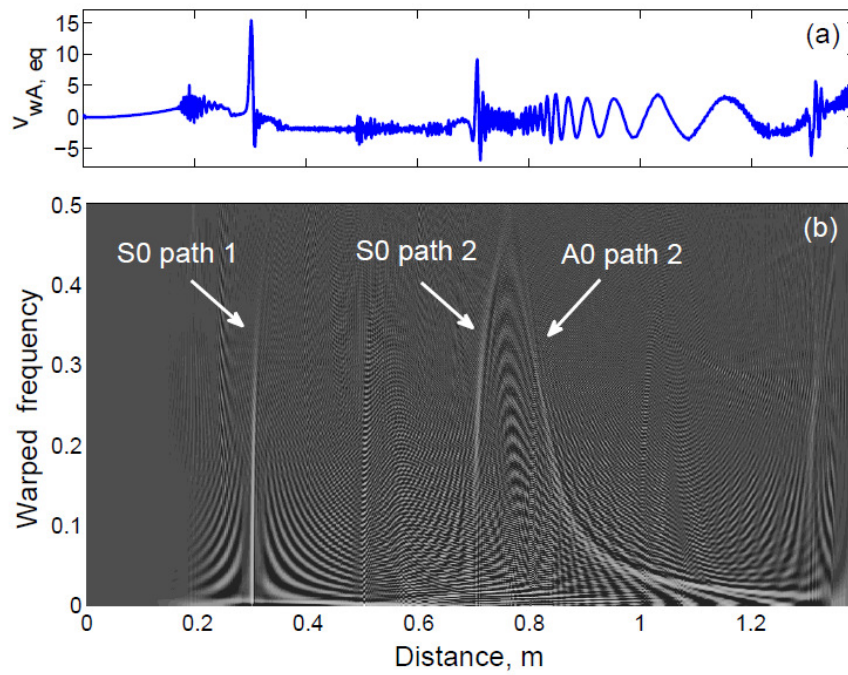


Figure 9.6: (a) Result of the equalization procedure applied to signal v_{wC} in Figure 9.5(c). (b) Wigner-Ville distribution.

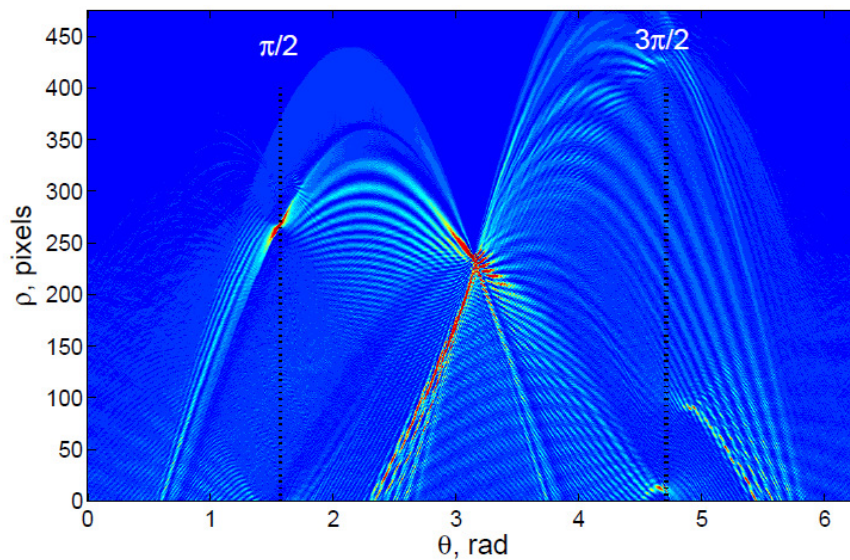


Figure 9.7: Wigner-Hough Transform of the equalized warped signal in Figure 9.6(a). Peaks at $\theta = \{\frac{\pi}{2}, \frac{3\pi}{2}\}$ correspond to vertical lines in Figure 9.6(b); ρ coordinates provide the distance in pixels from the center of the analyzed image.

This procedure may encounter limitations in the presence of noisy signals, as spurious components might be erroneously amplified. However, several alternatives are possible, including more sophisticated preprocessing algorithms under investigation and the use of acquisition systems able to attenuate the A_0 component.

Thus, the HT appears as a suitable tool to isolate S_0 components and locate defect-induced reflections, as can be seen from Figure 9.7, where the WHT of the equalized warped signal is displayed.

Local maxima at $\theta = \frac{\pi}{2}$ and $\theta = \frac{3\pi}{2}$ can be easily detected and the corresponding ρ coordinates provide the distance traveled by the incident and reflected S_0 waveform components, respectively. By applying this procedure, the defect responsible for reflections was located at $x = 502$ mm. The detection algorithm was also tested on signals recorded at $x = 100$ mm and $x = 200$ mm (see Figure 9.4) and errors w.r.t the actual defect position ($x = 500$ mm) were found to be below 6 mm, which roughly corresponds to the minimum wavelength associated to the excited Lamb waves. Similar good results were found by considering different defect depths.

9.6 Discussion

This Chapter described the application of a Warped Wigner-Ville analysis to improve defect detectability of conventional Lamb wave inspection system. The adopted equalization approach effectively enhances the amplitude of relevant peaks in the warped WVD, so local maxima can be detected and the information about the distance traveled by the incident and reflected investigated mode can be easily recognized.

The presence of interference terms is largely compensated through the integration performed by the Hough operator, making the proposed method a suitable tool to separate overlapping Lamb waves and locate defect-induced reflections.

Chapter 10

Compressive Sensing

The willingness to take risks is our grasp of faith.

George Edward Woodberry

Compressive Sensing (CS) has emerged as a potentially viable technique for the efficient compression and analysis of high-resolution signals that have a sparse representation in a fixed basis.

In this Chapter we have developed a CS approach for ultrasonic signal decomposition suitable to achieve high performance in Lamb waves based defects detection procedures. The concept of sparse representations is also at the basis of the so called Compressive Sensing (CS) theory [87] which offers an intriguing alternative with respect to the classical process of acquiring signals according to the Shannon-Nyquist paradigm. CS theory proves that a signal which is sparse in a given representation can be compressed directly at the sampling stage. Then, the signal can be reconstructed by exploiting convex programming or greedy methods [88].

CS methods are becoming popular for ultrasonic data reduction [89], [90], [91] and their usage can be extremely useful even in signal decomposition and analysis [92].

In this Chapter a CS based approach is used to precisely extract the distances traveled by Lamb waves from the acquired signals while reducing consistently the dimension of the analysed data. To achieve this goal, the proposed CS strategy exploits the Warped Frequency Transform (WFT) as a mean to project the acquired data in a

sparsifying representation basis [73]. A signal processed by the WFT, i.e. a warped signal, is dispersion-compensated, and can be modeled as a *pulse stream*, that is the signal originated by the convolution of the system *Impulse Response* and the *Reflectivity Function* [93]. In this context, the impulse response models the actuating and sensing apparatus whereas the reflectivity function conveys the information about the distances of the actuator and the scatterers (damages or system edge reflections) from the sensor.

It has been shown in [94] and [95] how signals which can be represented by convolutional models can be efficiently deconvolved by employing CS algorithms. In this Thesis it will be shown how the combined effect of the WFT and a *model-based* CS algorithm allows to achieve a high-precision in the estimation of the distances traveled by Lamb waves.

The Chapter is organized as follows: a brief review of the mathematical theory of compressive sensing and the model-based framework for CS recovery is described in Section 10.3. Section 10.4 introduces the Warped Frequency Transform and the proposed algorithm to recover the reflectivity function from the acquired signal.

10.1 Review of Compressive Sensing

Compressive sensing theory states that with high probability we can reconstruct a signal from a relatively small number of measurements when the signal is sparse in a known basis. We say that a signal x is (K, δ) -sparse if at most K entries of x are greater than a small positive value δ . We say x is K -sparse if δ is zero.

An $M \times N$ measurement matrix Φ compresses a length- N input signal x to y , the M measurements from x . In other words, $y = \Phi x$.

We decode x by solving l_1 -minimization problem using linear programming:

$$\min \|x\|_{l_1} \quad \text{subject to } y = \Phi x \quad (10.1)$$

The restricted isometry property (RIP) of Φ ensures the existence of an unique l_1 -min solution for the reconstructed signal and allows a corresponding error bound.

A matrix W satisfies the RIP with parameters (ϵ, K) if for all x such that $x \neq 0$ and $\|x\|_{l_1} \leq K$ we have

$$\left| \frac{\|Wx\|_{l_2}^2}{\|x\|_{l_2}^2} - 1 \right| \leq \epsilon$$

It has been shown that with high probability an $M \times N$ measurement matrix Φ with randomly chosen entries satisfies the $(\epsilon, 2K)$ -RIP with a small ϵ if $M \geq cK \log(N/K)$. Suppose that we are given compressed measurements $y = \Phi x$, where Φ is an $M \times N$ measurement matrix that satisfies $(\epsilon, 2K)$ -RIP. Let x_K be the vector that equals x on the K largest elements of x and equals 0 otherwise. Candes et al. and Shalev-Schwartz have shown that the reconstructed signal x^* based on l_1 -minimization satisfies

$$\|x^* - x\|_{l_2} < 2(1 - \sqrt{2}\epsilon)^{-1} K^{-1/2} \|x_K - x\|_{l_1}$$

This implies that x^* is a good approximation of x when x is (K, δ) -sparse for some small δ . For an orthonormal basis Ψ , the matrix product $(\Phi\Psi)$ can also be shown to satisfy $(\epsilon, 2K)$ -RIP with high probability. If we know $x = \Psi s$ for some Ψ where s is sparse, we will be able to decode s by l_1 -minimization:

$$\min \|s\|_{l_1} \quad \text{subject to } y = (\Phi\Psi)s$$

After we obtain s , we can recover x from $x = \Psi s$. Joint decoding is an extension to the standard decoding described above. It resembles the use of overcomplete representations in signal processing.

10.2 Analog Compressive Sampling Acquisition

Suppose our analog signal has finite information rate K i.e., the signal can be represented using K parameters per unit time in some continuous basis. More concretely, let the analog signal $x(t)$ be composed of a discrete, finite number of weighted continuous basis or dictionary components

$$x[i] = \sum_{n=1}^N \alpha_n \psi_n[i] \tag{10.2}$$

with $t, \alpha_n \in \mathbb{R}$. In cases where there are a small number of nonzero entries in α , we may again say that the signal x is sparse. Although each of the dictionary elements ψ_n may have high bandwidth, the signal itself has few degrees of freedom. Our signal acquisition system consists of three main components; demodulation, filtering, and uniform sampling.

The CS acquisition scheme is shown in Figure 10.1

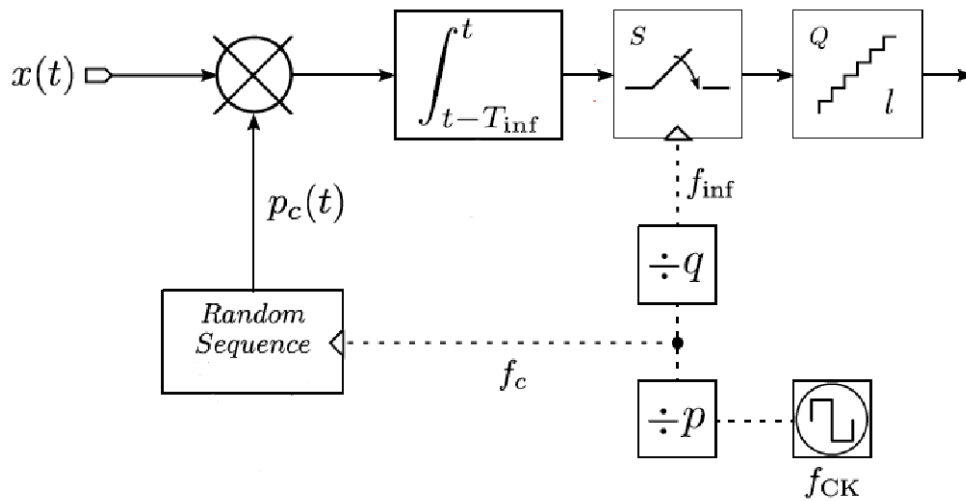


Figure 10.1: Compressed Sensing acquisition scheme: random modulation pre-integration

As seen in Figure 10.1, the signal is modulated by a pseudo-random maximal-length PN sequence of ± 1 . This chipping sequence $p_c(t)$ must alternate between values at or faster than the Nyquist frequency of the input signal. The purpose of the demodulation is to spread the frequency content of the signal so that it is not destroyed by the second stage of the system, a low-pass filter with impulse response $h(t)$. Finally, the signal is sampled at rate M using a traditional ADC. Although our system involves the sampling of continuous-time signals, the discrete measurement vector y can be characterized as a linear transformation of the discrete coefficient vector α . As in the discrete CS framework, we can express this transformation as an $M \times N$ matrix $\Theta = \Phi\Psi$ that combines two operators: Ψ , which maps the discrete coefficient vector α to an analog signal x , and Φ , which maps the analog signal x to the discrete set of measurements y . To find the matrix Θ we start by looking at the output $y[m]$, which

is a result of convolution and demodulation followed by sampling at rate M . Since our analog input signal in Eq. 10.2 is composed of a finite and discrete number of components of Ψ , we can write

$$y[m] = \sum_{n=1}^N \alpha_n \int_{-\infty}^{+\infty} \psi_n(\tau) p_c(\tau) h(mM - \tau) d\tau$$

It is now clear that an expression for each element $\theta_{m,n} \in \Theta$ can be separated out for row m and column n

$$\theta_{m,n} \int_{-\infty}^{+\infty} \psi_n(\tau) p_c(\tau) h(mM - \tau) d\tau$$

10.3 Model-based Compressive Sensing

The information content of an ultrasonic signal $s(t)$ can be represented by a N -dimensional vector of real numbers s , sampled according to the Shannon-Nyquist theory. In the CS approach, s is compressed in a vector y of $M \ll N$ linear measurements, i.e. vector components, by using an $M \times N$ sensing matrix Φ , such that

$$y = \Phi s$$

The fact that $M \ll N$ produces a considerable data reduction but also implies that the sensing matrix Φ is rank-deficient, i.e. for a particular signal s , an infinite number of signals s_x can yield the same measurements $y = \Phi s = \Phi s_x$. It follows that in general s cannot be uniquely reconstructed from the M linear measurements of y . However, if the signal s is K -sparse in a given representation, the matrix Φ can be designed to achieve the full recovery of s from the measurement vector y [87] with a considerable reduction in the number of measurements

$$M = O\left(K \log\left(\frac{N}{K}\right)\right)$$

To clarify the notion of K -sparsity, let us consider a given representation basis $\{\psi_i\}_{i=1}^N$ for \mathbb{R}^N . Arranging the ψ_i as columns into the $N \times N$ matrix Ψ , we can write succinctly that $s = \Psi \alpha$, with $\alpha \in \mathbb{R}^N$ being the representation coefficients. We say that a signal

s is K -sparse in Ψ if there exists a vector $\alpha_K \in \mathbb{R}^N$ with only $K \ll N$ nonzero entries such that

$$s = \Psi \alpha_K$$

The indices corresponding to the K nonzero elements of the signal α_K define a vector σ called *support* of α_K and the set of all K -sparse signals in \mathbb{R}^N is denoted by \sum_K . By a geometrical point of view, the set \sum_K can be modeled as an union of $\binom{N}{K}$ subspaces of \mathbb{R}^N , where $\binom{N}{K}$ denotes the binomial coefficient indexed by N and K .

The approximation procedure to recover the K -sparse signal α_K from the measurement vector may not be computationally feasible if all the $\binom{N}{K}$ possible supports are admissible. However, in many practical cases, just a small number of support configurations are physically meaningful. In these cases a *structured sparse model* \mathcal{M}_K can be defined as the union of m_K canonical K -dimensional subspaces of \mathbb{R}^N with $m_K < \binom{N}{K}$. If $\Omega = \{\Omega_1, \dots, \Omega_{m_K}\}$ denote the set of admissible supports, the model \mathcal{M}_K is defined as:

$$\mathcal{M}_K = \{\alpha_K : \text{supp}(\alpha_K) \in \Omega\} \quad (10.3)$$

10.3.1 Convolutional Models for Pulse Streams

Among the structured sparse models presented in literature, the *convolutional model* detailed in [95] is suited to represent pulse stream signals, as those acquired in ultrasonic applications.

Let $\mathcal{M}_S \subset \mathbb{R}^N$ be a union of S -dimensional canonical subspaces. Similarly, let $\mathcal{M}_F \subset \mathbb{R}^N$ be a union of F -dimensional canonical subspaces. A convolutional model is formally defined as the set

$$\mathcal{M}_{S,F}^s \doteq \{s \in \mathbb{R}^N : s = (x * h) \mid x \in \mathcal{M}_S, h \in \mathcal{M}_F\} \quad (10.4)$$

where $*$ denotes the circular convolution operator, h is the impulse response of the ultrasonic apparatus, and x is the reflectivity function of the inspected component. If $S \cdot F = K$, then the set $\mathcal{M}_{S,F}^z$ is a small subset of \sum_K . Such dimensionality reduction is very beneficial, as the number of measurements M necessary to recover

the signal s is logarithmic in the number of subspaces in the model (see [94]). A further reduction in the number of measurements can be achieved in the special case of streams of *disjoint pulses*, that is situations in which the ultrasonic impulse response h is concentrated in F contiguously located coefficients, while x is constituted by S sparse spikes separated at least by Δ locations, with $\Delta > F$. If \mathcal{M}_S^Δ is the structured sparse model for the spike streams x , and \mathcal{M}_F^C is the subspace of \mathcal{M}_F of the concentrated impulse responses, the disjoint convolutional model is defined as:

$$\mathcal{M}_{S,F,\Delta}^s \doteq \{s \in \mathbb{R}^N : s = (x * h) \mid x \in \mathcal{M}_S^\Delta, h \in \mathcal{M}_F^C\} \quad (10.5)$$

The disjoint convolutional model could represent many practical situations related to inspections with bulk ultrasonic waves, but it cannot capture a relevant phenomenon which affects guided wave (GW) propagation: the effect of dispersion (i.e. frequency-dependent propagation speed). In fact, dispersion causes the impulse response h to be shift-variant.

However, if the dependency of h on the wave propagation distance is predictable, it is possible to project the acquired signals in a representation basis in which the dispersion effect is compensated, allowing thus the use of disjoint convolutional models. In this work, such task is achieved by computing the dispersion curves for the plate-like structure of interest first, and then by exploiting such curves to design a WFT capable to project the acquired signals in the new basis, as will be shown in the next section.

In the novel representation domain, suitable model-based CS recovering algorithms can be adopted to recover the original signal from the measurement vector and to extract the relevant information about reflectors.

10.4 Recovery of dispersive pulse streams

10.4.1 Frequency Warped Convolutional Models

A sparse representation for guided wave signals can be obtained by using Warping Frequency Transforms (WFTs). These operators deform the frequency axis with a

proper warping map $w(f)$ [27]. In particular, given a generic signal s whose continuous Fourier transform is $\mathbb{F}s$, the continuous warping operator \mathbf{W} is defined as

$$(\mathbb{F}\mathbf{W}s)(f) = \sqrt{\dot{w}(f)}(\mathbb{F}s)(w(f)) \quad (10.6)$$

where $s_w = \mathbf{W}s$ is the so-called warped signal. \mathbf{W} is a unitary operator and the inverse transformation can be computed through its adjoint operator \mathbf{W}^\dagger .

A fast computation of the discrete warping operator and its inverse is achieved by means of FFT-based algorithms [96].

In order to use the WFT for compensating Lamb waves signals from the dispersion of a particular guided mode, $w(f)$ can be defined through its functional inverse, as:

$$K \frac{dw^{-1}(f)}{df} = \frac{1}{c_g(f)} \quad (10.7)$$

where $c_g(f)$ is the nominal group velocity curve of the considered mode, and K is a normalization parameter selected so that $w^{-1}(0.5) = w(0.5) = 0.5$. More details on warping map design can be found in [10].

Let's indicate with $s(t, D)$ an undamped guided wave signal generated by an ideal actuator, scattered by a defect and received by an ideal sensor, being D the sum of traveled distances from the actuator to the scatterer, and from the scatterer to the receiver. Then, the Fourier transform of $s(t, D)$ is given by:

$$(\mathbb{F}s)(f, D) = (\mathbb{F}s_0)(f, 0) \cdot e^{-j2\pi \int \frac{D}{c_g(f)} df} \quad (10.8)$$

where $(\mathbb{F}s_0)(f, 0)$ is the frequency transform of the applied input. In force of Eq. (10.7), Eq. (10.8) can be rewritten as:

$$(\mathbb{F}s)(f, D) = (\mathbb{F}s_0)(f, 0) \cdot e^{-j2\pi w^{-1}(f)KD} \quad (10.9)$$

where the dispersive effect results from the nonlinear phase term. The Fourier transforms of the warped signal $\mathbf{W}s(t, D)$ is given by:

$$(\mathbb{F}\mathbf{W}s(t, D))(f) = \sqrt{\dot{w}(f)} \cdot (\mathbb{F}s_0)(w(f), 0) \cdot e^{-j2\pi fKD} \quad (10.10)$$

As can be seen from this equation, the result of the warping procedure is a linear phase shift in the right hand term, which implies the desired shift invariance of the warped signal $s_w = \mathbf{W}s$ on the warped time axis.

It follows that the Lamb wave signal s can be modeled as the *antitransform* of the convolution $x_w * h_w$, where $h_w = \mathbf{W}s_0 \in \mathbb{R}^N$ is the F -sparse vector of the impulse response in the warped domain, and the sparse vector $x_w \in \mathbb{R}^N$ indicates the warped reflectivity function, which represents the scatterers position.

With the notation introduced in Section 10.3, the *warped* disjoint convolutional model is defined as:

$$\mathcal{M}_{S,F,\Delta}^{s,W} \doteq \{s \in \mathbb{R}^N : s = \mathbf{W}^\dagger(x_w * h_w) \mid x_w \in \mathcal{M}_S^\Delta, h_w \in \mathcal{M}_F^C\} \quad (10.11)$$

In force to the commutative property of the convolution operator, a signal s in $\mathcal{M}_{S,F,\Delta}^{s,W}$ can be represented as:

$$s = \mathbf{W}^\dagger(x_w * h_w) = \mathbf{W}^\dagger \mathbf{H}x_w = \mathbf{W}^\dagger \mathbf{X}h_w \quad (10.12)$$

where $\mathbf{H} = \mathbb{C}(h_w)$ (respectively, $\mathbf{X} = \mathbb{C}(x_w)$) is a square circulant matrix with its columns containing circularly shifted versions of the vector h_w (respectively, x_w).

10.4.2 Pulse Stream Recovery in the Frequency Warped domain

The reduced dimensionality of the union of subspaces captured by the model in Eq. (10.11) allows for an efficient and stable estimation of both the system impulse response \hat{h}_w and the reflectivity function \hat{x}_w from the compressed measurement vector

$$y = \Phi s + n = \Phi \mathbf{W}^\dagger \mathbf{H}x_w + n \quad (10.13)$$

being n the acquisition noise and where \hat{h}_w and \hat{x}_w denote an estimation of h_w and x_w , respectively. This problem is similar to performing sparse approximation with incomplete knowledge of the dictionary in which the target vector (either \hat{x}_w or \hat{h}_w) is sparse. The common approach has been to first assume that a training set of vectors \hat{x}_{w_i} exists for a fixed impulse response \hat{h}_w and then to infer the coefficients

of \hat{h}_w using a sparse learning algorithm (such as basis pursuit) and finally to solve for the coefficients \hat{x}_{w_i} . In the absence of training data, we must infer both the spike locations and the impulse response coefficients. Therefore, this task is also similar to blind deconvolution; the main differences are that we are only given access to the random linear measurements y as opposed to the Nyquist rate samples z and that our primary aim is to reconstruct z as faithfully as possible as opposed to merely reconstructing x .

The general approach is to obtain the “best possible estimate” of x_w given a tentative estimate of h_w , then update the estimate of h_w accordingly, and iterate. The target signal s is assumed to belong to the warped disjoint convolutional model of pulse streams $\mathcal{M}_{S,F,\Delta}^{s,W}$. This strategy is commonly known as *Alternating Minimization* (AM).

10.4.3 Alternating Minimization With Exhaustive Search

Consider $z \in \mathcal{M}(S, F, \Delta)$, so that $z_w = (x * h)_w$. This implies that the spikes in x are separated by a minimum separation distance Δ and that the impulse response h is concentrated. Suppose first that we are given noiseless CS measurements $y = \Phi z$. We fix a candidate support configuration σ for the spike stream (so that σ contains S nonzeros.) Then, we form the circulant matrix \hat{H} from all possible shifts of the current estimate of the impulse response \hat{h} (denote this operation as $\hat{H} = \mathbb{C}(\hat{h})$). Further, we calculate the dictionary $\Phi W^\dagger \hat{H}$ for the spike stream x and select the submatrix formed by the columns indexed by the assumed spike locations σ (denote this submatrix as $(\Phi W^\dagger \hat{H})_\sigma$). This transforms our problem into an overdetermined system, which can be solved using least-squares. In summary, we use a simple matrix pseudoinverse to obtain the estimate:

$$\hat{x} = \left(\Phi W^\dagger \hat{H} \right)_\sigma^\dagger y$$

This provides an estimate of the spike coefficients \hat{x} for the assumed support configuration σ . We now exploit the commutativity of the convolution operator $*$. We form the circulant matrix \hat{X} , form the dictionary $\Phi W^\dagger \hat{X}$ for the impulse response

and select the submatrix $(\Phi W^\dagger \hat{X})_f$ formed by its first F columns. Then, we solve a least-squares problem to obtain an estimate \hat{h} for the impulse response coefficients:

$$\hat{h} = \left(\Phi W^\dagger \hat{X} \right)_f^\dagger y$$

Finally, we form our signal estimate $\hat{z} = \hat{x} * \hat{h}$. The above two-step process is iterated until a suitable halting criterion (e.g., convergence in norm for the estimated signal \hat{z}). The overall reconstruction problem can be solved by repeating this process for every support configuration σ belonging to the structured sparsity model \mathcal{M}_S^Δ and picking the solution with the smallest norm of the residual $r = y - \Phi \hat{z}$. This algorithm performs alternating minimization for a given estimate for the support of the underlying spike stream x and exhaustively searches for the best possible support.

10.4.4 Iterative Support Estimation

The runtime of Algorithm 1 is exponential in N . Fortunately there is a simpler means to the same end. Instead of cycling through every possible support configuration σ_i for the spike stream x , we instead retain an estimate of the support configuration, based on the current estimates of the spike stream \hat{x} and impulse response \hat{h} and update this estimate with each iteration. In order to ensure that the support estimate belongs to \mathcal{M}_S^Δ , we leverage a special CS recovery algorithm for signals belonging to \mathcal{M}_S^Δ that is based on CoSaMP. At each iteration, given an estimate of the spike coefficients x , we need to solve for the best \mathcal{M}_S^Δ -approximation to x . Let $x = (x_1, x_2, \dots, x_N)^T$. Given any binary vector $s = (s_1, s_2, \dots, s_N)^T$ of length N , let

$$x_{|s} \doteq (s_1 x_1, s_2 x_2, \dots, s_N x_N)$$

so that $x_{|s}$ is the portion of the signal x lying within the support s . Our goal is to solve for the choice of support s so that $x_{|s}$ belongs to \mathcal{M}_S^Δ and $\|x - x_{|s}\|_2$ is minimized. The following constraints on the support vector s follow from the definition of \mathcal{M}_S^Δ :

$$\begin{aligned} s_1 + s_2 + \dots + s_N &\leq S & (10.14) \\ s_j + s_{j+1} + \dots + s_{j+\Delta-1} &\leq 1, \quad \text{for } j = 1, \dots, N \end{aligned}$$

where the subscripts are computed modulo N . The first inequality in 10.14 specifies that the solution contains at most S nonzeros; the other N inequalities 10.14 specify that there is at most one spike within any block of Δ consecutive coefficients in the solution. It can be shown that minimizing $\|x - x|_s\|_2$ is equivalent to maximizing $c^T s$ where $c = (x_1^2, x_2^2, \dots, x_N^2)$, i.e., maximizing the portion of the energy of x that lies within s . Define $W \in \mathbb{R}^{(N+1) \times N}$ as a binary indicator matrix that captures the left-hand side of the inequality constraints 10.14. Next, define $u \in \mathbb{R}^{N+1} = (S, 1, 1, \dots, 1)$; this represents the right-hand side of the constraints (19) and (20). Equations 10.14 can be performed by the following binary integer program:

$$s^* = \arg \min_{s \in \{0,1\}} c^T s, \quad \text{subject to } Ws \leq u$$

Next, we relax the integer constraints on s to obtain a computationally tractable linear program. Denote this linear program by $\mathbb{D}(\cdot)$. Once an updated support estimate has been obtained, we repeat Steps 2, 3 and 4 in Algorithm 1 to solve for the spike stream x and impulse h . This process is iterated until a suitable halting criterion (e.g., convergence in norm for the estimated pulse stream \hat{x}). The overall algorithm can be viewed as an iterative sparse approximation procedure for the \mathcal{M}_S^Δ model that continually updates its estimate of the sparsifying dictionary.

In the initialization phase, the algorithm set a tentative value for \hat{x}_w and \hat{h}_w and then update their value starting from the estimation of the support σ of \hat{x}_w . The support estimation (steps 1 \rightarrow 5 in the Algorithm 1) is performed by running \mathbb{D} , that is a linear program which returns the best K -term approximation v_K^* of a given vector v under the model \mathcal{M}_S^Δ so that the norm $\|v - v_K^*\|_2$ is minimized. Further details on the computation of \mathbb{D} are given in [88].

The support σ is a binary vector which highlights the scatterers locations. The columns of $\Phi_{wh} = \Phi \mathbf{W}^\dagger \hat{\mathbf{H}}$ which corresponds to these locations are used to form the submatrix $(\Phi_{wh})_\sigma = (\Phi \mathbf{W}^\dagger \hat{\mathbf{H}})_\sigma$ whose pseudoinverse is used to obtain an updated estimation of \hat{x}_w (steps 6 \rightarrow 7).

Finally, by exploiting the commutativity of the convolution operator $*$, the estimation of the impulse response is performed (steps 8 \rightarrow 9). The illustrated steps are iterated

until a halting criterion is fulfilled. In particular, in the proposed approach the halting criterion is selected so that the discrepancy between the measurement vector and the product $\Phi \cdot \hat{s}$ is minimized.

The implemented algorithm, summarized in Table 1, is a modified version of the one firstly presented in [95] which has been adapted to perform in the warped domain.

Algorithm 1: Model-based Compressive Sensing for pulse stream reconstruction

Input : Warping Operator \mathbf{W} , Sensing Matrix Φ ,
measurement vector y , model parameters S, F

Output : $\hat{x}_w, \hat{h}_w, \hat{s}$

$i = 0$: Initialization, $\hat{x}_w = 0, \hat{h}_w = (1_F, 0, \dots, 0)$

for $\sigma \in \mathcal{M}_S^\Delta$ **do**

while $\|y - \Phi \mathbf{W}^\dagger \mathbf{H} \hat{x}_w\| < \varepsilon$ **do**

1. $i \leftarrow i + 1$
2. $\hat{\mathbf{H}} = \mathbb{C}(\hat{h}_w)$, {form dictionary for spike stream}
 $\Phi_{wh} = \Phi \mathbf{W}^\dagger \hat{\mathbf{H}}$
3. $e \leftarrow \Phi_{wh}^T (y - \Phi_{wh} \hat{x}_w)$ {residual}
4. $\sigma_e \leftarrow \text{supp}(\mathbb{D}(e))$ {residual support estimate}
5. $\sigma \leftarrow \sigma_e \cup \text{supp}(\hat{x}_w^{(i-1)})$ {merge supports}
6. $x|_\sigma \leftarrow (\Phi_{wh})_\sigma^\dagger y$, {update reflectivity estimate}
7. $\hat{x}_w \leftarrow \mathbb{D}(x)$ {prune reflectivity estimate}
8. $\hat{\mathbf{X}} = \mathbb{C}(\hat{x}_w)$, {dictionary for impulse response}
 $\Phi_{wx} = (\Phi \mathbf{W}^\dagger \hat{\mathbf{X}})_f$
9. $\hat{h}_w \leftarrow \Phi_{wx}^\dagger y$ {update impulse response estimate}

end while

return $\hat{x}_w, \hat{h}_w, \hat{s} \leftarrow \mathbf{W}^\dagger \hat{\mathbf{H}} \hat{x}_w$,

Chapter 11

Model-Based Compressive Sensing for Damage Localization

To be ignorant of one's ignorance is the malady
of the ignorant.

Amos Bronson Alcott

11.1 Introduction

To illustrate the effect of the CS procedure described in Chapter 10, the proposed algorithm is tested on a Lamb wave time-waveform $s(t)$ generated synthetically as the superposition of three undamped waveforms due to:

- i) the pulse generated by the actuator (A) which travels along the direct path (P1) to the receiver (R);
- ii) the pulse scattered by the defect (D) which travels along the second path (P2);
- iii) the pulse reflected by the edge (E) of the plate system which travels along the third path (P3), as schematically depicted in Figure 11.1.

Suppose also that the group velocity of the propagating waves is $c_g(f)$.

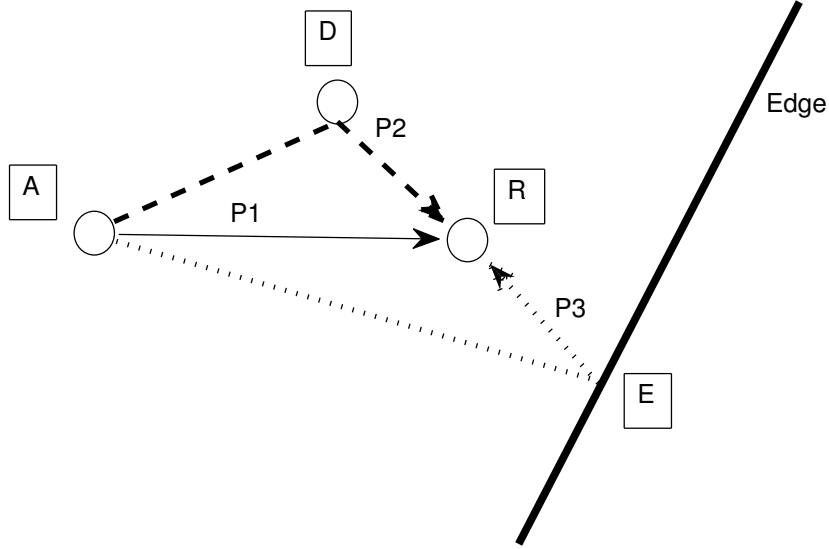


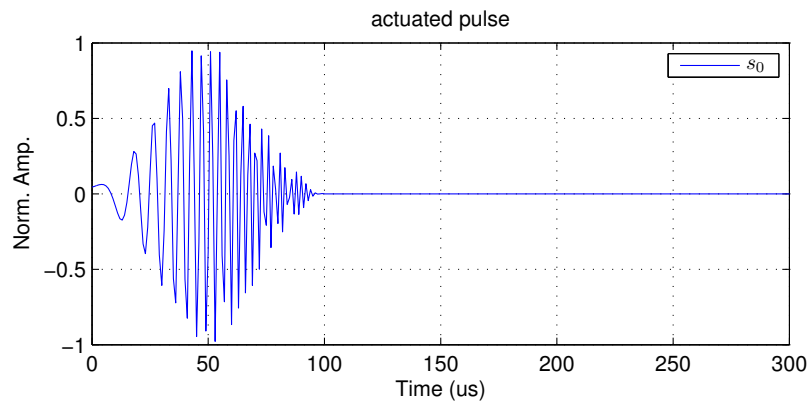
Figure 11.1: Sketch of the considered example: the signal is actuated in A, scattered by the defect D, reflected by the edge E, and sensed in R. Consequently, three waves are captured in the acquired waveform: those traveling along paths P1, P2 and P3, respectively.

Then, s can be generated as:

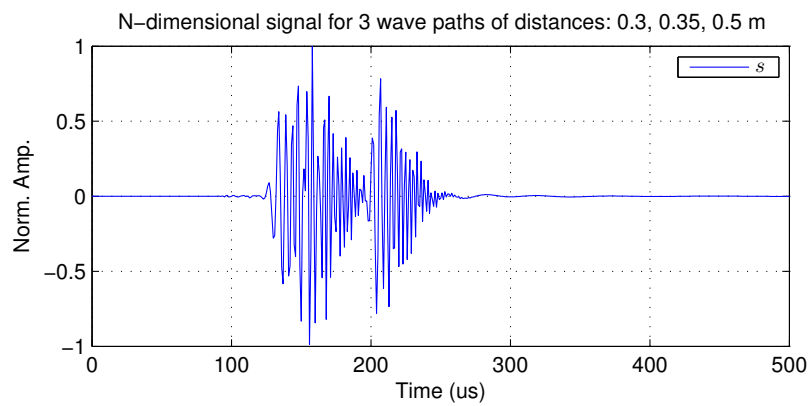
$$s = \mathbb{F}^\dagger [\mathbb{F}s_0 \cdot (e^{-j2\pi \int \frac{D_1}{c_g(f)} df} + e^{-j2\pi \int \frac{D_2}{c_g(f)} df} + e^{-j2\pi \int \frac{D_3}{c_g(f)} df})], \quad (11.1)$$

where s_0 is the actuated pulse, and D_1 , D_2 , D_3 are the lengths of paths P1, P2 and P3, respectively. The actuating pulse s_0 is a chirp with a linear frequency modulation ranging from 10 kHz to 500 kHz (see Figure 11.2(a)). The synthetic signal s generated by forcing the chirp to the A_0 mode of a 3 mm-thick aluminum plate (Young's modulus $E = 69$ GPa, Poisson's coefficient $\nu = 0.3$ and material density $\rho = 2700$ kg/m³) is shown in Figure 11.2(b) for $D_1 = 0.3$ m, $D_2 = 0.35$ m and $D_3 = 0.5$ m.

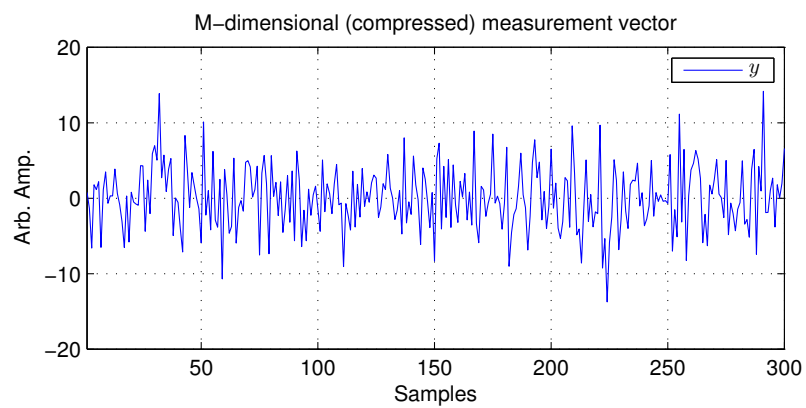
In the CS framework, the N -dimensional signal s is compressed in the M -dimensional vector $y = \Phi s$ shown in Figure 11.2(c). In the considered example N and M are equal to 900 and 300, respectively, and the entries of the $M \times N$ measurement matrix Φ are chosen randomly from independent and identically distributed (i.i.d.) Gaussian distributions [94].



(a)



(b)



(c)

Figure 11.2: (a) Actuated pulse s_0 , (b) N-dimensional synthetic signal s , (c) M-dimensional measurements vector y . In this example $N=900$ and $M=300$.

The application of the proposed CS scheme, considering a warping operator \mathbf{W} designed according to Eq. (10.7) by using the $c_g(f)$ of the A_0 mode, $S = 6$ and $F = 100$, leads to results shown in Figure 11.3.

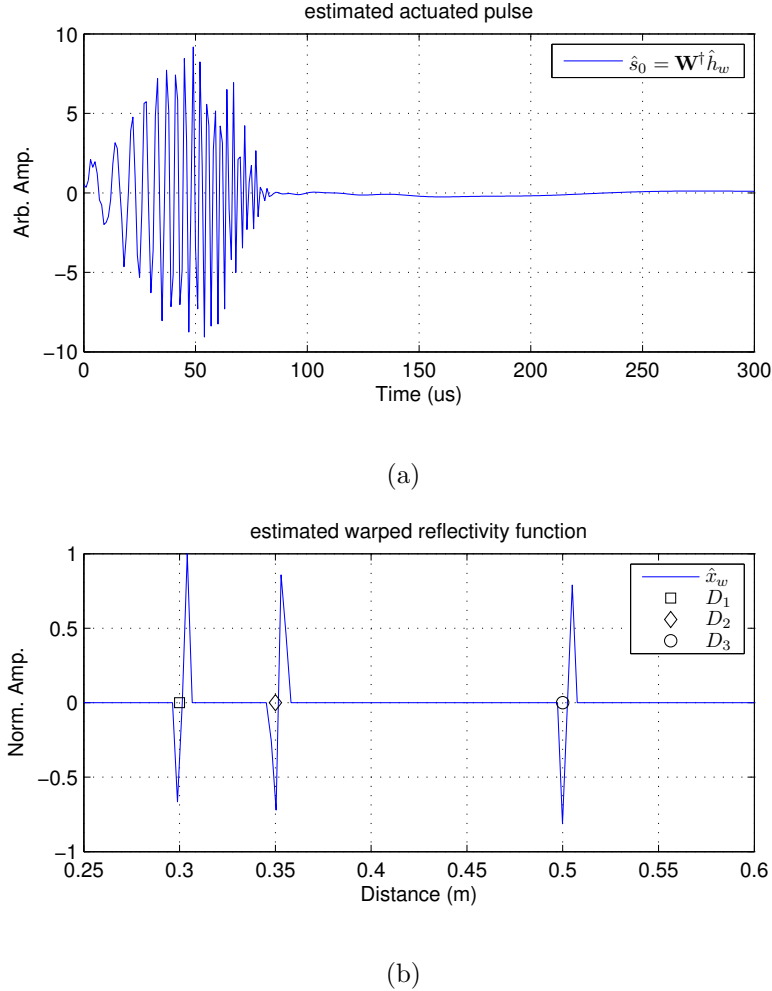


Figure 11.3: Results of the CS decomposition procedure in terms of (a) estimated actuated pulse $\hat{s}_0 = \mathbf{W}^\dagger \hat{h}_w$ (where \hat{h}_w is the estimated impulse response in the warped domain), and (b) estimated warped reflectivity function \hat{x}_w .

In particular, it can be observed both the good reconstruction of the estimated actuated pulse which can be computed as the antitransform of the estimated warped impulse response $\hat{s}_0 = \mathbf{W}^\dagger \hat{h}_w$ as well as the accurate paths length detection within the estimated warped reflectivity function \hat{x}_w .

It must be remarked that the synthetic signal in Eq. (11.1) does not include models of the actuator and the sensor (and so does not account for actuator-plate and plate-

sensor interaction), it considers the ideal generation of a single guided wave, and an undamped wave propagation. The computation of the synthetic signal s can be extended to the case of multi-modal and damped guided wave propagation.

The effect of more modes can be easily obtained by adding the related synthetic responses, keeping in mind that without a wavelength tuning model the considered modes are equally actuated and received by the ideal actuator and sensor, respectively. The effect of mechanical and geometrical guided waves attenuation could be included in the generation of the synthetic signal by multiplying the dispersive frequency response Eq. (11.1) for each mode by its frequency dependent attenuation information (e.g. the dispersive mechanical guided wave attenuation can be computed by SAFE formulations as the one coded in the tool [97]).

Notwithstanding the assumed simplifications, it will be shown in the next section how the developed CS scheme can be successfully applied in real applications.

11.2 Experimental verification

In active techniques a known waveform is sent to a piezoelectric (PZT) actuator and a network of piezoelectric (PZT) sensors acquire data. The aim of the CS signal processing is the detection of waves scattered by defects.

The recovered warped reflectivity function \hat{x}_w is constituted by a stream of spikes whose position is related to the distance traveled by the different waves. Since the geometry of the plate and the positions of the PZT sensors (actuator and sensors) are known, from an acquired and processed signal it is easy to distinguish spikes due to the direct path (actuator-receiver) and caused by edge reflections, from spikes related to defects. This latter information (distance sensor-defect) recovered from at least three sensors, allows to fruitfully feed positioning procedures aimed at recovering the position of the defect.

As a case study, we exploited the proposed compressive sensing tool to compute the sensor-defect distances in an aluminum 1050A square plate 1000×1000 mm and 3 mm thick.

The experimental set-up is shown in Figure 11.4.

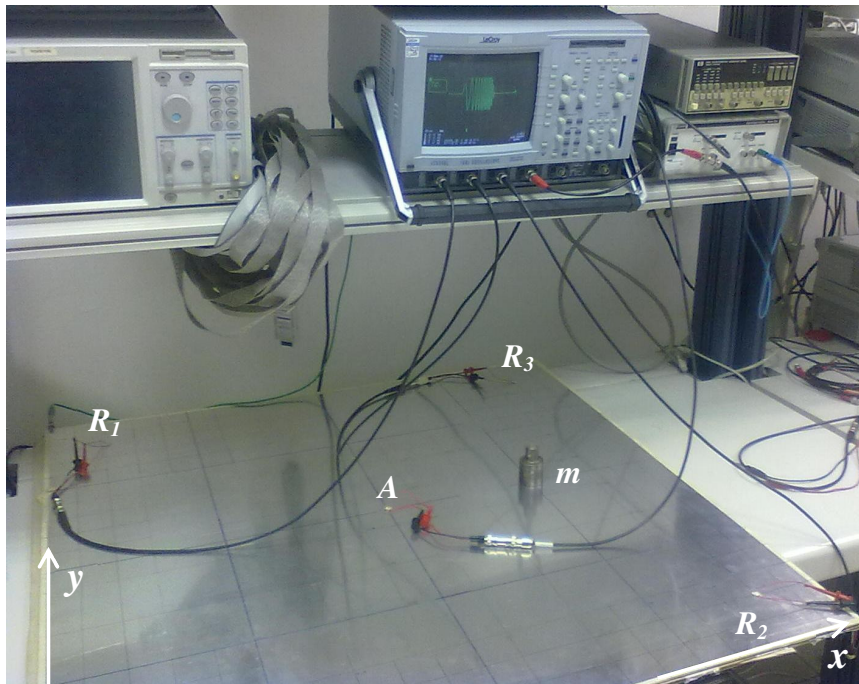


Figure 11.4: Experimental set-up used to validate the proposed CS procedure: A actuator, R receivers, m added mass.

Four PZT discs (PIC181, diameter 10 mm, thickness 1 mm) were bonded to the plate using a high-strength Loctite glue.

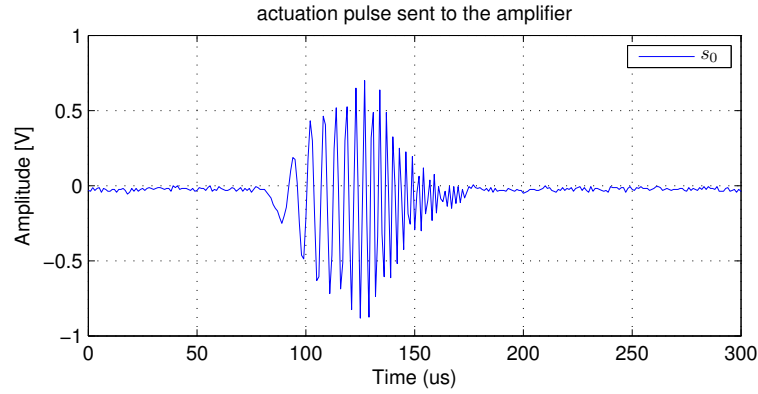
The position of the transducers is defined in Table 11.1.

Coordinates	Actuator	Receivers		
	A	R_1	R_2	R_3
x (m)	0.50	0.10	0.90	0.90
y (m)	0.50	0.90	0.10	0.90

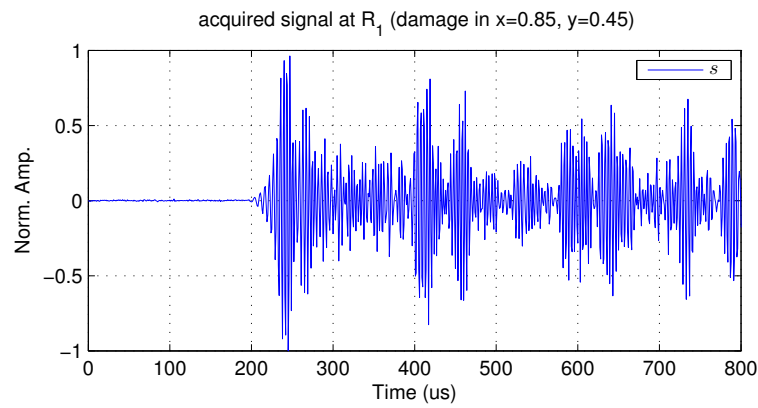
Table 11.1: Actuator and receivers topology.

Defects have been emulated by a small steel cylindrical mass (indicated with m in Figure 11.4), 20 mm of diameter and 500 gr of weight, posed in different positions on the plate and acoustically coupled simply with water, so that it generates quite weak reflections.

Guided waves were excited by actuating the central PZT transducer (A) with the linear chirp signal shown in Figure 11.5(a) amplified by 50 times.



(a)



(b)

Figure 11.5: Experimental results: (a) input chirp signal sent to the power amplifier and then to the PZT actuator (A), (b) signal acquired by sensor R_1 when the mass is placed at coordinates $x = 0.85$ m and $y = 0.45$ m.

The acquired waveforms at the three receivers R_1 , R_2 and R_3 , were recorded using the LC534 series LeCroy oscilloscope at a sampling frequency of 1 MHz, since the frequency content of the acquired signal vanishes above 400 kHz. Acquisitions were triggered when the actuated signal reached a threshold level of 140 mV. It was verified that for the considered plate only the A_0 and S_0 Lamb waves exist within the excited frequency range (0 – 400 kHz) [97]. The waveform detected by the receiver R_1 , when the mass is placed at coordinates $x = 0.85$ m, $y = 0.45$ m, is shown in Figure 11.5(b).

As can be seen from the acquired time waveform, it is extremely difficult (if not impossible) estimating the time of arrival of waves echoes due to the mass among the other direct and edges reflected A_0 and S_0 Lamb waves. Moreover, such estimation is complicated by the effect of dispersion which introduces a mode distance dependent group delay shift. On the contrary, designing the warping operator \mathbf{W} on the A_0 mode of the plate and processing the acquired signal in Figure 11.5(b) with the proposed CS approach yields to quite impressive results, both in terms of estimated actuated pulse and estimated reflectivity function, as can be noted from Figure 11.6.

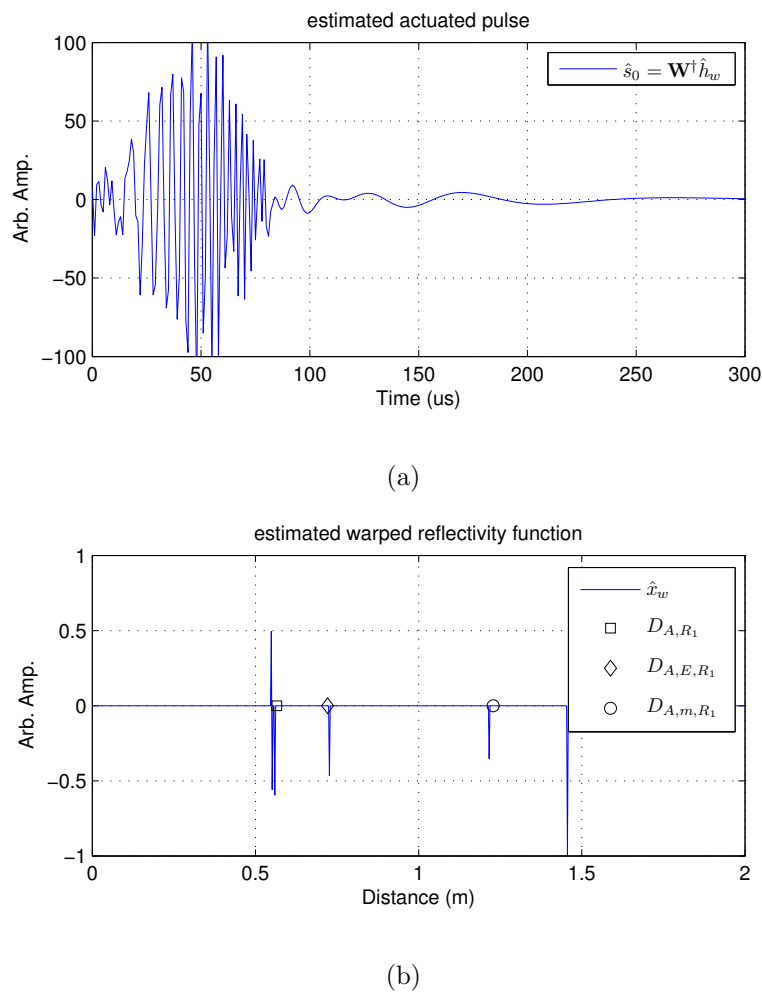
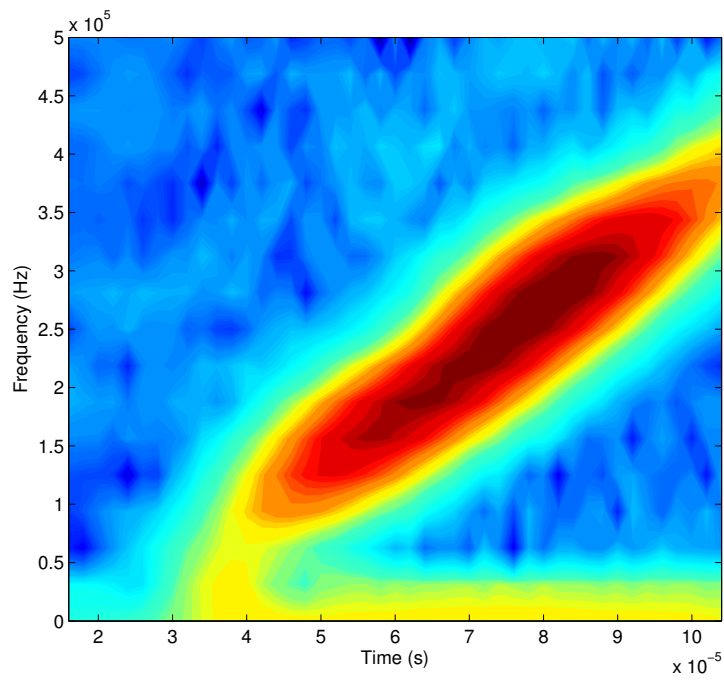
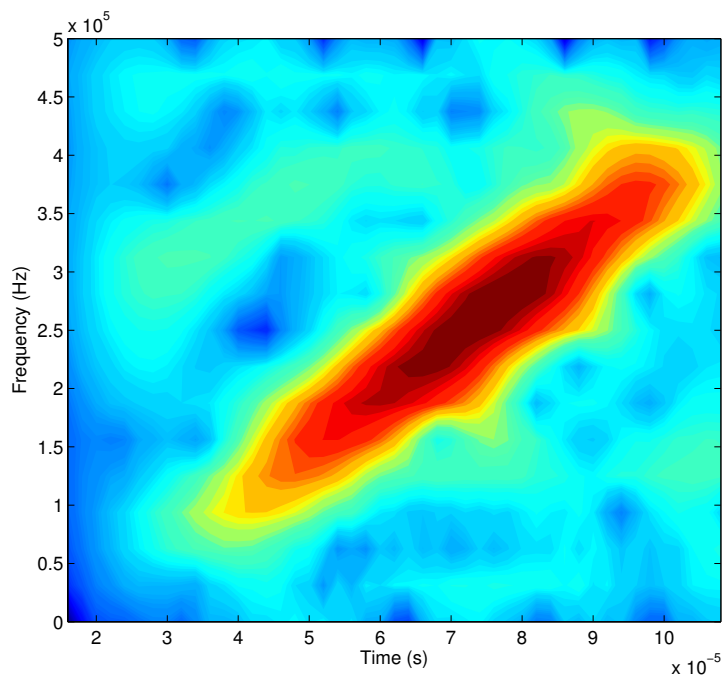


Figure 11.6: Experimental results achieved by processing the acquired signal in Figure 11.5(b) with the proposed CS approach: (a) estimated actuated pulse, (b) reflectivity function reconstructed by the CS algorithm with superimposed the real distances related to the direct, scattered by the defect, and reflected paths.



(a)



(b)

Figure 11.7: Spectrogram of (a) the actuated chirp s_0 and of (b) the recovered estimated chirp \hat{s}_0 .

In particular, the estimated actuated pulse $\hat{s}_0 = \mathbf{W}^\dagger \hat{h}_w$ is very similar to the actuated pulse s_0 ; the slight discrepancies in the time domain can be due to the filtering effect imposed by the piezoelectric transducers in actuation and sensing. However, the comparison of the spectrograms of s_0 and \hat{s}_0 in Figure 11.7(a) and (b), respectively, shows how the linear-chirp frequency modulation is properly recovered.

Regarding the reflectivity function, the spikes in \hat{x}_w are almost perfectly overlapped to the actual distances traveled by the waves:

- $D_{A,R_1} = 0.5657$ m, the length of the direct path between the actuator A and the receiver R_1 ,
- $D_{A,E,R_1} = 0.7211$ m, the length of the path from the actuator A to the edge of the plate E and to the receiver R_1 ,
- $D_{A,m,R_1} = 1.2282$ m, that is path length of the defect-scattered waves from the actuator A to the mass m and to the receiver R_1 .

The peaks in the reflectivity function are affected by the guide waves attenuation (mode attenuation and spreading) as it can be noted by comparing Figure 11.3(b) (synthetic reflectivity) with Figure 11.6(b) (experimental reflectivity).

The synthetic reflectivity peaks are almost constant in amplitude regardless the traveled distances (so not influenced by mode dispersion), whereas the experimental reflectivity function shows peaks of different amplitudes. The link between mode attenuation and reflectivity function peak amplitude can be seen by looking at the difference between the two peaks D_{A,R_1} and D_{A,E,R_1} that are both related to the same A_0 mode only.

The overall performance of the proposed algorithm can be evaluated by looking at the cumulative distribution function of the error $eD_{A,m,X}$ in the estimation of the distance traveled from the actuator A to the receiver X (with $X \in \{R_1, R_2, R_3\}$) by the wave scattered by the mass (m), shown in Figure 11.8.

To generate this plot, 63 signals (related to 21 positions of the mass) acquired by R_1 , R_2 and R_3 were considered.

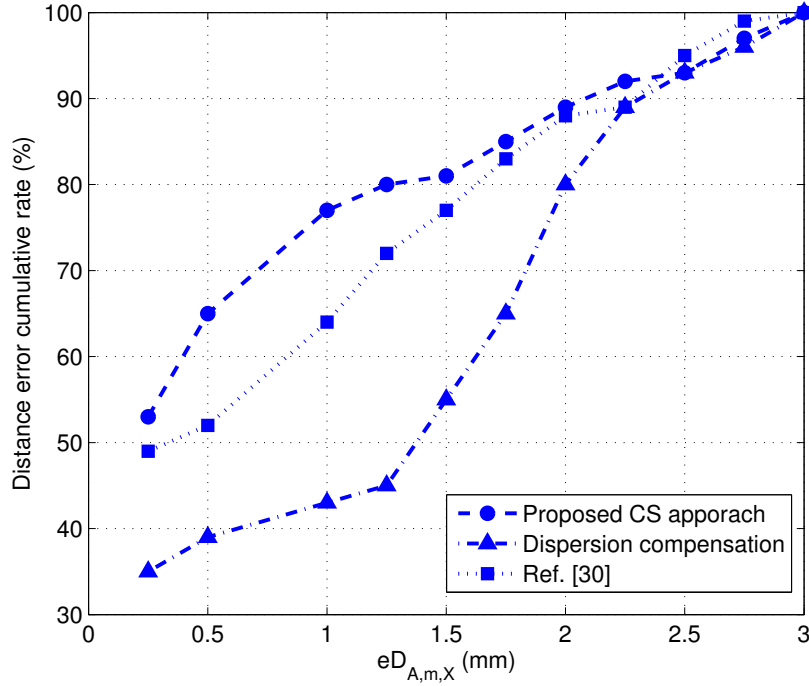


Figure 11.8: Cumulative error distribution in the estimation of $D_{A,m,X}$.

As can be seen, the error of the proposed CS scheme for the 77% of the 63 measures is less than 1 mm (see the bulleted (\bullet) data in Figure 11.8). Averaging these results, we obtained a mean error of 0.97 mm in the estimation of distance $D_{A,m,X}$. This result compares favourably with the mean error achieved by extracting the peaks of the signals processed through a dispersion compensation procedure (1.76 mm - \blacktriangle in Figure 11.8), since classical dispersion compensation algorithms [51] [70] are not suited to process chirp signals. More interestingly, the proposed CS tools outperforms also procedures specifically dedicated to chirped actuations (1.18 mm - \blacksquare in Figure 11.8) as the one proposed in [10].

To achieve these results, a very important step is the selection of the model parameters S and F . In the described experiments, F and S were set to 100 and 6, respectively. This choice allows for a compression ratio of $\frac{M}{N} = 0.37$. In particular, the model parameter F was set at a value equal to the length of the warped actuating chirp, while S selection was performed by taking into consideration two opposite effects:

(i) lowering S reduces the computational effort and minimizes the compression ratio, thanks to the dimensionality reduction of the union of subspaces $\mathcal{M}_{S,F,\Delta}^{s,W}$, whereas (ii) increasing S allows to better modelling multiple wave reflections.

11.3 Discussion

In this Chapter the development of a Compressive Sensing (CS) acquisition and reflectivity function estimation was presented. The proposed CS scheme improving the detection of the distance traveled by guided waves can be proficiently used in conventional Lamb wave inspection systems. The tool exploits the Warping Frequency Transform to project the acquired signals in a dispersion compensated basis. In the reconstruction stage an Alternating Minimization (AM) procedure is performed to recover both the excitation shape and the reflectivity function. Experimental validations shows the effectiveness of the proposed algorithm as a suitable tool to locate defect-induced reflections with compressed acquisitions.

Future developments include the generalization to applications characterized by anisotropic and multi-modal propagation, such as the detection of defects in composite plates. In such cases, it is foreseen that instead of projecting the signal in a given warped domain, novel decomposition strategies will be implemented, based on the construction of a redundant representation basis which can capture multiple dispersive behaviors (see Ref. [73]). If so, all the considered modes would contribute to estimate the sought sensors-defect distances.

It is worth noticing that the implemented algorithm operates as a blind deconvolution tool, without exploiting the information about the actuating waveform, therefore the proposed tool has the potential to be applied also in contexts where no prior knowledge about the incipient pulse is given, such as in acoustic emissions monitoring, or in impact localization tasks.

Chapter 12

Multi-Channel Distributed Compressed Sensing for Impact Localization in Composite Plates

It is impossible to enjoy idling thoroughly unless one has plenty of work to do.

Jerome Klapka

12.1 Introduction

Aerospace structures comprising of metals and composites are exposed to extreme loading and environmental conditions which necessitates regular inspection and maintenance to verify and monitor overall structural integrity; the accurate detection of structural cracking, delamination are of major concern in the operational environment. There is increasing emphasis on using composites in structural components due to the reduction in weight and increased strength. but in general this materials are usually neither isotropic nor homogeneous.

In this Chapter a new framework for joint compressed sensing of anisotropic ultrasonic propagating waves that exploits intra-signal correlation structures has been

developed. The proposed algorithm has been applied on impact localization for composite plate inspection.

The development of an in situ health monitoring system that can inspect large areas and communicate remotely to the inspector is highly computational demanding due to both the huge number of piezoelectric sensors needed and the high sampling frequency, so the main aim of the proposed framework is to lower the data dimension and to enhance impact localization performances.

In the proposed approach, a CS algorithm based on a Alternating Minimization (AM) procedure is adopted to extract the information about both the system *Impulse Response* and the *Reflectivity Function*.

The implemented tool exploits the dispersion compensation properties of a multiple Warped Frequency dictionary for each direction of propagation as a mean to generate the a family of sparsifying basis for the anisotropic signal representation.

As a result, an automatic procedure to locate impact has been demonstrated and successfully tested on Lamb waves propagating in a carbon fiber reinforced polymer (CFRP) plate. The proposed algorithm is suitable for impact detection and can be implemented in future for real application to structural health monitoring.

The Chapter is organized as follows: Section 12.2 introduces the Warped Frequency Transform and the proposed algorithm to recover the reflectivity function from the acquired signal from anisotropic and dispersive medium. Finally, in Section 12.3, the validating experiments are presented.

12.2 Recovery of Anisotropic Dispersive Pulse Streams

In this work we deal with signals which can be considered as a sum of components sparse in the frequency warped domain with different maps; in particular in the anisotropic propagation the wave signal can be represented as a sum of path-terms with different wave velocity according to the angle of propagation. In detail an impact generates an ultrasonic wave which propagates through different directions related to the direct path, reflections, ecc; since that in anisotropic waveguides the propagation

velocity depends on the angle, in order to isolate this contributions it is necessary to represent the signal by a family of frequency warped basis designed using the simulated dispersion velocity curves for a set of angles.

It is worth noticing to detail the logical steps which compose the propose CS framework for impact acoustic emission localization in anisotropic media.

1. **Family dictionary design to match the anisotropic dispersive propagation:** the proposed dictionary design steps is described in the following:
 - a priori simulation of a set of dispersion curves for several angles of propagation with Semi-Analytical Finite Element method (SAFE);
 - design a dictionary of frequency warped basis with the previous simulated maps;
 - using the family of basis computed in the CS recovery algorithm as the sparsifying dictionary.

2. **Model for jointly sparse anisotropic propagating signals:** the interdependencies between signals acquired by the sensors network can be exploited through the use of a Joint Sparsity Model (JSM) of the 3th type, as detailed in []; in particular the signal propagating in an anisotropic medium can be expressed as sum of sparse component in the proper family of basis.

3. **Model-based CS and Alternating minimization Recovery:** finally in order to reduce the computational cost of the impulse recovery for each component of the signal, the convolutional model of the system has been exploited as presented in []; in detail in the recovery stage the search is made only on a subset of all possible supports and this subset is chosen according to a specific model related to the physic model of the system, i.e. in a mathematical point of view the convolutional relation between the input signal and the impulse response.

In the following Sections a detailed description of each step is presented.

12.2.1 Frequency Warped Dictionary Design

A sparse representation for guided wave signals can be obtained by using Warping Frequency Transforms (WFTs). These operators deform the frequency axis with a proper warping map $w(f)$ [27]. In particular, given a generic signal s whose continuous Fourier transform is $\mathbb{F}s$, the continuous warping operator \mathbf{W} is defined as

$$(\mathbb{F}\mathbf{W}s)(f) = \sqrt{\dot{w}(f)}(\mathbb{F}s)(w(f)) \quad (12.1)$$

where $s_w = \mathbf{W}s$ is the so-called warped signal. \mathbf{W} is a unitary operator and the inverse transformation can be computed through its adjoint operator \mathbf{W}^\dagger . A fast computation of the discrete warping operator and its inverse is achieved by means of FFT-based algorithms [96]. In order to use the WFT for compensating Lamb waves signals from the dispersion of a particular guided mode, $w(f)$ can be defined through its functional inverse, as:

$$K \frac{dw^{-1}(f, \theta_i)}{df} = \frac{1}{c_g(f, \theta_i)} \quad (12.2)$$

where $c_g(f, \theta_i)$ is the nominal group velocity curve of the considered mode for a specific angle of propagation θ_i and K is a normalization parameter selected so that $w^{-1}(0.5) = w(0.5) = 0.5$. It is important to point out that in anisotropic propagation the nominal velocity curve $c_g(f, \theta_i)$ can be slightly different according to the direction of the propagation of the wave so respect to the procedure described in 11 in this Chapter is presented an extention.

More details on warping map design can be found in [10]. Let's indicate with $s(t, D, \theta_i)$ an undamped guided wave signal generated by an ideal actuator and received by an ideal sensor, being D the traveled distances from the actuator to the receiver. Then, the Fourier transform of $s(t, D, \theta_i)$ is given by:

$$(\mathbb{F}s)(f, D, \theta_i) = (\mathbb{F}s_0)(f, 0) \cdot e^{-j2\pi \int \frac{D}{c_g(f, \theta_i)} df} \quad (12.3)$$

where $(\mathbb{F}s_0)(f, 0)$ is the frequency transform of the applied input. In force of Eq. (12.2), Eq. (12.3) can be rewritten as:

$$(\mathbb{F}s)(f, D, \theta_i) = (\mathbb{F}s_0)(f, 0) \cdot e^{-j2\pi w^{-1}(f, \theta_i)KD} \quad (12.4)$$

where the dispersive effect results from the nonlinear phase term. The Fourier transforms of the warped signal $\mathbf{W}s(t, D, \theta_i)$ is given by:

$$(\mathbb{F}\mathbf{W}s(t, D, \theta_i))(f) = \sqrt{\dot{w}(f, \theta_i)} \cdot (\mathbb{F}s_0)(w(f, \theta_i), 0) \cdot e^{-j2\pi fKD} \quad (12.5)$$

12.2.2 Warped Convolutional Anisotropic Models

Among the structured sparse models presented in literature, the *convolutional model* detailed in [95] is suited to represent pulse stream signals, as those acquired in ultrasonic applications. Let $\mathcal{M}_S \subset \mathbb{R}^N$ be a union of S -dimensional canonical subspaces. Similarly, let $\mathcal{M}_F \subset \mathbb{R}^N$ be a union of F -dimensional canonical subspaces. A convolutional model is formally defined as the set

$$\mathcal{M}_{S,F}^s \doteq \{s \in \mathbb{R}^N : s = (x * h) \mid x \in \mathcal{M}_S, h \in \mathcal{M}_F\} \quad (12.6)$$

where $*$ denotes the circular convolution operator, h is the impulse response of the ultrasonic apparatus, and x is the reflectivity function of the inspected component. If $S \cdot F = K$, then the set $\mathcal{M}_{S,F}^z$ is a small subset of \sum_K . Such dimensionality reduction is very beneficial, as the number of measurements M necessary to recover the signal s is logarithmic in the number of subspaces in the model (see [94]). A further reduction in the number of measurements can be achieved in the special case of streams of *disjoint pulses*, that is situations in which the ultrasonic impulse response h is concentrated in F contiguously located coefficients, while x is constituted by S sparse spikes separated at least by Δ locations, with $\Delta > F$. If \mathcal{M}_S^Δ is the structured sparse model for the spike streams x , and \mathcal{M}_F^C is the subspace of \mathcal{M}_F of the concentrated impulse responses, the disjoint convolutional model is defined as:

$$\mathcal{M}_{S,F,\Delta}^s \doteq \{s \in \mathbb{R}^N : s = (x * h) \mid x \in \mathcal{M}_S^\Delta, h \in \mathcal{M}_F^C\} \quad (12.7)$$

The disjoint convolutional model could represent many practical situations related to inspections with bulk ultrasonic waves, but it cannot capture a relevant phenomenon which affects guided wave (GW) propagation: the effect of dispersion (i.e. frequency-dependent propagation speed). In fact, dispersion causes the impulse response h to

be shift-variant. However, if the dependency of h on the wave propagation distance is predictable, it is possible to project the acquired signals in a representation basis in which the dispersion effect is compensated, allowing thus the use of disjoint convolutional models. In this work, such task is achieved by computing the dispersion curves for the plate-like structure of interest first, and then by exploiting such curves to design a WFT capable to project the acquired signals in the new basis, as will be shown in the next section. In the novel representation domain, suitable model-based CS recovering algorithms can be adopted to recover the original signal from the measurement vector and to extract the relevant information about reflectors.

As can be seen from Eq. 12.5, the result of the warping procedure is a linear phase shift in the right hand term, which implies the desired shift invariance of the warped signal $s_w = \mathbf{W}_{\theta_i} s$ on the warped time axis. It follows that the Lamb wave signal s can be modeled as the *antitransform* of the convolution $x_w * h_w$, where $h_w = \mathbf{W}_{\theta_i} s_0 \in \mathbb{R}^N$ is the F -sparse vector of the impulse response in the warped domain, and the sparse vector $x_w \in \mathbb{R}^N$ indicates the warped reflectivity function, which represents the scatterers position.

With the notation introduced in Chapter 10, the *warped* disjoint convolutional model is defined as:

$$\mathcal{M}_{S,F,\Delta}^{s,W_{\theta_i}} \doteq \{s \in \mathbb{R}^N : s = \mathbf{W}_{\theta_i}^\dagger (x_w * h_w) \mid x_w \in \mathcal{M}_S^\Delta, h_w \in \mathcal{M}_F^C\} \quad (12.8)$$

In force to the commutative property of the convolution operator, a signal s in $\mathcal{M}_{S,F,\Delta}^{s,W_{\theta_i}}$ can be represented as:

$$s = \mathbf{W}_{\theta_i}^\dagger (x_w * h_w) = \mathbf{W}_{\theta_i}^\dagger \mathbf{H} x_w = \mathbf{W}_{\theta_i}^\dagger \mathbf{X} h_w \quad (12.9)$$

where $\mathbf{H} = \mathbb{C}(h_w)$ (respectively, $\mathbf{X} = \mathbb{C}(x_w)$) is a square circulant matrix with its columns containing circularly shifted versions of the vector h_w (respectively, x_w).

12.2.3 Separation-Based Joint Decoding

According to the superposition principle valid in such a system the acquired propagating wave can be represented as:

$$s_a = s_{\theta_1} + \dots + s_{\theta_i} + \dots + s_{\theta_K}$$

where the signal components s_{θ_i} are sparse in Ψ_{θ_i} , i.e. $s_{\theta_i} = \Psi_{\theta_i} x_{\theta_i}$.

The previous relation leads to the following representation of the acquired signal in the new frequency warped domain:

$$s_a = \Psi_{\theta_1} x_{\theta_1} + \dots + \Psi_{\theta_K} x_{\theta_K}$$

Let $\Psi = [\Psi_{\theta_1} \dots \Psi_{\theta_K}]$; that is, Ψ is an $N \times N \times K$ matrix, then

$$\begin{aligned} s_a &= s_{\theta_1} + \dots + s_{\theta_K} = \Psi_{\theta_1} x_{\theta_1} + \dots + \Psi_{\theta_K} x_{\theta_K} = \\ &= [\Psi_{\theta_1} \dots \Psi_{\theta_K}] \cdot \begin{bmatrix} x_{\theta_1} \\ \dots \\ x_{\theta_K} \end{bmatrix} = \Psi x \end{aligned}$$

Thus, we can decode x using $y = (\Phi\Psi)x$, and recover s using $s = \Psi x$.

This process finds x_{θ_i} simultaneously in the domains associated with Ψ_{θ_i} , thus we call it joint decoding. Joint decoding uses the same minimization process as that in standard compressive sensing, but it involves an increased number of variables (that is, $N \times K$ variables rather than original N variables) in the minimization due to the use of the $N \times (N \cdot K)$ overcomplete basis Ψ . We refer this method the conventional joint decoding. Note that for the same number of measurements M , the measurement matrix satisfies $(\epsilon, 2K)$ -RIP with a larger K if a smaller N is used in decoding. This implies that $\|x_K - x\|_{l_1}$ is smaller, and consequently the error bound given earlier on $\|x * -x\|_{l_2}$ is also smaller. This provides a motivation of our goal - to reduce the number of variables in joint decoding by variables separation. Joint decoding uses an overcomplete basis to simultaneously exploit sparsity in multiple domains. As discussed in Section III, the number of variables in decoding is the number of components in all domains. Having more variables leads to increased decoding time and reduced compression rate (M/K) for achieving the same decoding quality.

We now explain our separation-based method that reduces the number of variables in joint decoding. For the clarity of presentation, we consider a case with only two domains. We consider a composite input signal of length N , $s_a = s_{\theta_1} + \dots + s_{\theta_i} + \dots + s_{\theta_K}$ with $s_{\theta_i} = \Psi_{\theta_i} x_{\theta_i}$ where x_{θ_i} is K_{θ_i} -sparse. The separation-based joint decoding departs from the conventional joint decoding by employing the following two steps:

1. **Separation step:** we perform decoding for a selected subset of domains or separation domains, which are the ones that we anticipate to have stronger components. Then, we identify the leading variables in these domains based on the reconstruction. Suppose the domain associated with Ψ_{θ_i} is selected. Then, we reconstruct an approximate solution to x_{θ_i} by decoding x'_{θ_i} using

$$y = (\Phi \Psi_{\theta_i}) x'_{\theta_i}$$

Note that

$$\begin{aligned} y &= \Phi(s_{\theta_1} + \dots + s_{\theta_i} + \dots + s_{\theta_K}) = \\ &= \Phi(\Psi_{\theta_1} x_{\theta_1} + \dots + \Psi_{\theta_i} x_{\theta_i} + \dots + \Psi_{\theta_K} x_{\theta_K}) = \\ &= \Phi \Psi_{\theta_i} (\Psi_{\theta_i}^{-1} \Psi_{\theta_1} x_{\theta_1} + \dots + x_{\theta_i} + \dots + \Psi_{\theta_i}^{-1} \Psi_{\theta_K} x_{\theta_K}) = \\ &= \Phi \Psi_{\theta_i} x'_{\theta_i} \end{aligned}$$

where $x'_{\theta_i} = x_{\theta_i} + \Psi_{\theta_i}^{-1} \Psi_{\theta_1} x_{\theta_1} + \dots + \Psi_{\theta_i}^{-1} \Psi_{\theta_K} x_{\theta_K}$. Thus x'_{θ_i} is an approximate of x_{θ_i} with an error term $\Psi_{\theta_i}^{-1} \Psi_{\theta_1} x_{\theta_1} + \dots + \Psi_{\theta_i}^{-1} \Psi_{\theta_K} x_{\theta_K}$. We sort the elements in the reconstructed x'_{θ_i} according to their magnitudes, and keep only the largest L elements. We call them the distinguished variables for the domain associated with Ψ_{θ_i} , and use \hat{x}_{θ_i} to denote the set of these variables. The parameter L is so chosen that \hat{x}_{θ_i} includes the K_{θ_i} largest nonzero variables in x_{θ_i} with a good chance.

2. **Joint decoding step:** to compute x_{θ_j} and rectify the possible errors in x_{θ_i} computed from the previous step, we perform joint decoding for all domains with a reduced overcomplete basis. For the separation domain, the basis contains

only those basis vectors that correspond to the distinguished variables. We decode x_{θ_j} and \hat{x}_{θ_i} with the reduced overcomplete basis:

$$y = \left(\Phi \left[\dots \Psi_{\theta_j} \dots \hat{\Psi}_{\theta_i} \dots \right] \right) \cdot \begin{bmatrix} \dots \\ x_{\theta_j} \\ \dots \\ \hat{x}_{\theta_i} \\ \dots \end{bmatrix}$$

where $\hat{\Psi}_{\theta_i}$ consists of a subset of columns of Ψ_{θ_i} that correspond to the distinguished variables in \hat{x}_{θ_i} . Our separation-based decoding method has general applicability.

12.2.4 Pulse Stream Recovery in the Frequency Warped domain

The reduced dimensionality of the union of subspaces captured by the model in Eq. (12.8) allows for an efficient and stable estimation of both the system impulse response \hat{h}_w and the reflectivity function \hat{x}_w from the compressed measurement vector

$$y = \Phi s + n = \Phi \mathbf{W}_{\theta_i}^\dagger \mathbf{H} x_w + n \tag{12.10}$$

being n the acquisition noise and where \hat{h}_w and \hat{x}_w denote an estimation of h_w and x_w , respectively. The general approach is to obtain the “best possible estimate” of x_w given a tentative estimate of h_w , then update the estimate of h_w accordingly, and iterate. The target signal s is assumed to belong to the warped disjoint convolutional model of pulse streams $\mathcal{M}_{S,F,\Delta}^{s,W}$. This strategy is commonly known as *Alternating Minimization* (AM). The implemented algorithm is a modified version of the one firstly presented in [95] and in Chapter 10 which has been adapted to perform in the warped domain.

12.3 Verification

Finite element analysis of an aircraft wing was performed by PZFlex (Weidlinger Assoc. Inc. CA) and, as a case study, the proposed framework was exploited to locate defects in an aluminum 1050A wing 1000×1000 mm and 3 mm thick. Four piezoelectric discs (PIC181, diameter 10 mm, thickness 1 mm) were bonded to the wing. The simulated setup designed with Solidworks (Dassault Systèmes ,USA) is shown in Figure 12.1 and the position of the transducers is defined in Table 12.1.

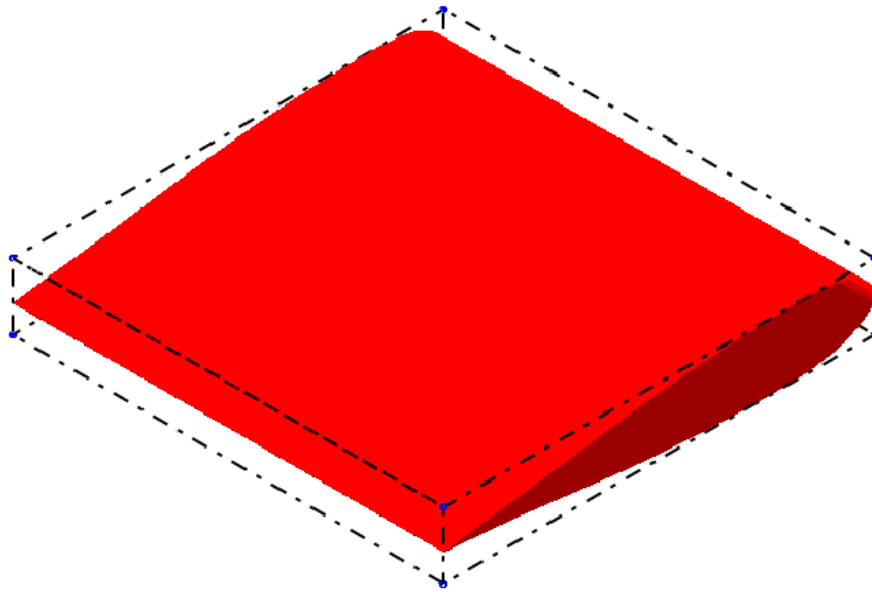


Figure 12.1: Simplified aircraft wing model used in the simulations. Simulated set up used to validate the defect location procedure with PZFlex and Solidworks CAD importing

Table 12.1: Actuator and receivers topology.

Coordinates	Actuator	Receivers		
x (m)	0.10	0.10	0.90	0.90
y (m)	0.10	0.70	0.10	0.70

The sampling frequency chose for the simulations was $f_s = 500$ kHz, sufficiently high to avoid aliasing effects, as the frequency content of the acquired signals vanishes

above 60 kHz. The active monitoring was performed by simulating a chirp as voltage input in (0.1, 0.1) m on the top of the surface (active piezoelectric discs) and recording the wave propagation by two sensors on the top surface.

In PZFlex simulation the structural damage was emulated as a cubic mass of 10 mm on the top of the wing surface. For example, the waveforms detected by the 3 receivers, after having placed the mass at the coordinates $x = 0.20$ m and $y = 0.55$ m, are shown in Figure 12.2.

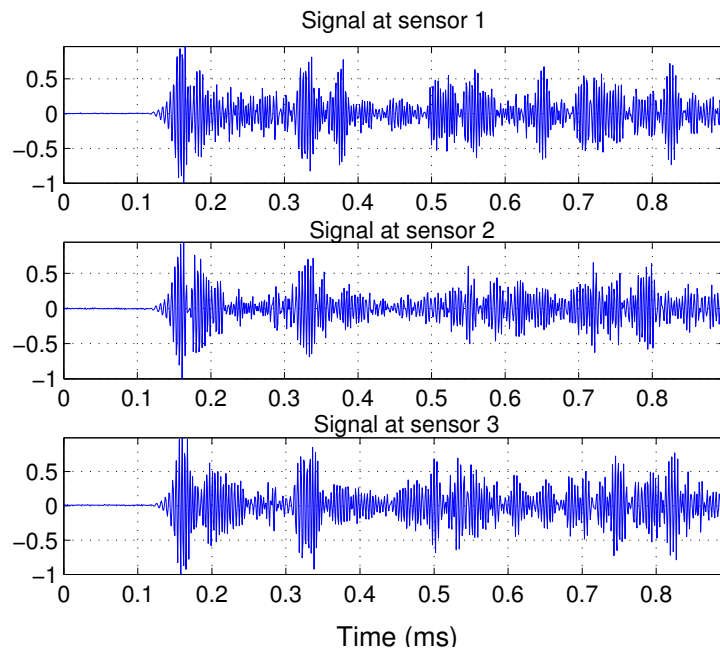


Figure 12.2: Simulated signals acquired by the 3 sensors whose coordinates are reported in Table 12.1.

As can be seen from the time waveforms, it is difficult estimating the time of arrival of echoes due to the mass (emulated defect) among the other interfering waves caused by edge reflections and multimodal propagation.

The acquired signals were processed through the random modulator pre-integrator implemented in Matlab (Mathworks Inc., MA) with the frequency specifications are the following: chipping frequency equal to 500 kHz and the information frequency $f_{inf} = 50$ kHz. In order to compensate for dispersion, first the WFT operator must be defined. In the $[0 - 300]$ kHz frequency range, only the two fundamental A_0 and

S_0 Lamb waves can propagate through this plate. The group velocity curve of the A_0 mode was used to shape the warping operator according to Eq. 12.2 because the energy in the A_0 mode is considerably greater than that retained by the S_0 mode for out-of-plane excitation.

In the recovery stage the orthogonal matching pursuit algorithm was applied to recover the sparse signal in the warped domain.

Figure 12.3 shows the sparse estimated signal related to the defect located in $x = 0.20$ m and $y = 0.55$ m and the passive sensor 2 at 0.6 m from the active sensor.

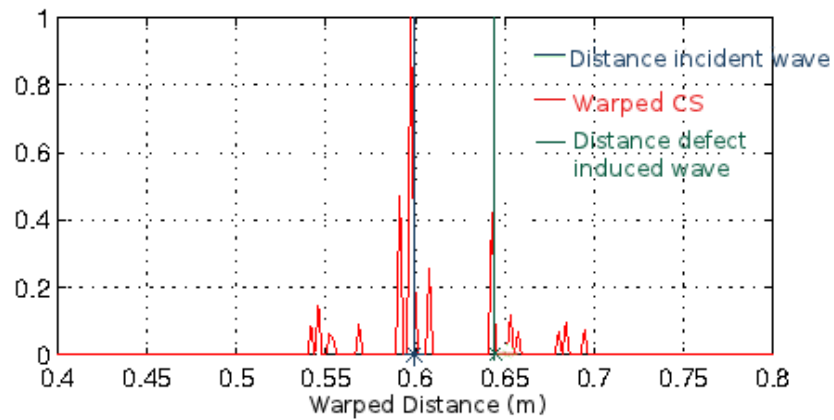


Figure 12.3: Sparse signal after the CS recovery

The local maxima of the reconstructed sparse signal are close to the real distance of the incident wave (blue) and the distance due to the reflection of the defect (green). The warped distance can be detected and the corresponding coordinates provide the distance traveled by the incident wave and the total distance of the wave reflected by the defect.

12.3.1 Results

To assess the feasibility of the proposed technique, a study on the dependence of the localization error with the number of bits used in the quantization stage was performed. In Table 12.2 the localization error and the mean absolute error (%) which is defined as the between the localization error and the actual defect position are shown.

Table 12.2: Localization error dependency on the quantization.

Number of Bits	Localization Error (mm)	Mean absolute error
8	19.3	2.9%
16	8.7	1.3%
24	3.1	0.5%

It is possible to see how using few bits, for example 8 bits, the error tends to rise reaching 2 cm. The choice of the number of bits depends on the specific control and application; a good compromise can be between 16-24 bits.

It is important to notice how the obtained results with the CS framework are very close to the localization error achieved applying only the compensation operator without lowering the sampling frequency using the random modulator as acquisition module. In Figure 12.4 the localization error comparison between compensation with and without Compressed Sensing acquisition is presented.

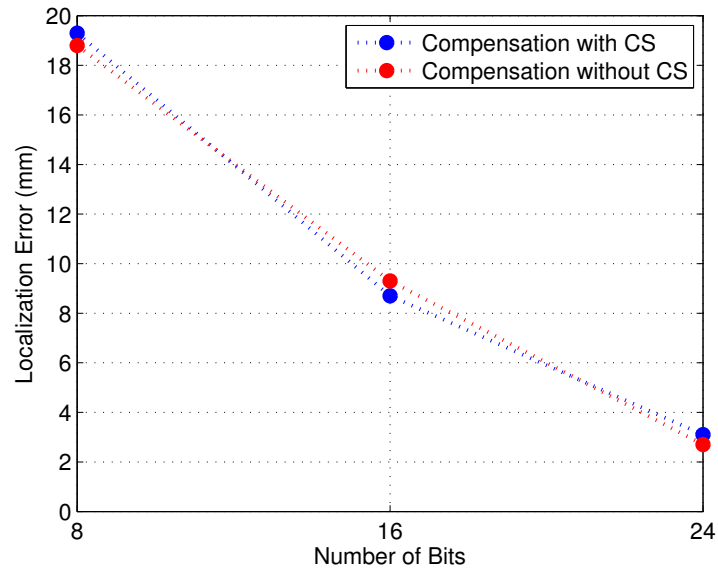


Figure 12.4: Localization error comparison between compensation with and without Compressed Sensing acquisition

It is possible to underline that the performance of the CS proposed algorithm was very close with the simple dispersion compensation warping procedure.

Chapter 13

Compressive Sensing for Wireless Transmission

Defeat is not the worst of failures.

Not to have tried is the true failure.

George Edward Woodberry

13.1 Introduction

A novel signal compression and reconstruction procedure suitable for guided wave based structural health monitoring (SHM) applications is presented in this Chapter. The integration of wireless communication technologies into SHM methods has to be investigated since they eliminate the cost of cable deployment and reliability issues due to aging and de-bonding of cables of traditional SHM systems, and have distinct advantages such as simple, cost-effective, flexible, and reconfigurable, thus allowing scalable installation.

A major limitation of wireless GW monitoring technology is the incompatibility between the high frequency content of ultrasonic signals and the limited data throughput of existing wireless transponders. However, in embedded sensing devices, the wireless connectivity may consume a large fraction of the available energy. Therefore, in order to achieve long battery lifetime, performing data reduction *locally*, i.e. within the

wireless smart sensor, is of primary importance. By doing so communication traffic can be greatly reduced, minimizing the need of storing or transmitting large amount of multichannel data.

Data reduction could consist either in the extraction of relevant information (such as time of flight or energy [98], [99], [100]) from the acquired waveform, or in signal compression. When the information extraction task is too much computationally onerous to be performed on an local embedded processor, the best option is to efficiently compress the acquired signal, and then to transmit it to a central unit where the signal is recovered and the processing is performed.

In this work, a signal compression strategy specifically dedicated to Lamb wave signals for SHM, and aimed at achieving high compression ratio with low distortion in signal recovery is proposed.

For signal compression, a novel approach is proposed whose starting point is the design of a suitable signal representation basis.

The framework rely on the assumption that Lamb wave signals can be sparsified in a frequency warped domain [21]. The warping procedure allows to design a time-frequency decomposition matched to the dispersive behaviour of Lamb waves a Wavelet Packet (WP) decomposition warped basis has been developed and applied. In the proposed approach, maximally sparse representations were achieved by implementing a basis optimization routine, namely the *Best Basis* algorithm, to design the wavelet filter banks which compute the transformation.

The proposed decomposition basis was exploited in the implementation of two well-known data compression schemes: the first one is based on an Embedded Zerotree (EZT) coding [101] the second one on Compressive sensing (CS) [102]. Both the approaches rely on the assumption that Lamb wave signals can be represented as sparse linear combinations of basis functions. It will be shown that this assumption is true when Wavelet Packet (WP) decomposition bases are considered. In the proposed approach, maximally sparse representations were achieved by implementing a basis optimization routine, namely the *Best Basis* algorithm, to design the wavelet filter banks which compute the transformation.

In particular, a transformation based on the Wavelet Packet (WP) transform and Embedded Zerotree Wavelet (EZW) coding in which the mother wavelet is parametrized and optimized with respect to the signal is proposed for signal decomposition.

The structure of this Chapter is as follows: in Section 13.2 the Wavelet Packet transform and the Best Basis parametrical optimization is presented, while Section 13.3 is devoted to the data compression procedures: the Embedded Zerotree WP encoding is presented in Section 13.3.1, and the Compressive Sensing procedure with the Best Basis WP as sparsifying basis is presented in Section 13.3.2.

The proposed Frequency Warped CS framework is described in Section 13.4.

The conclusions end the work.

13.2 Parametrized Discrete Wavelet Packet Transform

Multiscale transformations such as the wavelet transform (WT) analyse and represent efficiently ultrasonic [103], [104], [21], [100] or Electrocardiogram (ECG) signals [105]. Let us call $x \in \mathbb{R}^N$ the real-valued vector which may represent the discretized guided Lamb wave signal, in the considered application domain. The WT operator

$$\Psi = [\psi_1 | \psi_2 | \dots | \psi_N]$$

where each column-vector ψ_i is a *wavelet atom*, can be used to decompose the signal x such that $x = \Psi\alpha$, where α is the N -dimensional WT *coefficients vector*.

The signal is said to be *sparse* in the new representation basis, if the vast majority of the entries of $\alpha = [\alpha_1, \alpha_2, \dots, \alpha_N]$, are zero-valued or negligible. Sparse signals can be approximated using just the K largest entries of α and setting all other terms to zero:

$$x \approx \sum_{k=1}^K \alpha(k)\psi(k), \quad \text{with } K \ll N. \quad (13.1)$$

where the functions $\psi(k)$ are elements of the wavelet basis.

As for the WT, the inner products between the signal and the elements of the adjoint operator Ψ^\dagger which produce the wavelet coefficients can be computed efficiently by

applying nested low-pass h and high-pass g filters to the original signal x as suggested by the Multiresolution Analysis theory developed by Mallat [59]. Depending on the sequence (tree) of the low and high pass filters, different wavelet transforms take place.

For instance, Figure 13.1 depicts the tree which implements the so called Discrete Wavelet Transform (DWT). This structure of computation is equivalent to an octave-band finite impulse response (FIR) filter bank.

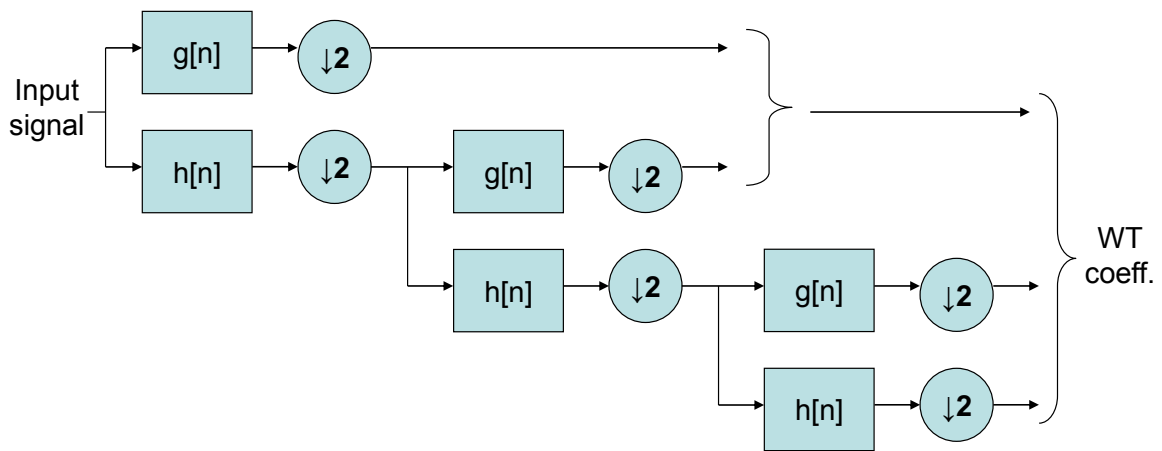


Figure 13.1: Computational tree of the Discrete Wavelet Transform.

As known, the frequency resolution which can be achieved by using an octave-band filter is limited, especially at high frequencies. This limits the use of the DWT in guided waves based applications.

The Wavelet Packet (WP) transform is a generalization of the DWT decomposition. In the DWT only the outputs of the filters h , the signal *approximations*, are filtered further, as can be seen from Figure 13.1.

In the corresponding WP situation also the outputs of the filters g , the *details*, are filtered while stepping in the next decomposition level.

This offers a richer analysis and the complete decomposition tree shown in Figure 13.2 is produced.

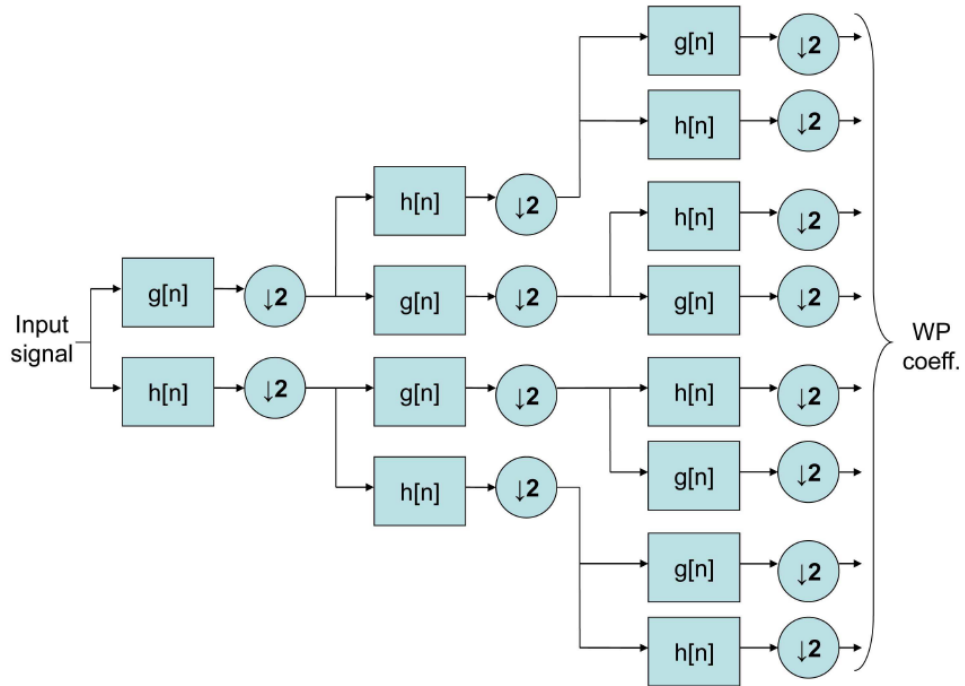


Figure 13.2: Computational tree of the Wavelet Packet decomposition.

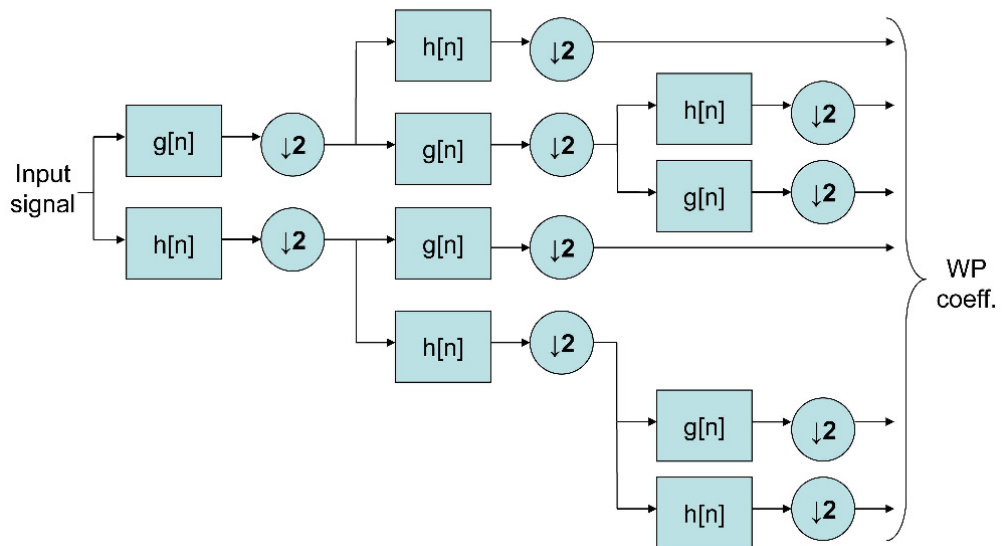


Figure 13.3: Pruned (Best Basis) Wavelet Packet decomposition.

Alternatively, instead of choosing a priori the basis functions as for the DWT or the full WP decomposition tree, the number of filtering stages of the full WP tree can be limited (*pruning*) by selecting the decomposition depending on the signal characteristics, as schematically represented in the example in Figure 13.3.

As for guided Lamb wave signals, a suitable pruning allows to obtain a discrete representation of the signal better matched to its inherent multi-scale structure.

To such aim, in this work a procedure that couples the pruning (*Best-Basis*) technique [106] with the lattice parametrization of the wavelet basis [107] is proposed. More specifically, the wavelet basis is defined by a proper parametrization of the coefficients of the scaling filter h . For a finite impulse response filter of length L , there are $L/2+1$ conditions to ensure that the wavelets define an orthogonal Discrete Wavelet Packet Transform (DWPT) and thus there are $L/2 - 1$ degrees-of-freedom to design the scaling filter h . The lattice parametrization presented in [107] offers the opportunity to design orthogonal wavelet filters via unconstrained parameters.

In particular, for $L = 6$ the design parameters α and β gives

$$\begin{aligned}
 i = 0, 1 : h[i] &= \frac{1}{4\sqrt{2}} \times [(1 + (-1)^i \cos \alpha + \sin \alpha)(1 - (-1)^i \cos \beta - \sin \beta) + \\
 &\quad + (-1)^i 2 \sin \beta \cos \alpha] \\
 i = 2, 3 : h[i] &= \frac{1}{2\sqrt{2}} \times [(1 + \cos(\alpha - \beta) + \sin \alpha + (-1)^i \sin(\alpha - \beta))] \\
 i = 4, 5 : h[i] &= \frac{1}{\sqrt{2}} - h(i - 4) - h(i - 2)
 \end{aligned}$$

The optimal parameters are chosen to minimize the distortion of the signal after decoding for a given compression rate, in the case of signal compression. The metric used to quantify the difference between the original signal $x[k]$ and the reconstructed signal $\hat{x}[k]$ after decoding is the percent residual difference (PRD)(%)

$$PRD = \sqrt{\frac{\sum_k (x[k] - \hat{x}[k])^2}{\sum_k x[k]^2}} \times 100$$

In other words, the selected decomposition is optimal in the sense that corresponds to a time frequency tiling that best concentrates the Lamb wave signal energy in few WP coefficients.

13.3 Data compression procedures

13.3.1 Embedded Zerotree wavelet coding

The Embedded Zerotree (EZT) wavelet technique [108] is a *transform-encoder* which operates on signals which have been acquired, digitized, and wavelet-transformed. EZT exploits the efficiency of the representation offered by the WP transform to effectively compress the signal. In particular, the EZT algorithm uses interrelations and self-similarities among WP coefficients in different sub-bands.

Thanks to these relations it is possible to organize the wavelet coefficients in *sub-trees*. If the lowest frequency wavelet coefficient in a subtree is zero or nearly zero (that is if its absolute value is below a given threshold) it is highly probable that all the other coefficients in the same subtree are also zero valued (i.e. the considered coefficient tree is a *zerotree*). If this is the case, the whole subtree can be encoded with a very limited number of bits. Threshold has to be accurately selected to achieve a predefined target compression ratio (CR%). Over-threshold coefficients are usually a very small subset of the total, and can be encoded with the Huffman algorithm [109] which produces a lossless data compression.

It is worth noting that the subtrees structure for a given wavelet transformed signal can be defined dynamically for an arbitrary WP decomposition [110], so that the EZT algorithm can be easily extended to the Best Basis WP decomposition.

The computational scheme based on EZT compression of the Best Basis WP coefficients and Huffman coding is reported in Figure 13.4. The basis optimization procedure is halted when the wavelet representation is maximally sparse.

Then the EZT procedure and the Huffman coding are launched. After transmission, the acquired waveforms can be recovered by performing sequentially:

- i) Huffman decoding
- ii) the inverse zerotree encoding (IEZT)
- iii) the inverse WP transformation (IWP)

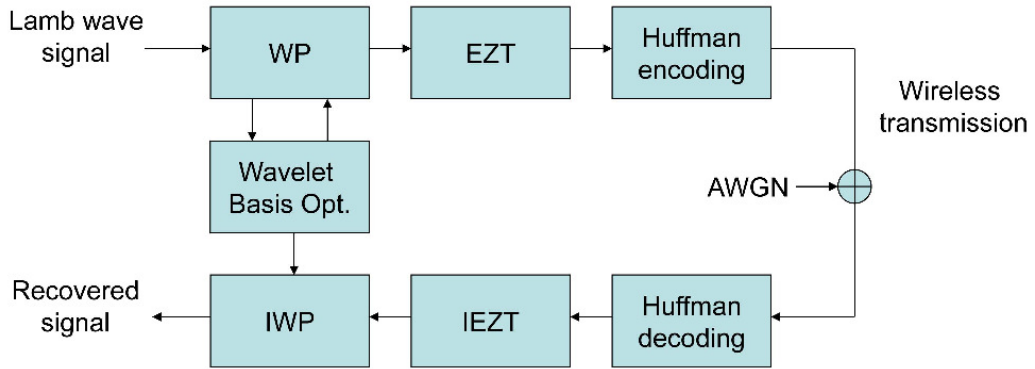


Figure 13.4: Wavelet Packet with Embedded Zerotree-Huffman coding System

13.3.2 Compressed Sensing Best-Basis Wavelet Packet

The Compressed Sensing (CS) approach differs considerably from that of the transform encoders, such as the EZT, but it also relies on the fact that the signal to be compressed is sparse in the WP Best Basis representation described in Section 13.2. Indeed, the CS theory states that if x is sparse, one can recover its K -term approximation by only collecting $M = O(K \log N/K)$ measurements, thus *sensing and compressing at the same time*.

The so called M -dimensional measurement vector y is acquired by computing this product:

$$y_i = \Phi x \quad (13.2)$$

To guarantee a robust and efficient signal recovery, the sensing matrix Φ must be properly designed. In particular, it must be verified that Φ and the WT operator Ψ are incoherent, that is the parameter μ :

$$\mu(\Phi, \Psi) = \sqrt{N} \cdot \max_{1 \leq k, j \leq N} |\langle \phi_k, \psi_j \rangle| \quad (13.3)$$

must be small enough. This property is usually fulfilled when the sensing matrix Φ is a random matrix with Gaussian distributed entries.

Several different hardware architectures have been proposed to perform the multiplication in Eq. 13.2, some solutions are based on analog circuits [111], some others, as the one used in this work, on the multiplication of digital signals [112].

Finally, an accurate reconstruction of the signal x from the linear measurement vector y can be accomplished by solving the following convex optimization problem

$$\min_{\tilde{\alpha} \in \mathbb{R}^N} \|\tilde{\alpha}\|_1 \quad \text{subject by} \quad \|\Phi\Psi\tilde{\alpha} - y\|_2 \leq \sigma \quad (13.4)$$

where σ bounds the amount of noise unavoidably corrupting the data, and $\tilde{\alpha}$ is the N -dimensional sparse approximation of the coefficient vector.

The full compression and reconstruction scheme is shown in Figure 13.5.

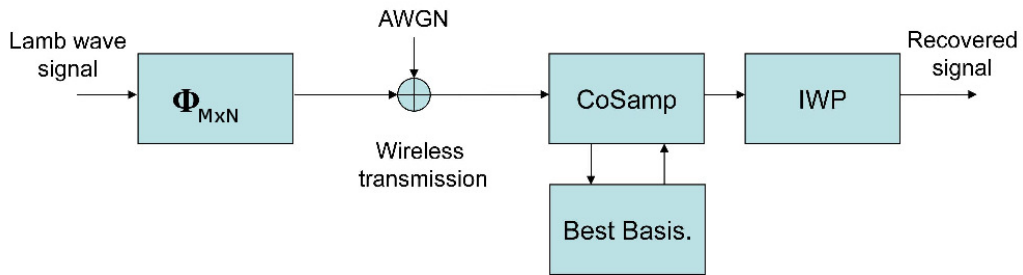


Figure 13.5: Best Basis WP Compressed Sensing scheme

Such method performs an iterative joint estimation of the signal x (*CoSamp* block) and of the Best Basis WP operator Ψ . The optimization of WP tree pruning is performed by selecting the wavelet filters h and g a priori with the procedure described in [107], as in the EZT case.

In the acquisition stage a multiplication between the signal and a random matrix $M \times N$ is performed; in the reconstruction stage from the measurement y the algorithm described in Table 13.1 is applied to recover the signal x .

The Best Basis Compressive Sensing algorithm perform an iterative estimation of the signal x , updating at each iteration the best wavelet packet tree. The main difference between the algorithm [113] is related to the wavelet filter that in this work is optimize a priori as described in Section 13.2.

Initialization	: $k = 0, x_0 = 0$
repeat	
Update the Estimate	: $\tilde{x}_k = x_k + 1/(\mu\Phi^T(y - \Phi x_k))$
Update the Best Basis	: $\lambda_{k+1} = \arg \min C(\tilde{x}_k, \mathcal{B}_{best\ basis}^\lambda)$ using algorithm in [113] with mother wavelet ϕ obtained using the optimal parametrization
Denoise the estimate	: $x_{k+1} = \left(\sum_m \max \left(0, 1 - \frac{1}{ \langle s, \psi_m \rangle } \right) \langle s, \psi_m \rangle \right) \psi_m$
until	$\ x_{k+1} - x_k\ \leq \eta$

Table 13.1: Best-Basis Compressed Sensing Algorithm

13.4 Compressed Sensing in Group-Delay Covariant Basis

In this section, the procedure to extend the applicability of CS framework to dispersive signals is described: it is based on the use of the frequency warped operator to further enhance the sparsification of the signal $s(t)$.

Like ordinary scaling functions, warped scaling functions are strategical for the construction of warped wavelet bases. In the Fourier domain the warped wavelets are related to the dyadic wavelets as follow:

$$\bar{\Psi}_{n,m}(f) = (\mathbf{W}\psi_{n,m})(f) = \sqrt{\frac{dw(f)}{df}} \Psi_{n,m}(w(f)) = \sqrt{2^n \frac{dw(f)}{df}} \Psi(2^n w(f)) e^{-j2^n m w(f)}$$

The warped wavelets are not simply generated by dilating and translating a mother wavelet. Rather, the translated wavelets are generated by all-pass filtering $e^{-j2^n m w(f)}$. Scaling also depends on the warping map $w(f)$.

Figure 13.6 shows how the Wavelet tiling of the TF plane leads to match with a single propagating mode as reported in Figure 13.7, but the resolution on the frequency axis is not variable. Atoms change their shape versus time with the dispersive properties of the single mode.

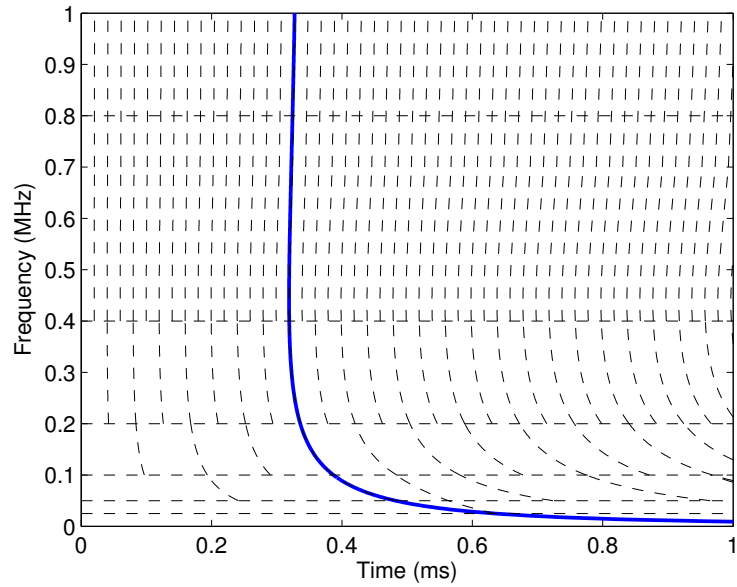


Figure 13.6: Tiling of the time-frequency plane for the frequency warped wavelet transform for the A_0 . The solid curves represent the dispersive group delay curves for the Lamb waves for a traveled distance of 1 m.

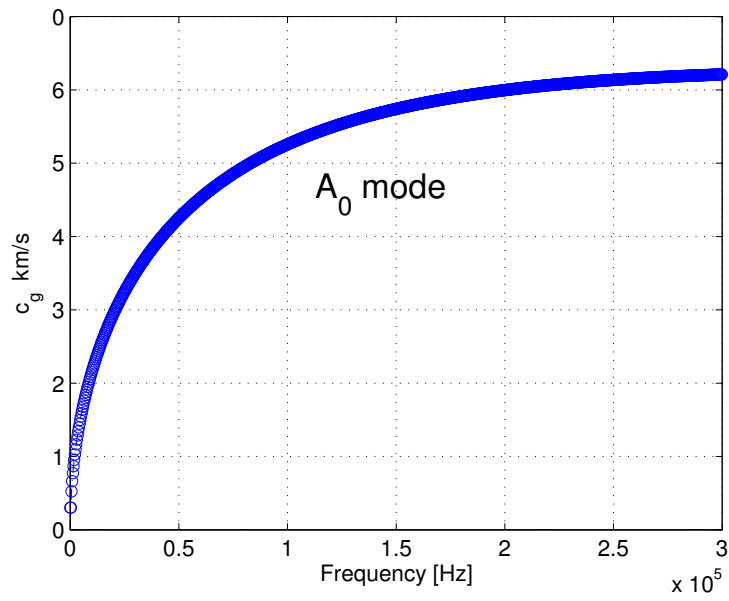


Figure 13.7: Group velocity curve for the propagating A_0 mode for an aluminum plate of 3 mm of thickness

Given an orthogonal and complete set of dyadic wavelets $\{\psi_{n,m}\}_{n,m \in \mathbb{Z}}$ where

$$\psi_{n,m}(t) = 2^{-\frac{n}{2}} \psi(2^{-n}t - m) = D_{\frac{1}{2}}^n S^m \psi(t)$$

where S^m represents the shift-by- m operator, one defines the warped wavelets as $\bar{\psi}_{n,m} = \mathbf{W}\psi_{n,m}$. The set $\{\bar{\psi}_{n,m}\}_{n,m \in \mathbb{Z}}$ is orthogonal since \mathbf{W} is a unitary operator, such that:

$$\langle \mathbf{W}\psi_{n',m'}, \mathbf{W}\psi_{n,m} \rangle = \langle \psi_{n',m'}, \mathbf{W}^\dagger \mathbf{W}\psi_{n,m} \rangle = \langle \psi_{n',m'}, \psi_{n,m} \rangle = \delta_{n',n} \delta_{m',m}$$

and complete since, by unitary equivalence, given $x \in \mathbf{L}^2(\mathbb{R})$ it is always possible to find $y \in \mathbf{L}^2(\mathbb{R})$ such that $s = \mathbf{W}y$. Hence, by expanding y over the dyadic wavelet set and exploiting the continuity of the warping operator, we have

$$s(t) = \mathbf{W}y(t) = \mathbf{W} \cdot \sum_{n,m \in \mathbb{Z}} y_{n,m} \psi_{n,m} = \sum_{n,m \in \mathbb{Z}} y_{n,m} \bar{\psi}_{n,m}(t)$$

where $y_{n,m} = \langle y, \psi_{n,m} \rangle = \langle x, \mathbf{W}\psi_{n,m} \rangle = \langle x, \bar{\psi}_{n,m} \rangle = \langle \mathbf{W}^\dagger x, \psi_{n,m} \rangle$.

Therefore the signal is sparsified by means of the inverse warping operator \mathbf{W}^\dagger , then the expansion coefficients on a nonstationary wavelet basis in the classical sense are computed within the Compressed sensing framework.

The resulting block scheme is reported in Figure 13.8.

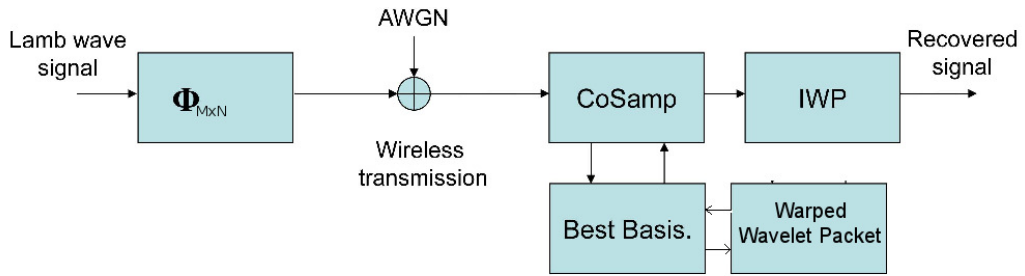


Figure 13.8: Best Basis Frequency Warped Wavelet Packet Compressed Sensing scheme

13.5 Experimental Verification

The compression algorithms detailed in the previous sections have been applied to the passive monitoring setup schematically depicted in Figure 13.9.

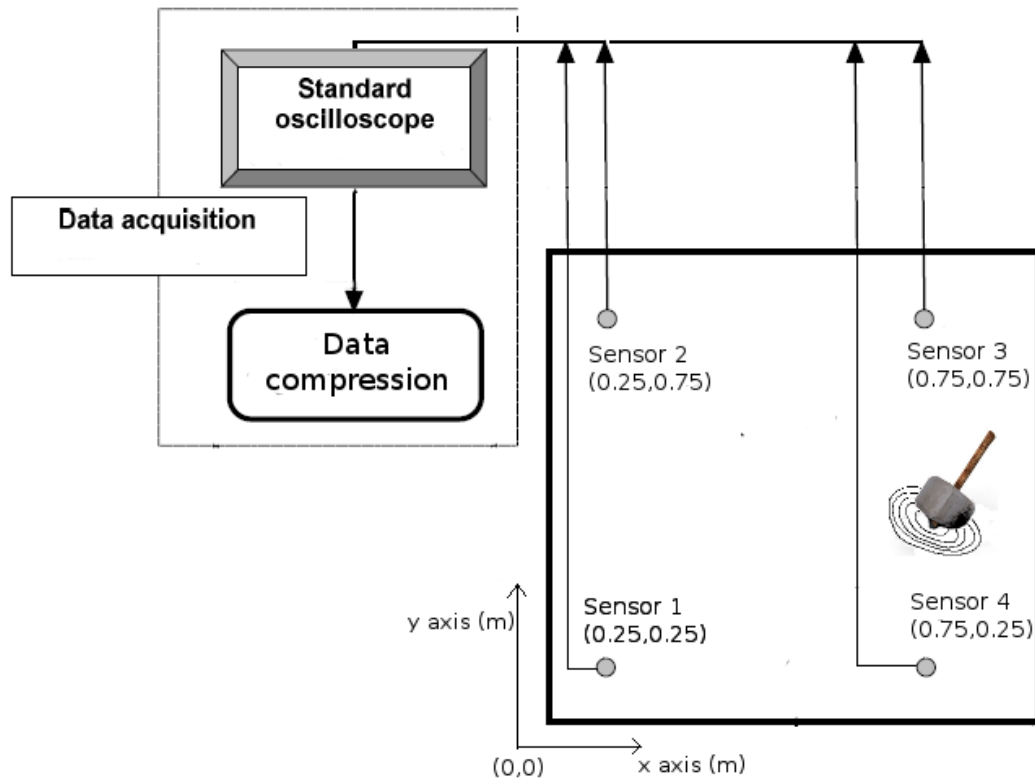


Figure 13.9: Sketch of the experimental setup adopted to acquire the lamb wave signals generated by impacts

An aluminium 1050A plate 1 m \times 1 m wide and 0.003 m thick was sensorized with piezoelectric transducers (PZT discs, diameter 0.01 m, thickness 0.001 m).

Guided waves were excited by hitting the plate with an impact hammer.

The generated signals were recorded using a LC534 series LeCroy oscilloscope at a sampling frequency of 300 kHz.

A first set of acquisitions was used as a reference to select the wavelet filter coefficients with the procedure detailed in [107].

The coefficients are reported in the following table:

n	1	2	3	4	5	6
h_n	-0.2	0.5	0.3	-0.1	0.5	0.2
g_n	-0.2	0.5	0.3	-0.1	0.5	0.2

Table 13.2: WP Filter coefficients.

Then, the Best Basis WP filter bank was selected according to the pruning procedure described in Section 13.2. The proposed WP analysis provides a very efficient representation of the acquired signals.

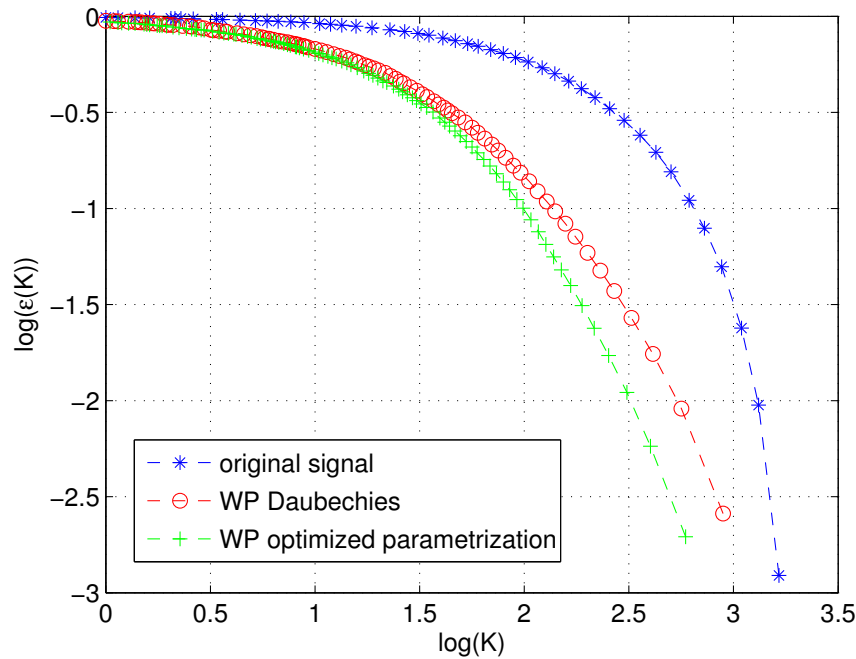


Figure 13.10: Error ϵ in the nonlinear approximation of the acquired signals through the largest M coefficients for the parameterized Best Basis WP representation.

This is illustrated in Fig 13.10, where K is the sparsity of the signal and the error

$$\epsilon(K) = \frac{\|x - x_M\|^2}{\|x\|^2}$$

associated with the non-linear approximation x_M (see Eq.13.1) of the acquired wave x is plotted versus the number of coefficients, M , used in the selected linear expansion.

The error is calculated for a database of 84 signals. Figure 13.10 shows that the use of the Best Basis WP filters in Table 13.2 (green line) instead of the well known Daubechies filter (red line), in the analysis, yields to a more sparse codification of the informative content associated with the acquired signals.

13.5.1 Best Basis Wavelet Packet with Embedded Zerotree Coding

The performance of the EZT coding has been studied by considering the trade off between the Compression Ratio (CR) and the distortion of the reconstructed signal. The distortion metric used to quantify the difference between the original signal x and the reconstructed signal \hat{x} is the Percent Residual Difference (PRD)(%)

$$PRD = \sqrt{\frac{\sum_n (x[n] - \hat{x}[n])^2}{\sum_n x[n]^2}} \times 100$$

The Compression Ratio is varied by changing the value of the EZT threshold.

In Table 13.3, the values of the CR and PRD obtained on a experimental signal resulting from an impact in (0.45, 0.30) cm are reported.

Threshold EZW	CR	PRD (%)
0.001	26.97	0.84
0.003	43.22	2.25
0.007	56.29	6.18
0.013	73.12	7.71
0.035	87.53	33.55
0.100	94.55	43.24

Table 13.3: Performances of the wavelet parametrized filter according to the EZW threshold.

It is worth noting that an optimal PRD is achieved with low EZT threshold but this leads to a low CR; on the contrary an high threshold produces a good compression but an high PRD. A good compromise between CR and PRD can be obtained when

the EZW threshold is equal to 0.013. In Figure 13.11 is shown the acquired guided wave and the recovered signals for different EZT threshold values.

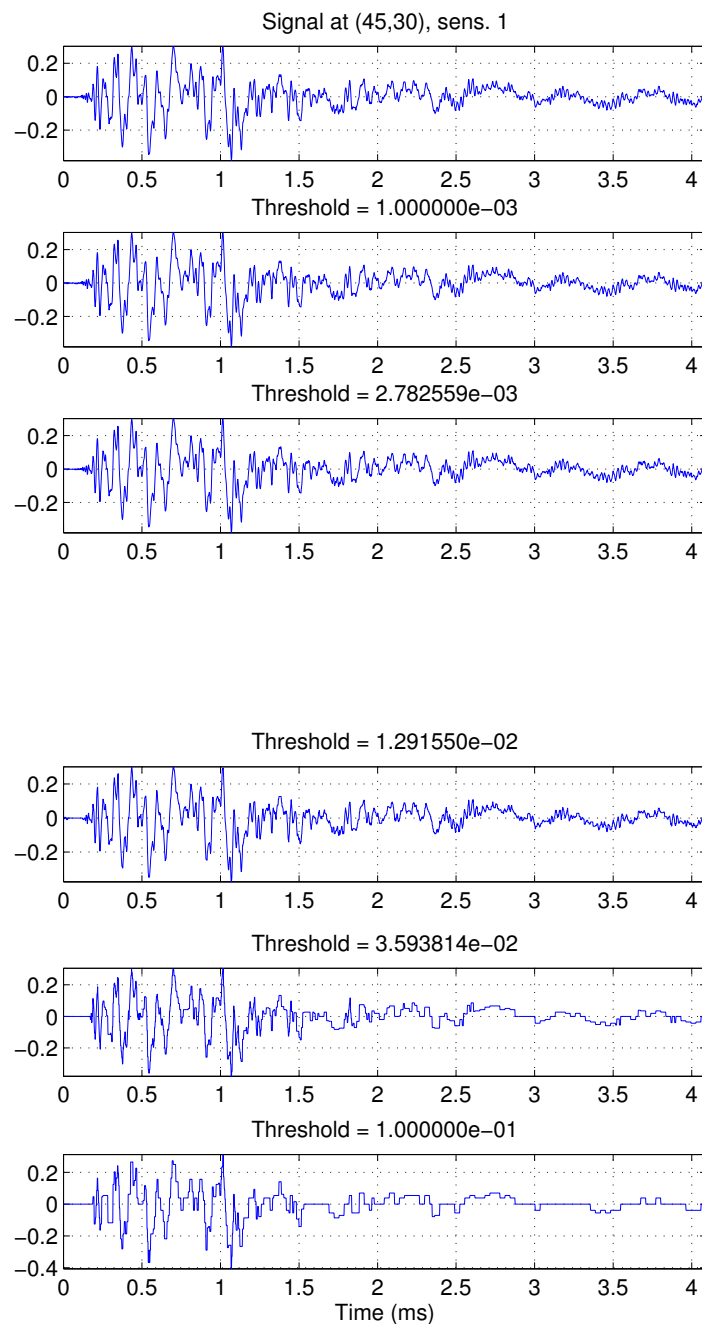


Figure 13.11: Reconstructed signals results in dependence of the EZT threshold

In the Best-Basis CS approach, the performance in terms of CR is determined by the ratio $\frac{m}{n}$, where m and n are the dimensions of the sensing matrix $\Phi_{m \times n}$.

The wavelet filter used in the procedure is again the one detailed in Table 13.2.

In Table 13.4 is reported the PRD obtained for different CR values in two cases:

1. pure wavelet packet basis as sparsified dictionary (“without \mathbf{W} ”);
2. by using the warped wavelet packet basis (“with \mathbf{W} ”).

CR (%)	PRD	
	without \mathbf{FW}	with \mathbf{FW}
50	3.17	2.52
62,5	5.18	4,21
70	6.71	5.37
75	7.32	6.08

Table 13.4: Performance comparison of the Compressed Sensing framework with and without frequency warping (impact in (0.30, 0.30) m)

13.5.2 Performance comparison

In Figure 13.12, the performance comparison between the EZT algorithm and the CS framework is reported. The results are related to 84 acquisitions. Such dataset was generated by recording the acoustic emissions produced by 21 different impacts with the described 4 PZT sensors.

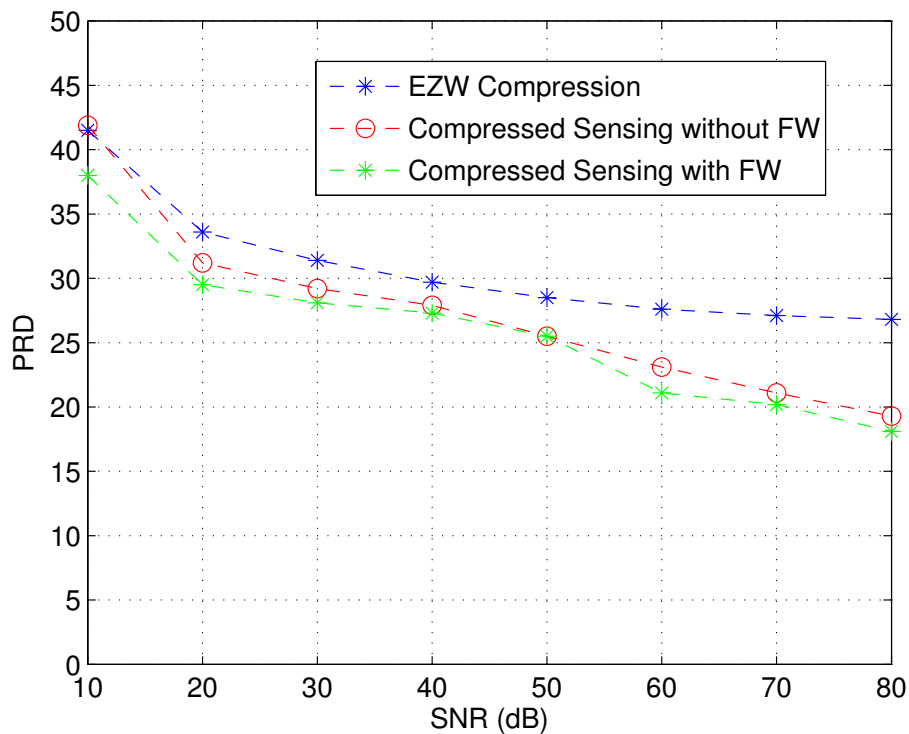


Figure 13.12: Performance comparison between EZT algorithm and Wavelet Compressed Sensing related to the PRD at different SNRs with CR = 70%.

The compression and recovery algorithms were applied both on the acquired signals and on corrupted versions of the same signals, obtained by adding white gaussian noise (AWGN) to the transmitted waveforms. The EZT threshold was set equal to 0.013. The PRD has been calculated between the original signal without noise and the reconstructed signal.

It can be seen how the PRD achieved by the proposed Frequency Warped CS approach is lower than the one achieved by EZT for all the considered SNR levels.

In Figure 13.13, the comparison between the EZT algorithm and the proposed CS framework related to the PRD at different compression ratios CR(%) when the signal to noise ratio is kept constant (SNR= 30) is reported.

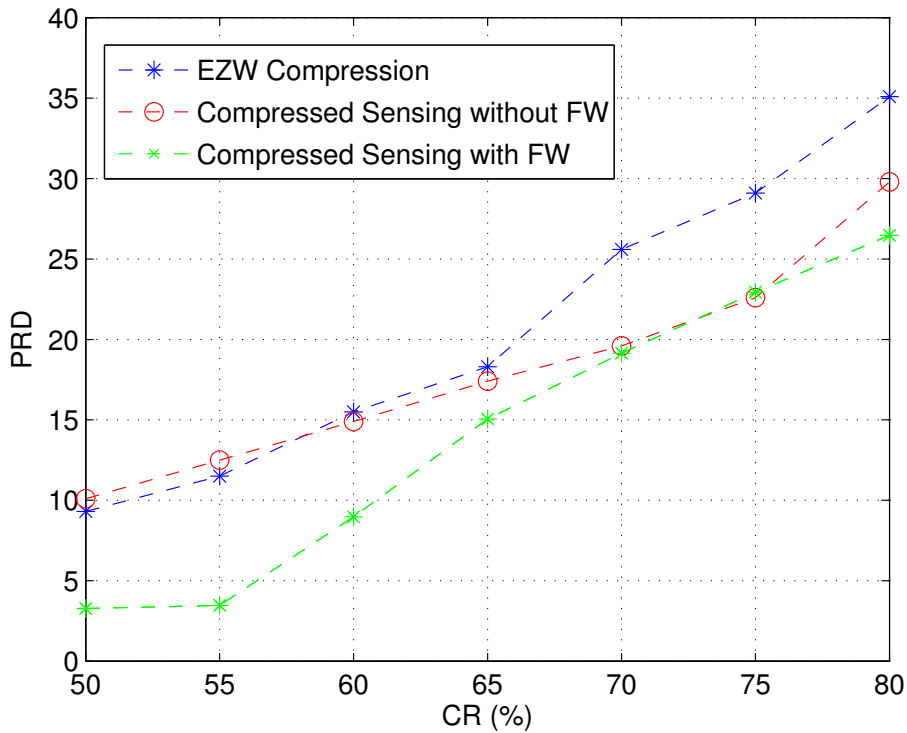


Figure 13.13: Performance comparison related to the PRD at different compression ratios with SNR= 30dB.

It can be noticed that for high CR with the traditional CS approach it is possible to achieve lower reconstruction error, while for low CRs the EZT approach gives slightly better results.

Finally, it worth noticing that the CS performed in the warped decomposition basis produces slightly better results w.r.t. the one performed in the Best-Basis wavelet packet domain in all the considered scenarios.

13.5.3 Impact Localization Performances with and without signal compression

In SHM applications the data compression is necessary to send the acquired signals to a central base station which perform a proper algorithm in order to find for example a possible failure or impact from the ultrasound propagating wave. It is important to compare the localization performances of a reference algorithm using compressed or not compressed signals.

In order to estimate the of the localization error the compressed signals and the original ones have been applied to the algorithm described in [53].

Figure 13.14 shows the localization cumulative error rate with an without signal compression

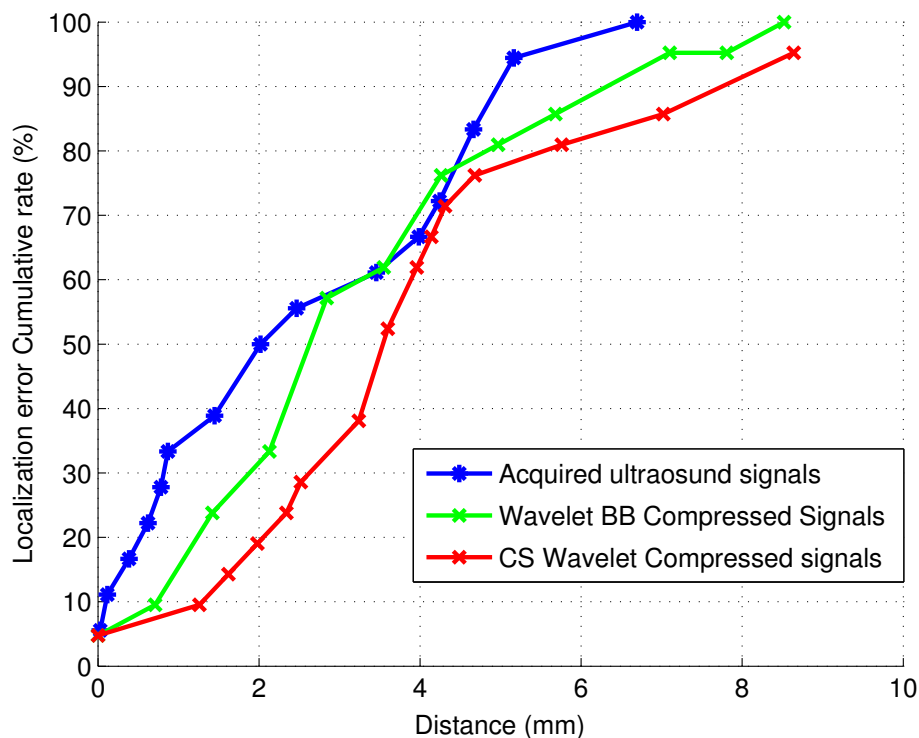


Figure 13.14: Comparison of the localization cumulative error with and without signal compression.

The blue line represents the results obtained and reported in [100] without data compression; the red line represents the cumulative error with Best-Basis wavelet compression with threshold 0.013. The green line represents the localization error cumulative rate (%) for the novel CS procedure which incorporates the BB frequency warping wavelet. It is worth noticing that despite to the obvious performance degradation with the compressed signal, the error is less than 5 mm in more than the 60% of the cases.

The difference of the mean localization error with/without compression is reported in Table 13.5; this parameter has been calculated with the formula

$$\frac{\bar{e}_{comp} - \bar{e}_{acq}}{\bar{e}_{acq}} (\%),$$

where \bar{e}_{comp} is the mean error value obtained with compressed signals and \bar{e}_{acq} is the mean error value obtained without compression, for the whole set of impact depending on the EZW threshold:

Threshold EZW	CR	$\frac{\bar{e}_{comp} - \bar{e}_{acq}}{\bar{e}_{acq}} (\%)$
0.001	26.97	6.2
0.003	43.22	6.2
0.007	56.29	6.8
0.013	73.12	7.3
0.035	87.53	15.7
0.100	94.55	21.5

Table 13.5: Localization error performances without and with compression according to the EZW threshold.

13.6 Discussion

In this work, Lamb wave signal compression and reconstruction procedures were presented. In particular, the Compressive Sensing approach is compared with the Embedded Zerotree algorithm with Huffman coding. Both the considered approaches

are based on wavelet filters optimization procedures to generate a sparse but accurate multiscale representation of the acquired dispersive signal. The wavelet filter bank is optimized to match the signal characteristics using lattice parametrization which offers the opportunity to design orthogonal wavelet filters via unconstrained parameters. Experimental results show how the compression strategies are suitable for data transmission reaching a percent residual difference of 8 – 10% and a Compression Ratio of 75%. In conclusion, CS applied to Best Basis wavelet coefficients and optimization of the mother wavelet through parametrization is particularly suited to provide an adaptive approach for optimal signal representation with low Signal-to-Noise Ratios and high compression ratios.

Conclusions

In this thesis, the study and development of techniques for processing of ultrasonic signals and time-frequency analysis in the context of applications of non-destructive testing of structures were presented. In particular, the activity was focused on the implementation of embedded system for the localization of impacts on aluminum plates and of composite material using a proper time-frequency analysis techniques for compression and reconstruction of the ultrasonic signals and compressive sensing techniques for the acquisition with a sampling frequency lower than the Nyquist one. A method to extract the difference in distance travelled by stress guided waves was proposed. The method applies a dispersion compensation procedure on the signals acquired by passive sensors, thus overcoming the difficulties associated with arrival time detection based on classical thresholding procedures. Then, a suitable wavelet decomposition is applied to the cross-correlating signals to reduce the effect of multiple edge reflections. The analysis of the wavelet transform magnitude reveals the difference in distance travelled by the wave to reach the different sensors. Finally, multilateration is applied. Excellent performance in terms of the point of impact localization is shown through experiments since the estimated impact positions are very close to the Cramèr-Rao lower bound. Further, the reliability of the proposed approach in the presence of reverberation makes the new tool suitable for automatic acoustic emission localization procedures. Future developments include the generalization of the proposed approach to applications in which higher-order modes contaminate the acquired data, and to applications characterized by anisotropic propagation, such as

detection of impacts in composite plates. Furthermore an efficient wireless embedded structural monitoring system for impact localization based on Lamb waves dispersion compensation tool described before was proposed. The processing framework and the algorithm are implemented on a STM32F4 discovery board with advantages of compactness, low-power consumption, high efficiency and precision. The system was validated experimentally to locate impacts in a aluminum plate with four sparse PZT sensors.

For the active monitoring application, a signal processing strategy aimed at locating defects in plates by analyzing actuated and received Lamb waves by PZT sensors was proposed. The method is suitable for chirped pulse actuations, and it is based on a two-step procedure applied to the acquired signals. The signal processing reveals directly the distance traveled by the dispersive waves thus overcoming the difficulties associated to arrival time detection. In particular, by exploiting the dispersion compensation properties of the WFT, waveforms characterized by a unique time-frequency pattern are obtained. The actuated chirp frequency modulation is compressed in a subsequent processing step. Excellent performances in terms of defects localization are shown through experiments. It is worth noticing that the robustness of the wave traveled distance estimation allows to achieve such performances with sparse arrays of conventional transducers. Thanks to its unique potential the developed tool could pave a new class of procedures to locate defects in waveguides. Optimized and adaptive selection of the array shape and size are under investigation to further improve accuracy of the proposed approach.

Furthermore a procedure to transmit ultrasonic data with high compression is presented based on a novel Compressed Sensing procedure. The proposed approach combines the Wavelet Packet multiresolution analysis, best basis selection and coefficients thresholding to generate a sparse but accurate time-frequency representation of the acquired dispersive signal. The mother wavelet choice is optimized to match the signal characteristics using lattice parameterization. In the reconstruction stage a modified CS Matching Pursuit algorithm was implemented based on best basis selection. Experimental validation shows how the proposed model is suitable for data

transmission reaching a percent residual difference of 8-10% and a compression ratio of 75. Furthermore the CS procedure performance are comparable with the traditional EZW modified algorithm for wavelet packet but the proposed algorithm is immune to transmission noise. In conclusion, CS applied to best basis wavelet coefficients and optimization of the mother wavelet through parameterization provides an adaptive approach for optimal signal representation for compression with low Signal-to-Noise Ratio.

Finally the development of a compressive sensing (CS) acquisition and reflectivity function estimation was presented. The proposed CS scheme improving the detection of the distance traveled by guided waves can be effectively used in conventional Lamb wave inspection systems. The tool exploits the warping frequency transform to project the acquired signals in a dispersion-compensated basis. In the reconstruction stage, an alternating minimization (AM) procedure is performed to recover both the excitation shape and the reflectivity function. Experimental validation shows the effectiveness of the proposed algorithm as a suitable tool to locate defect-induced reflections with compressed acquisitions. Future developments include the generalization to applications characterized by anisotropic and multi-modal propagation, such as the detection of defects in composite plates. In such cases, it is foreseen that instead of projecting the signal in a given warped domain, novel decomposition strategies will be implemented, based on the construction of a redundant representation basis which can capture multiple dispersive behaviors. If so, all the considered modes would contribute to estimate the desired sensor-defect distances. Note that the implemented algorithm operates as a blind deconvolution tool, without exploiting the information about the actuating waveform; therefore, the proposed tool has the potential to be applied also in contexts where no prior knowledge about the incipient pulse is given, such as in acoustic emissions monitoring, or in impact localization tasks.

Publications

Journals

- A. Perelli, L. De Marchi, L. Flamigni, A. Marzani, G. Masetti
Compressed Sensing of Lamb Wave Signals in Wireless Structural Health Monitoring Applications, submitted to Digital Signal Processing, December 2013
- A. Perelli, T. Di Ianni, A. Marzani, L. De Marchi, G. Masetti, **Model-Based Compressive Sensing for Damage Localization in Lamb Wave Inspection**, IEEE Transactions on Ultrasonics, Ferroelectrics and Frequency Control, vol. 60, n. 10, pp. 2089-2097, October 2013, doi.org/10.1109/TUFFC.2013.2799
- A. Perelli, L. De Marchi, A. Marzani, N. Speciale
Frequency warped cross-wavelet multiresolution analysis of guided waves for impact localization, Signal Processing, vol. 96, Part A, pp. 51-62, March 2014, dx.doi.org/10.1016/j.sigpro.2013.05.008
- L. De Marchi, A. Perelli, A. Marzani
A signal processing approach to exploit chirp excitation in Lamb wave defect detection and localization procedures, Mechanical Systems and Signal Processing, vol. 39, pp. 20-31, 2013, doi.org/10.1016/j.ymsp.2012.10.018

- A. Perelli, L. De Marchi, A. Marzani, N. Speciale
Acoustic emission localization in plates with dispersion and reverberations using sparse PZT sensors in passive mode, Journal of Smart Materials and Structures, vol. 21 n. 2, February 2012, doi.org/10.1088/0964-1726/21/2/025010

Book Chapter

- R. Rotili, C. De Simone, A. Perelli, S. Cifani, S. Squartini
Joint Multichannel Blind Speech Separation and Dereverberation: a real-time algorithmic implementation, Advanced Intelligent Computing Theories and Applications, 2012, vol. 93, p. 85-93, Springer

Conferences

- A. Perelli, L. De Marchi, A. Marzani, S. Freear
Compressive Sensing for Damage Detection in Composite Aircraft Wings, IWSHM 2013: 9th International Workshop on Structural Health Monitoring
- L. De Marchi, A. Perelli, N. Testoni, A. Marzani, D. Brunelli, L. Benini
A small, light and low-power passive node sensor for SHM of composite panels, IWSHM 2013: 9th International Workshop on Structural Health Monitoring
- A. Perelli, S. Harput, L. De Marchi, S. Freear
Compressive Sensing with Frequency Warped Compensation for Damage Detection in Composite Plate, IEEE International Ultrasonics Symposium IUS 2013
- A. Perelli, S. Harput, L. De Marchi, S. Freear
Frequency Warping Compressive Sensing for Structural Monitoring

- of Aircraft Wing**, DSP 2013: 18th International Conference on Digital Signal Processing
- L. De Marchi, N. Testoni, A. Perelli, A. Marzani
Extension of Lamb Waves Defect Location Techniques to the case of Low Power Excitation by Compressing Chirped Interrogating Pulses, Key Engineering Materials vol. 570 pp. 940-947 2013
 - A. Perelli, L. De Marchi, L. Flamigni, A. Marzani, N. Speciale
Wavelet Best Basis Compressed Sensing of Ultrasonic Guided Waves, Proceedings of SPIE 2013
 - L. De Marchi, A. Marzani, M. Miniaci, A. Perelli, N. Testoni
Localization of defects in irregular waveguides by dispersion compensation and pulse compression, Proceedings of SPIE 2013
 - A. Perelli, C. Caione, L. De Marchi, D. Brunelli, A. Marzani, L. Benini
Design of a Low-Power Structural Monitoring System to Locate Impacts based on Dispersion Compensation, Proceedings of SPIE 2013
 - A. Perelli, C. Caione, L. De Marchi, D. Brunelli, A. Marzani, L. Benini
Design of an ultra-low power device for aircraft structural health monitoring, Design, Automation and Test in Europe DATE 2013
 - A. Perelli, T. Di Ianni, L. De Marchi, N. Testoni, N. Speciale
Compressive Sensing with Warped Frequency Models in Lamb Waves Damage Detection Procedures, IEEE International Ultrasonic Symposium, October 2012
 - A. Perelli, L. De Marchi, E. Baravelli, A. Marzani, N. Speciale
Warped-Wigner-Hough Transformation of Lamb Waves for Automatic Defect Detection, IEEE International Ultrasonic Symposium, October 2011

- A. Perelli, L. De Marchi, A. Marzani, N. Speciale
Passive Impacts Localization based on Dispersion Compensation and Cross-Correlated Signals Wavelet Analysis, International Congress on Ultrasonics, September 2011
- L. De Marchi, A. Marzani, A. Perelli, N. Testoni, N. Speciale
Guided Waves Characterization of Bamboo Fibers Reinforced Composites, International Congress on Ultrasonics, September 2011

Bibliography

- [1] D. Balageas, C. P. Fritzen, and A. Guemes, *Structural Health Monitoring*. ISTE Ltd, London, UK, 2006.
- [2] C. Boller, “Next generation structural health monitoring and its integration into aircraft design,” *International Journal of Systems Science*, vol. 31, no. 11, pp. 1333–1349, 2000.
- [3] R. P. Dalton, P. Cawley, and M. Lowe, “Propagation of acoustic emission signals in metallic fuselage structure,” *IEE Proc.-Sci. Meas. Technol.*, vol. 148, no. 4, pp. 169–177, 2001.
- [4] —, “The potential of guided waves for monitoring large areas of metallic aircraft fuselage structure,” *Journal of Nondestructive Evaluation*, vol. 20, no. 1, pp. 29–46, 2001.
- [5] L. De Marchi, A. Marzani, A. Perelli, N. Testoni, and N. Speciale, “Guided waves characterization of bamboo fibers reinforced composites,” in *AIP Conference Proceedings*, vol. 1433, no. 1. American Institute of Physics, 2012, pp. 447–450.
- [6] A. Perelli, L. De Marchi, A. Marzani, and N. Speciale, “Passive impacts localization based on dispersion compensation and cross-correlated signals wavelet analysis,” in *AIP Conf. Proc.*, vol. 1433, no. 1, May 2012, pp. 431–434.

- [7] —, “Acoustic emission localization in plates with dispersion and reverberations using sparse PZT sensors in passive mode,” *Smart Materials and Structures*, vol. 21, no. 2, 2012.
- [8] A. Perelli, C. Caione, L. De Marchi, D. Brunelli, A. Marzani, and L. Benini, “Design of an Ultra-low Power Device for Aircraft Structural Health Monitoring,” in *Design, Automation & Test in Europe Conference & Exhibition (DATE), 2013*. IEEE, 2013, pp. 1127–1130.
- [9] A. Perelli, L. De Marchi, A. Marzani, and N. Speciale, “Frequency Warped Cross-Wavelet Multiresolution Analysis of Guided Waves for Impact Localization,” *Signal Processing*, vol. 96, pp. 51–62, March 2014.
- [10] L. De Marchi, A. Perelli, and A. Marzani, “A signal processing approach to exploit chirp excitation in Lamb wave defect detection and localization procedures,” *Mechanical Systems and Signal Processing*, pp. 1–12, 2012.
- [11] L. De Marchi, A. Marzani, M. Miniaci, A. Perelli, and N. Testoni, “Localization of defects in irregular waveguides by dispersion compensation and pulse compression,” in *Proceedings of SPIE - Health Monitoring of Structural and Biological Systems 2013*, vol. 8695. SPIE-International Society for Optical Engineering, 2013, pp. 1–10.
- [12] A. Perelli, L. D. Marchi, E. Baravelli, and A. Marzani, “Warped-Wigner-Hough Transformation of Lamb Waves for Automatic Defect Detection,” in *IEEE International Ultrasonics Symposium (IUS), 2012*, pp. 1084–1087.
- [13] A. Perelli, T. Di Ianni, A. Marzani, L. De Marchi, and G. Masetti, “Model-Based Compressive Sensing for Damage Localization in Lamb Wave Inspection,” *IEEE Transactions on Ultrasonics, Ferroelectrics and Frequency control*, vol. 60, no. 10, pp. 2089–2097, 2013.
- [14] A. Perelli, L. De Marchi, L. Flamigni, and A. Marzani, “Wavelet Best Basis Compressed Sensing of Ultrasonic Guided Waves,” in *Proceedings of SPIE -*

- Health Monitoring of Structural and Biological Systems 2013*, vol. 8695. SPIE-International Society for Optical Engineering, 2013, pp. 1–8.
- [15] A. Vary, *Nondestructive testing handbook*, McGraw-Hill, Ed. McGraw-Hill, 2007, vol. 7.
- [16] B. Castagnede, Y. Kwang, W. Sachse, and M. Thompson, *Journal of Applied Physics*, vol. 70, pp. 150–157, 1990.
- [17] G. Liu, X. Han, and K. Lam, *Journal of Composite Material*, vol. 35, pp. 954–971, 2001.
- [18] K. Balasubramaniam and N. Rao, “Inversion of composite material elastic constants from ultrasonic bulk wave phase velocity data using genetic algorithms,” *Composites Part B: Engineering*, vol. 295, pp. 171–180, 1998.
- [19] J. Vishnuvardhan, C. Kishnamurthy, and K. Balasubramaniam, “Genetic algorithm based reconstruction of the elastic moduli of orthotropic plates using an ultrasonic guided wave single transmitter-multiple-receiver SHM array,” *Smart Materials and Structures*, vol. 16, pp. 1639–1650, 2007.
- [20] I. Bartoli, A. Marzani, F. Lanza di Scalea, and E. Viola, “Modeling wave propagation in damped waveguides of arbitrary cross-section,” *Journal of Sound and Vibration*, vol. 295, pp. 685–707, 2006.
- [21] L. De Marchi, A. Marzani, S. Caporale, and N. Speciale, “Ultrasonic guided waves characterization with warped frequency transforms,” *IEEE Trans. on Ultrasonics, Ferroelectrics, and Frequency Control*, vol. 56, no. 10, pp. 2232–2240, 2009.
- [22] P. Flandrin, F. Auger, and E. . Chassande-Mottin, “Time- frequency reassignment: From principles to algorithms.” pp. 179–203., 2003.
- [23] P. Wilcox, “Omni-directional guided wave transducer arrays for the rapid inspection of large areas of plate structures,” *IEEE Trans. on Ultrasonics, Ferroelectrics and Frequency Control*, vol. 50, no. 6, pp. 699–709, 2003.

- [24] J. S. Hall and J. E. Michaels, “Adaptive dispersion compensation for guided wave imaging,” in *AIP Conference Proceedings*, vol. 1430, 2012, pp. 623–630.
- [25] L. Yu and V. Giurgiutiu, “In situ 2-D piezoelectric wafer active sensors arrays for guided wave damage detection,” *Ultrasonics*, vol. 48, no. 2, pp. 117–134, 2008.
- [26] R. Baraniuk and D. Jones, “Unitary equivalence: a new twist on signal processing,” *IEEE Trans. on Signal Proc.*, vol. 43, no. 10, pp. 2269–2282, october 1995.
- [27] A. Oppenheim and D. Johnson, “Discrete representation of signals,” *Proceedings IEEE*, vol. 60, no. 6, pp. 681–691, 1972.
- [28] J. Fessler and B. Sutton, “Nonuniform fast Fourier transforms using min-max interpolation,” *IEEE Trans. on Signal Proc.*, vol. 51, no. 2, pp. 560–574, 2003.
- [29] B. Yoo, A. Purekar, Y. Zhang, and D. Pines, “Piezoelectric-paint-based two-dimensional phased sensor arrays for structural health monitoring of thin panels,” *Smart Mater, and Struct.*, vol. 19, p. 075017, 2010.
- [30] W. J. Staszewski, K. Worden, R. Wardle, and G. R. Tomlinson, “Fail-safe sensor distribution for impact detection in composite materials,” *Smart Mater. Struct.*, vol. 9, pp. 298–303, 2000.
- [31] D. Akopian, A. Melkonyan, and C. Chen, “Validation of HDOP Measure for Impact Detection in Sensor Network-Based Structural Health Monitoring,” *Sensors Journal, IEEE*, vol. 9, no. 9, pp. 1098–1102, 2009.
- [32] J. Markmiller and F. Chang, “Sensor Network Optimization for a Passive Sensing Impact Detection Technique,” *Structural Health Monitoring*, vol. 9, no. 1, p. 25, 2010.
- [33] E. B. Flynn and M. Todd, “A Bayesian approach to optimal sensor placement for structural health monitoring with application to active sensing,” *Mech. Sys. and Signal Proc.*, vol. 24, pp. 891–903, 2010.

- [34] W. J. Staszewski, C. Boller, and G. R. Tomlinson, *Health Monitoring of Aerospace Structures*. John Wiley & Sons, Ltf, 2004.
- [35] T. Kosel, I. Grabec, and P. Muzic, “Location of acoustic emission sources generated by air flow,” *Ultrasonics*, vol. 38, no. 1-8, pp. 824–826, 2000.
- [36] B. Wang, J. Takatsubo, Y. Akimune, and H. Tsuda, “Development of a remote impact damage identification system,” *Structural Control and Health Monitoring*, vol. 12, no. 3-4, pp. 301–314, 2005.
- [37] F. Ciampa and M. Meo, “Acoustic emission source localization and velocity determination of the fundamental mode A0 using wavelet analysis and Newton-based optimization technique,” *Smart Mat. and Struc.*, vol. 19, 2010.
- [38] M. Vetterli and J. Kovacevic, *Wavelets and Subband Coding*. Prentice, 1995.
- [39] A. Papandreou-Suppappola, R. Murray, B.-G. Iem, and G. Boudreaux-Bartels, “Group delay shift covariant quadratic time-frequency representations,” *IEEE Trans. on Signal Proc.*, vol. 49, no. 11, pp. 2549–2564, 2001.
- [40] S. Franz, S. Mitra, and G. Doblinger, “Frequency estimation using warped discrete Fourier transform,” *Signal Proc.*, vol. 83, no. 8, pp. 1661–1671, 2003.
- [41] S. Caporale, L. De Marchi, and N. Speciale, “Fast Computation of Frequency Warping Transforms,” *IEEE Trans. on Signal Processing*, vol. 58, no. 3, pp. 1110–1121, 2010.
- [42] F. Schäfer and R. Janovsky, “Impact sensor network for detection of hypervelocity impacts on spacecraft,” *Acta Astronautica*, vol. 61, no. 10, pp. 901–911, 2007.
- [43] T. Kundu and K. Jata, “Detection of the point of impact on a stiffened plate by the acoustic emission technique,” *Smart Mater. Struct.*, vol. 18, p. 035006, 2009.

- [44] M. Tracy and F. Chang, "Identifying Impacts in Composite Plates with Piezoelectric Strain Sensors, Part II: Experiment," *J Intel. Mat. Syst. Str.*, vol. 9, no. 11, p. 929, 1998.
- [45] R. Seydel and F. Chang, "Impact identification of stiffened composite panels: I. System development," *Smart Mater. Struct.*, vol. 10, no. 2, pp. 354–369, 2001.
- [46] P. White, "Cross Correlation in Structural Systems: Dispersion and Nondispersion Waves," *J. Acoust. Soc. Am.*, vol. 45, pp. 1118–1128, 1969.
- [47] M. Azaria and D. Hertz, "Time Delay Estimation by Generalized Cross Correlation Methods," *IEEE Trans. on Acoustic Speech*, no. 2, April 1984.
- [48] M. Cobos, A. Marti, and J. J. Lopez, "A Modified SRP-PHAT Functional for Robust Real-Time Sound Source Localization With Scalable Spatial Sampling," *IEEE Signal Proc. Letter*, vol. 18, no. 1, Jan. 2011.
- [49] Y. Chan and K. Ho, "A simple and efficient estimator for hyperbolic location," *IEEE Trans. on Signal Proc.*, vol. 42, no. 8, pp. 1905–1915, aug 1994.
- [50] A. Urruela, J. Sala, and J. Riba, "Average performance analysis of circular and hyperbolic geolocation," *IEEE Trans. on Vehic. Technology*, vol. 55, no. 1, pp. 52–66, jan. 2006.
- [51] P. D. Wilcox, "A rapid signal processing technique to remove the effect of dispersion from guided wave signals," *IEEE Trans. Ultrason., Ferroelectr., Freq. Control*, vol. 50, no. 4, pp. 419–427, 2003.
- [52] J. Fessler and B. Sutton, "Nonuniform fast Fourier transforms using min-max interpolation," *IEEE Trans. Signal Process*, vol. 51, no. 2, pp. 560–573, 2003.
- [53] L. De Marchi, A. Marzani, N. Speciale, and E. Viola, "A passive monitoring technique based on dispersion compensation to locate impacts in plate-like structures," *Smart Materials and Structures*, vol. 20, 2011.

- [54] O. Diligent, M. J. S. Lowe, E. L. Clézio, M. Castaings, and B. Hosten, “Prediction and measurement of nonpropagating Lamb modes at the free end of a plate when the fundamental antisymmetric mode A0 is incident,” *J. of the Ac. Soc. of Am.*, vol. 113, no. 6, pp. 3032–3042, 2003.
- [55] M. Misiti, Y. Misiti, G. Oppenheim, and J. M. Poggi, *Les ondelettes et leurs applications*. Hermes, Feb. 2003.
- [56] D. Marquardt, “An Algorithm for Least-Squares Estimation of Nonlinear Parameters,” *SIAM Journal on Applied Mathematics*, vol. 11, pp. 431–441, 1963.
- [57] M. Deffenbaugh, J. Bellingham, and H. Schmidt, “The relationship between spherical and hyperbolic positioning,” *Oceans Mts IEEE. Conf. Proc.*, vol. 2, pp. 590–595, 1996.
- [58] C. De Boor, R. DeVore, and A. Ron, “On the construction of multivariate (pre)wavelets,” *Constructive Approximation*, vol. 9, no. 2-3, pp. 123–166, 1993.
- [59] S. Mallat, *A Wavelet Tour of Signal Processing*. Ac. Press Elsevier, 2009.
- [60] M. Unser and T. Blu, “Cardinal exponential splines: Part I - Theory and filtering algorithms,” *IEEE Trans. on Signal Proc.*, vol. 53, no. 4, pp. 1425–1438, 2005.
- [61] D. Boyle, M. Magno, B. O’Flynn, D. Brunelli, E. Popovici, and L. Benini, “Towards persistent structural health monitoring through sustainable wireless sensor networks,” in *Intelligent Sensors, Sensor Networks and Information Processing (ISSNIP), 2011 Seventh International Conference on*, 2011, pp. 323–328.
- [62] L. Benini, D. Brunelli, C. Petrioli, and S. Silvestri, “GENESI: Green sEnzor NEtworks for Structural monItoring,” in *Sensor Mesh and Ad Hoc Communications and Networks (SECON), 2010 7th Annual IEEE Communications Society Conference on*, 2010, pp. 1–3.

- [63] X. Zhao, T. Qian, G. Mei, C. Kwan, R. Zane, C. Walsh, T. Paing, and Z. Popovic, “Active health monitoring of an aircraft wing with an embedded piezoelectric sensor/actuator network: II wireless approaches.” *Smart Material and Structures*, vol. 16, pp. 1218–1225, 2007.
- [64] L. Liu and F. Yuan, “Active damage localization for plate-like structures using wireless sensors and a distributed algorithm,” *Smart Material and Structures*, vol. 17, p. 055022, 2008.
- [65] B. Aygun and V. Gungor, “Wireless sensor networks for structure health monitoring: recent advances and future research directions,” *Sensor Review*, vol. 31, no. 3, pp. 261–276, 2011.
- [66] J. L. Rose, *Ultrasonic Waves in Solid Media*. Cambridge University Press., 1999.
- [67] Z. Su and L. Ye, *Identification of damage using Lamb waves*. Springer., 2009.
- [68] M. Niethammer, L. Jacobs, J. Qu, and J. Jarrzynski, “Time-frequency representations of lamb waves,” *J. Acoust. Soc. Am.*, vol. 109, pp. 1841–1847, 2001.
- [69] A. Leger and M. C. Deshamps, *Ultrasonic Wave Propagation in Non Homogeneous Media*. Springer, 2009.
- [70] R. Sicard, J. Goyette, and D. Zellouf, “A numerical dispersion compensation technique for time recompression of Lamb wave signals,” *Ultrasonics*, vol. 40, no. 1-8, pp. 727–732, 2002.
- [71] R. Benz, M. Niethammer, S. Hurlebaus, and L. J. Jacobs, “Localization of notches with Lamb waves,” *J. Acoust. Soc. of Am.*, vol. 114, no. 2, pp. 677–685, 2003.
- [72] A. Raghavan and C. Cesnik, “Guided-wave signal processing using chirplet matching pursuits and mode correlation for structural health monitoring,” *Smart Material and Structures*, vol. 16, no. 2, p. 355, 2007.

- [73] L. De Marchi, M. Ruzzene, B. Xu, E. Baravelli, and N. Speciale, “Warped basis pursuit for damage detection using Lamb waves,” *Ultrasonics, Ferroelectrics and Frequency Control, IEEE Transactions on*, vol. 57, no. 12, pp. 2734–2741, 2010.
- [74] M. Pollakowski and H. Ermert, “Chirp signal matching and signal power optimization in pulse-echo mode ultrasonic nondestructive testing,” *IEEE Trans. Ultrasonic Ferroelect. Freq. Control*, vol. 41, pp. 655–659, 1994.
- [75] D. Cowell and S. Freear, “Quinary excitation method for pulse compression ultrasound measurements,” *Ultrasonics*, vol. 48, pp. 98–108, 2008.
- [76] L. De Marchi, A. Marzani, N. Speciale, and E. Viola, “A passive monitoring technique based on dispersion compensation to locate impacts in plate-like structures,” *Smart Mater. and Struct.*, vol. 20, 2011.
- [77] —, “Prediction of pulse dispersion in tapered waveguides,” *NDT International*, vol. 43, pp. 265–271, 2010.
- [78] K. Xu, D. Ta, P. Moilanen, and W. Wang, “Mode separation of lamb waves based on dispersion compensation method,” *The Journal of the Acoustical Society of America*, vol. 131, pp. 2714–2722, 2012.
- [79] L. De Marchi, A. Marzani, and M. Miniaci, “A dispersion compensation procedure to extend pulse-echo defects location to irregular waveguides,” *NDT & E International*, vol. 54, pp. 115–122, 2013.
- [80] R. S. Edwards, B. Dutton, A. R. Clough, and M. H. Rosli, “Enhancement of ultrasonic surface waves at wedge tips and angled defects,” *Applied Physics Letters*, vol. 99, 2011.
- [81] M. El-Kettani, F. Luppè, and A. Guillet, “Guided waves in a plate with linearly varying thickness: experimental and numerical results,” *Ultrasonics*, vol. 42, pp. 807–812, 2004.

- [82] P. Marical, M. El-Kettani, M. G. w. i. e. p. w. g. s. v. E. Predoi, and numerical results, *Ultrasonics*, vol. 47, pp. 1–9, 2007.
- [83] M. Predoi, M. Kettani, Z. Hamitouche, and C. C. Petre, “Guided waves in plates with linear variation of thickness,” *The Journal of the Acoustical Society of America*, vol. 123, pp. 3834–3834, 2008.
- [84] L. Shapiro and G. Stockman, *Computer Vision*, 2001st ed. Prentice-Hall, Inc.
- [85] S. Barbarossa, “Analysis of multicomponent LFM signals by a combined Wigner-Hough transform,” *IEEE Transation on Signal Processing*, vol. 43, no. 6, pp. 1511–1515, 1995.
- [86] I. Bartoli, A. Marzani, F. L. di Scalea, and E. Viola, “Modeling wave propagation in damped waveguides of arbitrary cross-section,” *Journal of Sound and Vibration*, vol. 295, pp. 685–707, 2006.
- [87] E. Candes and M. Wakin, “An Introduction To Compressive Sampling,” *IEEE Signal Processing Magazine*, vol. 25, no. 2, pp. 21–30, 2008.
- [88] D. Needell and J. Tropp, “CoSaMP: Iterative signal recovery from incomplete and inaccurate samples,” *Applied and Computational Harmonic Analysis*, vol. 26, no. 3, pp. 301–321, 2009.
- [89] M. F. Schiffner and G. Schmitz, “Fast Pulse-Echo Ultrasound Imaging Employing Compressive Sensing,” in *Proc. IEEE Int. Ultrasonics Symposium (IUS)*, 2011, pp. 688–691.
- [90] C. Quinsac, A. Basarab, and D. Kouamé, “Frequency Domain Compressive Sampling for Ultrasound Imaging,” *Advances in Acoustics and Vibration*, vol. 2012, 2012.
- [91] N. Wagner, Y. C. Eldar, and Z. Friedman, “Compressed beamforming in ultrasound imaging,” *Signal Processing, IEEE Transactions on*, vol. 60, no. 9, pp. 4643–4657, 2012.

- [92] J. Harley and J. Moura, “Sparse Recovery of the Multimodal and Dispersive Characteristics of Lamb Waves,” *Journal of the Acoustical Society of America*, vol. in press.
- [93] K. Kaaresen and E. Bolviken, “Blind deconvolution of ultrasonic traces accounting for pulse variance,” *Ultrasonics, Ferroelectrics and Frequency Control, IEEE Transactions on*, vol. 46, no. 3, pp. 564–573, 1999.
- [94] R. Baraniuk, V. Cevher, M. Duarte, and C. Hegde, “Model-based compressive sensing,” *IEEE Transactions on Information Theory*, vol. 56, no. 4, pp. 1982–2001, 2010.
- [95] C. Hegde and R. Baraniuk, “Sampling and recovery of pulse streams,” *IEEE Transactions on Signal Processing*, vol. 59, no. 4, pp. 1505–1517, 2011.
- [96] S. Caporale, L. De Marchi, and N. Speciale, “Frequency warping biorthogonal frames,” *Signal Processing, IEEE Transactions on*, vol. 59, no. 6, pp. 2575–2584, 2011.
- [97] P. Bocchini, A. Marzani, and E. Viola, “Graphical User Interface for Guided Acoustic Waves,” *Journal of Computing in Civil Engineering*, vol. 25, no. 3, pp. 202–210, 2011.
- [98] L. De Marchi, A. Ceruti, A. Marzani, and A. Liverani, “Augmented Reality to support on-field post-impact maintenance operations on thin structures,” *submitted to Journal of Sensors*, 2013.
- [99] M. L. Fowler, M. Chen, J. A. Johnson, and Z. Zhou, “Data compression using {SVD} and Fisher information for radar emitter location,” *Signal Processing*, vol. 90, no. 7, pp. 2190–2202, 2010.
- [100] A. Perelli, L. De Marchi, A. Marzani, and N. Speciale, “Acoustic emission localization in plates with dispersion and reverberations using sparse PZT sensors in passive mode,” *Journal of Smart Materials and Structures*, vol. 21, no. 2, p. 025010, 2012.

- [101] M. Nielsen, E. N. Kamavuako, M. M. Andersen, M. F. Lucas, and D. Farina, “Optimal wavelets for biomedical signal compression,” *Med. Biol. Eng. Comput.*, vol. 44, pp. 561–568, 2006.
- [102] D. Donoho, “Compressed sensing,” *IEEE Transactions on Information Theory*, vol. 52, no. 4, pp. 1289–1306, 2006.
- [103] M. Holschneider, M. S. Diallo, M. Kulesh, M. Ohrnberger, E. Luck, and F. Scherbaum, “Characterization of dispersive surface waves using continuous wavelet transforms,” *Geophysical Journal International*, vol. 163, no. 2, pp. 463–478, 2005.
- [104] G. L. Touzè, B. Nicolas, J. I. Mars, and L. J. L, “Matched Representations and Filters for Guided Waves,” *IEEE Transactions on Signal Processing*, vol. 57, no. 5, pp. 1783–1795, 2009.
- [105] M. Abo-Zahhad, A. F. Al-Ajlouni, S. M. Ahmed, and R. Schilling, “A new algorithm for the compression of {ECG} signals based on mother wavelet parameterization and best-threshold levels selection,” *Digital Signal Processing*, vol. 23, no. 3, pp. 1002–1011, 2013.
- [106] R. R. Coifman and M. L. Wickerhauser, “Entropy based algorithms for best basis selection.” *IEEE Transactions on Information Theory*, vol. 38, no. 2, March 1992.
- [107] P. P. Vaidyanathan, “Multirate Systems and Filter Banks,” 1993.
- [108] L. Shapiro, “Embedded image coding using zerotrees of wavelet coefficients,” *IEEE Transactions on Signal Processing*, vol. 41, no. 12, 1993.
- [109] C. E. Leiserson, R. L. Rivest, C. Stein, and T. H. Cormen, *Introduction to algorithms*. The MIT press, 2001.
- [110] L. Brechet, M. F. Lucas, C. Doncarli, and D. Farina, “Compression of Biomedical Signals With Mother Wavelet Optimization and Best-Basis Wavelet Packet

- Selection,” *IEEE Trans. on Biomedical Engineering*, vol. 54, no. 12, pp. 2186–2192, 2007.
- [111] G. Shi, J. Lin, X. Chen, F. Qi, D. Liu, and L. Zhang, “UWB echo signal detection with ultra-low rate sampling based on compressed sensing,” *Circuits and Systems II: Express Briefs, IEEE Transactions on*, vol. 55, no. 4, pp. 379–383, 2008.
- [112] F. Chen, A. P. Chandrakasan, and V. M. Stojanovic, “Design and analysis of a hardware-efficient compressed sensing architecture for data compression in wireless sensors,” *Solid-State Circuits, IEEE Journal of*, vol. 47, no. 3, pp. 744–756, 2012.
- [113] G. Peyré, “Best Basis Compressed Sensing,” *IEEE Transactions on Signal Processing*, vol. 58, no. 5, pp. 2613–2622, 2010.